

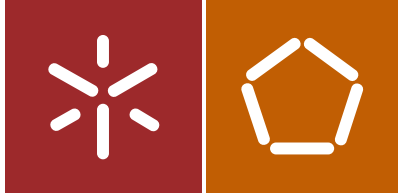


Universidade do Minho
Escola de Engenharia

Ricardo Figueirêdo de Sá | Industrial machine structural components' optimization and redesign

Ricardo Figueirêdo de Sá

Industrial machine structural
components' optimization and redesign



Universidade do Minho
Escola de Engenharia

Ricardo Figueirêdo de Sá

Industrial machine structural
components' optimization and redesign

Tese de Doutoramento
Doutoramento em Líderes para as Indústrias Tecnológicas

Trabalho efetuado sob a orientação de
Professor Doutor João Pedro Lourenço Gil Nunes
Professor Doutor Ferrie Wander Joseph van Hattum
Professor Doutor José Manuel de Almeida César de Sá

Direitos de autor e condições de utilização do trabalho por terceiros

Este é um trabalho académico que pode ser utilizado por terceiros desde que respeitadas as regras e boas práticas internacionalmente aceites, no que concerne aos direitos de autor e direitos conexos.

Assim, o presente trabalho pode ser utilizado nos termos previstos na licença abaixo indicada.

Caso o utilizador necessite de permissão para poder fazer um uso do trabalho em condições não previstas no licenciamento indicado, deverá contactar o autor, através do RepositóriUM da Universidade do Minho.



Atribuição

CC BY

<https://creativecommons.org/licenses/by/4.0/>

Acknowledgments

My first acknowledgement is for my supervision team, namely Professors João Pedro Nunes, Ferrie van Hattum, and João César Sá. Amongst these, I would like to leave a special word of gratitude to Professor João Pedro Nunes, for the availability, patience, and interest in the past few years. I would not be able to complete this work without your support, key in many situations. He went beyond his obligations as a supervisor many times, and my gratitude for that is immense.

To the whole team at Adira - Metal Forming Solutions, S.A, namely Tiago Brito e Faro and João Paulo Santos, I would like to express my gratitude for all the time dedicated to this project and information and knowledge shared.

I would also like to thank to the whole MIT Portugal Program organization, more specifically the one linked to LTI along the years, both the faculty and administrative staff. This programme has led me learn a lot, experience new things, both in Portugal and abroad and, probably most importantly, make friends along the way. These constitute the most valuable result of this experience.

The number of fields touched by this thesis led me to look for support in many fields of knowledge. At University of Minho, I always found open doors and minds to help with my struggles. In this aspect I must point out Professor Ismael Vaz, from Department of Production and Systems/Algoritmi Research Center. His contributions for the implementation of the optimization routine were of incredible value and made me fan of this field of knowledge and its immense potential.

PIEP is an institution that is very special to me, not only because of the development I had there as a person and as a professional, or because the people I have met there and became true and valuable friends, but also because of the help that both the institution and the technical staff gave in the materialization of this

work. I will be missing people, but I would like to mention Carlos Azevedo, Nuno Gonçalves, Luis Oliveira, Bruno Barros, Ricardo Ferreira, Rafael Alves, Nuno Vieira, Agnieszka Rocha, and, as the director in charge at the time, Rui Magalhães. Despite these being the ones more directly involved, other have also contributed to my work.

I would also like to thank the availability that three people demonstrated in the period closer to the conclusion of my PhD thesis production. Professors Alexandre Ferreira da Silva, Pedro Arezes, and Guilherme Pereira were kind and patient enough to help me with the conclusion process that, thanks to them, was much smoother.

Many times, I needed support from family and friends, and I, as throughout my whole life, I was able to find it from an extensive group of people that truly care for me and are constantly willing to make room for me and my needs, regardless of what these might be. There are too many to mention all, but there are a few I must point out. My parents are incredible and have always shown their unconditional love. I am a proud son, profoundly grateful for them. My wife is the driver that helps me to overcome my struggles without missing the ephemeral relevant episodes that constitute happiness. To my beautiful and bright son Gonçalo, the main character of many of such episodes, thank you so much and may you always feel as loved and supported as I have been all my life. As for all my friends and family, who stayed with me through, also, all this experience, knew how to support me, even when it included not mentioning my PhD, I truly appreciate your presence and dedication and hope to continue to enjoy your presence for many years.

Lastly, I would like to thank the Portuguese Foundation for Science and Technology, for providing financial support to this project through scholarship number SFRH/BD/51106/2010.

Statement of Integrity

I hereby declare having conducted this academic work with integrity. I confirm that I have not used plagiarism or any form of undue use of information or falsification of results along the process leading to its elaboration. I further declare that I have fully acknowledged the Code of Ethical Conduct of the University of Minho.

Resumo

O corte por laser é um processo altamente flexível com numerosas vantagens sobre tecnologias concorrentes. O crescimento do mercado é revelador do seu potencial, totalizando 4300 milhões de dólares americanos em 2020. O processo é utilizado em muitas indústrias e as tendências atuais passam por melhorias ao nível do tempo de ciclo, qualidade, custos e exatidão.

Os materiais compósitos (nomeadamente polímeros reforçados por fibras) apresentam propriedades mecânicas atrativas para várias aplicações, incluindo a que se relaciona com o presente trabalho: componentes de máquinas industriais. A utilização de compósitos resulta tipicamente em máquinas mais eficientes, exatidão dimensional acrescida, melhor qualidade superficial, melhor eficiência energética e menor impacto ambiental.

O principal objetivo deste trabalho é aumentar a produtividade de uma máquina de corte laser, através do redesign de um componente crítico (o pórtico), grande influenciador da exatidão da máquina. Pretende-se com isto criar uma metodologia genérica capaz de auxiliar no processo de redesign de componentes industriais. Dado que o problema lida com dois objetivos concorrentes (redução de peso e aumento de rigidez) e com um elevado número de variáveis, a implementação de uma rotina de otimização é um aspeto central. É crucial demonstrar que o processo de otimização proposto resulta em soluções efetivas. Estas foram validadas através de análise de elementos finitos e de validação experimental, com recurso a um protótipo à escala.

O algoritmo de otimização usado é uma metaheurística, inspirado no comportamento de grupos de animais. Algoritmos *Particle Swarm* são sugeridos com sucesso para problemas de otimização semelhantes. A otimização focou-se na espessura de cada laminado, para diferentes orientações.

A rotina de otimização resultou na definição de uma solução quase-ótima para os laminados analisados e permitiu a redução do peso da peça em 43% relativamente à solução atual, bem como um aumento de 25% na aceleração máxima permitida, o que se reflete na produtividade da máquina, enquanto a mesma exatidão é garantida.

A comparação entre os resultados numéricos e experimentais para os protótipos mostra uma boa concordância, com divergências pontuais, mas que ainda assim resultam na validação do modelo de elementos finitos no qual se baseia a otimização.

Palavras-chave: Componentes mecânicos; Compósitos; Corte Laser; Otimização.

Abstract

Laser cutting is a highly flexible process with numerous advantages over competing technologies. These have ensured the growth of its market, totalling 4300 million United States dollars in 2020. Being used in many industries, the current trends are focused on reduced lead time, increased quality standards and competitive costs, while ensuring accuracy.

Composite materials (namely fibre reinforced polymers) present attractive mechanical properties that poses them as advantageous for several applications, including the matter of this thesis: industrial machine components. The use of these materials leads to machines with higher efficiency, dimensional accuracy, surface quality, energy efficiency, and environmental impact.

The main goal of this work is to increase the productivity of a laser cutting machine through the redesign of a critical component (gantry), also key for the overall machine accuracy. Beyond that, it is intended that this work lays out a methodology capable of assisting in the redesign of other machine critical components. As the problem leads with two opposing objectives (reducing weight and increasing stiffness), and with many variables, the implementation of an optimization routine is a central aspect of the present work. It is of major importance that the proposed optimization method leads to reliable results, demonstrated in this work by a finite element analysis and through experimental validation, by means of a scale prototype.

The optimization algorithm selected is a metaheuristic inspired by the behaviour of swarms of animals. Particle swarm algorithms are proven to provide good and fast results in similar optimization problems. The optimization was performed focusing on the thickness of each laminate and on the orientations present in these.

The optimization routine resulted in a definition of a near-optimal solution for the laminates analysed and allowed a weight reduction of 43% regarding the current solution, as well as an increase of 25% in the maximum allowed acceleration, which reflects on the productivity of the machine, while ensuring the same accuracy.

The comparison between numeric and experimental testing of the prototypes shows a good agreement, with punctual divergences, but that still validates the Finite elements upon which the optimization process is supported.

Keywords: Composite materials; Laser Cutting; Machine components; Optimization.

Table of Contents

Direitos de autor e condições de utilização do trabalho por terceiros.....	ii
Acknowledgments.....	iii
Statement of Integrity	v
Resumo.....	vi
Abstract.....	vii
Table of Contents	viii
Acronyms and Abbreviations.....	xiii
List of Figures.....	xv
List of Tables.....	xxi
Chapter 1: Introduction.....	1
1.1 Laser Cutting Machine Context.....	1
1.2 Work Performed and document structure.....	2
1.3 Research Objectives.....	4
Chapter 2: Literature review.....	5
2.1 Laser Cutting Machines.....	5
2.2 Composite Materials.....	9
2.2.1 Polymer Matrix Composites	12
2.2.1.1 Polymer matrices.....	14
2.2.1.2 Reinforcements	15

2.2.1.3	Fields of application	16
2.2.1.4	Production techniques	18
2.3	Finite Elements	23
2.4	Optimisation Methods.....	25
2.4.1	Derivative-free optimisation algorithms.....	27
2.4.2	Metaheuristic	30
2.4.3	Optimisation of Mechanical Structures	35
Chapter 3:	Theoretical Framework	43
3.1	Deflection and torsion of beams	43
3.1.1	Distributed loads	44
3.1.2	Point loads	46
3.2	Geometry	49
3.2.1	Definition of a plane.....	49
3.2.2	Determination of the intersection between a line and a plane	51
3.2.3	Reflection as Rotation of 180° about an arbitrary axis.....	52
3.3	Finite Elements	56
3.3.1	Steps of the Finite Element Method application	57
3.3.1.1	Discretization.....	57
3.3.1.2	Interpolation Model.....	60
3.3.1.3	Deriving the element stiffness matrix and equations.	63
3.3.1.4	Assembling element equations to obtain overall equilibrium equations.....	64
3.3.1.5	Calculation of nodal displacement.....	65
3.3.1.6	Computation of the desired secondary quantities.....	66
3.4	Optimisation.....	70
3.4.1	Types of optimization problems.....	72

3.4.1.1	Constraints.....	72
3.4.1.2	Admissible values for functions	73
3.4.1.3	Linearity	73
3.4.1.4	Objective Function Surface.....	73
3.4.1.5	The nature of optimisation algorithms used	74
Chapter 4:	Experimental Procedure.....	75
4.1	Equipment under study	75
4.2	Loading scenario	79
4.2.1	Identification of the most critical Loading Scenario	82
4.2.1.1	Calculating Deformations	83
4.2.1.2	Calculate the laser path through reflection.....	84
4.2.1.3	Combining deformations and reflection to calculate the precision loss	85
4.3	Section estimation of an equivalent composite gantry.....	87
4.3.1	Analysis of the metallic gantry.....	87
4.3.2	Analytical dimensioning of a composite gantry.....	91
4.3.3	Numerical analysis of the composite gantry.....	95
4.4	Optimization of the composite gantry.....	98
4.4.1	Geometry optimization.....	101
4.4.2	Thickness optimization	105
4.4.2.1	Part Geometry	106
4.4.2.2	Material Properties	107
4.4.2.3	Layup.....	110
4.4.2.4	Discretization.....	111
4.4.2.5	Loads.....	115
4.4.2.6	Interaction between the parts.....	116

4.4.2.7	Boundary conditions	117
4.4.2.8	Information contained in the output file.	117
4.4.2.9	Optimization loop.....	118
Chapter 5:	Production and Numerical Simulation of the Gantry Prototypes.....	123
5.1	Numeric model Validation.....	123
5.1.1	Material Mechanical Characterization.....	124
5.1.1.1	Raw materials.....	124
5.1.1.2	Standards followed	125
5.1.1.3	Preparation of samples	125
5.1.1.4	Testing equipment.....	128
5.1.1.5	Tensile tests	129
5.1.1.6	Shear testing adhesives	129
5.1.2	Production of the prototype gantry	130
5.1.2.1	Moulds manufacture.....	131
5.1.2.2	Production of the composite parts.....	134
5.1.2.3	Composite parts finishing.....	140
5.1.2.4	Thickness verification.....	144
5.1.2.5	Adhesive inspection	146
5.1.3	Mechanical testing of the gantry prototypes.....	150
5.1.4	Numerical Simulation of the mechanical behaviour of the composite prototype gantry.....	152
5.1.4.1	Mechanical Properties	153
5.1.4.2	Layup.....	154
5.1.4.3	Load.....	155
5.1.4.4	Interaction Between the Parts	156
5.1.5	Discretization.....	157

Chapter 6: Results and Discussion	160
6.1 Identification of the most critical Loading Scenario	160
6.2 Numerical analysis of the metallic gantry	165
6.3 Section estimation of an equivalent composite gantry.....	168
6.3.1 Numerical analysis of composite gantry	168
6.4 Optimization of the composite gantry	173
6.5 Numeric Model Validation.....	180
6.5.1 Tensile Tests	180
6.5.2 Lap shear tests.....	183
6.5.3 Mechanical testing of the gantry prototypes.....	185
6.5.4 Numerical Simulation of the mechanical behaviour of the composite prototype gantry.....	188
6.5.5 Comparison between experimental and numerical results	190
Chapter 7: Conclusions.....	196
7.1 Main Conclusions.....	196
7.2 Future work.....	197
Bibliography	199
Appendix A – Woven Carbon Fibre Fabric Datasheet.....	215
Appendix B – Carbon Fibre Mechanical Properties	217
Appendix C – EPIKOTE™ Resin 04908 and EPIKURE™ Curing Agent 04908 Datasheet	219
Appendix D – EPIKURE™ Curing Agent 3253 Datasheet.....	224
Appendix E – EPX Adhesive DP490 Datasheet	228
Appendix F – Hysol® EA 9394 Datasheet.....	233
Appendix G – Hysol® Surface Preparation Guide	238
Appendix H – SikaBlock® M700 Datasheet	250

Acronyms and Abbreviations

3D	Three-dimensional
CAD	Computer-Aided Design
CFRP	Carbon fibre reinforced polymers
CIRTM	Co-injection RTM
CMC	Ceramic matrix composites
CNC	Computer Numerical Control
DRDF	Double RIFT diaphragm forming
FE	Finite Elements
FEA	Finite Element Analysis
FEM	Finite Element Method
FRC	Fibre Reinforced Composites
FRP	Fibre Reinforced Polymers
GA	Genetic Algorithms
GFRP	Glass Fibre Reinforced Polymer
HfC	hafnium carbide
ILCM	Industrial Laser Cutting Machine
LM	Liquid Moulding
LRI	Liquid Resin Infusion
LTI	Leaders for Technical Industries
LVDT	Linear Variable Differential Transformers
MDF	Medium Density Fibreboard

MMC	Metal Matrix Composites
MVI	Modified Vacuum Infusion
NDT	Non-Destructive Testing
NURBS	Non-Uniform Rational B-Splines
OoA	Out-of-Autoclave
PLC	Programmable Logic Control
PMC	Polymer Matrix Composites
PSO	Particle Swarm Optimization
PTFE	Polytetrafluoroethylene
QPSO	Quantum Behaved Particle Swarm Optimisation
RFI	Resin Film Infusion
RIFT	Resin infusion Under Flexible Tooling
RIRM	Resin Injection Recirculation Moulding
RO	Research Objective
RTM	Resin Transfer Moulding
SCRIMP	Seemann Composites Resin Infusion Moulding
SiC	silicon carbide
TaC	tantalum carbide
USD	United States Dollars
V(A)RTM	Vacuum-Assisted Resin Transfer Moulding
VAIM	Vacuum-Assisted Injection Moulding
VAP	Vacuum-Assisted Processing
VARI	Vacuum-Assisted Resin Injection System
VARIM	Vacuum-Assisted Resin Injection Moulding
VEPSO	Vector Evaluated Particle Swarm Optimisation
VI	Vacuum Infusion
VIM	Vacuum Infusion Moulding
VIMP	Vacuum Infusion Moulding Process
VIP	Vacuum Infusion Process
VM/RTM	A Hybrid RIFT/RTM

List of Figures

Figure 2.1 – Fixed optics ILCM Amada Lasmac 645 [13]	6
Figure 2.2 - Effect of fibre orientation on the tensile strength of FRP composite [0a] [23].	11
Figure 2.3 - Forms of woven fabrics: (a) plain weave, (b) twill weave, and (c) satin weave (from [28]).	11
Figure 2.4 - Hierarchical structure of FRC and associated lengths scales for each level [30]	12
Figure 2.5 – Ashby diagram of the specific strength and stiffness of metallic and FRP alternatives [53]. ...	18
Figure 2.6 - Seeman Composites Resin Infusion Manufacturing Process [63].....	20
Figure 2.7 - Vacuum infusion mould assembly: 1–inlet, 2–vacuum bag, 3–distribution medium, 4–peel ply, 5–reinforcement, 6–outlet, 7–vacuum seal, 8–mould die (adapted from [64]).	21
Figure 2.8 – Overview of the Vacuum infusion configuration	21
Figure 2.9 Typical structure of a wind blade (adapted from [181] and [183])	38
Figure 3.1 – General case of distributed load on a simply supported beam	44
Figure 3.2 – Uniform distributed load over the entire span of a simply supported beam	44
Figure 3.3 – Cross-section of a rectangular section tube.....	45
Figure 3.4 – Depiction of a simply supported beam subjected to a generic point load	46
Figure 3.5 – Simply supported beam subjected to torsion	47
Figure 3.6 – Reflection of a line (V) in a plane mirror (M), generating a new line (R). This can be considered as a rotation of 180° about n.....	53
Figure 3.7 - Effect of the variation of number of elements in the accuracy of the solution [95]	58
Figure 3.8 – Commonly used elements families (adapted from [202])	58
Figure 3.9 - Polynomial approximation in one dimension (adapted from [201])	62
Figure 3.10 - Force System for Macroequilibrium of a body (adapted from [95]).....	67

Figure 4.1 -Adira's LP 3015 Laser cutting Machine (from [206]).....	76
Figure 4.2 - LP3015's structure – Positioning system (1), Laser Source (2), Smoke extractor (2), Cooling System (4), Air Compression system, Lubrication system and Electric Power system (5), Laser Source electric system (6), External Protections (7) and Gantry. Cutting Head and Optical Path (8) (adapted from [208]).	76
Figure 4.3 - Schematic depiction of the LP 3015 working and the cutting process. a) supporting structure; b) gantry; c) cutting head; d) stationary optical components; e) movable optical components; f) laser source; g) cutting spot.	77
Figure 4.4 – CO ₂ ILCM optical system and laser path	78
Figure 4.5 – Routine implemented in SciLab, resulting in an analytical model of the gantry.....	83
Figure 4.6 – Overview of the metallic gantry.....	88
Figure 4.7 – Ribs for metallic gantry reinforcement	88
Figure 4.8 – Loading scenario for metallic gantry analysis	89
Figure 4.9 – Mesh generated for the FEA of the metallic gantry	90
Figure 4.10 – Two cells representing two alternative configurations of the gantry, one with a solution that results in the violation of the maximum deformations and the other with deflections bellow the defined thresholds.	94
Figure 4.11 - Overall aspect of the numeric model.....	96
Figure 4.12 – Construction solution for the designed composite gantry.....	98
Figure 4.13 - Example of a Linear Motor characteristic Curve	99
Figure 4.14 – Maximum possible accelerations as a function of the gantry's mass	100
Figure 4.15 – Shape restriction areas identified by colours	102
Figure 4.16 – Shape generation process implemented	104
Figure 4.17 – Different section to be optimized, resulting in different variables.....	105
Figure 4.18 – Part geometry used for thickness optimization.....	106
Figure 4.19 – Properties (namely Young Modulus) of a carbon fibre laminate as a function of the percentage of different orientations (adapted from [28])	108
Figure 4.20 - Properties (namely Shear Modulus) of a carbon fibre laminate as a function of the percentage of different orientations (adapted from [28])	109
Figure 4.21 – Initial layup that displays the orientations considered.....	111

Figure 4.22 – Displacement of centre of mass of the cutting head and time required for simulation to run as a function of the number of elements.....	112
Figure 4.23 – Overall aspect of the mesh generated.....	114
Figure 4.24 – Detail of the mesh (corners of the ribs).....	114
Figure 4.25 – Mesh displaying elements with regular shape and near square configuration.	115
Figure 4.26 – Overview of the interactions defined in the Finite Element Model.....	116
Figure 4.27 – Boundary conditions of the model	117
Figure 4.28 – Overview of the optimization loop created.....	122
Figure 5.1 - Preparation of samples for testing	126
Figure 5.2 - Dimensions of shear testing samples according to the ASTM D 3165-00 standard	127
Figure 5.3 - Glued overlap (highlighted in white) used in the shear tests.....	128
Figure 5.4 - Universal testing equipment used for mechanical testing	128
Figure 5.5 - Scale prototype gantry produced	130
Figure 5.6 - The two polyurethane based moulds used in this work: a) for the outer U-shaped parts and b) for the internal reinforcing.....	132
Figure 5.7 - Robotic set used for machining the polyurethane based moulds.....	132
Figure 5.8 - Different phases of the production of moulds.	133
Figure 5.9 - Carbon fabrics cut with fibres oriented at $\pm 45^\circ$	134
Figure 5.10 - Acrylic rulers used to allow forming the gluing tab.....	135
Figure 5.11 - Locals where fibre draping is particularly difficult. 1- rib corner; 2- 90° fold.....	136
Figure 5.12 - Carbon layers and tacky tape protected by a brown paper placed on the mould	137
Figure 5.13 - Photo showing the peel ply (in white) and flow mesh (yellow) placed in the mould.....	137
Figure 5.14 - Final setup of the vacuum infusion mould.....	138
Figure 5.15 - Infusion vacuum setup to switch on the vacuum.....	139
Figure 5.16 - Resin flow progress during vacuum infusion: 1) Beginning of process; 2) Interference in resin flow; 3) Normal resin flow at the middle of the process; 4) End of the resin flow	140
Figure 5.17 - T-Nut fasteners used to attach the necessary steel components to the composite parts.....	141
Figure 5.18 - MDF elements used to locate the position of ribs in the U-shaped shell mould.....	142
Figure 5.19 - Small laminate squares used to control the adhesive layer thickness.....	143
Figure 5.20 - Treated area of final composite shell area used to attach the steel bearing component.....	144

Figure 5.21 - Places to measure thicknesses marked on parts submitted to ultrasound inspection	145
Figure 5.22 - Measuring the thickness of external shell composite part: 1) with a calliper; 2) with the ultrasound probe	145
Figure 5.23 - Ultrasonic NDT tests made to verify the quality of parts joining.....	146
Figure 5.24 - Display of ultrasonic probe data	147
Figure 5.25 - Ultrasonic probe data obtained as function of time.....	148
Figure 5.26 - Results obtained from ultrasound tests made on the joint at the back of ribbed part.....	149
Figure 5.27 - Results obtained from ultrasound tests made after joint repairing.....	149
Figure 5.28 - Composite prototype gantry mounted in the testing structure and the L-shaped steel component where the load was applied (red area).....	150
Figure 5.29 - Composite prototype gantry mounted in the experimental testing apparatus.....	151
Figure 5.30 - Detailed views experimental testing set-up	152
Figure 5.31 - Some of prototype gantry main components considered in the numerical model	153
Figure 5.32 - Orientation and thickness of the layers in the composite lay-up.	155
Figure 5.33 - Load bearing element used in the numerical model.....	155
Figure 5.34 - Tie links between the part and ribs shown in yellow	156
Figure 5.35 - Abaqus green code for the partition used in the model developed in the present work	157
Figure 5.36 - Vertical displacement, y , plotted as function of number of elements for each model	158
Figure 5.37 - Mesh generated in prototype gantry by using forty six thousand elements	159
Figure 6.1 – Plot of the error as a function of the EI_z for loading scenario 2.....	161
Figure 6.2 – Relevant points considered for system behaviour assessment.....	162
Figure 6.3 – Comparison between the errors produced by gantries with the same EI_z depending on the loading case.	162
Figure 6.4 - Comparison between the errors produced by gantries with the same EI_y depending on the loading case.....	163
Figure 6.5 - Comparison between the errors produced by gantries with the same GJ_z depending on the loading case.....	163
Figure 6.6 – Ratio of the error produced by gantries with the same EI_z for load case 1 relatively to load case 2.....	164

Figure 6.7 - Ratio of the error produced by gantries with the same EI_y for load case 1 relatively to load case 2.....	164
Figure 6.8 - Ratio of the error produced by gantries with the same GJ for load case 1 relatively to load case 2.....	165
Figure 6.9 - Mesh independence of the results for the bending loading scenario.	166
Figure 6.10 - Deflection suffered on the y axis.....	167
Figure 6.11 - Outcome of FEM simulation for the metallic gantry subjected to realistic loading conditions. The colour display the translational displacement magnitude. The deformation is magnified by 1400 times. .	169
Figure 6.12 - Outcome of FEM simulation for the unreinforced composite gantry subjected to realistic loading conditions. The colour display the translational displacement magnitude. The deformation is magnified by 1400 times.	170
Figure 6.13 - Outcome of FEM simulation for the composite gantry reinforced closer to the edges and subjected to realistic loading conditions. The colour display the translational displacement magnitude. The deformation is magnified by 1400 times.	171
Figure 6.14 - Outcome of FEM simulation for the composite gantry subjected to realistic loading conditions. The colour display the translational displacement magnitude. The deformation is magnified by 1400 times.	171
Figure 6.15 – Numeric model of the composite part subjected to the realistic loads.....	172
Figure 6.16 – Results of initial optimization process.....	174
Figure 6.17 – Mass of the best elements of each iteration as optimization process evolves.....	175
Figure 6.18 - Acceleration and mass evolution for an α of 1 and a β of 0.01.....	176
Figure 6.19 - Acceleration and mass evolution for an α of 1 and a β of 0.1.....	177
Figure 6.20 – Positioning of the optimised solution vs the curve of maximum possible accelerations as a function of the gantry's mass.....	179
Figure 6.21 - Stress/strain curves obtained from the tensile tests of the $0^\circ/90^\circ$ plain weave samples.....	181
Figure 6.22 - Sample presenting the most common type of failure observed (code LAT of ASTM aD3039/D3039M-08)	182
Figure 6.23 - Stress/strain curves obtained from the lap-shear tests made on the adhesives according to the ASTM D3165-00 standard	183
Figure 6.24 - Bending phenomenon occurring during the lap-shear tests	184

Figure 6.25 - Displacement of the set-up geometry during testing	185
Figure 6.26 – Decomposition of the force applied by the actuator (F) into the components relative to the load bearing element's horizontal surface: normal (Fa), and parallel (Fb)	186
Figure 6.27 - Gap formed between the load bearing an shell caused by adhesive failure	187
Figure 6.28 - Gap formed between the composite shell component and pultruded plate.....	187
Figure 6.29 - Tsai-Hill criterion applied to the laminate of the part produced, with display of the isolated ribs of the produced prototype composite gantry submitted to 5kN vertical load. The images portrait highest value for Tsai-Hill criterion, regardless of the ply in which it is occurring.....	189
Figure 6.30 - Shear stresses developed in the mostly loaded composite gantry adhesives	190
Figure 6.31 – Positing of LVDTs in the experimental set-up	191
Figure 6.32 - Comparison between the deflections obtained from the numerical simulations and experimental testing.....	192
Figure 6.33 - Displacement/force curves obtained in the actuator from numerical simulations and experimental tests	192
Figure 6.34 - Strain gages placed in the prototype composite gantry produced.....	193
Figure 6.35 - Comparison between principal strain and their orientation obtained from the numerical and experimental results	195

List of Tables

Table 2.1 – Nomenclature for denominating the different LM processes [62].....	19
Table 2.2 – Classes of derivative-free optimisation algorithms (adapted from [113, 115])	27
Table 3.1 - Degrees of freedom are the variables that are calculated.....	59
Table 3.2 – Formulation and Conditions of different types of discrete problems	65
Table 4.1 – Description and Effects of the Forces present in both Load Cases	80
Table 4.2 – Illustrations of The Force’s effects on the Gantry.....	81
Table 4.3 - Equations previously presented are combined to develop the model of the deformations suffered by the gantry at the location of the optical components.	84
Table 4.4 – Mechanical properties of st33 steel grade.....	91
Table 4.5 – Mechanical properties used for thickness estimation of the composite gantry’s walls, adapted from [28].....	92
Table 4.6 - Maximum allowed deformations for the composite gantry	93
Table 4.7 - Different layers considered for the design of the composite component	93
Table 4.8 – Loads applied to the metallic gantry.	97
Table 4.9 - Loads applied to the composite gantry.....	97
Table 4.10 – Properties of the laminates considered for the optimization process.....	109
Table 4.11 – Quality indicators for the mesh used.....	113
Table 4.12 – Loads applied to the system. a is the 19 th variable and influences the y component of the considered loads	116
Table 5.1 - Failure modes according to ASTM D3039/D3039M-08.....	129
Table 5.2 - Composite lay-up of the prototype gantry components.....	135

Table 6.1 – Maximum deflections and rotations suffered by the metallic gantry as a cantilevered beam . 167

Table 6.2 - Minimum layer thicknesses that ensure enough rigidity for both Carbon Fibre and Glass Fibre.
Weight for the design gantry is also displayed..... 168

Table 6.3. Comparison between the displacement of the centre of gravity of the cutting head on the metallic
and on the composite component. 172

Table 6.4 – Optimization results regarding thickness related variables 178

Table 6.5 - Results obtained from the tensile tests made on the $0^{\circ}/90^{\circ}$ plain weave samples..... 181

Table 6.6 - Results obtained from the lap-shear tests performed on the adhesives 184

Chapter 1: Introduction

Summary

This chapter aims at introducing the subject matter of this dissertation, the research methodology and its main objectives. The introduction chapter contains some background information about Industrial Laser Cutting Machines (ILCM) in the current scenario of part production, as well as some general information about market dimension and trends.

Subsequently, there is a generic description of the work performed and of the document's structure throughout its different chapters.

The last part of the introduction chapter is related to the defined research objectives, their relevance, and how they guide the work presented in this document.

1.1 LASER CUTTING MACHINE CONTEXT

The ever-growing trend of global consumption leads to the continuous growth of the total volume of products produced to meet human needs and desires. But not only is the number of produced parts getting larger, the variety they come in is growing much faster as the life cycle of products shrinks under competitive pressure. The current situation presents a mix of huge product portfolios, reduced lead time, and increased quality standards and competitive costs which causes the immediate answer of running faster presses to hit a roadblock. This approach leads to more lost production per downtime, as smaller batch sizes are used. Dedicated cutting-tools also present limitations in this context due to its little to no flexibility for adjustments within controlled tooling costs. Upheavals in global consumption together with the limitations of the previous mentioned processes, motivated the adoption of Computer Numerical Control (CNC) and programmable logic control (PLC) machinery for plasma, waterjet, and laser cutting to the appreciable market share they enjoy

today, being laser-cutting technology the latest among metal-cutting processes for sheets and plates and is one of the most widely used thermal energy based non-contact type advance machining process [1-3].

The laser cutting machine market, with a relevant and growing dimension, is estimated to represent about 4300 million United States Dollars (USD) in 2020 and expected to reach 4900 million in 2024, although the current uncertainty climate makes it harder to predict the market behaviour [4-6].

The markets that have been a bigger driver for the growing application of ILCMs are automotive, consumer electronics, and defence. [7].

A machine's success in the market is highly dependent of two major key performance indicators, usually shared with for the evaluation of any manufacturing process: process productivity and product quality [8, 9]. Regarding productivity, high speed and acceleration are always the goals pursued in the machine design process [10]. On the case of laser cutting, higher accelerations will translate to a shorter cycle time, especially for smaller and more intricate parts, that, during its production, lead to constant direction changes in the movement of the cutting head. This aspect is particularly relevant, since modern manufacturing trends have shifted towards miniaturization as industries like aerospace, automotive and bioengineering have an increasing demand for smaller devices [8].

The second aspect, product quality, is deeply linked to the product's appearance, geometric and dimensional accuracy [8]. Depending on the motion system of the machine and on the stiffness of components, ILCMs can present high accuracy and edge quality superior to that of die blanking [1].

1.2 WORK PERFORMED AND DOCUMENT STRUCTURE

The work here presented focuses on the productivity increase of an ILCM through the improvement of its maximum allowed acceleration. The machine that will be the focus of this work dissertation is a flying optics with the gantry moved using linear motors and a CO₂ laser. The selection of this machine as a case-study in this dissertation is associated to its representativeness of current market trends and intense innovation cycles. It is intended that an analysis of this machine can be a proper basis to define a methodology that can in the future support optimization cycles of critical machine components. With the analysis of the machine's structure it was possible to identify the component that is critical for the definition of many of most relevant characteristics of the machine, namely accuracy and maximum allowed acceleration. Through the redesign of such component (the gantry) using composite materials (namely fibre reinforced polymers), which present

a higher Specific stiffness (the ratio between Young modulus and density), it is possible to achieve a higher maximum allowed acceleration for the same motion system and accuracy. The nature of the analysis is to be confined to the mechanical domain, meaning that the end result shall not require additional controls or electronics. The outcome of this project is directly associated to the machine being studied. Nonetheless, as previously mentioned the results obtained should be applicable to machines that have other laser sources or additional axis.

Due to the complexity of the loading conditions and structure of the component, Finite Element Analysis (FEA) was used to study the effect the machine operation has on the structure under study. A traditional dimensioning approach is initially followed but it shows severe limitations, since the projected part is required to present improved behaviour in competitive characteristics: higher stiffness (to maintain the same accuracy at higher accelerations) and lower mass (to allow for higher accelerations with the same motion system equipment. For this reason, a formal optimization process is implemented, resorting to a population-based optimization algorithm having the objective function (focused on the acceleration and part stiffness) evaluated through FEA. The FEA models were then validated through the comparison its results and the experimental testing, both performed on a scale model of the gantry.

In the end it was possible to obtain, through the implementation of a formal optimization process, a gantry that is lighter, stiffer, and that allows the machine to present a higher level of productivity while ensuring the same level of accuracy.

The document structure is divided in five main sections. Chapter 2 is the Literature Review and is focused on the main and most relevant literature published and that served as a basis for the work performed. This section is divided in four topics: ILCMs, composite materials, finite elements (FE) and optimization methods. Chapter 3 concentrates the presentation of the main theoretical principles that allow for the technical execution under the scope of this thesis. This chapter focuses analytical models of the mechanical behaviour of the gantry, analytical models for the geometric description of the laser beam path, the implementation steps of FE, and the practical aspects of the implementation of an optimization process. Chapter 4 describes the work done: the dimensioning of the gantry in composite material using the optimization process, while the production of a model of the part, its testing, and the comparison with the results obtained through FEA is addressed in Chapter 5. Chapter 6 presents the results and its discussions, being the conclusions drawn in Chapter 7.

1.3 RESEARCH OBJECTIVES

Based on what was previously mentioned, the research objectives (RO) to guide the efforts and act as milestones were defined. Parallel to the implementation of a method focused on creating a solution for the particular problem in hand is the creation of a mechanism capable of solving similar problems, where optimization can be used to optimize the configuration of mechanical components to respond to mechanical loading scenarios with variable degrees of complexity. The objectives are listed below:

RO1: Determine the critical loading scenario – The dimensioning that will occur throughout the work will have to account for the most demanding loading conditions. If a satisfactory solution is found for this scenario, then the part developed will ensure a behaviour that ensures adequate performance of the machine.

RO2: Dimension a gantry produced in composite material – The purpose of using fibre reinforced composite materials is to take advantage of their higher specific rigidity to create a part that ensures a higher machine performance. A gantry that ensures similar deformations with lower mass and at higher accelerations will represent a boost in productivity without the need of changing other components.

RO3: Implement an optimization routine to create a mechanical component capable of maximizing the advantages for the machine's performance – The dimensioning mentioned in RO2 comprises competing objectives. To manage this situation and ensure the potential benefits resulting of the change proposed, a formal optimization process is to be implemented. This optimization loop is to contain FEA as evaluation method.

RO4: Experimental validation of the numeric models used to dimension the gantry – To ensure that the optimization is based on valid assumptions and models, it is necessary to produce a comparable experimental evaluation of the behaviour of the analysed structure. This implies the experimental characterization of mechanical properties of the materials used on the parts production, as well as destructive and non-destructive testing (NDT) of the properly instrumented and monitored parts.

Chapter 2: Literature review

Summary

This chapter presents the current State of the Art of the relevant fields of knowledge for the work performed under this doctoral thesis. It starts with the description of the evolution and current trends in the field of Laser cutting machines. Next, it addresses aspects related with composite materials, their production methods and applications, namely in the field of machine components, such as the case studied in this work. The following section is dedicated to the current potential and limitations of FEA, on which the simulations of mechanical behaviour of the gantry and the optimization process are based on. Subsequently, different optimisation methods were analysed, namely the ones with a higher applicability to the mechanical optimisation of components having the objective function evaluation based on FEA. Finally, the last section is specifically focused on existing works that are aimed at objectives similar to the ones of the present thesis.

2.1 LASER CUTTING MACHINES

Laser cutting is the process that allows to cut by melting a narrow line of material via the energy conveyed by a laser beam. The laser beam is focused on a spot (with typical diameter around 0.2mm) in order to cause the material melting. Then, the liquid matter is immediately removed by a high-pressure (4–20 bar) jet of gas. Therefore, the main functions of the cutting head device include positioning and focusing the laser, as well as conveying a coaxial flow of pressurized gas [11].

The first industrial use of CO₂ lasers was the cutting of plywood dye boards for the packaging industry. Since this early application in 1971 the technology has developed enormously, being the lasers now inclusively

used for cutting super alloy panels for the aerospace industry. The laser cutting mechanism can be summarized as follows:

1. Generation of a high intensity infrared light beam;
2. Focusing the beam onto the surface of the workpiece by means of a lens;
3. Using the focused beam to heat and melt the material locally (spot generally with less than 0.5 mm diameter) and throughout all depth of the sheet;
4. Cleaning the molten material from the area by using a pressurized gas jet, which usually acts coaxially with the laser beam;
5. Generate the cut by moving the localized area of material removal across the surface of the sheet.

The movement mentioned in the last point is achieved by different mechanisms, depending on the ILCM in question [1, 12].

Laser cutting machines can be classified according to the number of axes of movement they present. Most common machines have 2 axes, although some three-axial ones are available in the market.

The earliest solutions for two dimensional ILCMs had the laser head fixed and the movement was performed by the supporting structure. This solution avoids complications that come from moving a complex optical system, but due to the severe limitations imposed on the processing speed caused by the structure's high mass (Figure 2.1) is not very common nowadays.



Figure 2.1 – Fixed optics ILCM Amada Lasmac 645 [13]

The inclusion of the cutting head movement has been firstly presented by hybrid machines. These machines combine the movement of the supporting structure along one axis while the optical system moves on the perpendicular direction. This configuration still is present in the market associated with systems for lower cutting speeds. Some of these systems process work envelopes longer than 30.5 m.

The next step in the evolution of ILCMs was the development of the so-called “flying optics”. They gave room to higher accelerations and larger dimensions of metal sheets to be cut. The maximum acceleration of this type of machines is, usually, achieved using linear motors in all axes. Maximum acceleration is of critical importance when considering cutting pieces with detailed geometry and holes implying changes in the direction of the machine movement.

Some derivations of design improve the output of such machines, such as the incorporation of one or two extra axes in the gantry. In small movements the only mass that requires to be moved is the gantry head and due to the lower mass high accelerations are achievable [14].

With the continuous growth of global consumption, the total volume of production for global consumption, as well as the quantity of parts, is also suffering a constant increase. The initial response consisted in increasing the speed of presses. This solution proved incapable of meeting just-in-time production requirements of customers and presented serious flexibility issues, such difficulties were only overcome through the use of the laser cutting technology [1].

The laser cutting process has a number of advantages over competing technologies (including CNC technologies, such as plasma and waterjet) which have ensured the growth of this branch of industry. This made possible to expand the application of the laser cutting far beyond from its traditional use in prototypes towards all segments fabricating metal sheets for being used on high volume production rate markets, such as the automotive, electronics, aerospace, appliance and shipyards. Apart from the flexibility, already mentioned, its main advantages are:

- To be a non-contact cutting technique, making the set-up easier and suitable for deformable materials;
- To allow extremely narrow cutting widths (kerf width typically from 0.1 to 1.0mm), turning much easier carrying out very detailed works;
- To enable a considerable reduction in the area to be actually heated (and potentially degraded) by the laser;
- To ensure cuts at much higher speeds than other profiling methods;

- To produce low quantities of waste material and, potentially, none;
- To have, in general, very low running costs;
- To be an extremely quiet as well as safe process in comparison to its competing techniques [12, 15, 16].

High-speed laser cutting always has been a prime concern for fabricators since the introduction of the first laser system in 1978. In the early days, ILCMs had no trouble keeping up with the capabilities of the beam. A low-powered CO₂ laser could only cut so fast without creating problems with edge quality and incomplete penetration [17, 18].

However, the evolution made the laser technology for manufacturing to become a much more holistic and interrelated process. If, on the one hand, the continuously enhanced requirements motivate the development of new laser systems, on the other hand the advanced lasers had enabled novel applications [19].

With the implementation of more powerful lasers, and the first flying-optics system in 1979, the race for higher processing speeds was initiated. For approximately 10 years, laser productivity gradually increased until the early 1990s. Nevertheless, by the mid-1990s the physical limit for large-gantry machines and their tremendous mass and accompanying high forces had been reached.

Only the introduction of linear-drive-motor technology allowed to overpass the problem and develop ability to generate high acceleration forces that made the increased speeds possible [18].

At early 2000s, ILCMs could already cut 1-mm-thick mild steel at 20 meters per minute or faster, and a 3,500-W laser perform cuts on mild steel up to 20 mm thick [20].

The speed, however, was limited by the acceleration the machine can generate. In order to cut complex shapes, a Cartesian motion system will suffer accelerations in different directions. In a part with complex contours and many 90-degree corners, the machine can cut at a speed as little as 1/10 of its maximum speed. For complex and intricate parts, the cutting performance is greatly dependent on the machine's capacity to decelerate, change direction, and accelerate again [18].

Rigid machine components were developed to support positioning speeds up to 300 m/min and accelerations of more than 20 m/s² while maintaining the path accuracy.

The recurring solution for avoiding poor cutting performance is reducing the masses involved, and develop a way to make a system more dynamic so that it takes less energy to accelerate and change direction.

Currently, the trend is still to maximize acceleration (thus creating more productive machines able to minimize the time to produce complex parts). The machines in the market capable of larger accelerations are the ones

that present two additional parallel kinematic drive axes placed on the cutting head, creating a ILCM with one dynamic and light cutting head capable of independent movement along two axes, but working in precise synchronicity with the machine's sweeping movement. As these additional axis have lower mass, they are capable of accelerations up to 6 G [20, 21].

There are other changes that have been happening in the field of laser cutting, mainly related to the laser source. There has been a proliferation in the number of choices available, and in recent years, fibre lasers have been getting more relevance and market share. They benefit from a less cumbersome setup (the light is transported directly from the source to the cutting head using optical fibre and without the need of such a complex system as is the case of the CO₂ laser) and present light at a wavelength that makes them more efficient at cutting metals [22].

Regardless of technological trends the basic principle of ILCMs is making the laser hit the cutting point with accuracy while decreasing the cutting time for a given part.

2.2 COMPOSITE MATERIALS

A composite material is a non-uniform and anisotropic material consisting of two or more chemically and physically distinct materials that are mechanically bonded together, presenting clearly defined interfaces between them. Each of the various components retains its identity and maintains its characteristic structure and properties in the final composite. A composite material usually exhibits more useful and unique structural or functional properties to a particular application than each of its individual components alone and that none of them could ever attain in an isolate configuration [23, 24]. Indeed, composites are produced when two or more materials or phases are used together to allow obtaining a combination of properties that cannot be achieved otherwise [25, 26].

Generally, the structure of a composite consists of two phases: matrix and reinforcement. The matrix has a continuous character and is, usually, more ductile and exhibits lower mechanical properties. Its main function is to hold the other phase (reinforcement), which is usually stronger [24].

On other hand, the main objective of the reinforcement is to significantly improve the mechanical properties of the composite, while the matrix has the responsibility of transferring and distributing the loads and bonding together the reinforcements. The types of reinforcement mostly used in polymer matrix composites are: i)

reinforcing particles; ii) short, long, continuous, chopped, chopped strand and woven fibres and, iii) nanomaterials [27].

Technologically, the most well-established composites are those using fibres as reinforcement. They are commonly referred as fibre-reinforced composites (FRC) [27]. FRC are being increasingly used in aerospace, automotive, naval and defence applications. The so-called advanced composite materials were developed for constructing components for aeronautical and aerospace vehicles during the second part of the last century. Fibres (yarn) consist of several hundreds or thousands of filaments, each of them having a diameter between 5 and 15 μm , which may be processed by textile machines [24, 28]. Their high-strength derives from the small diameters the filaments have, which means far fewer defects (normally surface defects) compared to the same material in bulk form [29]. As a general rule, the smaller the diameter of the fibre the higher is its strength, but often the cost increases.

The issues that prevent the direct application of fibres, such as their negligible compressive strength due to buckling, can be overcome by adding a polymeric matrix, to impregnate, determining the final shape of the composite and transferring and uniformly distributing all applied loads to them [30]. For this reason, matrices should present good adhesion to firmly bond the fibres together [25].

The properties of the resulting composite are a function of the particular characteristics of its constituents, their relative contents, and the geometry of the reinforcement. Specifically, the mechanical characteristics depend not only on the properties of the fibres in use, but also on their length, orientation, volumetric ratio as well as their surface adhesion to the matrix. All these parameters will have a significant influence on the resulting strength and stiffness of the material [27, 31, 32]. For selecting the composite constituents, one has to take into account that some reinforcements may not be physically and/or chemically compatible with matrices, which may cause premature failure and/or insufficient mechanical properties of composites [33]. Fibre orientation is another important aspect to take into account on composite material design. In this regard, fibres are usually used in the following available forms in composites: i) as continuous reinforcements, including in unidirectional yarns and woven fabrics, and ii) as discontinuous reinforcements, including chopped fibres and, in the case of glass fibres, as chopped strand mats (CSM), which means an ensemble random dispersed chopped fibres held together by a binder on a mat [27, 29].

Regarding mechanical properties of composites, the most representative ones can be obtained by tensile and compression tests [26]. Long and/or unidirectional arrangements of fibres usually cause anisotropic properties, with particularly good strength and stiffness in their direction, but much lower mechanical

characteristics in the direction transversal to them [23, 31, 32]. Figure 2.2 clearly illustrates this effect on the tensile strength of a unidirectional Fibre Reinforced Polymers (FRP) composite.

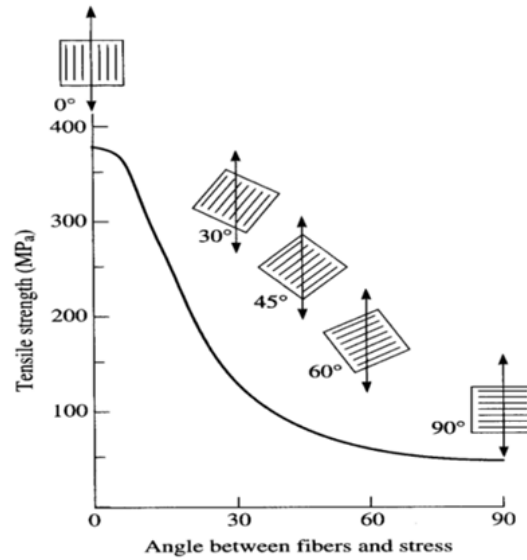


Figure 2.2 - Effect of fibre orientation on the tensile strength of FRP composite [0a] [23].

Woven fabrics exhibit fibres along two mutually perpendicular directions: the warp direction (along the roll's length of the woven fabric) and the weft direction. The fibre yarns are woven together, meaning the weft yarns pass over and under certain number of warp ones, following a pattern. Depending on the way the warp yarns and the weft yarns cross each other defines the type of weave. Some available weaves are presented in Figure 2.3 in ascending order according to their ability to drape complex surfaces, to attain higher strength and rigidity and their cost [28].

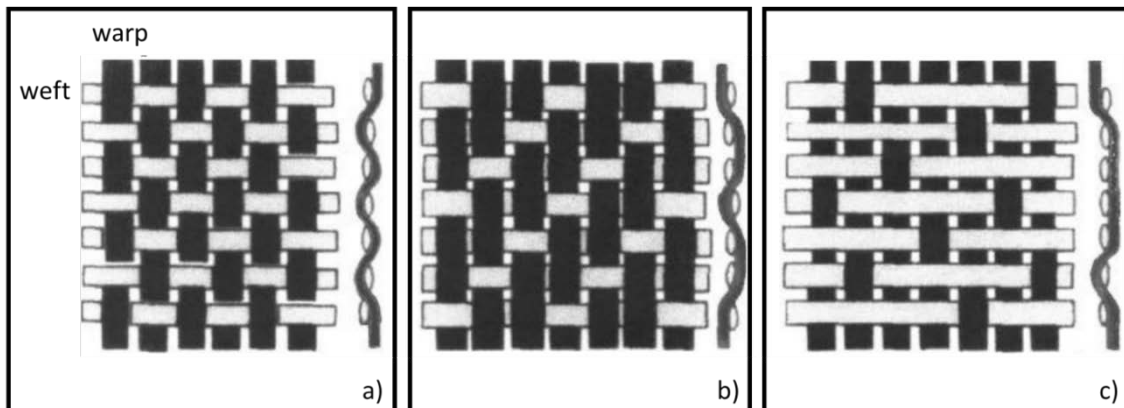


Figure 2.3 - Forms of woven fabrics: (a) plain weave, (b) twill weave, and (c) satin weave (from [28]).

Fibre reinforced composites usually are multi-layered laminate structures manufactured by stacking fibre laminae in different orientations in order to achieve the desired strength and stiffness [29]. These several layers or laminae are bonded together and each individual lamina is composed by oriented fibres adequately embedded in a matrix [34].

The hierarchical structure of FRC has three levels of organization: ply, laminate and final element, as presented in Figure 2.4.

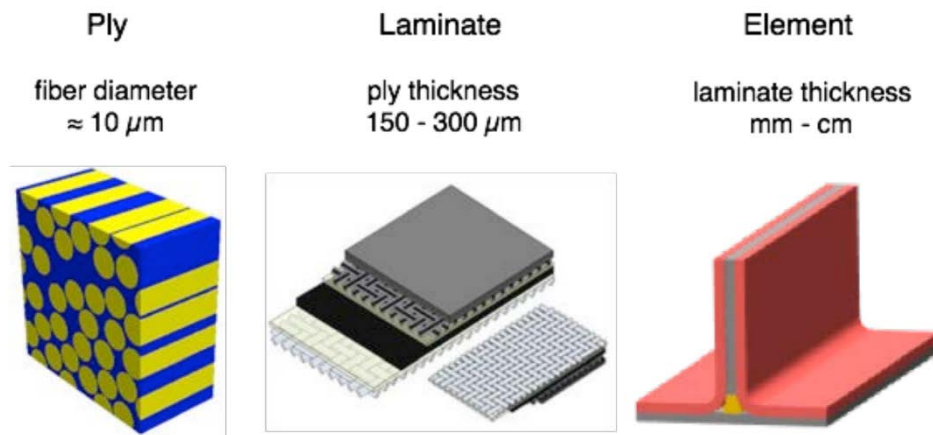


Figure 2.4 - Hierarchical structure of FRC and associated lengths scales for each level [30]

This bottom-up approach of the hierarchical structure allows to control the final properties of the element by defining different parameters such as matrix and fibres volume contents, spatial distribution at ply level, stacking sequence and fibre orientation and architecture in each ply at the laminate level and, finally, the spatial disposition of the laminate to form the structural element. By using this method, composite elements might be designed in order to optimise their own properties for a given application [30]. These allow FRCs to usually offer better combination of strength and modulus than other traditional metallic materials for each application. Their low specific gravities often lead these materials to present much better strength-weight and modulus-weight ratios than metallic ones.

2.2.1 Polymer Matrix Composites

Depending on the nature of the matrix phase, composites are typically classified as:

- Metal matrix composites (MMC);

- Ceramic matrix composites (CMC);
- Polymer matrix composites (PMC) [35, 36].

Among them, polymers are much more commonly used as matrix materials in a wider diversity of applications and with multiple functionalities [27, 37]. High costly CMCs are only used in high or ultra-high temperature applications, such as internal engine, exhaust systems and other “hot-zones” structures. They usually comprise a ceramic matrix reinforced with a refractory fibre, such as the silicon carbide (SiC) and are able to offer products presenting low density, high hardness and excellent creep, chemical and thermal resistance. Today, there are CMCs able to withstand working temperatures over 1300 °C, such as CMC reinforced with large diameter silicon carbide monofilaments (SCS-Ultra SiC), or even reaching 3000°C (ultrahigh-heat CMC materials (UHT-CMCs) that use tantalum carbide (TaC) and hafnium carbide (HfC) ceramic fibres as reinforcement.

High costly MMCs have also much less applications than PMCs. They usually consist of a low-density metal, such as aluminium or magnesium, reinforced with particulate or fibres of a ceramic material, such as silicon carbide or graphite. Compared with unreinforced metals, MMCs may offer higher specific strength and stiffness and greater operating temperature and wear resistance, as well as the opportunity to tailor these properties for a particular application. Their major drawback relatively to other traditional metals are the higher cost of fabrication and lower ductility and toughness. Presently, MMCs tend to cluster around two extreme types. One consists of very high performance composites reinforced with expensive continuous fibres and requiring expensive processing methods. The other consists of relatively low-cost and low-performance composites reinforced with relatively inexpensive particulate or fibres.

As already mention, polymer matrices were and still are by far the most interesting and successfully materials used in composites. FRP using glass fibres as reinforcement began to be used in large quantity during the 1950s, still are being nowadays the most widely used composites in almost all markets and have opened the doors to the successfully application of much higher performing composites in the advanced markets. The lightweight and outstanding mechanical performances of PMC when compared to traditional materials have attracted attention of these last high demanding markets, such as aeronautics, aerospace, marine, automotive sports, etc. [38-41]. PMCs allow combining and magnifying perfectly the best properties of the fibrous reinforcement and polymeric matrix materials. Polymers, as matrices, provide the almost all possible final solid shapes to composites and, at the same time, transfer and distribute homogeneously loads to the high mechanically resistant fibres. Popularity of polymers are mainly based on their low price and easy

processability in different shapes and sizes, although their reduced physical and mechanical performance limit their individual usage in advanced applications.

2.2.1.1 Polymer matrices

Polymeric matrices are divided in two main groups, thermoplastics and thermosetting. Thermoplastic polymers are composed by long molecular chains weakly linked between them by van der Waals forces and/or hydrogen bonds, which results in a material having high molecular mobility that can be always melted or softened by temperature increase, in order to be shaped with a desired geometry. Due to their characteristic high toughness they usually present better impact resistance in respect to thermosetting ones, but their typical high viscosity makes very difficult wetting and impregnating composites reinforcing fibres. Nonetheless, the ability of thermoplastics for being recycled and reprocessed has turned their application as matrix in composite more attractive and into a permanent technological challenge [39, 42].

Thermosetting polymer resins still are the most common matrices in composite materials. During the so-called cure reaction, they turn from liquid to a solid state characterized by a rigid three-dimensional molecular cross-linked network. Being solidified, this kind of polymers can't be reprocessed, unlike thermoplastic polymers. These resins are usually composed by two parts, resin itself and hardener, which once mixed together start the polymerization reaction, as well-known as cure, which is responsible for the creation of the above mentioned three-dimensional molecular structure. A post-cure at a higher temperature is often required to achieving total intermolecular cross-linking of the material [38, 43, 44].

Polyester, vinyl ester and phenolic thermosetting resins are widely used in non-structural, semi-structural and structural commercial applications, while epoxy, bis-maleimide and polyimide resins are often used as matrices in advanced markets due to their better mechanical performance and higher temperature resistance [38].

Epoxy resins present large variety of curing processes, the most common consists on adding a hardener (e.g., aliphatic and aromatic amines or polyamides) to the net resin (epichlorohydrin). They present outstanding chemical, wear and mechanical resistance, low volatile release during cure process, shrinkage and moisture absorption and also high adhesion to fibres. While they present some brittleness behaviour, the problem can be easily overcome by addition of toughness additives, e.g. rubbers or thermoplastics [38, 39, 44].

2.2.1.2 Reinforcements

Glass, carbon, and aramid are the most common fibre reinforcements incorporated into PMCs. The fibreglass is the cheapest and carbon the most expensive one. Aramid fibres have about the same cost as the lower grades of the carbon fibres [38, 40].

In order to adapt to the needs of high temperature resistant and multi-functional composite materials, a number of special fibres have also been developed. Silicon carbide and silicon nitride fibres, characterized by their high temperature resistance and semi-conductivity, are probably the most important ones [27].

A brief description of the major PMC reinforcements is given below:

Glass is by far the most popular as a fibre reinforcement material mainly because it is cheap, easy to process and manufacture using a wide range of production techniques. When embedded in a polymer matrix, glass fibre composites result in a material with very high specific strength [27]. One important aspect to take into account when using glass fibres is to protect their surface which can be easily damaged, affecting the tensile properties of the material. Despite of their high specific strength, stiffness is the main limitation to the use of glass fibres, particularly in high-tech and advanced applications and products (e.g., as structural members for aircraft, machines and bridges) [25, 27]. In addition to the low modulus, the low resistance of glass fibres to the heat and moisture exclude them from almost aerospace applications [23, 25, 45-47]

Carbon is a high-performance fibre material and is the most commonly used reinforcement in advanced polymer-matrix composite applications. One of the most crucial reasons for this is the fact that carbon fibres offer very high specific modulus and strength. Carbon fibres are also able to retain their high tensile modulus and high strength at elevated temperatures [25, 37]. Additionally, carbon fibres have a relatively good resistance to moisture and present noticeably less variability of tensile breaking stress and strain is than for glass fibres [23, 37]. Carbon fibre reinforced polymers (CFRP) are been increasingly applied in aircraft and aerospace industries, as well as automobile, sporting goods, and other applications which demand high strength and high modulus [47, 48].

The scope of application of carbon fibre composite materials has been enlarged with the decline of its average price. The demand of carbon fibres increased, for example, from 8,000 ton in 1995 to 40,000 ton in 2015, and estimated to have reached 98,000 ton in 2020 while their average price dropped from 50 USD/kg in 1995 and has stabilized at around 20 USD/kg (a 60% decrease). While some years ago it was only considered possible to use carbon fibre composites in high performance applications, nowadays the range of industries using it has expanded due to the decreasing of carbon fibres price [25, 48].

Aramid are synthetic organic fibres derived from polyamides. They have excellent impact, fatigue and creep resistance but relatively weak in compression [23, 25]. Because the aramid fibres are relatively flexible and somewhat ductile, they may be processed by most common textile operations to obtain woven fabrics that may be used in composites plies. Usually, it is not possible to achieve good chemical and mechanical bonding between aramid fibres and the matrix resin [23].

Some of the most frequent applications of aramid reinforced composites include bullet proof vests, cooling vehicles, ship hulls and lately towards structural strengthening of civil structures [37].

2.2.1.3 Fields of application

The combination of low density, high stiffness and strength, as well as toughness, design flexibility, corrosion resistance, high fatigue strength and faster assembly of PMCs, have led to a continuous growth on the application of these materials in the past 50 years. Composites, are considered an essential part of today's materials in applications such as aircraft structures, sports, electronic packaging for medical equipment, space vehicles and home building. They have also give a relevant contribute for the development of the automotive industry for several decades, with early noticeable application in the 1953 Corvette. Other fields include sports, construction, civil infrastructures, energy generation, as well as marine and offshore industries [24, 30, 36, 49].

Although the abovementioned advantages are well known to the industries listed, several factors have hindered large-scale mass automotive applications of FRP, namely high material costs, slow production rates, and concerns about recyclability. For a larger implementation of these materials in such a market, one must take into account that the cost of composite materials is usually higher (up to 10 times higher when carbon fibres are used) than conventional metals. Therefore, CFRP were/are many times only used where, for instance, they may represent high-value for stiffness reasons. Other reasons that can largely improve their applicability is focus on highly automated and rapid manufacturing processes including the application of intelligent preforms or half-finished goods.

One market that has invested more on the application of composites is the aircraft industry because weight reduction of utmost importance. Airplane manufacturers and airlines are willing to spend, in general, \$1000 to \$2000 to save around 0.45 kg (1 pound) of weight. This is largely driven by the idea of saving fuel over the lifetime of the airplane, which can be 20 to 30 years. The automotive industry is willing to spend around

\$1 to \$4 to save the same pound (≈ 0.45 kg) of weight, which is a much lower value. In this industry, weight savings are largely driven by how much the average consumer would be willing to pay to have a more efficient vehicle and, the value to be spent largely depends on the local where the weight savings occur, being higher values invested for saving weight above the centre of gravity of the vehicle. The focus on weight regardless of cost is also increasing the application of composite in automotive market [24, 50].

Another field of application of composite parts that has created growing interest is machine construction, especially in the machine tool sector. After CFRPs and other composite materials being predominantly used in scientific works and prototypes, a rising number of industrial implementations can be found nowadays [51]. The company MAP Werkzeugmaschinen GmbH, for example, designed, produced and uses a vertical CFRP axis slide in its products to achieved a mass reduction to 60% and decreased energy consumption of 70% of the conventional design [32, 52]. The advantages listed by this manufacturer regarding the use of carbon are:

- Reduced machining times thanks to higher cutting speeds
- Significant lower non-productive times
- Higher dimensional accuracy and surface quality
- Longer operating life due to the good damping behaviour
- Significant reduction in weight with the same stability of the assembly group
- Reduced maintenance costs thanks to an excellent fatigue strength.
- Reduced power requirement due to the reduction of the moved loads

The application of FRP lightweight structures contributes for the basic function of a machine tool: the manufacture of a workpiece having the required geometric form, acceptable surface finish and imperative accuracy at the highest feasible production-rate and lowest possible cost [53]. Achieving maximum positioning accuracy is only feasible by using machine tools with moving parts presenting high stiffness and low mass. In fact, one of the primary reasons of low productivity is the large mass of the moving parts of machine tools, which cannot afford high accelerations and decelerations during working operations [54].

The weight reduction of moving components is viewed as *sine qua non* condition for a high cornering accuracy. The importance of structural optimization and lightweight design is evident [32, 55]. Also, it leads to energy efficiency and reduces the environmental impact through material saving, low-cost and high-performance structures [32]. For this purpose, aluminium or titanium cannot replace the steel, which is

typically used in components of high-precision machines, because they present similar or lower specific stiffness and strength and higher prices (see Figure 2.5) [36, 53].

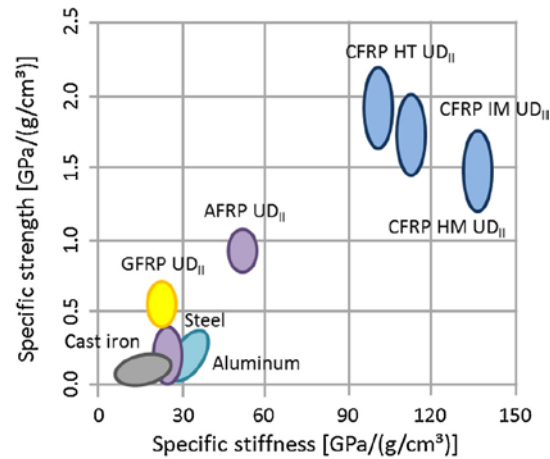


Figure 2.5 – Ashby diagram of the specific strength and stiffness of metallic and FRP alternatives [53].

The lightweight construction provides new possibilities of reducing moving masses, lower inertia moments, the relieve of drive systems of machines, enhance the feed motion dynamics and path accuracy, and improve also the energy efficiency of the machine tools during machining operations. Furthermore, due to their better material damping characteristics, composite materials allow achieving higher structural damping ratios [51]. The use of lighter components also helps to reduce the so called "air cutting time", corresponding to the period in which the tool is not performing operations on the workpiece but getting the new most correct position to perform the subsequent operational work. The impact of these dead times on the entire cycle is not negligible and may reach up to 70% of the overall cycle time [54, 56].

2.2.1.4 Production techniques

Manufacturing techniques for thermoset-based FRCs may be classified according to the way the resin is incorporated during processing.

The processing of a composite part can resort to prepreg sheets, which are semi-finished products consisting on a fibre fabric (unidirectional or woven fibres) pre-impregnated with a resin that is maintained in a semi-cured condition (B-stage) at low temperature. These materials are usually consolidated in an autoclave in order to allow obtaining composite parts presenting high fibre volume fraction ($\approx 65\%$) and low void content

(<2%). The drawback of this process is the large capital investments and operational costs required by autoclave manufacturing. As a response to these costs, alternative out-of-autoclave (OoA) Liquid Moulding (LM) processing methods are being successfully used, in which the resin is forced to infiltrate into a dry preform by means of a pressure gradient [30, 57-59]. In LM processes the fibre fabrics are fully impregnated in result of the resin propagation between fibres and fibre bundles. Different LM processes are nowadays well-established at the industrial level, including closed moulding techniques, such as resin transfer moulding (RTM), and open moulding ones [30]. The main advantages of RTM are related to the obtainment of manufactured parts having good finishing in both surfaces, very low void content, very good dimensional control as well as the reduction of volatiles generated during curing [60]. It should be finally noted that RTM technologies are limited to small to medium parts due to the pressure losses and the costs and difficulties in using moulds composed by two large tools (male and female) for producing composite products in a single shot [30].

Strategies to overcome this limitation resort to the use of open moulds, having a flexible polymeric film as a replacement of a solid tool face. The impregnation is driven by the atmospheric pressure as the bag is connected to a vacuum pump [61].

These LM techniques, very often simply called resin infusion, may take slight different forms and names depending on the manufacturer, being some of them listed in Table 2.1.

Table 2.1 – Nomenclature for denominating the different LM processes [62]

Abbreviation	Full Name/description	Originator
CIRTM	Co-injection RTM	
VI	Vacuum infusion	Scott Bader
DRDF	Double RIFT diaphragm forming	Warwick Uni
LRI	Liquid resin infusion	
MVI	Modified vacuum infusion	Airbus
RFI	Resin film infusion	
RIFT	Resin infusion under flexible tooling	ACMC, Plymouth
RIRM	Resin injection recirculation moulding	
SCRIMP	Seemann composites resin infusion moulding	TPI

VAIM	Vacuum-assisted injection moulding	
VAP	Vacuum-assisted processing	EADS patent
VARI	Vacuum-assisted resin injection system	Lotus cars
VARIM	Vacuum-assisted resin injection moulding	
V(A)RTM	Vacuum-assisted resin transfer moulding	
VIM	Vacuum infusion moulding	
VIMP	Vacuum infusion moulding process	
VM/RTM	A Hybrid RIFT/RTM	Magnum venus
VIP	Vacuum infusion process	

One of the major drawbacks of the vacuum infusion techniques, particularly for very large components, is the long infiltration time needed as consequence of the limited driving force (vacuum pressure). To speed up the process, a special high flow distribution medium fabric presenting much higher permeability (as compared to the fibre preform) can be placed on top of the fibre preform (e.g. SCRIMP or Seemann Composites Resin Infusion Molding Process), so infiltration takes place simultaneously in-plane and through-the-thickness in order to reduce significantly the filling time (see Figure 2.6).

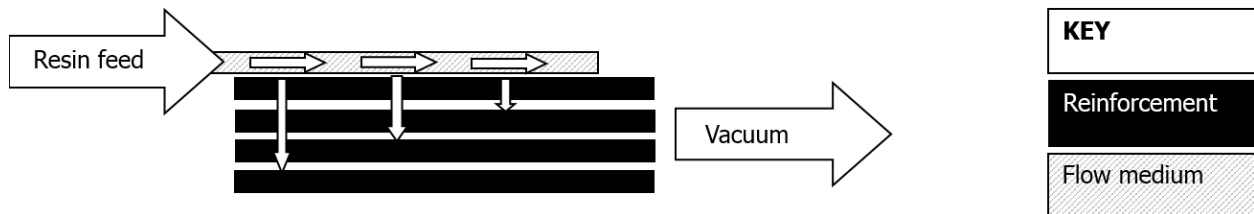


Figure 2.6 - Seeman Composites Resin Infusion Manufacturing Process [63]

As all LM techniques, SCRIMP is vulnerable to the presence of voids and air entrapments that may reduce the mechanical properties. In order to manufacture high quality composite parts with reduced porosity it is critical to understand the physical mechanisms that control the interaction between the liquid and the fabric during infiltration [30].

SCRIMP is widely used for its ability to produce large components with good quality and high complexity in limited series. When using SCRIMP, the parts to be produced are enclosed using a one-part rigid mould

sealed with a vacuum bag together with the distribution medium. An additional layer of peel ply can be added (Figure 2.7) [64-66].

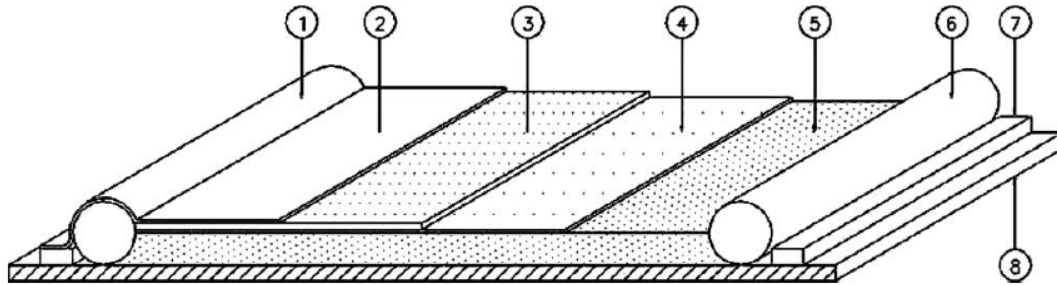


Figure 2.7 - Vacuum infusion mould assembly: 1—inlet, 2—vacuum bag, 3—distribution medium, 4—peel ply, 5—reinforcement, 6—outlet, 7—vacuum seal, 8—mould die (adapted from [64]).

Reinforcements are laid on the rigid mould with a layer of removable flow-enhancement medium, used to reduce fill time (known as flow mesh), along with peel ply to facilitate disposal. The flow-enhancement medium has a much higher in-plane permeability compared to the fibre fabric stack, thus allowing fast surface resin wet-out of the part. Subsequent resin penetration through the thickness allows for complete infusion of thick preforms. Inlets and outlets are placed and the vacuum bag is sealed to the rigid mould using a sealant tape [64, 67].

After vacuum is applied, thus removing air and achieving compaction of the dry materials, the input tube is dipped in the resin reservoir. Pressure difference makes the resin flow through the fibres until the part is completely impregnated. Vacuum is kept on until the part's cure is complete [64].

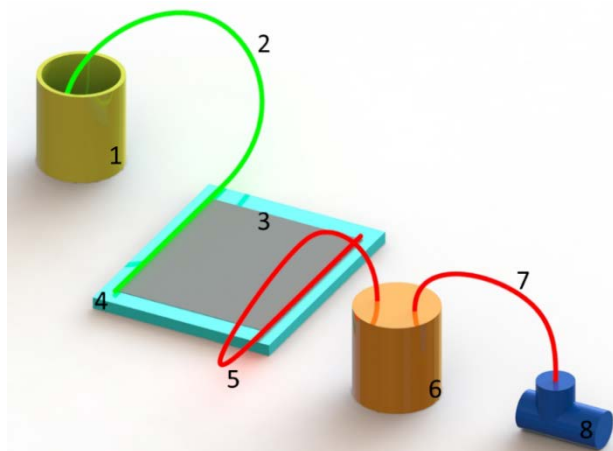


Figure 2.8 – Overview of the Vacuum infusion configuration

The process requires the preparation and insertion of the resin in a pot (Figure 2.8 – 1), which is then sucked in order to travel through the inlet tube (Figure 2.8 – 2) to the dry laminate placed in the cavity (Figure 2.8 – 3) of a leak tight mould that was previously treated with mould release (Figure 2.8 – 4). Then, the resin passes through an outlet tube (Figure 2.8 – 5) that leads to a resin trap pot where the resin in excess is retained (Figure 2.8 – 6). Vacuum is created by the vacuum pump (Figure 2.8 – 8) that is connected to the resin trap by a tube (Figure 2.8 – 7) [68, 69].

Parts produced by SCRIMP may present a very wide range of characteristics. The best results reported fibre and void weight as high as 70% and as low as 1%, respectively [65]. On the other hand, maximum fibre and voids weight contents, respectively, of 50% and ranging from 2% to 5% were obtained in other work [67]. Even lower fibre contents (40%) is reported in the literature [66]. It was also mentioned that variations of 10% in fibres volume fraction and thickness were obtained along a given panel [67]. Such variability of results demonstrates that the best result can only be achieved if one uses high expertise and skill personal and also high quality raw-materials in the production of composite parts.

In fact, the vacuum infusion process (VIP) has proven to be a good alternative to the conventional autoclave methods using prepregs for producing primary aircraft composite structures [70]. Autoclave results in higher cost parts, greatly associated to the investment of autoclave acquisition, and parts produced by VIP present properties and variability acceptable as those obtained by autoclave. This trade-off between cost and resulting mechanical properties justifies why VIP and derivative processes are so much used for the fabrication of marine structures [71, 72], wind blades [73], bridges [74] to military [75, 76] and other critical commercial components [77].

The major advantages usually assigned to the VIP processes are:

- Flexible mould tooling design and selection of mould materials;
- Low tooling costs due to low temperature resins;
- No need for oven;
- Easy storing of materials (resin and catalyst can be stored separately and mixed just before the resin infusion);
- Much lower emission of volatile organic compounds (VOC) than other open mould processing techniques. The resin mixing process is the only step causing VOC emission.
- Enabling the manufacture of large and complex composite parts with good quality;

Some disadvantages are also appointed to the process, namely:

- The resins used in the process usually must have low glass transition temperature (T_g);
- Risk of multiple flow fronts may lead to air pockets (which will be mitigated by defining an infusion procedure that has been tested and provided good results);
- Chance of air leakage is high (which will be mitigated by defining an infusion procedure that has been tested and provided good results);
- Vacuum bag, flow-enhancement medium, peel ply, sealing tape and resin tubing will not be reusable [66, 78].
- The trade-off between advantages and disadvantages, as well as the availability of equipment and consumables leads to the selection of SCRIMP for the production of the models to be produced as part of the work here presented.

2.3 FINITE ELEMENTS

Analysing the behaviour of fibre-reinforced laminates and composite structures presents huge modelling challenges. As they usually are not homogeneous and isotropic, anisotropic laminated composite structures often present many unique phenomena taking place at different geometric scales: the global (or laminate), the ply and the fibre-matrix levels. Hence, the global deformation of composite laminate structures is often characterized by complex couplings between the extension, bending, and shearing modes [79].

Analytical formal closed solutions are available only in very few cases. In most of the practical problems, the solution demands the applications of approximated computational methods [80]. Among the techniques developed, a predominant role has been played by Finite Element Method, FEM. Both research oriented and commercial FEM codes are, in fact, extensively used as standard tools in both academic and industrial institutions [81].

The name finite element wasn't introduced until 1960 by Clough [82]. However, the story of modern FEM has its origins in the 1940s, more precisely in the work by Hrennikoff [83] and McHenry [84]. At that time, the method was limited to linear (one-dimensional) elements (bars and beams) for the solution of stresses in continuous solids. Since then, efforts and work has been developed to address different aspects, structures and phenomena. Courant [85] introduced piecewise interpolation (or shape) functions. Two-dimensional elements were firstly published by Turner et al. [86] in 1956. This work included the establishment of stiffness matrices for truss elements, beam elements, and two-dimensional triangular and rectangular elements. In

this same work, and due to the development of the high-speed digital computer in the early 1950s, Turner et al. [86] presented finite element stiffness equations expressed in matrix notation. Melosh's work from 1961 [87] is considered to firstly introduce a flat, rectangular-plate bending-element stiffness matrix. On this same year Martin [88] published the first work on three-dimensional problems, while axisymmetric elements had their first appearance in 1965 by Clough and Rashid [89] and Wilson [90].

Large deflection analysis were made possible by Turner et al. [91] in 1960 and nonlinearities were first accounted for by Gallagher et al. [92] in 1962. Much later, in 1976, Belytschko [93] addressed problems with large-displacement and nonlinear dynamic behaviour.

A single unidirectional fibre reinforced lamina of composite is usually considered to behave as an orthotropic material [94]. [94]. The first research reported on anisotropic plates dates back to the 1920's, but greater interest was brought to this field by the increasingly common use of multi-layered fibrous composites.

Currently, the FEM is most commonly used in the field of structural mechanics, but its potentialities have made it successfully applicable to other engineering problems, such as ones related to heat conduction, fluid dynamics, seepage flow, and electric and magnetic fields [95].

FE for layered plates and shells can be grouped in the two following categories:

- Two-Dimensional Plates and Shell Elements, in which FE approximations are introduced with correspondence to a certain reference, plate/shell surface;
- Three-dimensional (3D) Plates and Shells Elements, introduced at 3D level, while two-dimensional hypotheses are imposed as constraints equations. This is the case of the so-called continuum based or degenerated plate/shell approach, in which a plate/shell is seen as a 3D continuum while kinematic assumptions are introduced as constraints by means of Lagrange multiplier [81].

The main obstacle in resorting to FEM for composite materials was the use of a conventional 3-D finite element model. While in theory presenting high accuracy, these models proved to be computationally expensive, thus preventing their general use in modelling an entire laminated structure [96, 97].

An example of this is a model created for modelling the behaviour of wind turbine rotor blades based on FE [97]. The solution implemented was a shell element approach because the use of solid brick elements would require an incredibly high number of elements to obtain an exact geometric thickness definition and a detailed geometry, which is less attractive for running several iteration steps or analyses with different loadings. Such solution enabled an adequately high mesh resolution without the constraint imposed by the thickness dimension.

The initial models for shell elements were based on the Kirchhoff-Love plate theory [98]. This theory is essentially an extension of the Euler-Bernoulli beam theory, which considers that the mid-plane surface can be used to represent a plate in a two-dimensional way [99]. These elements are generally used when the thickness of the shell is, at least, one order of magnitude lower than the element length. Since then, many computational techniques have been developed and applied to layered constructions. Anisotropy, nonlinear analysis and the couplings between in-plane and out-of-plane strains, make the analysis of layered composite structure complex in practice [100].

Studies on the convergence of these types of shell elements have already been performed since the 1980s [101, 102]. Earlier studies indicated severe stiffening, a numerical mechanism known as shear locking. This phenomenon was avoided [103-105] by adopting reduced integration shell elements. They were not only well-succeed to avoid shear locking, but were also able to obtain very accurate results. A case of such elements are ABAQUS S4R element: a 4-node, doubly curved element with reduced integration and hourglass control, appropriate for thick or thin shell applications [99, 106].

Second order shell elements were employed [107] to increase accuracy of the modelling. This strategy can be of relevance but brings additional computational costs that, once again, might be of major relevance when considering iterative processes or models with a considerable number of elements.

Another aspect to bear in mind is the shape of the element, being the possibilities triangles or quadrilaterals. The ideal choice greatly depends on the shape of the part to be analysed, requirement of calculation time and the specific loading and geometrical conditions. Most quadrilaterals exhibit better performance concerning convergence rates, while triangles are definitely easier to apply for free-meshing algorithms [108]. If possible, quadrilaterals are applied with manual meshing, ensuring acceptable aspect ratio [107]. Adequate meshing can be evaluated resorting to convergence criteria. This analysis is performed by improving mesh density step-by-step. A specific value should be considered and, upon a stabilization that meets the convergence criteria, the mesh can be considered capable of adequately discretizing the analysis domain [107].

2.4 OPTIMISATION METHODS

To make an overview of existing optimisation algorithms, it is essential to understand what originates the need for so many of them. In fact, there are many different kinds of optimisation tasks, each of them posing

particular difficulties [109]. Wolpert and al. [110] proved that assessing the performance of several black box optimisation methods leads to equivalent results when averaged across all possible problems (No Free Lunch Theorem). A universal problem solver does not exist in the literature. A particular method's success in a given application essentially depends on how well its operators match the problem. Whenever a poor analysis of the method's parameters is performed, it can simply not reach the global optima. This can occur regardless of how efficient the applied optimisation techniques were [109, 111].

Optimisation consists of a mathematical process of deriving the function and evaluating its behaviour in nearby points, trying to attain its minimum. In order to do so, the direction of higher slope of the function at a given derivable point may be evaluated. This information is obtained by calculating the function gradient. This mathematical concept is represented by a vector that points in the direction of the greatest rate of variation of the function, which magnitude is the slope of the graph in that direction. The algorithms that are based upon this same principle are generally addressed as gradient methods. This class encompasses several specific algorithms, all based on the same underlying principle. The algorithm defines the search direction by calculating the gradient at the point being evaluated. The gradient influences the distance between the current point and the following one and indicates the direction at which it can be found. If the gradient is determined with zero magnitude (the derivate equals zero at that point), the concerning point is considered to be the local optima.

The Newton Method used for optimisation (as well as Quasi-Newtonian Methods) also uses differentiation as a basis for calculation. However, in such cases the second derivate function is used to find the first derivate roots.

Both types of algorithms are iterative ones. Generally speaking, Newtonian methods require less iterations to meet the convergence criteria.

On a broader analysis, gradient-based algorithms tend to be the fastest ones when trying to determine a local optima. However, when the analysis aims to obtain a global optima, these algorithms aren't always able to do so. When global optimisation is to be performed to non-linear problems, other algorithms will present better results [109, 111].

2.4.1 Derivative-free optimisation algorithms

For problems with a costly and complex numerical procedure for objective function evaluation, the optimisation by derivative calculation might be deemed as undesirable [112]. Computer simulations usually do not return derivative information [113]. Even if the values obtained for the objective function allow for automatic derivation (i.e. the function is differentiable in point of the considered domain), noise introduced by the numeric solution might deem the local gradient evaluation as irrelevant for minima detection [112, 114].

Alternatives to the most traditional optimisation algorithms are, therefore, not based on mathematical derivation of the evaluated function. Table 2.2 shows a compilation of the essential four different classes of derivative free optimisation.

Table 2.2 – Classes of derivative-free optimisation algorithms (adapted from [113, 115])

Derivate-free Optimisation Algorithm Class	Underlying mechanism
Derivate approximation	Approximation of the objective function's derivatives (similar to derivate based methods)
Function approximation based methods	Explores the relation between the inputs and outputs of the function. Extreme values are established. Interdependence may be studied. Interpolation models are used.
Direct search algorithms	Does not account for gradient. Instead, the exploration of the variable space is performed using a geometric pattern independent of the function being optimized.
Metaheuristic methods	A group of methods mainly (but not only) based on characteristics and behaviour of biological systems or groups of individuals. These techniques use methods and phenomena present in foreign systems to optimize the analysed ones.

Methods presented in the first row of Table 2.2 are based on the previously mentioned processes (either gradient methods or Newton methods) that require function derivations to determine the next point in their iterative process for optima determination or if an optima was reached. Since the function that is being evaluated (or the method it is being evaluated by) does not allow for derivate determination, they approximate them. Such approximation can be performed by a number of techniques, being finite differences the most common one.

The second row of Table 2.2 refers to a methodology based on the approximation of the objective function. It involves a group of mathematical and statistical techniques commonly able to estimate the relationship between the input variables of a function and its output techniques that do not allow optimisation per se, but do allow to estimate the objective function that can later be analysed with optimisation algorithms [116]. More traditional methods would only evaluate the influence of one factor at a time on an experimental response, while others are kept at a constant level. However, the function approximation based methods account for the interaction among the studied variables, unlike more traditional ones. This approach might be beneficial when there is no information on the objective function or multiple evaluations of the objective function might be undesirable, such as, situations where the evaluation of the objective function is too lengthy or computationally demanding (simulation times in the range of weeks per objective function evaluation are not uncommon in contemporary engineering). They are also appealing because, as they might start with an experimental design (a set of experiments defined by a matrix composed by different level combinations of the variables to be studied which correspond to a group of points in the design space), statistical analyses can identify which input variables have higher contribution to the variance of the output [114, 117, 118]. There are mainly three different types of function approximation algorithms: i) Trust Region Methods, ii) Response Surface Methods and, iii) Surrogate Models. All of them require a number of evaluations of the system response to various input variables and then perform a function fit in the considered region (limited by the constraints). Finally, an evaluation of the function fitting must also be done. If the stopping criteria are met, the model is considered to correctly emulate the relation between input and output. Otherwise further function evaluations follow [114]. From the abovementioned algorithms, there are two particularly relevant: one because it is the most commonly used and, the other due to its applicability in computationally expensive objective functions evaluation.

Response Surface Methods are the most commonly used optimization methods technique [119]. Scientific fields that heavily resort to experimental methods, such as analytic chemistry are usual fields of application

of it [118]. The effect and interdependence of several factors is tested according to an experimental design [113].

Surrogate Models also aim at replacing the original objective function by a computationally cheap surrogate [114, 120]. Different accuracy levels can be required. A low accuracy model more easily complies with the needs of having a computationally cheap and preferably smooth approximation of the objective function, but might result in a less accurate representation of reality. Different levels of accuracy might come from defining a coarser discretization or from limiting the complexity of the considered phenomena [114].

Direct search algorithms (third row of Table 2.2) were firstly described as a “sequential examination of trial solutions involving comparison of each trial solution with the “best” obtained up to that time together with a strategy for determining (as a function of earlier results) what the next trial solution will be” [121]. These methods perform optimisation not by computing or approximating the derivatives of the function being optimized [122]. They are an effective solution and can be, in some cases, the only option to perform optimisation of difficult problems [123].

Amongst direct search methods are variations, being the pattern search algorithms the most common ones [124]. The strategy adopted is described as a search able to be performed in n -dimensional space evaluating several points in the hyperplane [124]. The points to be analysed are dependent on the vertices of a $n+1$ general simplex, being n the number of variables to be evaluated and the simplex a mathematical generalization of a triangle or tetrahedron to a given number of dimensions [124]. A new simplex is continually formed at the end of each evaluation. The newly formed simplex adapts itself to the local landscape, by elongating its sides when facing elevated slopes and reducing its dimensions when near a minimum [124]. In fact, Torczon [122] generalized the pattern defining feature from a simplex to any shape that is independent of the objective function. The shape of such feature can change during the optimisation performance, but it depends only on the updates that have been previously collected from the evaluation routine iterations and not on the surface configuration per se.

The Pattern search methods carry out a series of exploratory moves based on the current point being analysed before moving to a new point, which serves as a reference for the new pattern that is then defined. The analysis is carried out in a so deterministic manner around the current point that makes possible to determine the location of the future point of lowest value.

2.4.2 Metaheuristic

Stochastic optimization algorithms have an intrinsic characteristic of randomness, resulting in different paths towards the best solution as a result of the same input. They can be divided into two categories: heuristic and metaheuristic. While heuristics are mostly problem-dependent, a metaheuristic method makes almost no prior assumption about the optimization task, having applicability to a larger number of problems that they treat as black boxes [125].

Regarding optimisation, current needs require greater accuracy, efficiency, and speed. When applied to design of structural systems, these needs have been fulfilled by the development of new methods that fit optimal design of complex systems [126]. Practical design problems mix, for example, different types of variables and present discontinuous or nonconvex design spaces. The use of standard optimisation techniques for such problems will be computationally expensive and, possibly, have as result one relative optimum in the vicinities of the starting point [115]. Metaheuristic algorithms offer an alternative that explore searching spaces through the use of the combination of heuristics, making the method a more general framework and not problem-specific [127, 128]. This type of techniques includes both simple (such as local search procedures) and more complex processes (ranging up to sophisticated learning processes) [128].

Metaheuristic models share both the objective (solve optimisation problems) and their origins. They are inspired by analogies related to artificial or natural systems. These systems have no specific field and can be biological, chemical, electrical or thermal, amongst others. From a very simplistic point of view, all of these optimisation algorithms do the same: explore in a probabilistic way the feasible set towards better regions as fast as possible [109]. Although they differ amongst each other regarding the process they emulate and, as a result, on how they operationalize the optimisation, they are generally suitable for global search by exploring and finding promising regions at an affordable computational time. They tend to perform well in most optimisation problems [125, 129, 130].

Summarily, a metaheuristic is described as “an iterative generation process which guides a subordinate heuristic by combining intelligently different concepts for exploring and exploiting the search space, learning strategies are used to structure information in order to find efficiently near-optimal solutions.” [131].

These strategies have the ability to balance the accumulated search experience (called intensification or exploitation) and the exploration of the search space (commonly called diversification exploration). These same diversification mechanisms are also instrumental to avoid getting stuck in smaller parts of the search space [128]. This balance is what allows for identifying regions in the search space with high quality solutions

and not to focus too much in uninteresting regions [128]. Another aspect that makes these algorithms capable of finding the optimal solution within a reasonable computational time is that they are focused in reaching a solution that is close enough to one that is the global optima, but not necessarily exactly the optima. Metaheuristic algorithms belong to the class of approximate algorithms and are usually non-deterministic [125, 127, 128].

There are many ways to classify metaheuristic algorithms [128]. Some of the characteristics that can divide the algorithms are:

- the inspiration of the algorithm (nature-inspired or not nature-inspired) [109, 126]
- the number of states kept by algorithms (population-based or single point search).[109]

The most intuitive way of classifying metaheuristics is relative to their nature. The relevance of this classification is related to the recent growth in the number of algorithms that, due to hybridisation, are not capable of being placed in one of the two previous classes has been already discussed in some published works [128]. Nature-inspired optimization algorithms, including evolutionary and swarm algorithms, which are part of the computer intelligence discipline, are becoming increasingly popular in the recent past [132]. Regarding the division between population-based and single point search (called trajectory methods), the two classes differ on whether they consider the optimisation a multistate process, following a set of points or by describing a single point's trajectory in the search space [109, 128].

Simulated Annealing is one case of a trajectory metaheuristic. The technique mimics the annealing process when a metal cools and freezes into a crystalline state with the minimum energy [133]. It is a combinatorial method suitable for optimising problems with an objective function defined in the discrete domain, although, to a lesser extent, also capable to perform continuous optimisation [109, 134]. The way the algorithm aims at completing the discrete optimisation process is by comparing the values for two solutions (the current solution and a newly selected solution). While an improved solution is invariably accepted and assumed as the current solution, inferior solutions are accepted in order to escape local optima [134].

It still can be noticed that the algorithm can converge to a solution even if a better one is met during the search process and there is no guarantee a good solution will be obtained in a finite number of iterations [135, 136]. Plus, when performing optimisation on complex non-linear functions, often the process can be performed faster using population-based algorithms [137].

Population-based search methods can be synthesised in:

$$P' = m(f(P)) \quad \text{eq. 2.1}$$

where P is the population or a group of positions in the search space, f is the objective function that returns a vector of values representing the performance of each population member, and m is a population manipulation function that dictates the new population based on the old one's performance [137].

Compared with the other methods, the main characteristics of population based optimisation algorithm are:

- they search the solution space simultaneously using multiple points;
- individuals (each point dispersed through the solution space) have mechanisms to share information with others;
- they are stochastic, with randomness incorporated through behaviours, such as mutation, crossover, selection and others [111].

Different population based methods differ mainly in the manipulation function. The class of population based nature-inspired metaheuristics encompasses a group that is possibly the most widespread metaheuristic: Genetic Algorithms (GA) [129]. These algorithms are part of the Evolutionary Algorithms, based on Darwin's principle of survival of the fittest [138, 139]. Their manipulation function works by selection and breeding, relying on the competition between the elements of the population to reach a solution [109, 138]. Each population element consists of a string of zeros and ones. This is the binary representation of a design vector that assumes a given value for each variable. If each variable is denoted by a string of length q (a q -bit string) and there are n design variables, each solution will consist of a nq binary string [115]. Evolutionary Algorithms represent a large part of population based nature-inspired metaheuristics. Most of the remaining class can be classified as either a Swarm or a mix between Evolutionary and Swarm Algorithms.

Particle swarm's manipulation function is based on the behaviour of swarms. This approach resorts to mechanisms of cooperation between the agents, opposed to the competitive one, which is the trademark of the Evolutionary Algorithms [138, 140]. Swarm optimisation is performed considering a decentralised population structure instead of a sophisticated controller. The global behaviour of the system (swarm intelligence) results from many unsophisticated entities that interact and cooperate. Inspiration for these systems comes from the collective behaviour of social insects such as ants, termites, bees, and wasps, as well as from other animal societies: flocks of birds or schools of fish [132, 141]. This class of algorithms, initially introduced by Kennedy and Eberhart [142, 143], maintains a swarm of particles between iterations and associates a velocity vector associated at each population member. Using rules and the algorithm's

parameters, a new set of particles is produced from the previous swarm. These parameters include inertia, cognition and social influence [136]. The position (x) of the $i - th$ particle, which indicates where the particle is moving to at time $t + 1$, being t a time instant (an iteration in the optimisation context), is given by:

$$x^i(t + 1) = x^i(t) + v^i(t + 1), i = 1, \dots, s \quad \text{eq. 2.2}$$

where v is the velocity of such particle.

This means the particle's location is computed by adding to the old position at time t the velocity vector at $t + 1$ [144]. The velocity vector is a linear stochastic combination of the velocity in the previous time instant, of the direction to the particle's best position, and of the direction to the best swarm position (for all particles). Pham and al. [138] compared the performance of Evolutionary and Swarm algorithms. This was performed by observing the response obtained by elements of these two classes of algorithms to four standard test optimisation tasks. These include both unimodal (which have one peak) and multimodal functions (that have several local optima). The conclusion was that the Swarm algorithms will be faster to converge to a near optima location, but when in the vicinities of the optima, the manipulation function of Evolutionary Algorithms is capable to better adjust and perform a finer search. On the other hand, the issues demonstrated by Evolutionary (particularly Genetic) Algorithms in dealing with the multimodality of objective functions were revealed [145] and it was stated that the issues arise from the way Evolutionary Algorithms generate new populations. The processes involved in the generation of new population elements are divided between mutation and recombination operators. Recombination operators include two-parent crossover (the most common one), as well as multi-parent crossover. Mutations usually come in the form of a small perturbation in the design vector that constitutes a population element [129]. It is also possible for an element that is part of the current population to be directly translated to the new population. New elements are also introduced as means of exploration and to avoid being trapped in local optima [129]. As these operators are put to work, sections of successful elements are joined together to produce the next generation's population. In the case of a multimodal situation, it is possible that the parents are elements whose high fitness is due to their proximity to different optima. Also, mutations are usually applied to the most successful elements, making the convergence at later stages to the vicinity of the optima slower, especially for longer design vectors. It was demonstrated that, in problems which present larger design vectors or a larger number of local optima,

Swarm algorithms present better results, attaining global optima with less evaluations [146]. It was also concluded that Particle Swarm Optimization (PSO) presents lower computation costs despite both algorithms being suitable to achieve high quality solutions [147, 148]. Overall, it seems that while both Evolutionary and Particle swarm algorithms are both capable of producing reliable optimisation outputs, particle swarm algorithms do so faster. Geb and al. [34], while performing optimisation to heat sinks, confirmed that both algorithms are able to presenting similar solutions, and that PSO are able to achieve the optimum faster. Nonetheless, they point out that the algorithm's parameters where not fine-tuned. From these overview of the literature it is possible to conclude that PSO is able to reach near optima results equally good as the ones found by evolutionary algorithms and do so in a faster way. In general swarm algorithms outperform GA [138, 147-149], although their performance slightly decays as they approach the optima [138]. This is why a linearly decreasing scheme of this inertia weight can be particularly adequate, because in earlier stages of the optimisation process it allows for a more global search capacity, while in more advanced stages, it enables the refinement of the solution [150]. This has been overcome by creating hybrid algorithms that combine the global scope of the particle swarm search with faster local convergence algorithms [136, 144, 151-153].

Pattern search methods are a particular subset of direct search methods and one of the most popular methods to minimize functions without the use of derivatives or of approximations to derivatives [122, 123, 154]. They are based on generating search directions which positively span the search space. These methods can be designed to rigorously identify points for local minimization or incorporated in algorithms or heuristics for global optimisation. [154].

Pattern Search algorithms evaluate the objective function by investigating the behaviour of the objective function in the neighbourhood of the points iteratively considered. This way, they overcome the lack of information on the derivatives [155]. These algorithms consider two steps: exploratory step and updating step.

During the exploratory step, a collection of points, known as mesh, is selected around the current points. Each set of points in the mesh is multiplied by a given step size and then added to the current points. The objective function is evaluated at the resulting points. If the new value of the objective function shows improvement over the previous points, the exploratory step is considered successful. Otherwise, the next set of points in the mesh is used to evaluate the objective function.

During the updating step, the step size for the next exploratory step is defined. If the pattern move was successful, the step size is increased. If there was no improvement with any of the sets in the mesh, the step size is decreased. The resulting step size is used for the next exploratory step [155].

One example of Pattern Search and Particle Swarm hybrid algorithms is PSwarm [144, 154]. PSwarm is a derivative free algorithm for the minimisation of a function with variables restricted to upper and lower bounds. Nonlinear constraints can be implemented using a penalty method. This method penalises any solution that violates the constraints by making it infeasible. Most of the algorithms are comfortable with this constraint handling technique, as it is simple and efficient [144, 156]. Its search step performs global search based on the particle swarm algorithm. Its poll step relies on a coordinate search method. The search step was used to incorporate a dissemination scheme in an attempt to equip the overall method with the capability of finding a global minimizer. Whenever the search step fails, the poll step is applied at the best particle, which improved the overall robustness of the algorithm. In the vicinity of a global minimizer, the application of the poll step allows the use of a reduced number of particles which is trivially achieved by dropping particles once they become too close to each other, thus increasing the algorithm's efficiency. PSwarm has been proven to be both convergent to first-order stationary points and highly competitive with other global optimisation methods also based on function values [136, 144]. PSwarm is available both as a C and a Matlab implementation [157].

2.4.3 Optimisation of Mechanical Structures

Optimisation methods can be traced to the days of Newton, Lagrange, and Cauchy. The application of differential calculus methods to the optimisation was possible because of the contributions of Newton and Leibnitz to calculus [115].

The aim of structural optimisation is to find optimal shape/size/weight/material distributions in order to ensure the safety of structures under the assumed loading and boundary conditions [158].

The relevance of this application of optimisation has been growing with the recent advent of automated processes for composite manufacturing and associated growth of the use of laminated composites in a large spectrum of sectors, including aerospace, marine, and land. Design variables that are optimised to obtain laminated structures with excellent mechanical properties at minimum mass include fibre orientation, stacking sequence, and laminate thickness. Since there is more variability in material and structures, the

structural design of laminate composites can present higher complexity than that with conventional materials [159-161]. These works in particular, focuses on a selection process that accounts for the interaction between cross-section shape, material and layup in the chosen composite laminate, but lacks the implementation of an optimisation routine. In optimal design of composite materials and structures, Kirsch [162, 163] divided the design variables used to describe the material distribution, into three groups: size, shape and topological variables. For optimal design of composite multi-layered plated and shell structures, Muc [158] suggests two classes of variables: the ones representing both properties of composites and distributions of reinforcements in matrices and, geometrical variables for characterising the structural geometry, i.e. thickness distributions, forms of a shell midsurface, etc.

This field of study has been the target of many publications regarding the objective function and how it was assessed, the optimisation algorithm, the variables and the constraints considered. Regarding the optimizations algorithms, it is interesting to understand the need of solutions differing from the long-established gradient based techniques. Less traditional techniques, not based on derivatives, have been developed and are of interest in many instances where (at least some) derivatives are unavailable or unreliable [164, 165]. One of these situations comes from advances in FEM and the trend to use them to assess the objective function in optimisation strategies for composite structures [166]. In this case, alternative algorithms such as metaheuristics will present better results [109]. When dealing with vast and complex problems they will be computationally less expensive and present a framework that is not so problem-specific [115, 127, 128]. There are exceptions however, such as the works conducted by Lund [167-169], where the author tends to use gradient based algorithms in connection with Finite Elements. These works mainly vary the thickness and orientation of layers. However, other works [170] did not resort to FE to evaluate the natural frequencies of the structure (objective function) or stress, tip displacement, natural frequencies (constraints) but to an analytical model connected to a direct search optimisation algorithm.

Metaheuristics can be used to optimize structures without resorting to FE. For example, Particle Swarm Optimisation was used to maximize the bending stiffness of a functionally graded sandwich beam [150]. A similar approach for more complex structures will render high inaccuracies. The same methodology was also used by Omar *et al.* [171] to, with the usage of Particle Swarm, minimize multiple objectives (weight and the total cost) while ensuring a specified strength. The optimisation variables were the number of layers and stacking sequence [172]. The results obtained from an optimisation using Particle swarm algorithms and classical lamination theory to determine the stresses in a simple (composite) beam structure were also

presented [172]. These approaches, based in analytic calculations, avoid the computational costs of Finite Elements Analysis. Such approach, while valid, is only so for simple geometries. There are still other authors ([173-175]) that use surrogate based heuristics to perform a multi-objective minimization of weight and cost by varying material combination, shell thickness and layup.

For simple two-dimensional structures, Rohit, G., et al [176] implemented shape optimization process using both meshfree method FEA and swarm optimization. This process eliminates the needs for remeshing, extremely relevant when performing shape optimization and is computationally effective. With the implemented strategy, basic shape optimization was completed. There are challenges in the implementation of a similar strategy for three-dimensional/more complex structures and subjected to more complex loadings. For more complex structures, several publications have reported the combination of GA and FE. Coupling a FE programme and a GA leads to a powerful tool suitable for composite structure optimisation. No matter how demanding this process seems today, in a near future, the decrease of computer cost, the increase of computer memory core size and processor computing power will certainly allow the designers to deal with much more complex structures, putting such methods in user hands not especially confined to research laboratories [177, 178].

Amongst metaheuristics, population based ones often allow for faster processes [137]. A study that performs the optimisation of different composite structures with the help of a genetic algorithm has been presented [177] for using on structures representative of some typical industrial parts, such as, simple geometry wings, helicopter or wind turbine blades. The model considers a variable number of plies with different angles and allows varying the thickness along a part. To ensure manufacturability of the outcome, constraints are imposed to ensure ply continuity along contiguous areas at each optimisation step. This results in homogenisation of angles at a given level among a set of “feasible angles” for manufacturing reasons: 0, ± 15 , ± 30 , ± 45 , ± 60 , ± 75 , and 90° . The geometry and mesh are kept constant. The objective function aims at obtaining subdomains which exhibit the lowest number of plies as well as a Tsai–Hill criterion as close as possible to one for each ply, while staying below that value. The size of the FE model has been limited to a relatively small number of degrees of freedom, thus significantly reducing calculation time.

A similar structure was studied by Liu [179] in order to optimize a 13 m long glass-fibre epoxy composite wind turbine blade, aiming at reducing the material used and, thereby, the manufacturing costs. The Stiffness of the blade and its surface stresses were considered as constraints. The wind turbine blade was modelled using 3D plane stress shell elements to represent the thin-walled composite laminates from which the blade

is comprised. The FE models were generated using a Python code developed in-house. This code automatically generates the full FE model and performs the analysis. Many parameters can easily be considered for optimisation. However, the study presented focuses on the thickness distribution of the laminates and number of shear webs, in a total of 32 variables. The loads were applied to the blade using a form of multi-point constraint (MPC) and models used 4-node reduced integration (S4R) plane stress linear shell elements with hourglass control and 3-node triangular (S3) linear shell elements. Infeasible solutions receive a penalty application to the objective function values of individuals. The optimisation performed presented a 23% decrease in mass and 15.5% savings in total cost.

The field of wind turbine blades is a prime case of application of structural optimisation, since the cost of such blades represents about 15–20% of total wind turbine production cost and the aerodynamics of wind turbine blades has crucial influence on the efficiency of such equipment [180].

As may be seen in Figure 2.9, wind blades have a complex structure with several distinct zones. Each zone has typically different materials. The external surface of the blade is a skin used to construct the complex geometry of the blade [181]. Core areas (in blue) consist generally of foam, balsa or other engineered core materials [182]. The reinforcements (in yellow) are usually composed of layers of either carbon or glass fibre. Spar Caps consist of longitudinal reinforcements of the blade and are usually produced in either CFRP, Glass Fibre Reinforced Polymer (GFRP) or a combination of both [44]. Shear webs often use sandwich constructions. The spar cap and the webs form a box-like structure that acts like a main beam to improve the flap-wise stiffness [181].

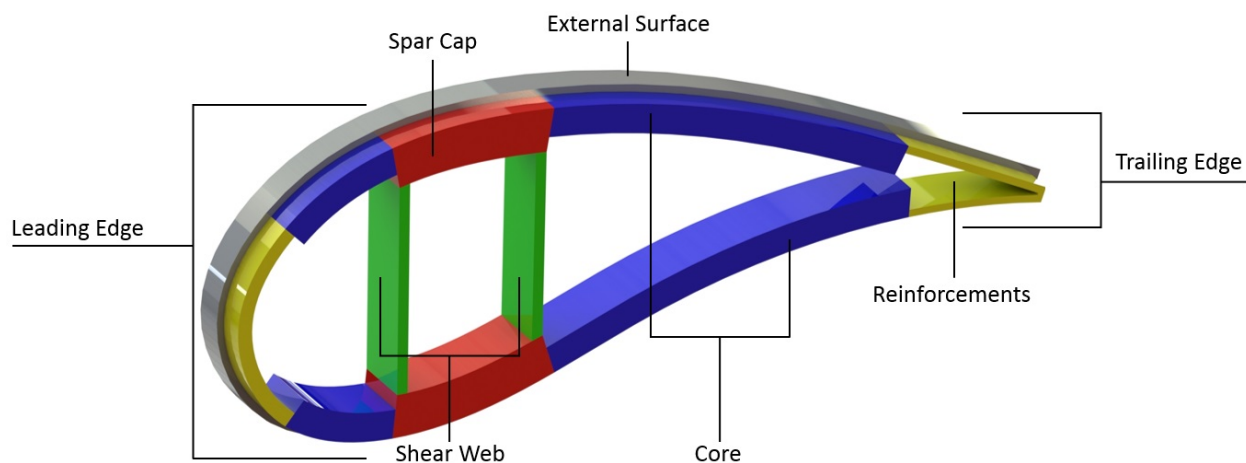


Figure 2.9 Typical structure of a wind blade (adapted from [181] and [183]) .

There are numerous cases of nature inspired population based metaheuristics used in the field of wind turbine optimisation. Examples of studies show the use of evolutionary algorithms [180, 184], and particle swarm has also used [181] mostly focused in minimising the mass by considering the thickness of layers and configuration of shear webs as variables.

A multi-objective optimisation of plate structures under stress criteria based on Genetic Algorithm has been also reported by Garambois [185]. The structure was optimised under a dynamic load with both discrete frequencies and frequency bands. However, and since the number of evaluations (or simulations) is high and dynamic simulations are computationally demanding, the model was quite simple and composed by little over 700 elements. Mixed Super-Elements were adopted to minimize the computation time. This study considered thickness parameters along the structure as variables and aimed at minimizing the mass and the Von Mises stress within the whole structure. Because these two objectives are antagonistic, multiple objective optimisation was chosen by the authors. The structure was optimized under a dynamic load with both discrete frequencies and frequency bands.

As previously discussed, particle swarm algorithms present higher convergence rates and, for this reason, many studies presented in the literature use them as a basis for structure optimisation [186].

Paluch and al. [187] have reported the use of Particle Swarm to maximize the globally optimum design of composite laminates subjected to fatigue in-plane loads. An empirical model that predicts the multiaxial fatigue failure for fibre reinforced materials was created to predict the fatigue life of composites. Since it does not require a complicated encoding and works directly with real numbers, Particle Swarm was used in this work due to its advantage over other global optimisation algorithms, e.g., the GA. The structure optimised was a symmetric 3-D multi-layered structure reinforced with continuous fibres subjected to in-plane normal loads. The study proved significant improvements in terms of the composite fatigue life.

Other work by Kovács [188] used experimentally obtained values, an analytical and a numerical models and Particle Swarm optimisation algorithm to find the best solution regarding the ply arrangement while complying with several criteria, such as deflection, bucking and stress. The structure analysed comprises both CFRP and aluminium components. The geometry of the part is also subjected to an optimisation procedure prior to the Particle Swarm application.

A modified Particle Swarm algorithm that allows multi-objective optimisation, based on Quantum behaved Particle Swarm Optimisation (QPSO) has also been proposed [171]. This was done by implementing an optimisation process that minimizes weight and cost while varying the number of layers, the stacking

sequence and the thickness of each layer. The evaluation of the design was based on Failure Mechanism, Failure criteria, Maximum stress failure criteria and the Tsai–Wu Failure criteria. The cost was estimated by considering the material cost (main contributor) and the time spent with the processing (directly proportional to the number of layers). A comparison between the QPSO and standard Particle swarm was performed. Particle swarm displays faster convergence, although QPSO might render slightly better results. A similar analysis has been performed by the same leading authors in Vector evaluated particle swarm optimisation (VEPSO) for multi-objective design optimisation of composite structures [189]. For this, the optimal design for a composite box-beam structure subject to strength constraints was developed. The ply angles were used as design variables. Authors tested the performance of the structure considering various loadings and particle swarm and gradient-based algorithms. The structure's evaluation was performed based on an analytical model and it was focused on the reserve factor. Reserve factor is a common factor by which all the applied loadings can be multiplied to reach a state of failure. For a structure to be safe, the reserve factor must always be greater than one. The methodology followed was quite similar to the one used in this work. However, both the geometry and the loadings considered were simpler. Therefore, the authors were not required to resort to numerical models. The end result for Particle swarm was superior or equivalent to the gradient-based method. The authors also reported that by allowing different walls to have different orientation angles gives a better design than forcing all the walls to have the same orientations.

Another optimisation technique that combines Particle Swarm and FE to minimizing absolute value of the free-edge delamination stresses considering both in-plane tensile load and uniform bending load has also been presented [190]. The results were compared to the ones obtained with pre-existing methods in commercially available software (ANSYS). Results obtained with Particle Swarm are generally closer to the global optima, converges in a lower number of iterations and less dependent on the starting points. The validation of the numerical model was accomplished by comparing the obtained results to the ones predicted by an analytical model for a relatively simple loading case of a given part. There was a low number of variables considered, maximum of two, representing the ply angle in relation to the previous one. The application of FEM regarding a simple geometry and Particle swarm for such a low number of variables may make this methodology suitable for more complex problems.

Alterations were also introduced to the traditional Particle swarm algorithm in order to improve search step and convergence [191]. Essentially the particles behaviour is made more uncertain in the search step but the boundaries dynamically change and narrow the search space as the search results remain unchanged

during consecutive iterations. Tests were performed with various problems showing that Particle swarm can be highly effective in the definition of the optimal stacking arrangement for composite materials to reduce weight while ensuring mechanical behaviour of the components

Meanwhile, results from tests made on particle swarm optimisation's performance using standard size and shape design problems selected from literature were published [192]. The concerned algorithm is compared to three gradient based methods, as well as genetic algorithm. At a stage in which particle swarm was still in its early years (when compared to the other competitors), it is concluded that particle swarm optimisation is superior to GA. The near-optima region is attained with comparable computational cost to that of the gradient based algorithm. Two distinct classes of problems were selected: optimal sizing design and optimal shape design. Minimum weight is selected as the objective function. These translate into the optimisation of truss (of different dimension) and shape of a torque arm problems. In the truss problems the variables were the sections and constraints representing displacement and stress. In the shape optimisation problem seven variables described the outline of the shape. Limits were implemented in order to prevent excessive mesh deformation. It was clear by convergence history analysis, that the performance of particle swarm was better than the competitors at early stages, but required significant large effort to refine the solution.

A design method was used for ultrasonic motors resorting to a combination of particle swarm optimisation and FEM [193]. The method was considered to be more efficient than traditional methods and more convenient than gradient based optimisation. Particle swarm optimisation was used, since it was considered robust, well suited to handle non-linear, non-convex design spaces with discontinuities and able to optimize problems with discontinuous and non-differentiable objective functions. These algorithms were also considered to be easy to implement and to have few parameters to adjust. Such design method was used to design an annular sector curvilinear ultrasonic motor. By changing its dimensions, the resonant frequencies are optimized in order to ensure the first two vibrating modes take place at frequencies as close as possible. Particle swarm method was also used to perform truss optimisation [194]. Four typical problems were considered and different sections of the beams were used as variables. Constraints were applied to the minimum cross sections of the beams, stresses and displacements. The objective function to be minimized respects the structure's weight. Effects of several algorithms parameters were investigated in terms of better global/local search behaviour, as well as avoiding premature convergence while converging to the optimal solution at suitable speed. The use of particle swarm optimisation was able to lead to optimal results, which are better, or at the same level of other structural optimisation methods against which the particle swarm

was benchmarked. The simplicity of implementation of this method was also pointed as a reason to make it a suitable selection for structural optimisation tasks.

It can be observed that Particle swarm optimization has shown outstanding performance in solving many realistic problems, presenting simplicity, effectiveness and low computational costs [195].

Chapter 3: Theoretical Framework

Summary

This chapter covers the fundamental theoretical concepts required for better understanding the work covered by this doctoral thesis. There are four main areas that are considered as particularly relevant and that, therefore, are detailed in the following pages. The first two sections are focused on the analytic models used to compute the deformations and impacts they have in the laser path. Thereafter, there is an overview of the theoretical principles associated to the Finite Elements Methods, and to the numeric method used to analyse the gantry's behaviour under more complex loading conditions. The last subject addressed is the main theoretical aspects of an optimization process.

3.1 DEFLECTION AND TORSION OF BEAMS

As mentioned, this work is focused in increasing the productivity of an ILCM, namely through the analysis and optimization of its gantry.

Understanding the deformations suffered by the gantry requires the analysis of two types of forces. One results from the gantry's own mass when subjected to accelerations (both the gravitational and the one imposed by the linear motors to move it). The other reflects the presence of additional components that move with and along the gantry. While the weight loads are distributed along the whole span of the gantry, there are other point forces, such as the one is applied by the cutting head.

3.1.1 Distributed loads

Consider a beam, simply supported at its both edges, subjected to a distributed load as it is shown in Figure 3.1.

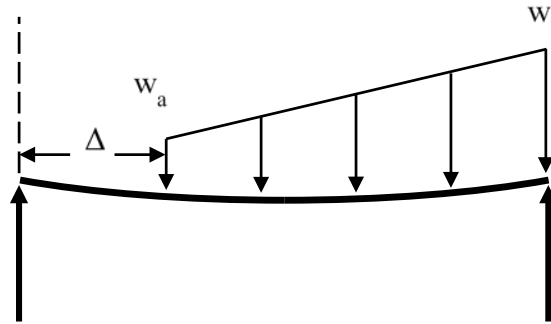


Figure 3.1 – General case of distributed load on a simply supported beam

Considering $\Delta = 0$ and $w_a = w_l$, which means a uniform load on the entire span, the loading scenario becomes the one represented in Figure 3.2.

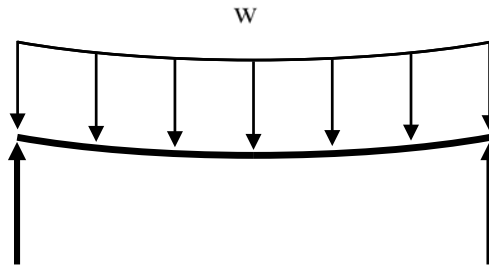


Figure 3.2 – Uniform distributed load over the entire span of a simply supported beam

For this case, the deflection (d) at a generic point along the length of the gantry, p , can be calculated by

$$d = \frac{m_g a (l - p)}{24EI l} [l^2 + p(l - p)] \quad \text{eq. 3.1}$$

where m_g is the mass of the gantry per unit of length, a is the acceleration along the considered axis, l is the length of the gantry, E is the Young's Modulus of the material and I is the Moment of Inertia of the beam cross-section and p is the distance of the point to the extremity of the gantry.

For a profile, having the hollow cross-section represented in Figure 3.3, its mass, m_g , may be calculated by eq. 3.2.

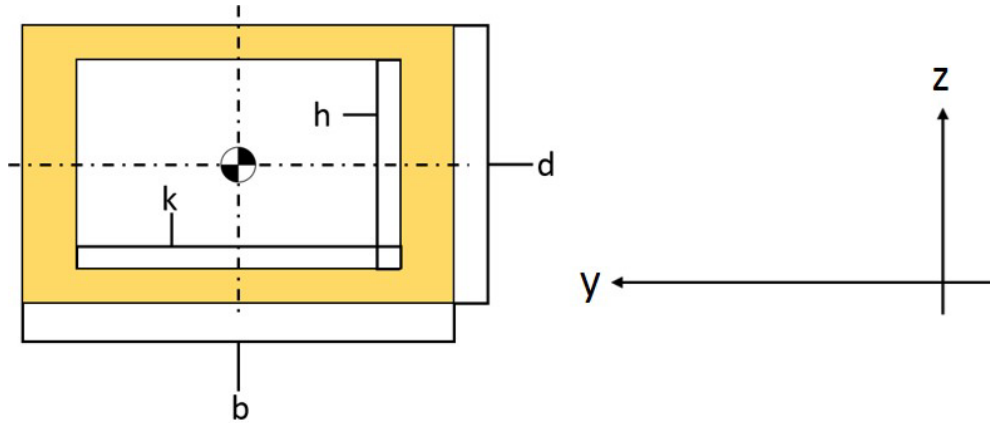


Figure 3.3 – Cross-section of a rectangular section tube

$$m_g = [(b \times d) - (k \times h)] \times l \times \rho \quad \text{eq. 3.2}$$

and, its both moments of inertia can be calculated as:

$$I_z = \frac{db^3 - hk^3}{12} \quad \text{eq. 3.3}$$

$$I_y = \frac{bd^3 - kh^3}{12} \quad \text{eq. 3.4}$$

from eq. 3.1 is also possible to deduce that the maximum deflection, verified at the mid-point lengthwise, can be calculated by:

$$d = \frac{5(m_g \times a)l^4}{384EI} \quad \text{eq. 3.5}$$

and, that the maximum rotation at the edge is given by:

$$r = \frac{(m_g \times a)l^3}{24EI} \quad \text{eq. 3.6}$$

3.1.2 Point loads

These loads can be represented as shown in Figure 3.4.

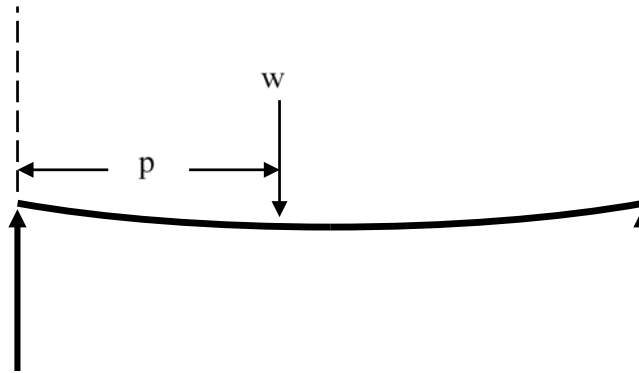


Figure 3.4 – Depiction of a simply supported beam subjected to a generic point load

In this case, the deflection at the point where a force is applied to the gantry can be calculated as:

$$d = \frac{m_{ch} \times a \times p^2 \times q^2}{3EI} \quad \text{eq. 3.7}$$

where m_{ch} is the mass of the cutting head and q is given by:

$$q = l - p \quad \text{eq. 3.8}$$

On other hand, the rotation at the load application point may be calculated as:

$$r = \frac{m_{ch} \times a \times p \times (l^2 - p^2)}{6EI} \quad \text{eq. 3.9}$$

while the rotation at the edge is given by

$$r = \frac{m_{ch} \times a \times q \times (l^2 - q^2)}{6EI} \quad \text{eq. 3.10}$$

When $p = l/2$, meaning the application point is in the middle of the gantry, the deflection and rotation angle become:

$$d = \frac{(m_{lh} \times a)l^3}{48EI_x} \quad \text{eq. 3.11}$$

Also for this loading case, the maximum rotation at the edge is given by:

$$r = \frac{(m_{lh} \times a)l^2}{16EI} \quad \text{eq. 3.12}$$

Regarding torsion, for a simple supported beam on both extremities, as represented in Figure 3.5, it is relevant to analyse the effects mentioned bellow.

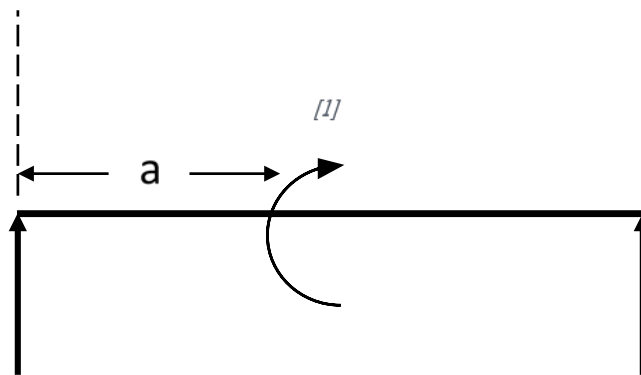


Figure 3.5 – Simply supported beam subjected to torsion

The angle of torsion may be calculate as,

$$r = \frac{Tl}{8JG} \quad \text{eq. 3.13}$$

where T is the Torsion Moment, J is the Polar Moment of Inertia and G is the Shear Modulus of the Material. Considering the cross-section represented in Figure 3.3, by making:

$$t = \frac{b - k}{2} \quad \text{eq. 3.14}$$

and,

$$t_1 = \frac{d - h}{2} \quad \text{eq. 3.15}$$

J can be calculated as:

$$J = \frac{2tt_1(b - t)^2(d - t_1)^2}{bt + dt_1 - t^2 - t_1^2} \quad \text{eq. 3.16}$$

If the torsion momentum is applied midway lengthwise, T, can be calculated as:

$$T = (m_{ch} \times a) \times d_{g,ch} \quad \text{eq. 3.17}$$

where $d_{g,th}$ is the distance in the considered direction, between the axis of the gantry and the centre of mass of the cutting head.

When the momentum is applied at a generic point p, T is given by:

$$T = \frac{p \times m_{lh} \times a_z \times d_{g,lh}}{l} \quad \text{eq. 3.18}$$

3.2 GEOMETRY

3.2.1 Definition of a plane

A plane M can be described by the following equation:

$$M = ax + by + cz - d \quad \text{eq. 3.19}$$

where a , b and c are the components of the vector n , normal to the plane.

$$n = \{a, b, c\} \quad \text{eq. 3.20}$$

The conditions that describe a plane might be derived from one point of the plane and two vectors that lay on it.

Considering point P , and vectors v and u , with coordinates:

$$P = (xp, yp, zp) \quad \text{eq. 3.21}$$

$$v = \{xv, yv, zv\} \quad \text{eq. 3.22}$$

$$u = \{xu, yu, zu\} \quad \text{eq. 3.23}$$

The equation of the normal vector to this plane is obtained from:

$$n = \det \begin{bmatrix} e_1 & e_2 & e_3 \\ xv & yv & zv \\ xu & yu & zu \end{bmatrix} \quad \text{eq. 3.24}$$

where e_1 , e_2 and e_3 are the unitary Euclidean vectors in the direction of each of the three axis (x , y and z).

The calculation of the determinant is performed according to eq. 3.25:

$$n = e_1(yv \times zu - zv \times yu) + e_2(zv \times xu - xv \times zu) + e_3(xv \times yu - yv \times xu) \quad \text{eq. 3.25}$$

The values that are multiplied in eq. 3.25 by the three components (e_1 , e_2 and e_3) correspond to a , b and c from eq. 3.19 respectively.

Thus, eq. 3.19 can be rewritten as:

$$M = (yv \times zu - zv \times yu)x + (zv \times xu - xv \times zu)y + (xv \times yu - yv \times xu)z + d \quad \text{eq. 3.26}$$

Considering, X , as a generic point of the plane with generic coordinates:

$$X(x, y, z) \quad \text{eq. 3.27}$$

X must respect the condition expressed by eq. 3.28:

$$n \cdot (X - P) = 0 \quad \text{eq. 3.28}$$

which means that being X and P two points of a plan and n the normal to it, the dot product between n and the generic vector in the plane must be equal to zero.

Thus, eq. 3.28 can be rewritten as:

$$nX = nP \quad \text{eq. 3.29}$$

Which, by replacing in eq. 3.26, translates to:

$$\begin{aligned}
M = & (yv \times zu - zv \times yu)x + (zv \times xu - xv \times zu)y \\
& + (xv \times yu - yv \times xu)z - (yv \times zu - zv \times yu)xp \\
& - (zv \times xu - xv \times zu)yp - (xv \times yu - yv \times xu)zp
\end{aligned}
\tag{eq. 3.30}$$

3.2.2 Determination of the intersection between a line and a plane

Considering the following generalised coordinates of the point, I, that represents the intersection between a line and a plane:

$$I = (xi, yi, zi) \tag{eq. 3.31}$$

By knowing that point I must be contained both in the plane (M) and the line (V), if V is not parallel or coincident to the plane M, the following equation with only one solution can be used to determine the point under consideration:

$$V = M \tag{eq. 3.32}$$

Thus, considering the line, V, defined by the following generalised equation:

$$V = L + tv \tag{eq. 3.33}$$

where, L, is a point of the line, v, the vector that indicates its direction and, t, a real number.

By decomposing eq. 3.33 into its components:

$$\begin{cases}
x = xL + t \times xv \\
y = yL + t \times yv \\
z = zL + t \times zv
\end{cases}
\tag{eq. 3.34}$$

The coordinates of interception point, I, may be rewritten as:

$$\begin{cases} xi = xL + t \times xv \\ yi = yL + t \times yv \\ zi = zL + t \times zv \end{cases} \quad \text{eq. 3.35}$$

As pointed, I, must also be contained in plane, M, eq. 3.19 must be accomplished and rewritten as:

$$axi + byi + czi + d = 0 \quad \text{eq. 3.36}$$

Thus, by replacing in eq. 3.36 the coordinates xi, yi and zi defined in eq. 3.35, it is possible to get:

$$a \times xL + a \times t \times xv + b \times yL + b \times t \times yv + c \times zL + c \times t \times zv + d = 0 \quad \text{eq. 3.37}$$

which may be solved in order to retrieve t as:

$$t = \frac{a \times xL + b \times yL + c \times zL + d}{a \times xv + b \times yv + c \times zv} \quad \text{eq. 3.38}$$

and by replacing this value of parameter, t, in eq. 3.34, it is finally possible to rewrite the coordinates of the interception point as:

$$\begin{cases} xi = xL - \frac{a \times xL + b \times yL + c \times zL + d}{a \times xv + b \times yV + c \times zv} \times xv \\ yi = yL - \frac{a \times xL + b \times yL + c \times zL + d}{a \times xv + b \times yV + c \times zv} \times yv \\ zi = zL - \frac{a \times xL + b \times yL + c \times zL + d}{a \times xv + b \times yV + c \times zv} \times zv \end{cases} \quad \text{eq. 3.39}$$

3.2.3 Reflection as Rotation of 180^a about an arbitrary axis

Having determined the equation of the plan, its normal vector and the point of intersection between a line and a plane, it is also possible to calculate the line reflection of the line V when it hits Plane M in point I (see

Figure 3.6). This line can be well defined by the direction vector and a point. As the point of interception is common to both lines it can be used to define the reflected one. Still, in order to define the vector of direction, a new point must be considered. This point can be achieved by calculating the reflection of a given point in the incident (V) line.

The angles of incidence of V in M,

outgoing wave vectors respectively and the line normal to the mirror. The law of reflection states that

θ_i , and reflection

$\theta_r = \theta_i$.

Any that lays in a line resultant from the reflection (R) of a known incident line (V) in a plane (M) with a defined normal (n) at a given point (I) can be defined as a rotation of 180° about an axis of a point belonging to line V (Figure 3.6).

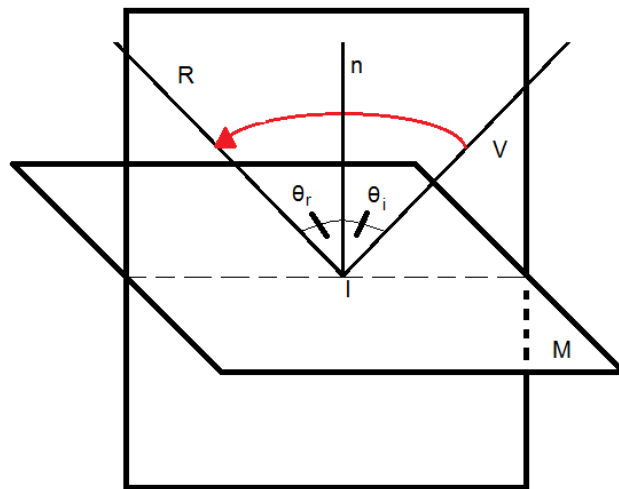


Figure 3.6 – Reflection of a line (V) in a plane mirror (M), generating a new line (R). This can be considered as a rotation of 180° about n.

Considering this, the second point that will allow the determination of the direction vector of the reflected line can be defined by the rotation of any known point of the incident line (except the incident point) and the incident point.

The rotation about an arbitrary line (in this case the line defined by point I and the normal vector n) can be implemented by translating this line so it contains the origin and rotated so it is aligned with the z axis. After this is performed the rotation in z is implemented. The process is then reverted and the line set back to its original position. The process is:

1. Translate space so that the point in the line's equation becomes coincident with the origin.

2. Rotate space about the z axis so that the rotation axis lies in the xz plane.
3. Rotate space about the y axis so that the rotation axis lies along the z axis.
4. Perform the desired rotation by θ about the z axis.
5. Apply the inverse of step (3).
6. Apply the inverse of step (2).
7. Apply the inverse of step (1).

The matrix that allows performing the operation above defined in point 1 is:

$$T_{IO} = \begin{bmatrix} 1 & 0 & 0 & -xi \\ 0 & 1 & 0 & -yi \\ 0 & 0 & 1 & -zi \\ 0 & 0 & 0 & 1 \end{bmatrix} \quad \text{eq. 3.40}$$

The multiplication with this matrix is equivalent to summing the vector [-a, -b, -c]

Point 2 is achieved by a multiplication with the following matrix:

$$T_{xz} = \begin{bmatrix} \frac{a}{\sqrt{a^2 + b^2}} & \frac{b}{\sqrt{a^2 + b^2}} & 0 & 0 \\ -\frac{b}{\sqrt{a^2 + b^2}} & \frac{a}{\sqrt{a^2 + b^2}} & 0 & 0 \\ 0 & 0 & 1 & 0 \\ 0 & 0 & 0 & 1 \end{bmatrix} \quad \text{eq. 3.41}$$

The operation depicted in point 3 is performed using the following matrix:

$$T_z = \begin{bmatrix} \frac{c}{\sqrt{a^2 + b^2 + c^2}} & -\frac{\sqrt{a^2 + b^2}}{\sqrt{a^2 + b^2 + c^2}} & 0 & 0 \\ \frac{\sqrt{a^2 + b^2}}{\sqrt{a^2 + b^2 + c^2}} & \frac{c}{\sqrt{a^2 + b^2 + c^2}} & 0 & 0 \\ 0 & 0 & 1 & 0 \\ 0 & 0 & 0 & 1 \end{bmatrix} \quad \text{eq. 3.42}$$

The rotation about the z axis is represented by the following matrix:

$$R_z(\theta) = \begin{bmatrix} \cos(\theta) & -\sin(\theta) & 0 & 0 \\ \sin(\theta) & \cos(\theta) & 0 & 0 \\ 0 & 0 & 1 & 0 \\ 0 & 0 & 0 & 1 \end{bmatrix} = \begin{bmatrix} -1 & 0 & 0 & 0 \\ 0 & -1 & 0 & 0 \\ 0 & 0 & 1 & 0 \\ 0 & 0 & 0 & 1 \end{bmatrix} \quad \text{eq. 3.43}$$

The matrixes inverse to these ones will result in the opposite operations.

By multiplying the matrixes here displayed in the above sequence and then multiplying their inverses in the inverse sequence it is possible to get the transformation matrix that allows performing actions 1 to 7 when a multiplication is performed.

$$T_{IO}T_{xz}T_zR_z(180^\circ)T_z^{-1}T_z^{-1}T_{xz}^{-1}T_{IO}^{-1} \quad \text{eq. 3.44}$$

This can be expanded to get eq. 3.45.

$$\begin{bmatrix} \frac{a^2 - (b^2 + c^2)}{a^2 + b^2 + c^2} & \frac{2ab}{a^2 + b^2 + c^2} & \frac{2bc}{a^2 + b^2 + c^2} & \frac{2(xi(b^2 + c^2) - a(yi \times b + zi \times c))}{a^2 + b^2 + c^2} \\ \frac{2ab}{a^2 + b^2 + c^2} & \frac{b^2 - (a^2 + c^2)}{a^2 + b^2 + c^2} & \frac{2bc}{a^2 + b^2 + c^2} & \frac{2(yi(a^2 + c^2) - b(xi \times a + zi \times c))}{a^2 + b^2 + c^2} \\ \frac{2ac}{a^2 + b^2 + c^2} & \frac{2bc}{a^2 + b^2 + c^2} & \frac{c^2 - (a^2 + b^2)}{a^2 + b^2 + c^2} & \frac{2(zi(a^2 + b^2) - c(xi \times a + yi \times b))}{a^2 + b^2 + c^2} \\ 0 & 0 & 0 & 1 \end{bmatrix} \quad \text{eq. 3.45}$$

Normalizing n so it is a unit vector (so that $a^2 + b^2 + c^2 = 1$) and multiplying it by any point in line V with coordinates

$$Pv(xv, yv, zv) \quad \text{eq. 3.46}$$

It is possible to calculate the correspondent point in line R (Pr) with coordinates

$$Pr(xr, yr, zr) \quad \text{eq. 3.47}$$

by using:

$$\begin{bmatrix} xr \\ yr \\ zr \end{bmatrix} = \begin{bmatrix} 2(xi(b^2 + c^2) - a(yi \times b + zi \times c - a \times xv - b \times yv - c \times zv)) - xv \\ 2(yi(a^2 + c^2) - b(xi \times a + zi \times c - a \times xv - b \times yv - c \times zv)) - yv \\ 2(zi(a^2 + b^2) - c(xi \times a + yi \times b - a \times xv - b \times yv - c \times zv)) - zv \end{bmatrix} \quad \text{eq. 3.48}$$

The direction vector of the reflected line R (r) can now be calculated by:

$$r = \{xr - xi, yr - yi, zr - zi\} \quad \text{eq. 3.49}$$

And, the equation of line R can finally be defined as:

$$R = I + tr \quad \text{eq. 3.50}$$

3.3 FINITE ELEMENTS

To estimate the response of a physical system subjected to a set of loading conditions (e.g., displacement, stress, temperature, pressure or velocity) one may try an analytic or a numeric approach. As problems in mechanics are governed by differential or partially differential equations that state the equilibrium and continuity states of the system, analytical solutions can be obtained from established mathematical functions in some cases. Such functions allow determining the values of the variables that one needs to evaluate at any location in the body. When the equations cannot be solved in order to find adequate mathematical solving functions and no other convenient method is available to even estimate the solutions (which can be caused by the presence of complex geometries, loadings and/or material properties), numerical methods must be used. The Finite Elements Method (FEM) [95, 196-198] as well as other approaches in the field of computational mechanics (such as, finite difference and finite volume methods) have helped to solve a lot of very challenging mechanical problems. The possibility of exploring them through simulation has become an essential and effective tool in solving complex problems and in supporting engineers to implement remarkable innovations and perform highly reliable product development processes [199]. When seen as a method of solving physical problems, FEM distinguishes itself from other numeric methods by using an integral

formulation to generate a system of algebraic equations and by approximating unknown quantities through the use of continuous piecewise smooth functions [198].

FEM finds solutions for complex problems by replacing them with simpler ones [95]. It does not solve the problem for an entire system under consideration in one single-shot but, instead, formulates the equations for smaller domains and then combines the results, hence rendering the solution for the global problem. As consequence, FEM does not present the exact theoretical solution for any actual problem but, by replacing it by an ensemble of simpler problems that can be solved, renders a final result that is a very good approximation to the exact solution [95]. The process of generating a system composed of smaller domains (called FE) equivalent to a system of interest is denominated discretization. This does not only return a discretized geometry, but also information regarding at which points (called nodes) and/or boundary lines and/or surfaces two or more elements interconnect [196]. The result of this approach is commonly denominated as mesh. The mesh of the whole system of interest is denominated as continuum or domain. From a mathematical perspective, FEM represents a method for approximating the solution of differential equations [200]. It does so at punctual points of the domain: the nodes. The nodes usually lie on the extremities of the elements through which the contiguous elements are connected. The nodal values will be obtained by solving the FEM equations. An approximation function or interpolation model is then used to calculate the field variable (the variable of interest) throughout the domain [95].

3.3.1 Steps of the Finite Element Method application

3.3.1.1 Discretization

The first step when implementing a FEM is to divide the system of interest into smaller domains or FE with associated nodes, in order to create the mesh. The selection of suitable elements is, therefore, of utmost interest. When performing this stage one must consider several element related parameters, namely type, size and arrangement. If care is not taken into this stage, it is possible that the final result does not accurately reflect the system of interest's global behaviour. On the other hand, attention must also be given to the required computational effort, so that it is not so large that an unaffordable time will be spent in getting the final solution [95, 196]. This logic is directly applied to the element size. Smaller size elements will result in

a more faithful representation of reality, but also on longer computational time for the same computational resources. A trade-off must be ensured because highly accurate solutions usually present unaffordable prices [201]. It is also important to take in account that accuracy and computational costs do not have a linear relationship and, as Figure 3.7 shows, after a proper number of elements, no significant improvements will be achieved on the final result's accuracy [95].

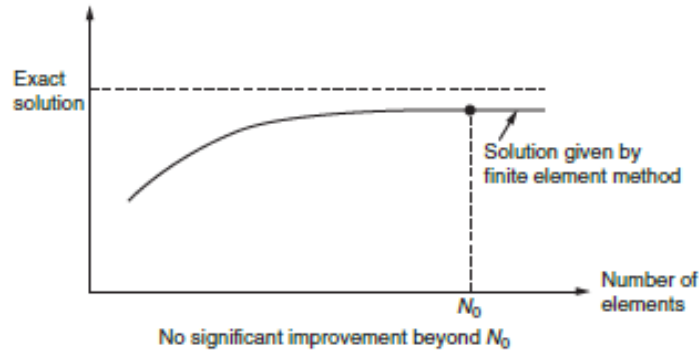


Figure 3.7 - Effect of the variation of number of elements in the accuracy of the solution [95]

The choice of the element type is directly related to the body layout and stands one of the most critical tasks to be performed during the FEM implementation [196]. There are five aspects that characterise the elements:

- Family;
- Degrees of freedom;
- Number of nodes;
- Formulation;
- Integration [202]

Figure 3.8 shows some of the most common families of FE used.

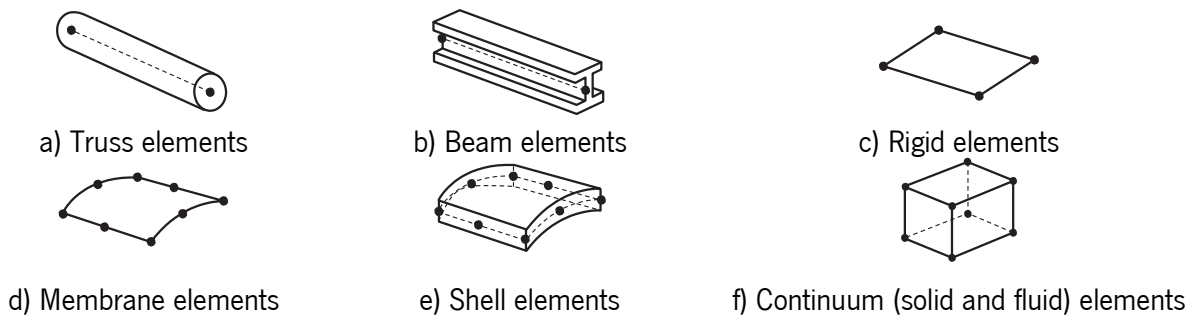


Figure 3.8 – Commonly used elements families (adapted from [202])

FE families greatly differ amongst them regarding their dimensionality, which can range from one to three. Truss and beam elements, consisting of a bar to which a section can be assigned, have one dimensionality. Although higher order elements are also available these simplest two nodes bar elements (linear) are usually used to model trusses and frame structures [196].

Rigid, membrane and shell elements are abstractions used to represent domains in which one of the dimensions is significantly larger than the other ones. Between them, each formulation is varied and they are used to represent particular situations with such configuration. Shell elements are of particular interest and will be further discussed in the present work. In particular, conventional shell elements, in which the thickness is defined by a section property applied to a reference surface, are commonly used to model composite structures [202]. Continuum elements, on other hand, are often used to represent volumes and when a three dimensional stress analysis is required [196, 202].

The degrees of freedom are the number of variables to be calculated during a FEA. In the case of a stress/displacement simulation, the degrees of freedom are translation and, for some element families, such as shell, rotation. Thus, for this type of simulations and depending on the family of elements selected, the nodal output will involve three or six values (although this number can vary in particular situations) according to the degrees of freedom presented in Table 3.1.

Table 3.1 - Degrees of freedom are the variables that are calculated

Degree of Freedom	Meaning
1	x-displacement
2	y-displacement
3	z-displacement
4	Rotation about the x-axis, in radians
5	Rotation about the y-axis, in radians
6	Rotation about the z-axis, in radians

Another point to be taken into account is the interpolation model chosen to estimate the variable of interest value in locations of elements other than the nodes. This will be further addressed ahead along the description of FEM implementation steps, but is highly dependent on the element's order. However, regardless of the

interpolation method used, the accuracy of its output largely depends on how much the elements are distorted. In two-dimensional domains, for example, the triangular and rectangular geometries are the fundamental element shapes used. The best outputs come when triangular equilateral and square elements are used. There are several measurements of distortion. The aspect ratio, for example, which establishes the relation between the length of the largest and shortest sides and also the internal angles might be used to determine the distortion of elements [201].

The proper formulation of elements will greatly depend on the application. For mechanical applications the element's behaviour is commonly described as Lagrangian, in which the element deforms with the materials. Fluid mechanics applications usually resort to an Eulerian model, in which the element is considered as fixed in space and material flows through it.

Integration is also another related subject that will be better analysed later along the discussion of the FEM implementation stages.

3.3.1.2 *Interpolation Model*

The second step in the implementation of FEM is the definition of an interpolation model.

Considering a function f , continuous in an interval $I = [x_0, x_1]$, the linear interpolant πf in that interval is defined as:

$$\pi f = f(x_0)\varphi_0 + f(x_1)\varphi_1 \quad \text{eq. 3.51}$$

where φ_0 and φ_1 are known as hat functions.

These functions, varying in a linear fashion, take the value of 1 at its node and 0 on the other ones. This means that $\varphi_0(x_0) = 1$ and $\varphi_0(x_1) = 0$ and the opposite happens to φ_1 . Thus, $\pi f(x_0) = f(x_0)$ and $\pi f(x_1) = f(x_1)$ [203]. Another characteristic of these hat functions is that for any x contained in that interval, the sum of them is one.

This principle is used by linear FE to estimate the value throughout the element. As mentioned previously, the variable of interest is calculated for nodes and then approximated to the rest of the element. Considering the simplest case, a two-dimensional linear element, where nodes act as extremities of the interval the hat functions are named shaped functions [198].

The linear approximation is the simplest model to perform the interpolation. For a linear one dimensional element of length L , with nodes i and j placed at a distance x_i and x_j from the origin, it takes the form of a polynomial of degree one that obeys to the following equation:

$$\phi = \alpha_1 + \alpha_2 x \quad \text{eq. 3.52}$$

Where ϕ is the unknown nodal variable and α_1 and α_2 can be calculated by the following equations:

$$\alpha_1 = \frac{\phi_i x_j - \phi_j x_i}{L} \quad \text{eq. 3.53}$$

$$\alpha_2 = \frac{\phi_j - \phi_i}{L} \quad \text{eq. 3.54}$$

by substituting eq. 3.53 and eq. 3.54 in eq. 3.52, one gets:

$$\phi = \frac{\phi_i x_j - \phi_j x_i}{L} + \frac{\phi_j - \phi_i}{L} x \quad \text{eq. 3.55}$$

that may be rearranged as:

$$\phi = \frac{x_j - x}{L} \phi_j + \frac{x - x_i}{L} \phi_i \quad \text{eq. 3.56}$$

where the term,

$$\frac{x_j - x}{L} \quad \text{eq. 3.57}$$

returns 0 when $x = x_j$ and 1 for $x = x_i$, therefore being the shape function for node i . The opposite also happens for $\frac{x - x_i}{L}$ being, consequently, both the shape functions for the element [201].

If the element under consideration has not linear behaviour, but rather of higher order, the same will happen to the shape functions. In fact, shape functions are always of the same order of that one defined for the interpolation method in use [198]. For higher order interpolation, the element needs to present a higher node count [201].

As the order of the polynomial function used for interpolation increases so does the accuracy of the result [95], as shown in Figure 3.9.

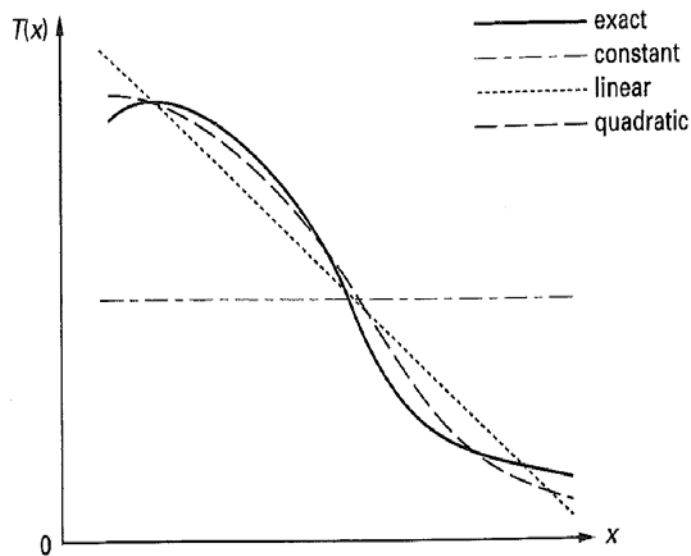


Figure 3.9 - Polynomial approximation in one dimension (adapted from [201])

In terms of accuracy, fewer higher order elements are needed to reach the same degree of accuracy. Higher order elements are mainly used in cases in which the gradient of the variable is expected to vary rapidly through the element [95].

For higher dimensionalities and similar order, the variable of interest will be calculated at a given generic point by considering more nodal values and more shape functions [201].

The same interpolation model is then applied throughout the domain and, therefore, FEM approximates a continuous quantity by a discrete model composed of piecewise-continuous functions, defined within each element.

3.3.1.3 *Deriving the element stiffness matrix and equations.*

FEM is many times used with success to analyse stress problems. It can cope with numerous types of loads, namely, concentrated, distributed pressure and body force loads (inertia or gravitational), initial strains and prescribed displacements. It also deals very well both with single load scenarios, in which one load acts isolated, and with those in which several loads act upon a same body by applying the principle of superposition. This principle is used to yield the nodal displacements and after, based on the obtained result, stresses and strains are then calculated [201].

Depending on the scenario where the method is used to analyse, the way to derive the equations that represent the nodal behaviour of the element needs to accomplish different requirements.

In the direct method the physical phenomena is directly analysed to establish the element properties. This method is applicable only to simple problems and overwhelmingly difficult to apply to problems involving two- and three-dimensional elements. It has, therefore, a quite limited application [95, 196].

To derive the finite element equations for two and three-dimensional elements, the variational approach is the most straight forward formulation. It resorts to the minimization of the potential energy of the system [196, 201]. The FEA is taken as an approximation for solving variational problems by applying variational calculus, which deals with the extremisation of functionals in the form of integrals. A limitation of the method arises from the fact that not all problems can be stated in such way [95].

Weighted residual approach result in the same equations as variational approach when both can be applied [201]. Yet, it is able to be applied to a larger number of problems. It is the most general approach and can be applied to almost all science and engineering problems [95, 196].

Using any of these methods leads to the application of equations capable of describing the behaviour of an element. The matrix formulation presents the following general form:

$$\begin{Bmatrix} f_1 \\ \vdots \\ f_n \end{Bmatrix} = \begin{bmatrix} k_{11} & \cdots & k_{1n} \\ \vdots & & \vdots \\ k_{n1} & \cdots & k_{nn} \end{bmatrix} \begin{Bmatrix} d_1 \\ \vdots \\ d_n \end{Bmatrix} \quad \text{eq. 3.58}$$

or, written in a compact way:

$$\{f\} = [k]\{d\} \quad \text{eq. 3.59}$$

where $\{f\}$ is the vector of element nodal forces, $[k]$ is the element stiffness matrix (normally square and symmetric) and, $\{d\}$ is the vector of unknown element nodal degrees of freedom or generalized displacements (actual displacements, slopes, or even curvatures) [196].

These three matrices essentially describe how an element with a given geometry and material properties (coded in the stiffness) deforms under a given loading scenario. Such equation is, therefore, required to be specifically tailored for each type of element.

3.3.1.4 Assembling element equations to obtain overall equilibrium equations.

Once the individual element's matrices and vectors equations are established, this step will enable the analysis of the domain of interest [201]. This procedure follows the preliminary process described in the next paragraph, which is independent of the problem dimension and types of elements used. In the end, it will be possible to respect the compatibility requirement at that given node, according to which the value(s) of the variable(s) of interest is the same for all elements that share one connection in that node [95].

Depending on specificities of the problem or on how the previous stages were performed, the stage of equation assembly might require a preliminary step of coordinate transformation. Such step is required when resorting to FEM to evaluate vector quantities, such as displacement and velocity, or when element matrices are computed in local coordinates to minimize computational effort. The process transforms the element matrices and vectors derived to local coordinate systems and refers the elemental equations to a common global coordinate system [95].

The process of assembling the equations is merely a matter of adding the coefficients of each element stiffness matrix $[k]$ into the corresponding places of the global stiffness matrix and summing the force vector coefficients $\{f\}$ into the global force vectors [201].

Upon the completion of assembling the global stiffness equations, the boundary conditions are assembled. Properly restraining the body will prevent rigid body motion and, thus, allow for an effective evaluation [201].

3.3.1.5 Calculation of nodal displacement

Once the equations are assembled, the FEM becomes a matter of solving a system of simultaneous linear algebraic equations [196]. The discrete problem described by these equations can belong to one of three types: steady-state or static equilibrium, eigenvalue, or propagation (transient).

In a general manner, these types of problems can generally be formulated by one of the matrix forms presented in Table 3.2.

Table 3.2 – Formulation and Conditions of different types of discrete problems

Problem Type	Formulation	Boundary Conditions	Initial Conditions
Equilibrium or linear	$[A]\vec{X} = \vec{b}$	$[B]\vec{X} = \vec{g}$	
Eigenvalue	$[A]\vec{X} = \lambda[B]\vec{X}$	$[C]\vec{X} = \vec{g}$	
Transient	$[A] \frac{d^2\vec{X}}{dt^2} + [B] \frac{d\vec{X}}{dt} + [C]\vec{X} = \vec{F}(\vec{X}, t), t > 0$	$[D]\vec{X} = \vec{g}, t > 0$	$\vec{X} = \vec{X}_0, t = 0$ $\frac{d\vec{X}}{dt} = \vec{Y}_0, t = 0$

In Table 3.2 $[A]$, $[B]$, $[C]$ and $[D]$ are square matrices whose elements are known, \vec{X} is the vector of unknowns (or field variables) in the problem and, \vec{b} , \vec{g} , \vec{X}_0 and \vec{Y}_0 are vectors of known constants; λ is the eigenvalue; t is the time parameter; and \vec{F} is a vector whose elements are known functions of \vec{X} and t [95]. Equilibrium problems allow a relatively easy calculation of \vec{X} . Other problems require larger efforts for solution achievement.

When solving equilibrium, steady-state, or static problems with FE (such as in the case of the current work), the values of \vec{X} are calculated in order to satisfy the formulation presented in Table 3.2. In a practical finite element problem, $[A]$ can be quite large and, in a simple problem, its dimensions can be in the order of thousands. On the other hand, most commonly, the matrices involved are sparse and symmetric.

The methods for solving systems of linear equations can be direct or iterative. Direct methods are those that, except if errors exist, will yield the exact solutions. Due to limitations to computational methods, round-off and truncation will sometimes result in extremely poor or even useless results from direct methods. Iterative methods are those that start with an initial approximation and then look for successively better approximations by applying a suitably chosen algorithm lead. When the process converges, we can expect to get a good approximate solution.

Gaussian elimination is the most common method used to solve linear systems of equations in a direct fashion. Even within this class, there is large number of choices of methods with various computational efficiencies and accuracies.

Iterative methods present as main advantages the simplicity and uniformity of performed operations. They are also much less sensitive to the growth of round-off errors [95, 196].

3.3.1.6 Computation of the desired secondary quantities.

Secondary quantities are usually the stress and strain. Moment and shear forces are other common unknowns determined in this step. Usually, they can be directly correlated to the displacements calculated in a previous step. The link between displacements and other quantities is based upon equations of solid or structural mechanics.

These equations include external and internal equilibrium equations and account for the material's constitutive model.

External equilibrium aims at ensuring that a body under a specified set of static loads, develops reactive forces at its support points that balance the external applied loads. Therefore, considering the body illustrated in Figure 3.10 supported on points B, C and D, eq. 3.60 and eq. 3.61 must be respected.

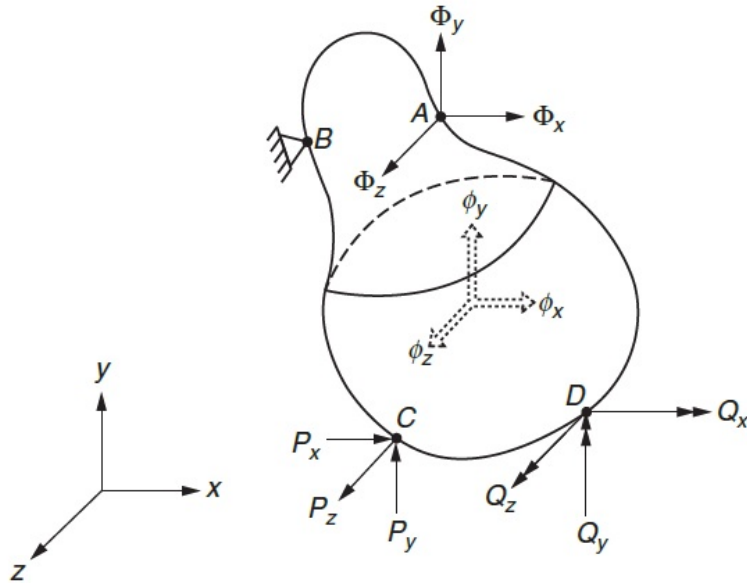


Figure 3.10 - Force System for Macroequilibrium of a body (adapted from [95])

$$\left. \begin{aligned} \int_s \Phi_x ds + \int_V \phi_x dV + \sum P_x &= 0 \\ \int_s \Phi_y ds + \int_V \phi_y dV + \sum P_y &= 0 \\ \int_s \Phi_z ds + \int_V \phi_z dV + \sum P_z &= 0 \end{aligned} \right\} \text{eq. 3.60}$$

$$\left. \begin{aligned} \int_s (\Phi_z y - \Phi_y z) ds + \int_V (\phi_z y - \phi_y z) dV + \sum Q_x &= 0 \\ \int_s (\Phi_x z - \Phi_z x) ds + \int_V (\phi_x z - \phi_z x) dV + \sum Q_y &= 0 \\ \int_s (\Phi_y x - \Phi_x y) ds + \int_V (\phi_y x - \phi_x y) dV + \sum Q_z &= 0 \end{aligned} \right\} \text{eq. 3.61}$$

where ϕ_x , ϕ_y , and ϕ_z are the body and, Φ_x , Φ_y , and Φ_z the surface (distributed) forces, respectively, P_x , P_y , and P_z are the external concentrated loads (including reactions at support points), Q_x , Q_y , and Q_z are the external concentrated moments (including reactions at support points) and S is surface and V volume of the solid body.

Internal equilibrium relates to the stresses developed inside the body as a result of load application. The stress at any point of a body can be defined resorting to nine components: σ_{xx} , σ_{yy} , σ_{zz} , σ_{xy} , σ_{yx} , σ_{yz} , σ_{zy} , σ_{zx} and σ_{xz} , where the first three components are normal stresses and the rest shear stresses. Considering that there are no body moments applied, the one gets [95]:

$$\sigma_{yx} = \sigma_{xy}, \sigma_{zy} = \sigma_{yz}, \sigma_{zx} = \sigma_{xz} \quad \text{eq. 3.62}$$

Therefore, there are six independent stress components (or stress tensors) at a given point of a 3D solid and these can be express by the following vector form:

$$\vec{\sigma}^T = \{ \sigma_{xx} \ \sigma_{yy} \ \sigma_{zz} \ \sigma_{yz} \ \sigma_{xz} \ \sigma_{xy} \} \quad \text{eq. 3.63}$$

which, by considering an equilibrium of forces in the x, y and z directions, may be written as:

$$\left. \begin{aligned} \frac{\partial \sigma_{xx}}{\partial x} + \frac{\partial \sigma_{xy}}{\partial y} + \frac{\partial \sigma_{zx}}{\partial z} + \phi_x &= 0 \\ \frac{\partial \sigma_{xy}}{\partial x} + \frac{\partial \sigma_{yy}}{\partial y} + \frac{\partial \sigma_{yz}}{\partial z} + \phi_y &= 0 \\ \frac{\partial \sigma_{zx}}{\partial x} + \frac{\partial \sigma_{yz}}{\partial y} + \frac{\partial \sigma_{zz}}{\partial z} + \phi_z &= 0 \end{aligned} \right\} \quad \text{eq. 3.64}$$

as for the case of stresses, the six strain tensors may equally be written in the following form:

$$\vec{\varepsilon}^T = \{ \varepsilon_{xx} \ \varepsilon_{yy} \ \varepsilon_{zz} \ \gamma_{yz} \ \gamma_{xz} \ \gamma_{xy} \} \quad \text{eq. 3.65}$$

where ε and γ represent the normal and shear strains, respectively.

Since strains represents displacements per unit length, they can be calculated by the following well-known eq. 3.66 to eq. 3.71.

$$\varepsilon_{xx} = \frac{\partial u}{\partial x} \quad \text{eq. 3.66}$$

$$\varepsilon_{yy} = \frac{\partial v}{\partial y} \quad \text{eq. 3.67}$$

$$\varepsilon_{zz} = \frac{\partial w}{\partial z}; \quad \text{eq. 3.68}$$

$$\gamma_{xy} = 2\varepsilon_{xy} = \frac{\partial u}{\partial y} + \frac{\partial v}{\partial x}; \quad \text{eq. 3.69}$$

$$\gamma_{xz} = 2\varepsilon_{xz} = \frac{\partial u}{\partial z} + \frac{\partial w}{\partial x}; \quad \text{eq. 3.70}$$

$$\gamma_{yz} = 2\varepsilon_{yz} = \frac{\partial v}{\partial z} + \frac{\partial w}{\partial y}; \quad \text{eq. 3.71}$$

where u , v and w are the displacements in x , y and z directions, respectively.

On the other hand, the relationship between σ and ε may be written as:

$$\vec{\varepsilon} = [C] \vec{\sigma} \quad \text{eq. 3.72}$$

where $[C]$ is the compliance matrix of elastic coefficients that can be written for an isotropic material as:

$$[C] = \frac{1}{E} \begin{bmatrix} 1 & -\nu & -\nu & 0 & 0 & 0 \\ -\nu & 1 & -\nu & 0 & 0 & 0 \\ -\nu & -\nu & 1 & 0 & 0 & 0 \\ 0 & 0 & 0 & 2(1+\nu) & 0 & 0 \\ 0 & 0 & 0 & 0 & 2(1+\nu) & 0 \\ 0 & 0 & 0 & 0 & 0 & 2(1+\nu) \end{bmatrix} \quad \text{eq. 3.73}$$

3.4 OPTIMISATION

The process of developing composite structures that meet structural specifications is an interesting optimisation problem [204]. The many aspects that can be manipulated during composite structures design make them largely customisable. But they also translate into many variables that need to be evaluated to determine the best design configuration [177]. Therefore, an optimisation process becomes of great value and complexity when dealing with problems involving such a high number of variables, particularly, if the definition of “optimisation” is taken as that one given by the Merriam Webster dictionary, which is: “act, process, or methodology of making something (as a design, system, or decision) as fully perfect, functional, or effective as possible”.

When considering engineering applications, the optimisation’s goal is either to minimise the required effort or to maximize the desired benefit. Systems can usually be parameterised in a way that several configurations are possible to be emulated. One or more functions can then be defined to quantify how well they fulfil the requirements under consideration. This way, by changing the parameters, the system’s configuration can be made more desirable. The application of optimisation algorithms makes this task much more feasible and ensures that all the variables taken into account are being evaluated and attributed values that allow for a better overall performance of the system [115].

For the purpose of optimization, such parametrised systems or components are defined as a set of parameters, some of which viewed as variables during the design process. On the other hand, other parameters, called preassigned parameters, are made fixed. Those treated as variables in the optimization process are called design or decision variables [115]. When the variables are changed, the system configuration also changes. The variables of design or decision will be inputs for the function(s) established to estimate the behaviour of a given system configuration.

The functions’ graphic representation can range from a two-dimensional plot (one variable) to an n-dimensional. The design variables are represented as a the design vector $X = [x_1, x_2, \dots, x_n]^T$. Although virtually there is no limitation to the number of variables being considered, the analysis grows in complexity with the increase of parameters being considered. Since the purpose of optimization is to choose the best of the array of possible configurations, these functions represent the criterion for comparing the different acceptable alternatives and are known as objective function [115]. The objective functions need to, therefore, represent what one is trying to evaluate and optimise. Regarding the number of objective functions, problems might have one or more. Situations that require the analysis of only one aspect of the system’s performance

also have a single objective function. In other situations, multiple objectives might be taken into account. In such cases two approaches are feasible: to consider various objective functions (corresponding to the so-called multi-objective optimisation) or only one objective function that consists on a linear combination of the various functions which could otherwise be relevant for the system performance. The situations represented in such problems might aim at optimising considering contradicting objectives. If a multi-objective approach is followed, a set of different solutions will be produced, representing various trade-offs of different objectives. Each of these solutions represents an optimal solution where a gain in one objective calls for the sacrifice of other(s). Regardless of some solutions being superior to others regarding isolated objectives, all of them are optimal when considering the combination of objectives. These solutions are named the Pareto Front. Higher level information is then analysed in order to choose one of the optimal solutions obtained from the optimisation process [139].

Since there is no essential difference between the maximisation and minimisation of a function, an optimisation algorithm can be used for both purposes. For example, when aiming at

$$\text{maximization}_{x \in S} f(x) \quad \text{eq. 3.74}$$

with an algorithm that is thought for minimisation, the issue can be overcome by performing

$$\text{minimization}_{x \in S} (-f(x)) \quad \text{eq. 3.75}$$

and multiplying the optimal value by -1 [205]. For this work an optimisation process will be defined as minimisation.

A point x^* classifies as a local minimum if

$$f(x^*) \leq f(x^* + h) \quad \text{eq. 3.76}$$

for all values of h sufficiently close to zero.

The function $f(x)$ is said to have a global minimum at x^* if

$$f(x^*) \leq f(x) \quad \text{eq. 3.77}$$

for all x [115].

Finally, it may be said that an optimisation mathematical problem, in a general manner, can be stated as:

$$FIND X = \begin{Bmatrix} x_1 \\ \dots \\ x_n \end{Bmatrix} \text{ which minimizes } f(x) \quad \text{eq. 3.78}$$

subjected to the constrains:

$$g_j(X) \leq 0, \quad j = 1, 2, \dots, m \quad \text{eq. 3.79}$$

$$l_j(X) = 0, \quad j = 1, 2, \dots, p \quad \text{eq. 3.80}$$

where X is an n -dimensional vector called design vector that contains the variables under analysis, $f(x)$ is the so-called objective function and $g_j(X)$ and $l_j(X)$ are known as inequality and equality constraints, respectively.

3.4.1 Types of optimization problems

Apart from the already described as single/multi-objective types, optimisation problems can also be classified regarding other aspects, such as: constraints, admissible values for functions, linearity, objective function surface and nature of optimisation algorithms used.

3.4.1.1 Constraints

Some optimisation problems might present some limitations regarding the configurations the system can assume. Therefore, the variables may only be able of assuming a given set of values. The optimization might be performed considering only a limited number of points (the feasible set) [205]. The limitations are

represented in Equations eq. 3.79 and eq. 3.80 by $g(X)$ and $l(X)$. The number of variables n and the number of constraints m and/or p are not required to be related in any way [115]. If dealing with unconstrained optimisation problems, such constraints are non-existent.

3.4.1.2 Admissible values for functions

Apart from restrictions coming from constraints on the values that can be assumed by variables, some problems also limit them to being integers. If one or all the variables are required to assume integer or discrete values, the optimisation problem is an integer one. If such a limitation is not imposed, the problem is classified as real-value optimisation problem [115].

3.4.1.3 Linearity

The optimization problems may be classified in two groups regarding the operators used both to define the objective function and to restrain the possible values for the variables. Linear optimization implies considering only linear functions (polynomial functions of degree zero or one) [205]. If a non-linear function is used for representing the system behaviour or variables restrains, the problem is considered Non-Linear.

3.4.1.4 Objective Function Surface

Regarding the function surface, an optimization problem might be classified either as convex or nonconvex. The definition of a convex feasible set is that any two given points of the feasible set must be able to be connected by a line segment also belonging to the feasible set [205]. A convex function has only one optimum, which is both local and global. A function with an irregular surface will have several peaks. Some of these peaks might represent local optima. Unless a convex problem is being considered, it is possible that the optimisation algorithm will converge to a local optimum. When the surface presents various peaks, there is the possibility that the algorithm converges to a local optimum that may be quite inferior to the global one. This comes from the fact that the optimisation has a limited knowledge of the function behaviour and may not consider more distant points that present more attractive results. A convex function leads optimisation

algorithms to a successful and univocal identification of the minimum value for that function. This situation occurs for all linear optimization problems [205].

3.4.1.5 The nature of optimisation algorithms used

A distinction between optimisation problems arises from the nature of the implemented algorithms (stochastic or deterministic). Stochastic optimisations simulate stochastic processes based on probabilities. They are likely to discover a very good feasible solution, but not necessarily an optimal one, although a well-designed one should reach a nearly optimal result [126]. As result, their output can vary from one execution to another. Deterministic algorithms always present the same result for a given set of initial conditions [109].

Chapter 4: Experimental Procedure

Summary

This chapter is focused on the description of the work performed in order to obtain a gantry to replace the current one and create a machine presenting higher productivity without accuracy loss.

This implies the characterization of the machine being studied, analysis of the loading scenarios and their effect on the current part, dimensioning of the new solution adopted and the experimental validation of the methods and outcome of this process.

The analysis and dimensioning was performed using both analytic and numeric models. The difficulty in achieving a balanced solution between weigh/stiffness/acceleration, led to the implementation of an optimization routine linked to the numerical evaluation of the performance of the solutions created. This method implied a numeric evaluation that needed to be extremely fast to perform.

4.1 EQUIPMENT UNDER STUDY

The machine to be studied and improved with the work here presented was a 2-dimensional ILCM having 2 axis flying optics produced by Adira.

Adira is a leading manufacturer of sheet metal working machinery, specialized in the production of Hydraulic, Electric and hybrid Press Brakes, Shears and Laser Cutting Machines for steel, stainless steel, aluminium, brass, etc. It was founded in 1956 by António Dias Ramos and entered the market with completely new and disruptive products, following the digital Industry 4.0 revolution, specifically the Additive Manufacturing for Large Parts [14, 206].

The first steps towards the laser cutting market took place in 2002, with the design of the CCL 3015 machine. The name, which comes from the initials Laser Cutting Centre (Centro de Corte Laser, in Portuguese) has since changed to LP (Laser Premium). The number indicates the size of the largest sheet metal the machine has the capacity to operate on. 3015 means that the metal sheet has maximum dimensions of 3.0×1.5 (m). There is also the version 4020. LP 3015 is displayed in Figure 4.1. LP 3015 is a CO₂ slab-type Laser, presenting as its main advantages reduced maintenance and high movement speed through linear motors [206, 207].



Figure 4.1 -Adira's LP 3015 Laser cutting Machine (from [206])

Another view of the machine disclosing its several components and auxiliary systems is presented in Figure 4.2.

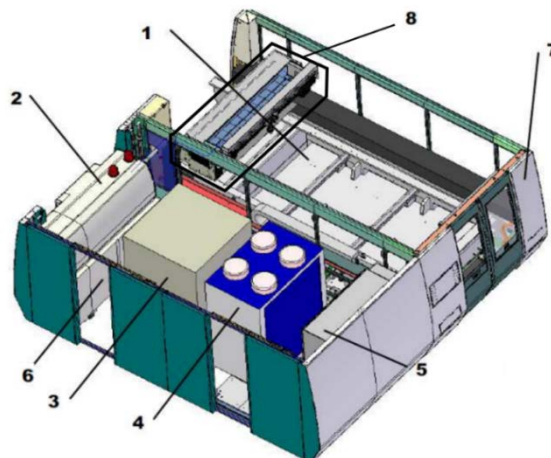


Figure 4.2 - LP3015's structure – Positioning system (1), Laser Source (2), Smoke extractor (2), Cooling System (4), Air Compression system, Lubrication system and Electric Power system (5), Laser Source electric system (6), External Protections (7) and Gantry. Cutting Head and Optical Path (8) (adapted from [208])

Because the laser source used in the LP3015 machine is the CO₂, the optical path consists of a set of lenses, mirrors and is completely airtight, as it must ensure the laser beam is not disrupted by dust or other impurities [209].

A better understanding of the machine's working can be achieved through Figure 4.3

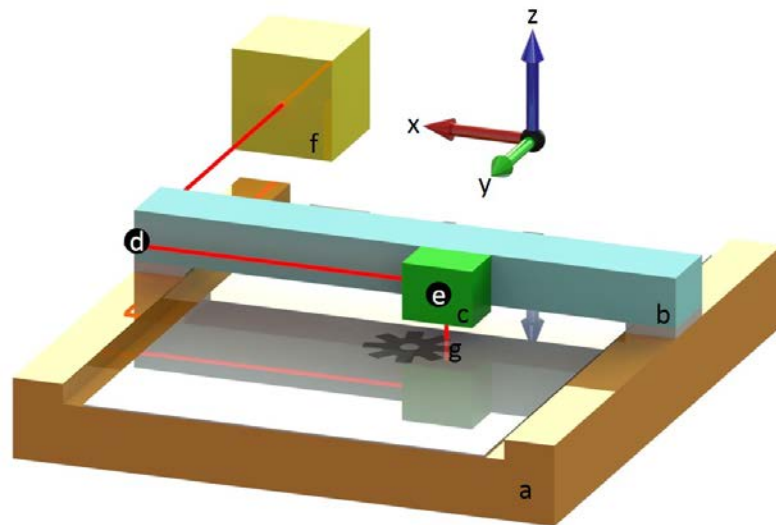


Figure 4.3 - Schematic depiction of the LP 3015 working and the cutting process. a) supporting structure; b) gantry; c) cutting head; d) stationary optical components; e) movable optical components; f) laser source; g) cutting spot.

As illustrated, the ILCM under analysis consists of three different main parts: supporting structure (a), gantry (b) and cutting head (c). Attached to the gantry, on one of its ends, are the stationary optical components (d). These components project the laser beam to the movable optical components (e) that are contained in the cutting head (c). All these components have one main purpose: to ensure that the laser beam follows a path that takes it from the laser source (f) to the cutting spot (g), the point where it must hit the target to allow for the production of the desired piece. The gantry moves along the length of the supporting structure (y direction) and the movable components of the optical system move within the cutting head along the gantry (x direction). The combination of these orthogonal movements allows for the covering of the two dimensional space defined by the target (or part that is to be cut). The gantry is, therefore, a critical component in terms of the cutting performance of the Industrial Laser Cutting Machine (ILCM). The gantry movement is produced by linear motors that allow for high placement precision and accelerations. The rigidity of the gantry must be such that

the deformations it suffers prevent a distance between the spot where the laser effectively hits the target and the desired cutting spot to be lower than the machines accuracy.

More focused on the optical path, this is composed by three mirrors and a focus lens.

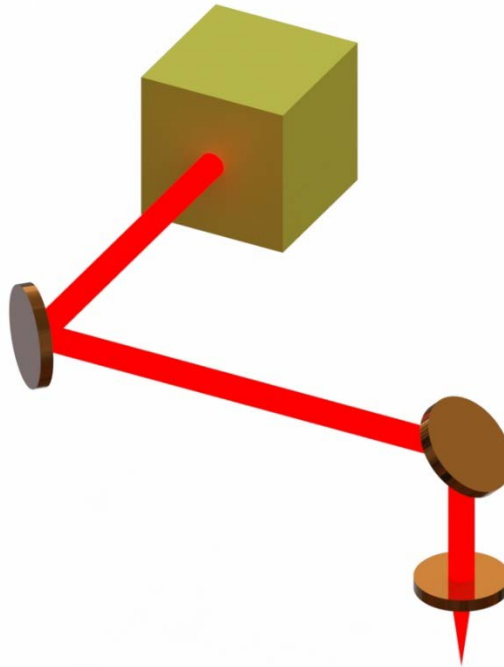


Figure 4.4 – CO₂ ILCM optical system and laser path

One mirror remains fixed throughout the machine functioning, while the other two are placed on the gantry, the last of which being located at the cutting head. The laser travels, during the first segments along the horizontal plane, making 90° turns, while the last segment is vertical, traveling towards the target to perform the cut. Up until the lens, the beam is collimated, meaning the radiation travels approximately unidirectional. As it travels through the focusing lens, it becomes focused, such that the maximum energy is concentrated in the cutting spot. The focus point has to be adjusted to cause a fast heating of the material to be cut to enable the operation [210].

Figure 4.4 presents a simplification of the optical system, representing exclusively the mirrors assembled in the gantry and the focusing lens.

The speed of operation is result of a trade-off between productivity and quality. Therefore, a greater productivity of the machine is reached if the required accuracy is still ensured at higher accelerations.

A benchmarking between the Adira CCL 3015 machine and other 48 machines of similar dimensions was executed [209]. The comparison was performed considering 60 aspects of the machines, including cost, energy consumption, positioning accuracy and speed, and maximum acceleration. Out of these characteristics, 29 were considered by Adira's technical staff to be closely related to the gantry's design and performance. This critical component is a construction solution widely chosen by most brands and the most common one in the market. The gantry is supported on both sides of the body and moves along it to reach all of the target's length. The biggest advantage of this solution is the structural rigidity and the precision that it ensures [209].

It makes sense that to ensure a better performance of the machine the Gantry is studied and optimized. This component is required to be rigid while a mass reduction leads to higher maximum accelerations. The combination of both properties maximizes the machine's productivity [211].

4.2 LOADING SCENARIO

When the gantry suffers acceleration (as it is moved towards the cutting spot – g in Figure 4.3), it becomes subjected to forces and suffers deformations. The implications for precision come from the fact that components of the optical path are attached to the gantry. As these components suffer displacements in the 6 degrees of freedom, the precision of the machine is affected and the point of incidence differs from the one desired. The deviations from the target must be minimum, as to ensure a precise cut. In order to design the gantry, it is essential to understand how the deformations in the gantry translate into changes of the geometry of the optical path of the laser and, therefore, cause distortions to the optical path, affecting the precision of the machine.

The identification of forces relevant for the machine's operation starts with the definition of situations (Load Cases) that represent extreme mechanical solicitations of the gantry.

There are 2 load cases that are considered particularly relevant:

1. The laser head is in the centre while maximum acceleration is applied in the gantry y direction
2. The laser head is in the extreme of the gantry (maximizing the distance between mirrors d and e) while maximum acceleration is applied to the gantry in the y direction

Load Case 1 is considered relevant as the laser head is at the midpoint of the gantry length. This means that not only will the displacement caused by the gantry's inertia be maximum, but also the deformation caused by the presence of the cutting head is at its highest value.

In Load Case 2 the distance between mirrors is maximized. This might create great losses in precision as rotations of mirrors have their effect amplified. This happens despite the potential deformations being lower than when a centred load is applied.

In both these cases the forces involved are similar. Table 4.1 describes them and presents their main effects in the gantry.

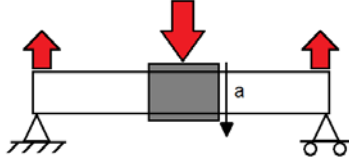
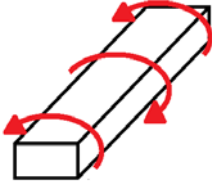
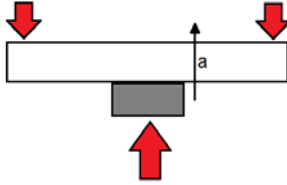
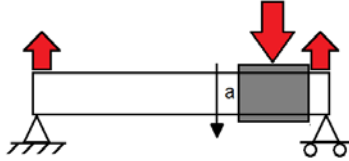
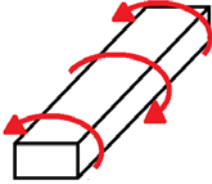
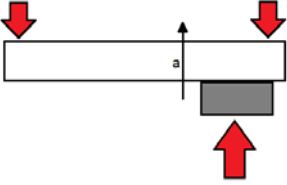
Table 4.1 – Description and Effects of the Forces present in both Load Cases

Load Number	Description of Load	Effects of Load
1	The weight of the gantry when subjected to the gravitational acceleration in the z direction.	Deflection in z direction
2	The load applied on the gantry by the cutting head when subjected to the gravitational acceleration in the z direction.	Deflection in z direction Torsion (rotation in the x axis) due to decentered load
3	The weight of the gantry when subjected to the acceleration in the y direction.	Deflection in y direction
4	The load applied on the gantry by the cutting head when subjected to the acceleration in the y direction.	Deflection in y direction

Because the laser head's centre of mass is not in the same vertical or horizontal planes as the gantry's axis, there will be torsion caused by a moment that results from the combined action of z and y acceleration on the cutting head. Also, because the model considers a simply supported beam, there will be rotation relative to y and z of the ends of the gantry when there is deflection.

Both Load Case 1 and Load Case 2 can be described as the combination of all of these forces. The difference is the position of the laser head. Table 4.2 summarises the effects of forces on the gantry.

Table 4.2 – Illustrations of The Force's effects on the Gantry

Load Case	Force	Illustration
	1 and 2	 <p>A horizontal beam is shown with a fixed support on the left and a roller support on the right. A downward force is applied at the center of the beam. A distance 'a' is marked from the center of the beam to the right support. Upward reaction forces are shown at both supports.</p>
1	2	 <p>A 3D perspective view of a rectangular beam. Red curved arrows indicate torsional forces being applied to the beam.</p>
	3 and 4	 <p>A horizontal beam is shown with a central support underneath. Downward forces are applied at both ends of the beam. A distance 'a' is marked from the center of the beam to the right end. An upward reaction force is shown at the central support.</p>
	1 and 2	 <p>A horizontal beam is shown with a fixed support on the left and a roller support on the right. A downward force is applied near the right support. A distance 'a' is marked from the center of the beam to the right support. Upward reaction forces are shown at both supports.</p>
2	2	 <p>A 3D perspective view of a rectangular beam. Red curved arrows indicate torsional forces being applied to the beam.</p>
	3 and 4	 <p>A horizontal beam is shown with a support underneath near the right end. Downward forces are applied at both ends of the beam. A distance 'a' is marked from the center of the beam to the right end. An upward reaction force is shown at the support.</p>

For each Loading Case, the effect of each load on the two main elements (stationary optical components and movable optical components) needs to be evaluated. These effects are then compiled and the new position

of the elements can be defined. In order to evaluate them correctly each of the 6 degrees of freedom of each element is assessed.

4.2.1 Identification of the most critical Loading Scenario

In order to quantify the losses in precision, meaning the distance between the real incidence point and the desired one due to gantry deformation, an analytical model was developed and implemented using SciLab. This enables the identification of the most critical Loading Case between 1 and 2. The identification of the most critical Loading Case will dictate which one will be considered in the following calculations and part development. The model is capable of computing the precision losses based on the gantry characteristics and the acceleration it is subjected to. This model presents limitations, namely in gantry's geometry and material properties, as well as the errors coming from the use of analytic models. It considers the material as homogeneous and isotropic and is based on the following three steps:

- Step 1: Calculating deformations

After the identification of the relevant loads that are applied to the gantry on the load cases considered critical, analytical calculations are performed to estimate the effects that the forces applied have on the optical path as they create deformations on the gantry.

- Step 2: Calculating the laser path through reflection

The second stage is to define the analytical basis underlying the reflection phenomena through the optical path. This includes the definition of the planes that represent the mirrors and the definition of a methodology that allows replicating the reflection phenomena.

- Step 3: Combine deformations and reflection to calculate the precision loss

At this point the calculated deformations are transformed in displacements of the 6 degrees of freedom (DOF) of the two mirrors that are part of the optical system of the ILCM

- Step 4: Compare the incidence point between the deformed and initial scenario

This step calculates the distance between the original point of incidence and the one after the effects of the accelerations are imposed on the mirrors. This distance indicates the accuracy loss caused by the gantry's deformation.

Figure 4.5 shows the workflow followed by the routine implemented in SciLab.

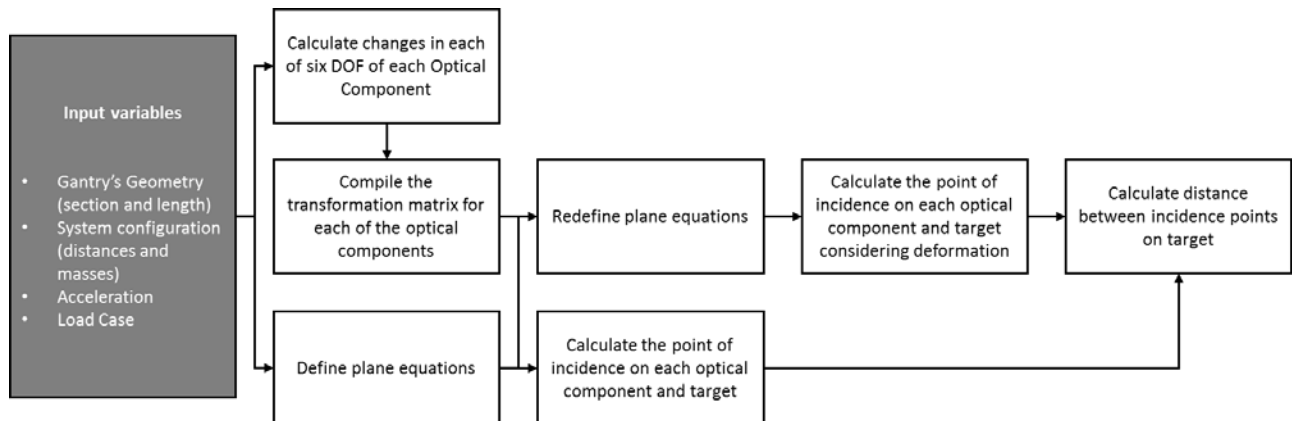


Figure 4.5 – Routine implemented in SciLab, resulting in an analytical model of the gantry

Some details on the implementation are further explained in the following points.

4.2.1.1 *Calculating Deformations*

The last stage's goal is to compute the distortions introduced by the forces applied to the gantry. This model was designed and implemented in SciLab to replicate the geometry of the gantry and the positioning of the elements of the optical path. This allows to calculate how affected the precision is by the forces applied to the gantry.

Based on the equations previously presented it was possible to develop an analytic model of the deformations suffered by the gantry and, with that, estimate the displacement of both the stationary and movable optical components.

Table 4.3 sums up how the equations previously presented were combined to develop the model of the deformations suffered by the gantry at the location of the optical components.

These calculations were performed according to the equations presented in section 3.1.

The model considered both the effect of the distributed and located loads. When two equations were considered their effect was summed. Although the movable optical components are not on the edge of the gantry in load case 2, the equation used to consider the effect of the distributed load (weight) on the rotation on the y and z directions was the one used for the edge. This approximation was used because the position should be quite near the edge and the values should not vary greatly.

Table 4.3 - Equations previously presented are combined to develop the model of the deformations suffered by the gantry at the location of the optical components.

DOF	Axis	Optical component	Load Case 1		Load Case 2	
			Acceleration	Equations Used	Acceleration	Equations Used
Translation	X	Stationary	-	-	-	-
		Movable	-	-	-	-
	Y	Stationary	-	-	-	-
		Movable	a_y	eq. 3.5; eq. 3.11	a_y	eq. 3.1; eq. 3.7
	Z	Stationary	-	-	-	-
		Movable	a_z	eq. 3.5; eq. 3.11	a_z	eq. 3.1; eq. 3.7
Rotation	x	Stationary	-	-	-	-
		Movable	a_z	eq. 3.12	a_z	eq. 3.12
	y	Stationary	a_y	eq. 3.6; eq. 3.12	a_y	eq. 3.6; eq. 3.10
		Movable	-	-	a_y	eq. 3.6; eq. 3.9
	z	Stationary	a_z	eq. 3.6; eq. 3.12	a_z	eq. 3.6; eq. 3.10
		Movable	-	-	a_z	eq. 3.6; eq. 3.9

4.2.1.2 Calculate the laser path through reflection

Having the deformations that occur as a consequence of the loads applied to the gantry characterised, the second stage was to calculate the effect on the optical components. The laser is reflected by the mirrors before hitting the target. The mirrors are plane. To be able to analyse the system, three operations need to be considered:

- Definition of a plane;
- Interception between a line and a plane;
- Rotation in 3D about a Line.

All these operations were performed according to the equations presented in section 3.2.

4.2.1.3 Combining deformations and reflection to calculate the precision loss

As the deformations that are applied to the gantry are characterized and the methodology for the determination of the laser's path through the reflections of mirrors is described the linking of these two phenomena needs to be put into practice.

Transformation matrixes are able to compile the changes imposed to the six degrees of freedom of the mirrors that have been previously studied.

In order to use matrix multiplication to achieve a 3D transformation that includes translation, homogeneous coordinates have to be used. With homogenous coordinates, 3D points were specified by four numbers instead of three. An extra dummy coordinate was added: w. The x coordinate was transformed into xw, y into yw and z into zw. The fourth coordinate is w. This implied the use of 4x4 matrixes instead of 3x3. This now allows that a matrix multiplication can be used to define a translation.

A translation matrix (T) is defined as:

$$T = \begin{bmatrix} 1 & 0 & 0 & t_x \\ 0 & 1 & 0 & t_y \\ 0 & 0 & 1 & t_z \\ 0 & 0 & 0 & 1 \end{bmatrix} \quad \text{eq. 4.1}$$

where t_x , t_y and t_z are the components of the vector that define the translation.

The rotation matrixes are also 4x4 matrixes. Depending on the axis of rotation, (x,y or z) these will be:

$$R_x = \begin{bmatrix} 1 & 0 & 0 & 0 \\ 0 & \cos \theta & \sin \theta & 0 \\ 0 & -\sin \theta & \cos \theta & 0 \\ 0 & 0 & 0 & 1 \end{bmatrix} \quad \text{eq. 4.2}$$

$$R_y = \begin{bmatrix} \cos \alpha & 0 & \sin \alpha & 0 \\ 0 & 1 & 0 & 0 \\ -\sin \alpha & 0 & \cos \alpha & 0 \\ 0 & 0 & 0 & 1 \end{bmatrix} \quad \text{eq. 4.3}$$

$$R_z = \begin{bmatrix} \cos \beta & \sin \beta & 0 & 0 \\ -\sin \beta & \cos \beta & 0 & 0 \\ 0 & 0 & 1 & 0 \\ 0 & 0 & 0 & 1 \end{bmatrix} \quad \text{eq. 4.4}$$

By multiplying these four matrixes it is possible to obtain a transformation matrix that encompasses the transformations in the 6 degrees of freedom.

Each of the matrixes is composed by compiling the output of the equations in Table 4.3 that represent the load case and system configuration.

Changes that refer to the same degree of freedom of a same element are summed and introduced in the corresponding matrix. For the example of Load Case 1 for the stationary optical components we have:

$$\left\{ \begin{array}{l} t_x = 0 \\ t_y = 0 \\ t_z = 0 \\ \theta = (\text{output eq. 3.36}) + (\text{output eq. 3.42}) \\ \alpha = 0 \\ \beta = (\text{output eq. 3.36}) + (\text{output eq. 3.42}) \end{array} \right. \quad \text{eq. 4.5}$$

The multiplication of the transformation matrix by the equation of the plane given by eq. 3.26 gives the mirror's plane equations after forces are applied to the gantry.

The routine implemented contains obvious simplifications but was complete enough to gain some insight on the whole system. Its main simplifications consist of:

- The geometry of the gantry is considered to be of constant section without reinforcements
- The optical components are considered to be infinite (there is not a deviation threshold that dictates that the laser does not hit the mirror)
- The equations that are on the basis of the model do not account for local deformations

However the knowledge that can be extracted from running simulations with this model enables the definition of what is the critical laser head position. Analytical calculations could be performed for a limited number of system configurations, but the implementation of such a model in SciLab allows that an extensive number of configurations is tested and analysed.

This model must account for an array of configurations, regarding section and material properties. Essentially the different configurations will result in different resistance of the gantry to suffer deformations. In the analytical model considered, that can be given by E and I in case of deflection or J and G in case of torsion. Because the analysis does not aim at understanding how these factor influence the behaviour of the gantry

but rather what is the loading scenario that is more demanding, the error will be plotted against the product of E and I or G and J.

To produce data a variation of the code was produced such that it is able to generate an output composed by EI (both Ely and Elz, since deflection is considered in these directions) and the error or JG and the error presented by the system under different configurations. The four dimensions of the section (b, d, h, k in Figure 3.3) were varied as well as E and G. The sections outer dimensions range from 100 mm and 600 mm and the wall thickness from 10 mm and 100 mm. Invalid sections (the sum of the thickness higher than the outer dimensions) are not considered. E was comprised between 30 GPa and 70 GPa and G between 3 GPa and 5 GPa. The minimum variation in all of these variable was defined so that it produces a total of 111747 of valid configurations.

The process of analytical calculation was then used to compare what loading scenario creates larger errors. The error for each configuration of the gantry was plotted as a function of Ely, Elz and GJ. Each configuration's performance was analysed considering the cutting head placed on the centre or on the extremity. By comparing results it was possible to draw a conclusion on what was the leading scenario that creates larger errors on the overall range of viable configurations.

4.3 SECTION ESTIMATION OF AN EQUIVALENT COMPOSITE GANTRY

4.3.1 Analysis of the metallic gantry

In parallel with understanding the Loading Cases, the current metallic part was analysed. The metallic gantry is composed by two U shaped halves that form a rectangular section tube.

The metallic gantry (reinforced with cross-axial ribs that are welded to the outer walls) is subjected to bending and torsion efforts. This initial analysis was performed resorting to numerical simulations.

The length of the gantry is 2380 mm (Figure 4.6).

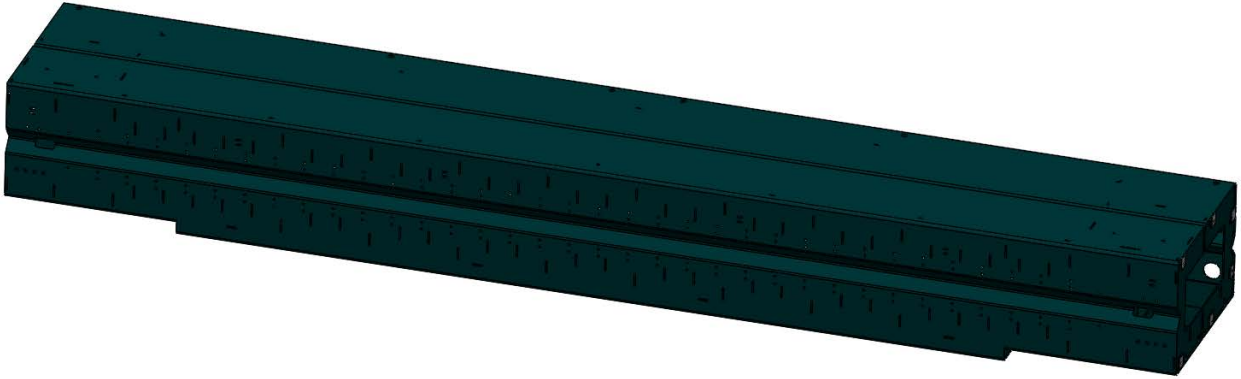


Figure 4.6 – Overview of the metallic gantry

For increased rigidity while keeping the mass as low as possible, the existing metallic gantry was reinforced by internal ribs. These were designed to provide better resistance to bending and torsion loads, as well as to stop local deformations on the gantry. The complex ribs structure (displayed in Figure 4.7) presented a challenging fabrication step.

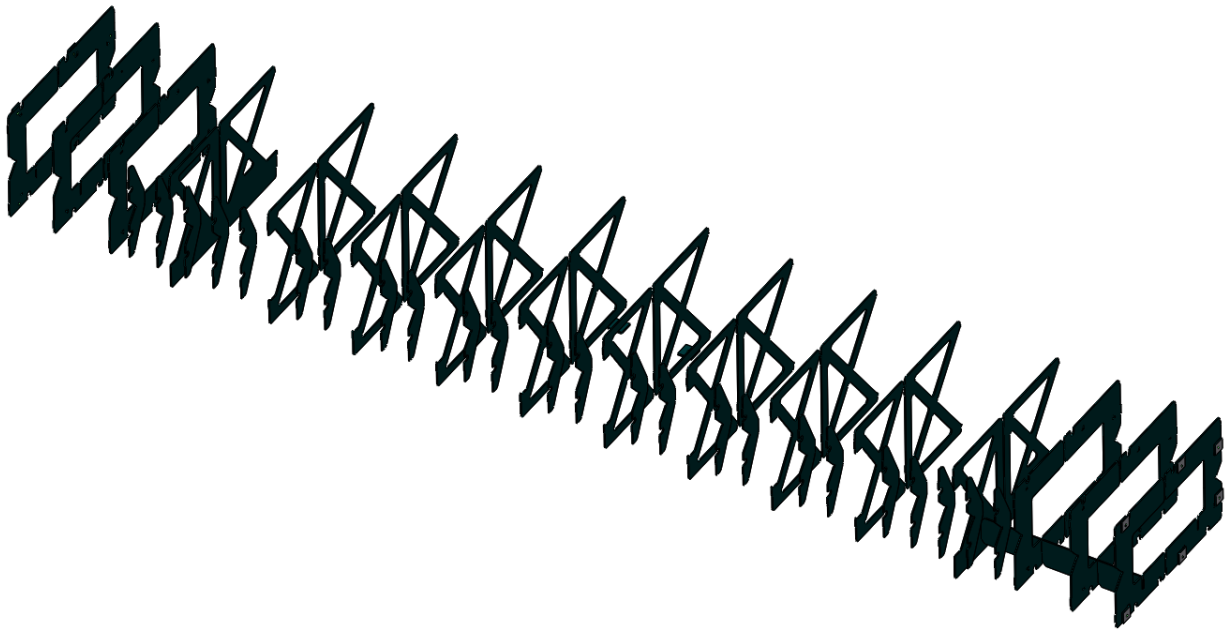


Figure 4.7 – Ribs for metallic gantry reinforcement

The gantry was produced from 2mm sheet metal parts that are laser cut, bent, assembled and welded. The final part presents a weight of roughly 100 kg.

The loading scenario that the gantry is subjected to is complex. An analysis focused on that, although obviously necessary for a quantitative analysis of the deformation suffered by the gantry in real conditions, will not allow for an understanding of the overall mechanical answer of the gantry. For a first draft of the new composite gantry's section, it was important to evaluate the overall mechanical behaviour of the current metallic part. A FE model that takes into account the actual loading conditions will be very sensible to local deformations and the end result will not be able to convey the general mechanical characteristics of the part that is being replaced. To overcome these issues, instead of a realistic loading scenario, the metallic gantry was considered as a cantilevered beam, having one edge totally fixed and a load or moment applied on the other extremity. Loads were applied along the y and z direction and Torsional Moments around the y axis. The applied load was of 980 N and the torsional moment of $5.0E+4$ Nm. The bending scenario is presented in Figure 4.8.

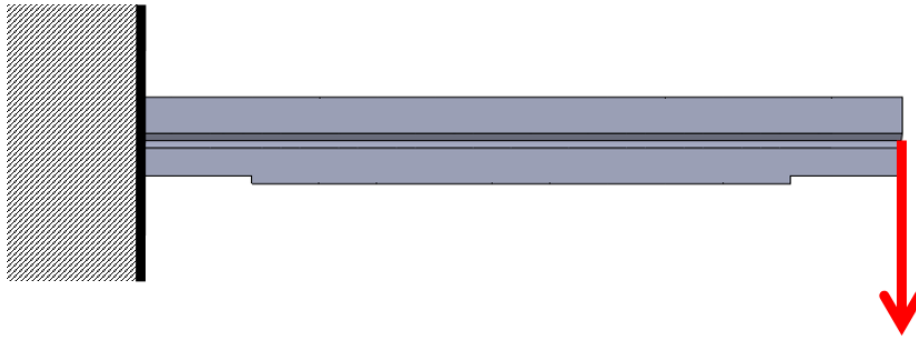


Figure 4.8 – Loading scenario for metallic gantry analysis

These loads do not replicate the real loading conditions of the gantry but they were used because, this method to access the torsion and bending behaviour of the part are easier to replicate with analytical calculations. The analytical models will be used to reach a first estimation of an equivalent composite gantry. This approach will render an initial approximation to a composite gantry with similar rigidity, despite not considering a complex loading scenario. A load applied to the external walls would cause local deformations and the values would not be able to compare with the analytical results. This effect is minimized by considering loads applied to a rigid end surface.

The analysis of the current metallic part was performed using FEM. The software used was Abaqus/CAE 6.11-1. The geometry of the current metallic component was obtained and, in order to reduce computational cost, both external shell and interior reinforcements were considered as a single part. This approximation requires no contacts to be defined and assumes rigid connections between different parts. This is very similar to what is verified in reality, as the internal reinforcement ribs are heavily soldered to the outer shell. A midplane shell mesh was generated in ANSA pre-processing software. Shell meshes were applied to parts with one of the dimensions is substantially smaller than the other ones, as in the case of the gantry, produced from sheet metal. The powerful meshing capabilities presented by this software allowed for a better discretization of the domain, thus leading to more reliable outcomes from the FEM software. A study of mesh independence of the results was performed for the loading scenario on which the gantry suffers bending and considering the value of the vertical displacement of the edge to which the load was applied. The final mesh presenting better trade-off between accuracy and computational costs is presented in Figure 4.9.

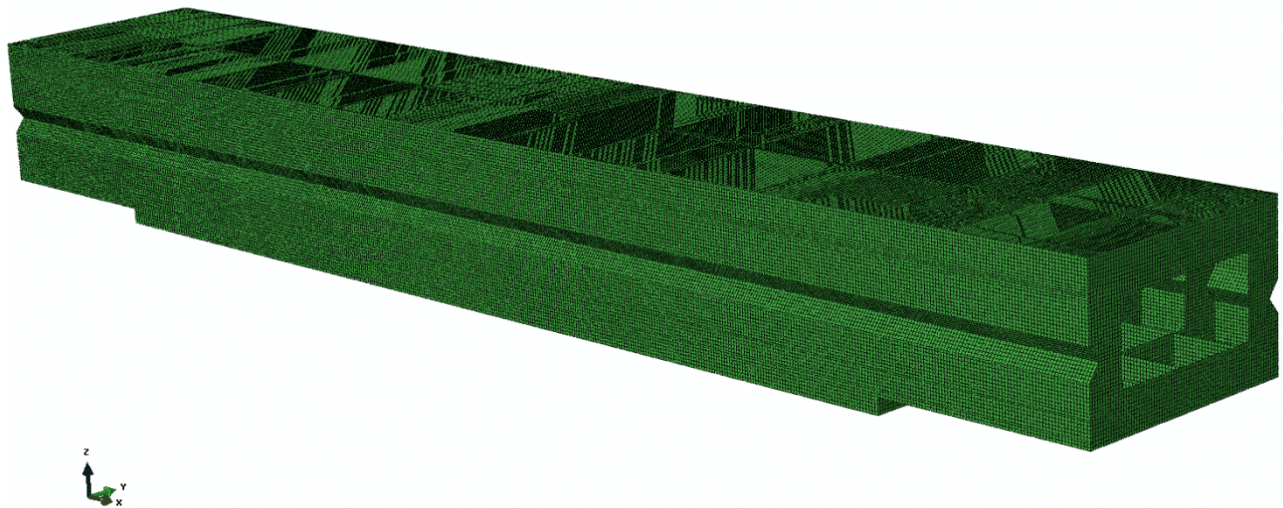


Figure 4.9 – Mesh generated for the FEA of the metallic gantry

The mechanical properties were attributed to the part. The mechanical properties of the steel were provided by the metal supplier regarding the specific steel grade (DIN 17100 St33 carbon structural steel plate). Because the generated mesh consists of shell elements, a thickness has to be attributed. The thickness of

the used sheet metal is of 2 mm. Gravitational acceleration is not considered and, therefore, the gantry's own weight does not influence the results. Table 4.4 shows the properties considered.

Table 4.4 – Mechanical properties of st33 steel grade

Property	Value
Young Modulus (GPa)	2.12
Poisson Ratio	0.3
Density (kg/m ³)	7850

From this numerical analysis results the deformations suffered by the part.

4.3.2 Analytical dimensioning of a composite gantry

The gantry's rigidity must ensure that deformations suffered will not cause deviations between the spot where the laser effectively hits the target and the cutting spot higher than the machines accuracy.

The material in which the new gantry will be produced must allow for high stiffness while ensuring a low mass. Multi-layered polymeric matrix composites (composites) present more attractive specific stiffness (E/ρ) than metals and other materials, including polymers.

The dimensioning of the new composite structure had, as goal, the conception of an alternative component that, while capable of insuring the same degree of precision, would allow for higher accelerations. The calculation performed at this stage aimed at performing a material selection, roughly defining a configuration that ensures the desired rigidity while, at the same time, minimizing the weight of the structure. The materials under consideration were the CFRP and GFRP composites.

After understanding the bending and torsional behaviour of the current metallic part, the next step was the definition of the section (external dimensions and thickness) of a composite material gantry required to produce a part that ensured equivalent machine level of accuracy.

Because of the loads described, two fibre orientations were selected for the design of the gantry. The unidirectional fibres are placed along the x direction and will be able to give higher bending rigidity. $\pm 45^\circ$

fibres are used for their higher Shear Modulus and, therefore, resistance to torsion. Table 4.5 shows the considered mechanical properties for these materials.

Table 4.5 – Mechanical properties used for thickness estimation of the composite gantry’s walls, adapted from [28].

Material	Young Modulus (GPa)	Shear Modulus (GPa)	Density (kg/m ³)
Unidirectional Carbon Fibre	134	N/A	1650
±45° Carbon Fibre	N/A	34.5	1650
Unidirectional Glass Fibre	45	N/A	1900
±45° Glass Fibre	N/A	12.8	1900

The dimensioning performed at this stage considered the thickness of each of the two layers as a continuous variable. The calculations were performed considering that only the unidirectional fibres would be subjected to the bending loads and that the torsion of the beam would only be dictated by the thickness of the ±45° fibres layer. The calculations were also performed considering that the end result of the composite gantry will be composed by two layers, a unidirectional one and a ±45° layer, being the later the external one. The interface between the unidirectional layer and the ±45° one will have the same dimensions as the midsurface of the metallic gantry’s FE model, having the unidirectional fibres in the inner layer and the ±45° fabric on the exterior.

The loading scenarios applied to the composite part being dimensioned were the same as the ones considered on 4.3.1. However, and because the composite component is supposed to lead to a maximum acceleration increase (at this stage estimated in 50%, resulting in a maximum acceleration of 3 G), the admissible deflections were reduced. This offset was performed considering that both the deflection and the torsion of the beam are directly proportional to the load applied and that this, in its turn, is directly proportional to the acceleration. However, the acceleration variation is to be considered only to occur along the y axis, since on the z axis the gantry is still subjected to 1 G accelerations and weight variations will not be considered at this stage. The maximum deformations admissible for the composite gantry are shown in Table 4.6.

Table 4.6 - Maximum allowed deformations for the composite gantry

Deformation	Value obtained for metallic gantry	Maximum allowed value for composite gantry
Deflection in z	0.618 mm	0.618 mm
Deflection in y	0.321 mm	0.214 mm
Rotation in x	0.0199 rad	0.0133 rad

Because an analytical model was used for this stage of the composite's gantry, some simplifications are in place, being the main one the assumption of having a constant section. This means the external dimensions of the gantry are constant throughout its length and there are no reinforcements. Despite the reinforcements being of great value when dealing with the actual loading scenarios, for the cantilevered scenario these are not of particular relevance. The dimensioning considered that the horizontal and vertical walls are distinct, as they are subjected to distinct forces. Therefore, the dimensioning considered 4 different layers, summed in Table 4.7.

Table 4.7 - Different layers considered for the design of the composite component

Layer Denomination	Description
$L_{uni,xy}$	Layer of unidirectional fibres in faces parallel to the xy plane
$L_{\pm 45,xy}$	Layer of $\pm 45^\circ$ fibres in faces parallel to the xy plane
$L_{uni,xz}$	Layer of unidirectional fibres in faces parallel to the xz plane
$L_{\pm 45,xz}$	Layer of $\pm 45^\circ$ fibres in faces parallel to the xz plane

Both $L_{uni,xy}$ and $L_{uni,xz}$ present fibres with the same orientation as the gantry's axis.

The first step was to determine the combination of $L_{uni,xy}$ and $L_{uni,xz}$ that allow for deflections in both y and z below the maximum ones established in Table 4.6 with a minimum weight. This was performed by creating a spreadsheet that, given a range of thicknesses, divides it in 20 intervals, each representing a 5% increase of the difference between the maximum and minimum thicknesses. To define a range for the

analysis, 4 values must be input: the maximum and minimum thickness for the vertical direction, and the maximum and minimum value for the horizontal one. This creates a spreadsheet containing an array of 21x21 possible configurations. For each of these configurations the deflections were calculated and considered valid if they are below the admitted ones, or invalid if the deformations were excessive. An approximation to the minimum value that ensures the required rigidity was performed by iteratively considering shorter intervals between maximum and minimum values for each of the layers.

For example, considering the unidirectional fibres, a spreadsheet was created having the thickness of $L_{uni,xy}$ in the horizontal direction and $L_{uni,xz}$ in the vertical one.

Each cell represents a configuration defined by the combination of these two thicknesses. Also on each cell is the resulting deflections in each direction, the volume of the solution (directly correlated to the mass) and a binary cell that indicates weather the solution is valid (meaning it respects the deflection restrictions) or not, in case the maximum deflection is violated. Figure 4.10 shows two cells, displaying $L_{uni,xy}$, $L_{uni,xz}$, the calculated deflection in y and z directions, the volume (in mm³) and the validity of the solution.

3.25	3.3
7.35	7.35
0.21447625	0.2139011
0.61865535	0.612617415
1.69960E+07	1.70512E+07
FALSE	TRUE

Figure 4.10 – Two cells representing two alternative configurations of the gantry, one with a solution that results in the violation of the maximum deformations and the other with deflections bellow the defined thresholds.

The process was repeated to calculate the thickness of the $\pm 45^\circ$ fibres layer. The values calculated this way defined both the inner dimensions of the unidirectional layer (and of the gantry) and the outer dimensions of the $\pm 45^\circ$ layer and, therefore, of the gantry.

The solution that presented lower weight and admissible deformations would be used to define the shorter interval to further analyse its surroundings. Several initial intervals were studied as to try to avoid the convergence towards a local minimum. The process proceeded to explore narrower intervals and was stopped when the thickness value reached a number with two decimal places. The minimum weight (or, in this case, volume) solution that complied with the desired behaviour was signalled by a yellow highlight of its volume (as shown in Figure 4.10).

4.3.3 Numerical analysis of the composite gantry

Having an overall geometric definition of the gantry, namely its material and sections, it became relevant to do an analysis that contemplates the realistic loads the gantry will be subjected to, meaning the machine's working conditions, as described in Table 4.2, namely the first load case. This case was selected since it was considered to be the most critical one in terms of accuracy loss.

In order to ensure that the machine's behaviour is analogous to the performance with the metallic gantry, a comparison was established between the metallic gantry and the CFRP one. The numerical model was assembled in an analogous way to the simulation for the initial assessment of the current metallic component, keeping the element type and dimensions.

Other components that apply more concentrated loads to the gantry were also taken into account, namely the optical path supports and the secondary engine, responsible for the movement of the laser head. The secondary engine load represents the force applied by the electromagnetic field of the linear motor that is responsible for the movement of the laser head. Although it has small influence, it was included in this analysis as it has little impact in the computational cost and it might have some local effect that is worth analysing with greater depth. These components are not geometrically represented in the numerical model. Instead a point, that has the same coordinates as their centre of gravity, is represented. This greatly reduces the computational costs of the model, by avoiding the need to represent additional geometry and having material properties assigned to them. The analysis is focused on the gantry and, therefore, the option was to avoid the introduction of other parts that will make the analysis slower not necessarily more relevant or precise. Therefore, to each of the points located in the centre of gravity of each component, loads were applied to emulate the effect of their presence, namely forces corresponding to their mass multiplied by the accelerations they are subjected to. Each point is subjected to loads that can have components in all three directions. The connection between centre of gravity of the components and the gantry were replaced by kinematic coupling. This way to model the connection between the gantry and surrounding components consisted of a group of slave nodes (the nodes where the components are attached to the gantry) constrained by the translation and rotation of a master node (the point to which the loads are applied). This method considers that the bodies attached to the gantry are rigid, an approximation that is considered valid since the deformations are quite small and an accurate representation of the mechanical behaviours would be quite complex to introduce. Figure 4.11 shows the overall aspect of the numeric model used to assess the metallic

gantry behaviour where additional structures (such as rails and supports for the optical path) are visible as solid structures.

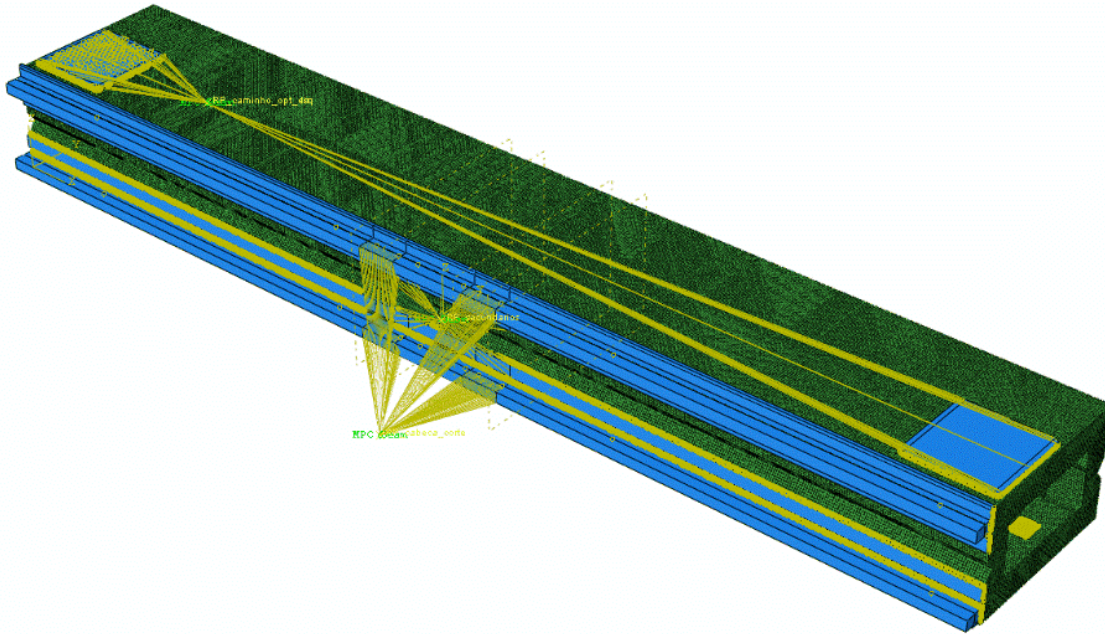


Figure 4.11 - Overall aspect of the numeric model

The loads applied to the metallic and composite gantry varied in magnitude, considering that the purpose of this work is to increase the acceleration the composite gantry is able to sustain along the y axis. Nevertheless, the points of application and the nodes that were considered as slaves were the same. It should be noted that the loading applied to the gantry also considered the maximum acceleration imposed to the cutting head when travelling along the gantry (2 G). For both the metallic and composite gantries, the considered outputs were the location of the point of maximum displacement and the displacement (both translational and rotational) of the point that represents the cutting head. This point was selected since it is both the endpoint of the optical system, thus crucial for the assessment of the machine's precision, and the source of larger loads applied to the gantry. The first step was to subject the metallic part to the loads that mimic the gantry's working conditions. Table 4.8 displays the application points (with the origin being midway lengthwise of the front top edge of the gantry) and loads considered for the metallic gantry.

Table 4.8 – Loads applied to the metallic gantry.

Load	Point of Application (mm)			Components (N)		
	X	y	Z	x	Y	Z
Optical path support left	-474,412	129,606	342,134	0	-4,802E+02	-2,401E+02
Optical path support right	-474,412	129,606	342,134	0	-2,058E+02	-1,029E+02
Cutting Head	0	180,693	-156,81	1,96E+03	-7,84E+03	-9,8E+02
Secondary engine	0	7	-11	0	5,488E+03	-1,960E+02

On the other hand, the loads applied to the composite gantry are displayed in Table 4.9.

Table 4.9 - Loads applied to the composite gantry.

Load	Point of Application (mm)			Components (N)		
	X	y	Z	x	Y	Z
Optical path support left	-474,412	-129,606	342,134	0	7,203E+02	-2,401E+02
Optical path support right	-474,412	-129,606	342,134	0	3,087E+02	-1,029E+02
Cutting Head	0	-180,693	-156,81	1,96E+03	8,820E+03	-9,8E+02
Secondary engine	0	-7	-11	0	-5,292E+03	-1,960E+02

Again, the loads are higher since they emulate a situation in which the composite model enables a machine working at higher acceleration.

An analysis such as this will allow the evaluation of the behaviour of the gantry, as well as the definition of where eventual reinforcements might be required to increase the rigidity of the part or to sustain local loads. The goal of a comparative analysis between the metallic and the CFRP one is to understand if the two structures, while distinct, can present a similar response when subjected to similar loads.

The outcome will define the configuration of a part that can, realistically, sustain the loads it will be subjected to while the machine is operating.

Regardless of the finer definition of layup, section dimensions, and other variables, the production of such a structure requires an external shell composed by two parts that are complementary (forming a box beam). In Figure 4.12, the two halves (in different shades of blue) are connected by a layer of adhesive (in red).

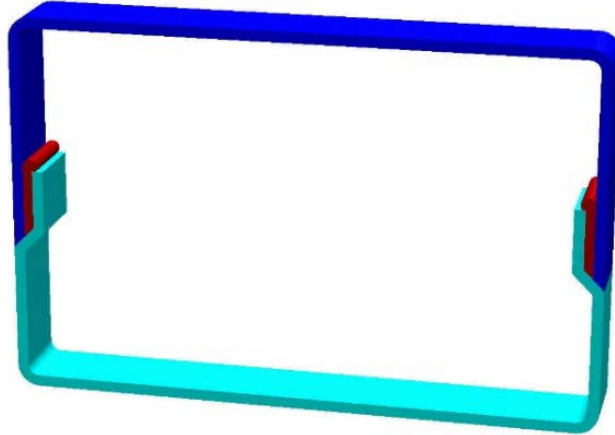


Figure 4.12 – Construction solution for the designed composite gantry.

Ribs that can eventually be required can be attached to the internal walls of the beam by using the same technique.

The results of this approach also delineate the limitation of a dimensioning process and highlights the need of a more dynamic approach that can lead to a better result which maximizes the potential of a machine resulting from a redesign process, while maintaining some of its characteristics.

4.4 OPTIMIZATION OF THE COMPOSITE GANTRY

In the particular case of the machine that is being analysed, the movement of the gantry was controlled by linear motors, which present characteristic curves (Figure 4.13). These curves show that the motor is capable of producing a constant force (F_{max}) up to a certain value of velocity ($v_{\max(F_{max})}$). After this value is reached the force drops reaching the feedrate force (F_{rated}). The ratio between F_{max} and F_{rated} depends on the desired working conditions: continuous load – lower ratio – or peak load.

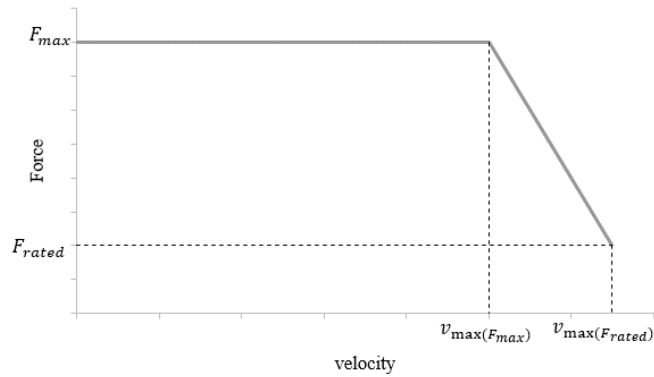


Figure 4.13 - Example of a Linear Motor characteristic Curve

The current machine comprises linear motors to move the gantry and the surrounding objects. This system is capable of an F_{max} of roughly 9760 N. The current maximum desired velocity is within the range that allows it to employ its highest force. By accounting for the mass of the surrounding components also moved by the motor, it was possible to calculate the maximum gantry's mass the motor can move at a given acceleration. This is expressed in eq. 4.6:

$$m_{mg} = \frac{F_{max}}{a} - m_{sc} \quad \text{eq. 4.6}$$

where m_{mg} is the maximum allowable mass of the gantry and m_{sc} is the mass of the surrounding components.

By assessing the minimum mass that allows the gantry to keep the minimum desired rigidity through an array of accelerations it is possible to determine what the maximum acceleration reachable by this approach is. The value for m_{mg} was estimated for several values of a . Maximum acceleration is reached at $m_{mg} = 0$. This value leads to a maximum possible acceleration between 2.9 and 3 G (more precisely, 2.94 G). Therefore, the goal of reaching 3 G acceleration exceeds the expectable optimal result with the current machine configuration.

A plot of the function of maximum allowed acceleration as a functions of the gantry's mass is presented in Figure 4.14.

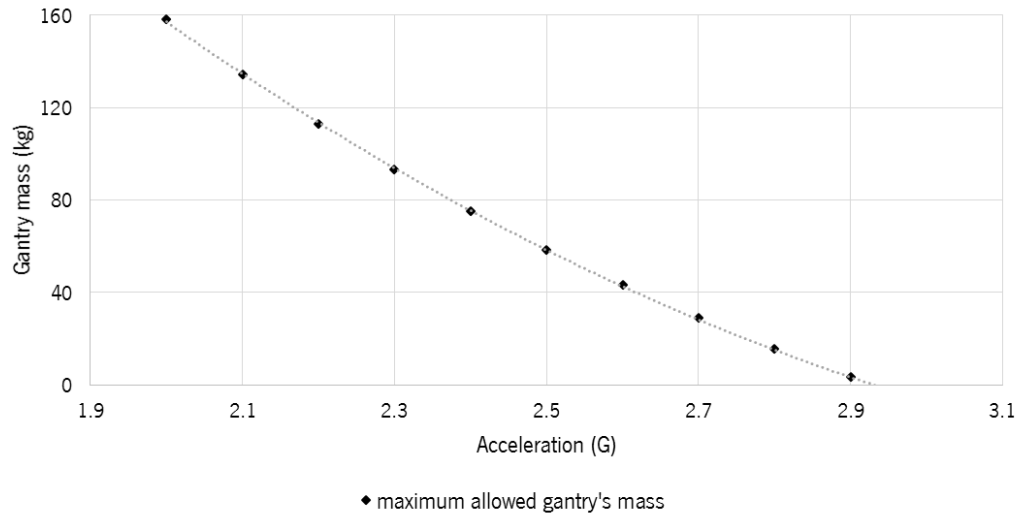


Figure 4.14 – Maximum possible accelerations as a function of the gantry's mass

A dimensioning process aimed at this acceleration will actually worsen the machine's performance, since the over dimensioning of the gantry will actually result in lower accelerations, given the fact that the linear motors, are not to be changed in the scope of this project, will have to carry extra load and, therefore, be able to only input lower accelerations.

The trade-off between weight and stiffness (required to ensure the precision of the machine) configures a scenario in which the implementation of a formal optimization process could be of great advantage [212]. Because of the work previously developed, this optimization will be based on FEA of the structure. This means that FEA will be used to perform the objective function evaluation and, because of that, derivative free methods should be applied.

The purpose was not the development of a new optimization algorithm. There is a multitude of algorithms able to guide the optimization process in hand. Instead the challenge consisted in linking the optimization algorithm to the FEM getting the algorithm as able to both define the simulation inputs and retrieve outputs. In this case, the selected algorithm was PSwarm, a Pattern Search and Particle Swarm hybrid algorithm. PSwarm is a derivative free, optimization algorithm and, therefore, suitable for working with FEA as a method to evaluate the objective function. It aims at the minimization of a function with variables restricted to upper and lower bounds. Nonlinear constraints, such as the weight/acceleration limitations imposed by the linear motors can be implemented using a penalty method.

The first step was to define the focus of the optimization. Several aspects of the gantry can be studied, changed and optimized with the help of this approach. These can encompass material selection, gantry external configuration, reinforcement location, thickness distribution amongst others. On the other hand, an optimization process, especially a population based one, although capable of obtaining a faster convergence when compared to the alternatives, implies a high number of objective function evaluations, and the number of these evaluations increases with the number of variables. This has implications on the practical aspects of this project. The access to computational resources is limited, meaning that more complex optimization processes will lead to an undoubtable increase in the time required for the optimization process to run. This produces the need of focusing on the most essential aspects of the beam, which are harder to assess using other methods, or the optimization process will become too long. The followed approach was defined by focusing in two aspects:

- Reducing the computational requirements to perform the optimization loop within an acceptable time frame (approximately 24 hours);
- Setting up an optimization routine able to account for the most relevant variables.

Some of the possible optimization variables were eliminated from the start. The material was selected based on the previous designing process (CFRP). The gantry's geometry is very limited due to machine configuration constraints, although an optimization attempt was performed, without a positive outcome. The results obtained with the comparison between the CFRP and metallic gantries has also defined the need for reinforcements to be included in the design of a CFRP gantry.

4.4.1 Geometry optimization

The next stage was to assess the methodology to follow to achieve an optimized geometry of the gantry. This aspect aims at taking advantage of the shape flexibility that CFRP produced through VIP could present. The material may adapt to complex curves in the mould and keep its shape once the curing process is concluded. However, to create geometries that can be applicable to a real part, it is required to:

- Understand the restrictions to the gantry's shape imposed by surrounding components and production limitations
- Parametrise the possible shapes
- Select the software to generate the shape

- Create constraints that ensure the generated shapes are realistic
- Understand how to import that shape for the FEA software
- Automatically generate a mesh that presents enough quality.

The restrictions to the shape come from various sources. The main ones are related to the surrounding components, including the ones that are attached to the machine. Figure 4.15 addresses some of the main restrictions.

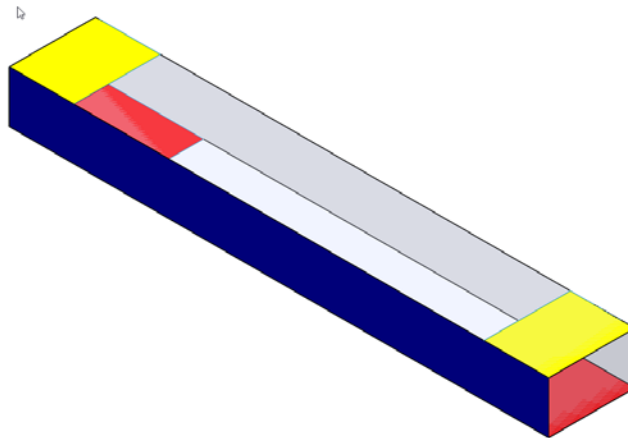


Figure 4.15 – Shape restriction areas identified by colours

The blue surface is the one to which the rails along which the laser head moves attach. This surface must provide a flat surface to which the rails can be attached to. Even in the case in which the rails are part attached to a metal surface that is, in turn, attached to the gantry, this surface should be flat, as to provide support throughout the whole extent of the rails. Otherwise the metallic attachment will be, in fact, responsible for ensuring stiffness. This also implies a minimum dimension of the surface, given by the distance of the rails (185 mm). The yellow surfaces represent connection points of other elements of the optical system. These also need to be flat. The same is presented by the red surfaces, the connections to the linear motor elements that are responsible for the gantry's displacement.

Maximum dimensions in both z and y directions also present limitations. Increases in these directions will have a positive influence in the gantry's rigidity (as I_y , I_z and J will increase) but will negatively influence other characteristics of the machine. Increases in the y direction will affect the maximum dimension of the target (the maximum dimensions of the machine are not to be changed and a gantry with higher dimensions in the y direction will allow lower displacements). The maximum variation in this direction was considered as 5 mm.

An increase in the z direction will make the gantry taller and make some components of the optical system less stable. Also it will not greatly influence I_z (the area moment of inertia in the direction of higher acceleration), although it will influence I_y and J . The maximum variation in this direction is also considered to be 15 mm. The length of the gantry is also about to remain the same.

Therefore, regardless of local configurations, the shape is to be a hollow beam with one of the faces flat and sections of two other equally planar. The rest of the gantry can have a free configurations as long as it is contained within dimensions specified above. The selected way to build these geometries was by a process consisting of three steps:

- Points are generated;
- Splines create a wireframe from the given points;
- A surface is created from the splines.

The points are created on planes that are perpendicular to the x axis, a spline forms on those plans and then splines are created on planes parallel to either xz or xy linking the initial parallel splines. Because all of the geometry definition takes the points as a starting point, its coordinates can be changed to create different gantry configurations. In fact, the coordinates can be treated as variables in the optimization process. Since points are grouped in x planes, its y coordinates can be kept constant or be varied for the whole group of points. Also some points can be defined as to only move in the y direction and some only in the z direction. These restriction result in the reduction of number of variables.

A code to perform this was implemented in Grasshopper scripting, an add-on tool for Rhinoceros 3D model software. Grasshopper is a parametric shape generation tool that allows the creation of shapes by changing parameters, such as desired in this case. Also it uses the Rhinoceros modelling tools, which has the ability of generating both spline and Surface Non-uniform rational Basis spline (NURBS). This mathematical model offers great flexibility and precision. The issue with this approach is the introduction of a new software in the optimization loop, which make the process longer and more error prone. Figure 4.16 shows the process through which the geometry was generated.

In Figure 4.16 a list of points is created and Grasshopper generates the points (b), the wireframe (c) and the surface (d).

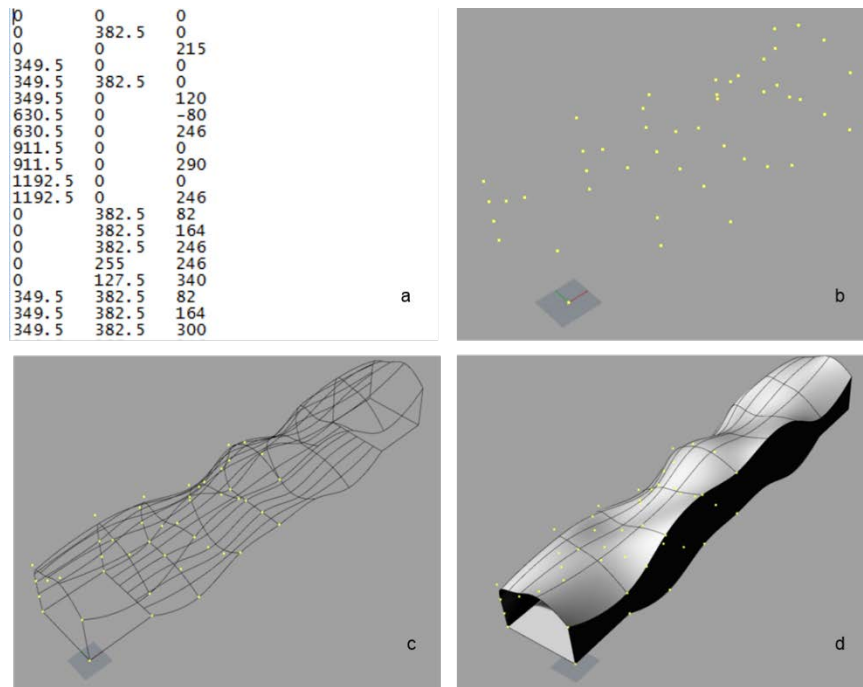


Figure 4.16 – Shape generation process implemented

The process is also capable of generating flat surfaces. It also shows that NURBS are not bound to reach all of the defined points. This means that the surface is not as prone to contain sharp angles and creases (which is positive both for production and stress concentration zones). Such approach is, therefore, capable of creating the desired shape and introducing external wall configuration in the optimization process. This has, however, downsides, apart from the fact that another software is added to the optimization loop. The created shape might be impossible (such as a gantry with self-intersecting walls) or that is extremely hard or impossible to produce (not respecting draft angles, very thin and deep features, causing a hard adequate fibre placement). The creation of variable meshes also has implications on the finite element model, mainly during the mesh generation step. Variable shapes imply an automatic verification of mesh quality and compliance with the software's requirements. This means requirements of higher computational resources and would, undoubtedly, lead to a much longer optimization problem, not only due to the increased number of variables, but also due to the analysis each shape must be subjected to [176]. This, associated with the constraints imposed by the industrial nature of this project (that result in requirements of standard production processes and little freedom given to increase the gantry's dimension), led to abandoning this line of research and considering a gantry with predetermined external dimensions, overweighting the relevance for the scientific component of this work.

4.4.2 Thickness optimization

The optimization has aimed therefore to determine the optimal layup of CFRP at each section of the gantry by considering that it would be produced by vacuum infusion. Therefore, the number of layers with a given fibre orientation can vary from section to section. As previously mentioned, and due to the loads imposed to the gantry, the layers were considered to have fibres orientated just at 0° (along the y direction) and $\pm 45^\circ$. The optimization problem also considered that layers with fibres at 90° could be required due to local loadings. A total of six sections was considered: One for the front vertical face on which the rails are applied, one for the back opposite vertical face, one for the top horizontal face and other for the bottom one, one for the ribs in the extremity and one for the central ribs, positioned throughout the gantry.

Figure 4.17 sums up the thickness related variables.

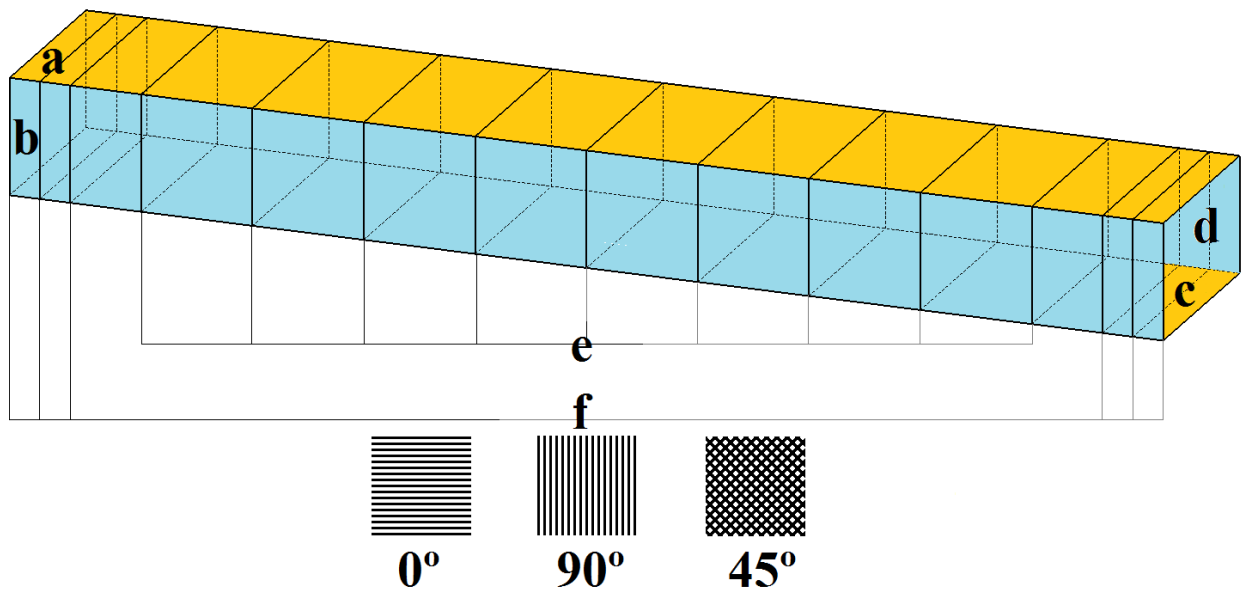


Figure 4.17 – Different section to be optimized, resulting in different variables

As a result, a total of 18 variables were created, each denominated by a letter, corresponding to the region, and the fibre orientation, for example e_{45} relates to the thickness of the $\pm 45^\circ$ fibres in the internal ribs of the gantry. But these are not the only variables that were used in the optimization process. Not only the gantry configuration was changed, but it was also necessary to vary its maximum acceleration. So, a nineteenth variable was added, the maximum acceleration.

These were the variables the optimization took into account. Nevertheless, the evaluation of the performance of a gantry also required performing a FE simulation and the definition of a metric to evaluate that performance.

Since the numerical model is the basis upon which the optimization process is built, there must be a good control on all of its aspects. To ensure the model considered the same in all optimization processes (including the testing of different objective functions), the model was created using python scripting. This strategy, although presenting a higher set up time, renders a model that is fully described by code. This allows the automatic definition of all of the finite element model's parameters at the beginning of the optimization process. These parameters include the geometry of the parts, their orientation and relative positions, the material properties, the layup, the discretization, the interaction between the parts, the relevant points (for load applications and results assessment), the boundary conditions and the loads, the number of increments and, finally, what information should be contained in the output file.

All of these points were common in all models, regardless of the variables with the exception of the layup and the loads.

4.4.2.1 Part Geometry

The geometry that was simulated is displayed in Figure 4.18. The domain of the simulation comprises two parts: the CFRP beam (in grey) and the metallic mask along which the laser cutting head moves (in green).

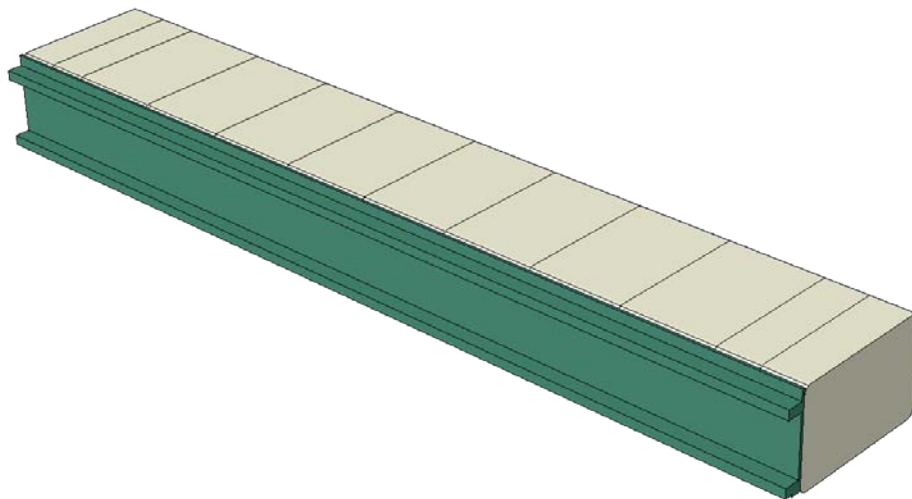


Figure 4.18 – Part geometry used for thickness optimization

The external shell and ribs were represented in a single part. This means that the connection between them was considered rigid. The geometry represented presents a limited number of features. These simplifications, adopted to keep the model simple and, therefore lighter, means that details such as tabs for the ribs and external shell connection (by adhesion and/or other process) and other features coming from the production process were not considered. What is represented in the geometry is the minimum that is required to render a relevant representation of the part to be produced while ensuring maximum celerity in result output.

The metallic and composite parts were also considered to be linked by a rigid connection. This is another simplification that was knowingly introduced in the model. This means that the load transmission will be performed throughout all of the contact surface and that the separation between the two components is not possible. In reality the connection between the two parts must be performed by either connectors and/or adhesives. The end-result will be a distributed load that will be different but able to be approximated by a rigid connection (named Tie in Abaqus).

The composite part was 2385 mm long and its section had 382.5 mm x 246 mm. The outer ribs were spaced by 110 mm and the middle ones by 243 mm. As mentioned, these dimensions are constant. The metallic mask had an overall thickness of 7 mm and the rails had the configuration and positioning as in the original part.

4.4.2.2 Material Properties

As mentioned before, because the gantry is expected to undergo low stresses and deformations, only the elastic component of the material's behaviour was considered.

Abaqus allows the selection amongst different types of material models. The selected type was "Lamina", as it is usually used to describe the properties of individual composite layers. This type requires, as input, the Young modulus for two orthotropic directions (E_1 , E_2), the Poisson's ratio (ν_{12}), and the Shear Modulus in three direction orthotropic directions (G_{12} , G_{13} and G_{23} – out of plane shear) to define an orthotropic material in a shell element. The properties were obtained from reference [28]. Figure 4.19 shows the properties along x for the carbon/epoxy laminate with a fibre volume percentage of 60%. For the unidirectional laminate with fibres at 0° the Young modulus was defined as 134 MPa (signalled in red on the bottom right of Figure 4.19). This was considered as E_1 . If all fibres present a 90° orientation, this modulus drops to 7 MPa, representing E_2 for the unidirectional lamina.

G_{12} (in plane shear) and G_{13} were considered the same and equal to 4.2 MPa, as from Figure 4.20. Finally, G_{23} was calculated by eq. 4.7

$$G_{23} = \frac{E_2}{2}(1 + \nu_1) \quad \text{eq. 4.7}$$

Considering that ν_{12} equals 0.1 for a unidirectional lamina, G_{23} was estimated as 3.85 MPa.

For a $\pm 45^\circ$ plainweave lamina, E_1 and E_2 will have the same values, estimated to be approximately 15 MPa, while G_{12} and G_{13} reach 34.5 MPa. G_{23} was estimated to be the same as the one for the unidirectional lamina.

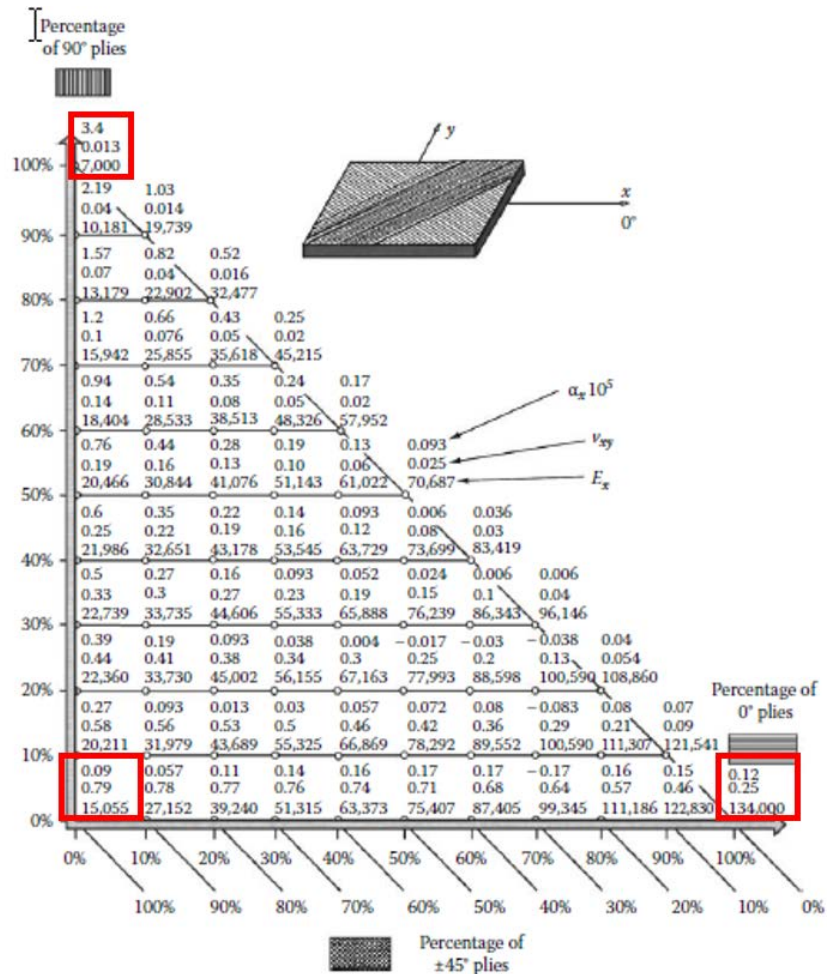


Figure 4.19 – Properties (namely Young Modulus) of a carbon fibre laminate as a function of the percentage of different orientations (adapted from [28])

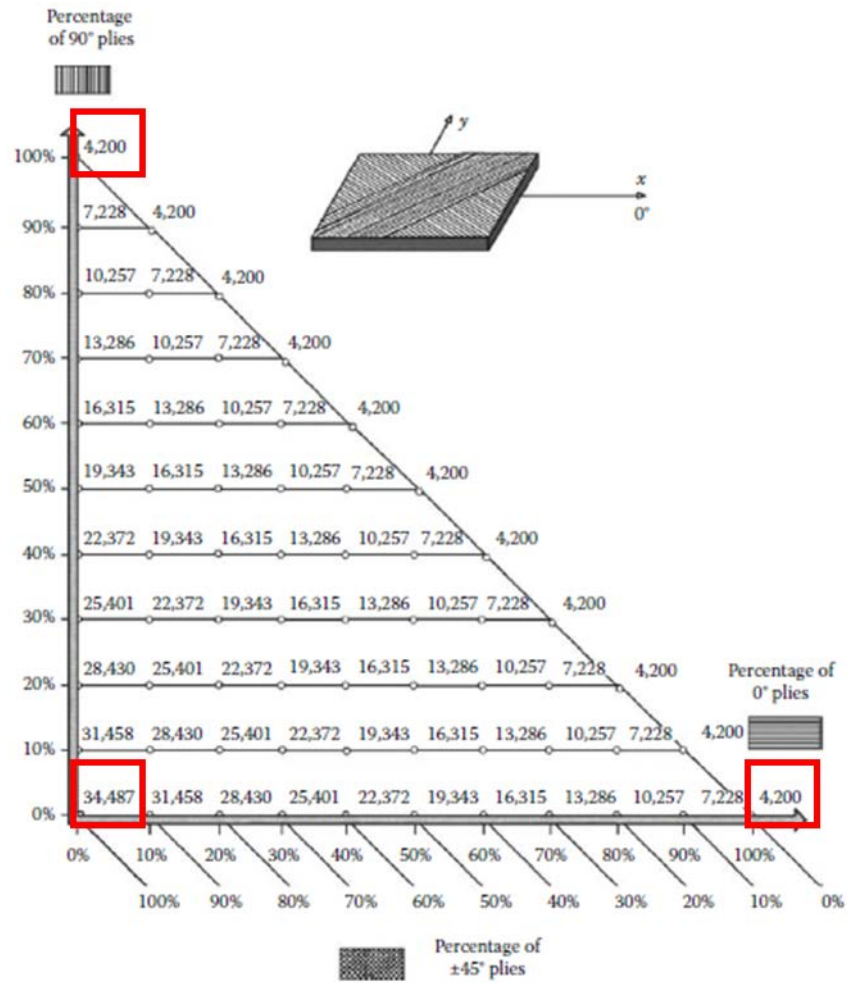


Figure 4.20 - Properties (namely Shear Modulus) of a carbon fibre laminate as a function of the percentage of different orientations (adapted from [28])

Table 4.10 sums up the properties considered for the laminate, which were used for the thickness optimization process.

Table 4.10 – Properties of the laminates considered for the optimization process

Fabric type	Property					
	E1 (MPa)	E2 (MPa)	ν_1	G12 (MPa)	G13 (MPa)	G23 (MPa)
Unidirectional 0°	134	7	0.1	4.2	4.2	3.85
Plainweave ±45°	15	15	0.1	34.5	34.5	3.85

4.4.2.3 *Layup*

The properties described in the above section 4.4.2.2 were the basis of the definition of the sections to all composite components. But because the gantry was represented by shell elements (which have no graphic representation of thickness), different properties can be given to different regions, resorting to the thickness and section definitions. Such method has a huge advantage for the optimization process as a geometry does not have to be defined each time a different configuration needs to be tested. The geometric part is the same and only the section attributed to the part is changed before each utility function evaluation. This means that elements, within the limitations of the mathematical model selected, will behave as having a particular thickness but, in order to have that, a part with walls with that thickness does not need to be modelled.

Thickness is one of the aspects involved in the definition of the part's walls. The layup definition requires the definition of mechanical properties of each layer (resorting to the mechanical properties previously listed in Table 4.10), the number and order of plies, their thickness and orientation and how the layup is placed relative to the surface defined by the shell elements.

These properties are defined early on the model. The section will be defined by defining the layer thickness and stack order. The optimization process considers three different types of lamina: 0° , 90° and plainweave $\pm 45^\circ$. These orientations were selected based on the results of previous dimensioning results. 0° layers are aligned with the gantry axis and, in the ribs, with a horizontal orientation. 90° layers are defined as a rotation by 90° of the 0° layers (each layer has an attribute that allows the definition of the orientation). Due to the results obtained in the previous dimensioning stages some aspects of the layup can be determined:

- The outer layer is always the $\pm 45^\circ$ layer, as the part requires large torsion rigidity (provided mainly by this layer) and the outer layer will have a larger torsional constant.
- The inner layer is the 90° layer
- To ensure layup symmetry the thickness of the $\pm 45^\circ$ layer and the 0° layer are divided in half and attributed to different layers.

Before the optimization loop takes place, all of the layers are attributed a thickness of 1 mm (Figure 4.21).

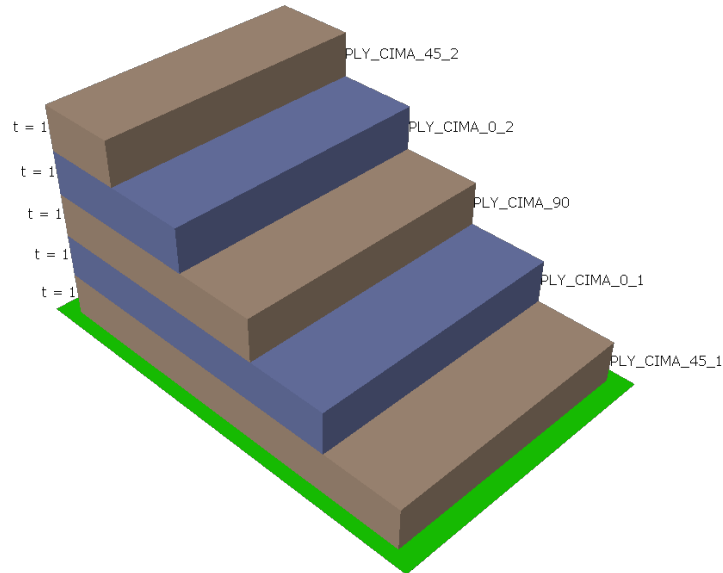


Figure 4.21 – Initial layout that displays the orientations considered

4.4.2.4 *Discretization*

The discretization step renders the distribution of the elements that compose the mesh. This is a critical step as elements with poor geometry will render inaccurate results. To ensure realistic load transmission between adjacent elements linked with rigid connections, it is desirable that the mesh presents nodes in that particular location. This creates the need for a series of operations that force the mesh generating algorithm (presented by Abaqus) to place nodes at given points. Apart from some options that are given by this algorithm, it is considered as a black box. The way of forcing the placement of nodes is the creation of partitions. A partition creates edges along a given surface. Nodes will be placed along edges the part presents upon mesh generation process. If two edges intercept, creating a vertex, a node will be placed at such point. Using Abaqus for mesh generation implies an iterative process of creation and removal of edges to create a mesh with nodes along the desired locations and a regular mesh with elements that present adequate dimension and shape. The shape that is considered is overall comprised of flat faces with constant width along its length. This is of great advantage as the mesh will tend to be regular and easily obtained.

After the partitions are in place, the discretization process requires the definition of the element dimension. This will also heavily impact the accuracy of the model. Elements that are too big will be less representative of the behaviour of the part they represent. On the other hand, elements that are too small will lead to a

model that is too heavy. A balance has to be established by considering the element size that is as large as possible while rendering relevant results.

A study was performed by changing the dimension of the elements used. Four meshes were created and tested, while the rest of the model stayed constant. Figure 4.22 shows that a mesh of roughly 96 thousand elements is time efficient (resulting in a running time of 2 minutes) and the increase in terms of elements that is verified for the next mesh does not return a large variation in terms of accuracy. On the other hand, the time required for the simulation to run is more than three times larger. The absolute values of displacement are quite large since the configuration in terms of thickness does not comply with the system that was previously dimensioned.

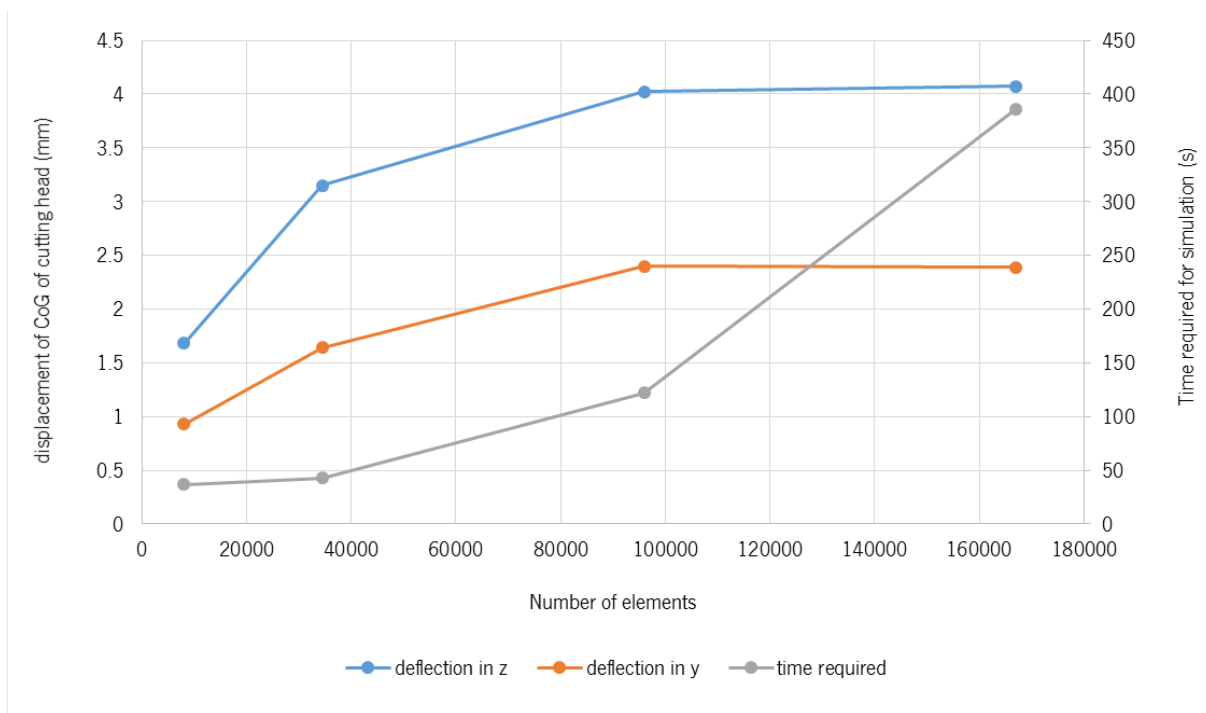


Figure 4.22 –Displacement of centre of mass of the cutting head and time required for simulation to run as a function of the number of elements

Table 4.11 summarizes some of the indicators of the mesh quality.

Table 4.11 – Quality indicators for the mesh used

Part	Element Type	Number of Elements	Avg min angle	Worst min angle	Average aspect ratio	Worst aspect ratio
CFRP Gantry	SR4	65212	89.92	69.01 (0.16%)	1.05	1.74 (0.16%)
Metallic Mask	C3D8R	30992	89.14	60.78 (1.93%)	1.94	3 (0.20%)

A difference between the carbon and the metal part is also presented in terms of element model: while the carbon laminate is represented by shell elements, the metallic mask is represented by 3D elements. The shell elements are SR4 elements, meaning that it is a 4-node general-purpose shell with reduced integration that considers 6 degrees of freedom of each of its four nodes. The reduced integration means that the calculation of the stiffness matrix is done in less time and with some accuracy loss as a lower number of integration points is used. However, SR4 elements are considered to be a robust, general-purpose element that is suitable for a wide range of applications. The solid elements are also reduced integration ones (C3D8R). Both types of selected elements have hourglass control in order to avoid the mesh deformations that can result from the hourglass phenomena. As the mesh dimension, also the elements types take into account the trade-off that has to be performed considering accuracy and computational costs.

As it is visible, while having a relatively small number of elements, the mesh is capable of a discretization of the geometry without much distortion of those elements. This comes from a good partition geometry, but also from a strategy that resulted in keeping the geometry simple while being representative of the analysed problem. Figure 4.23 shows an overview of the meshed part.

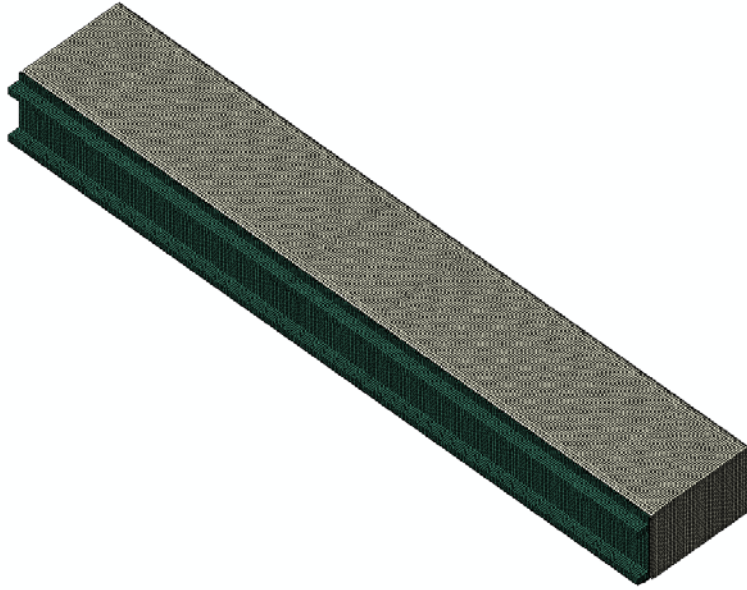


Figure 4.23 – Overall aspect of the mesh generated

From a side view, the shell mesh presents slight deformation relative to a plain square shape, especially when adjusting to the corners, as shown in Figure 4.24. However, this approach renders satisfactory results in terms of distortion level and adjustment to the shape without an increase in number of elements.

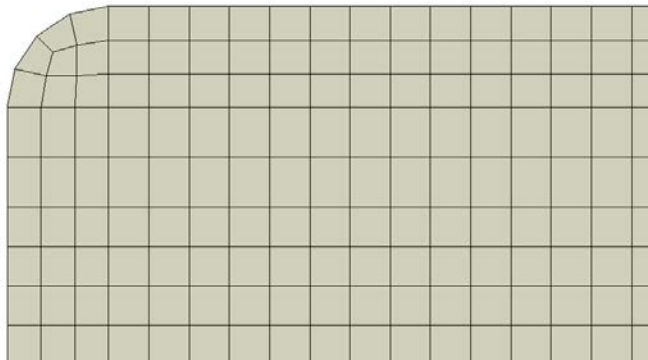


Figure 4.24 – Detail of the mesh (corners of the ribs)

From a top view it is possible to observe that the mesh presents a regular shape with elements that are quite similar to the desired perfect square shape (Figure 4.25).

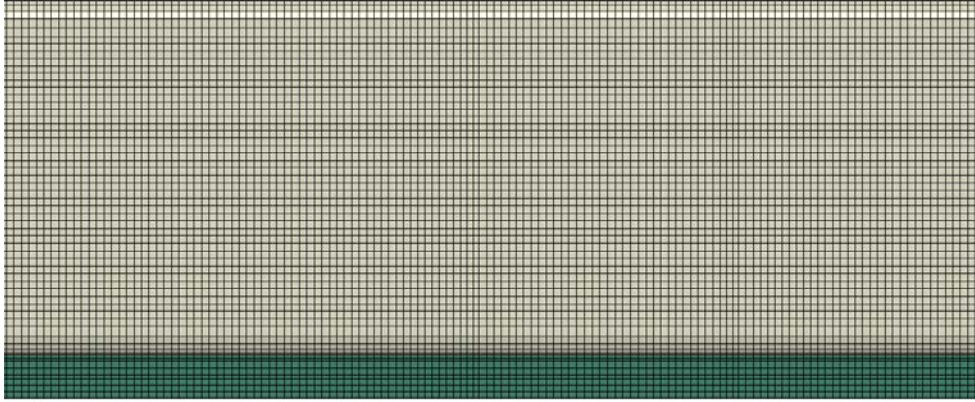


Figure 4.25 – Mesh displaying elements with regular shape and near square configuration.

4.4.2.5 *Loads*

As mentioned in point 4.3.3, the loads were applied as concentrated forces at specific points determined as the centre of mass of the components that exist around the gantry and that are considered to be of relevance when assessing the gantry behaviour and deformation. The static loads are applied at the coordinates displayed in Table 4.9.

While the coordinates are the same as the ones considered in the initial dimensioning stage, the loads vary as they are influenced by the acceleration that the gantry is subjected to.

Therefore, the acceleration is treated as a variable, being the 19th one and the only that is not related to the configuration of the layup. The loads that were considered in the finite element model varied with the acceleration, being the y component of these loads directionally proportional to it, given that the gantry moves along y. An additional load that was inserted in the model is the one imposed by gravity. This also affected the acceleration and, therefore, the loads that the gantry was subjected to. This means that the loads were constant in the x and z directions but vary in the y direction. The loads are summarized in Table 4.12.

Table 4.12 – Loads applied to the system. a is the 19th variable and influences the y component of the considered loads

Load	Components (N)		
	X	Y	Z
Optical path support left	0	2,401E+02*a	-2,401E+02
Optical path support right	0	1,029E+02*a	-1,029E+02
Cutting Head	1,96E+03	2,820E+03	-9,8E+02
Secondary engine	0	-5,292E+03	-1,960E+02

4.4.2.6 Interaction between the parts

The interaction between the parts that were not geometrically modelled were, instead, represented by forces applied to their centre of mass and, then, connected to the gantry by multiple point constraints (MPC), in this case a beam formulation kinematic coupling. This connection constrains a group of slave nodes to the translation and rotation of a master node by providing a rigid beam between two nodes.

As mentioned, the interaction between the composite component and the metallic mask is performed considering a tie between the two elements. Figure 4.26 shows the overall interactions defined (in yellow).

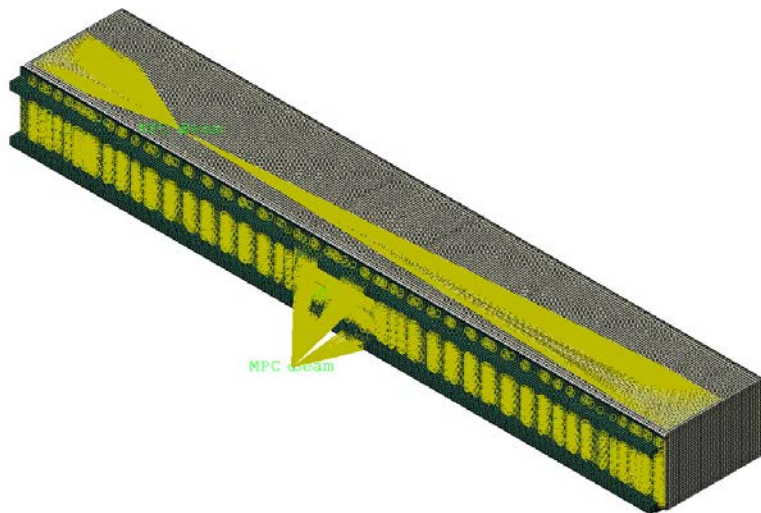


Figure 4.26 – Overview of the interactions defined in the Finite Element Model

4.4.2.7 *Boundary conditions*

The boundary conditions link the gantry to the machine's structure. It is performed in the interface of the gantry with linear motors, which will then produce the gantry's movement. These are attached to the gantry by metal slabs that are screwed to the gantry. One of the sides is totally fixed, restraining all of the degrees of freedom of those nodes to zero. The other side allows movement in one direction.

Figure 4.27 shows the two restrained areas, being the left one totally fixed (encastrated) and the right one allowing for translation along the axis of the gantry.

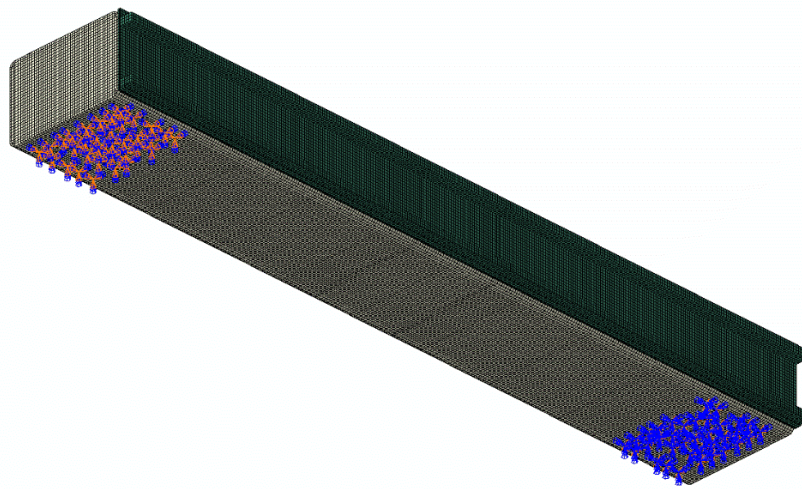


Figure 4.27 – Boundary conditions of the model

4.4.2.8 *Information contained in the output file.*

One critical point is determining the information that is required to perform the optimization process. This information will be written to the output file generated by Abaqus. A larger file contains more information, but because is larger also requires a longer writing period. The determination of whether the structure analysed is valid or not depends on two factors: the displacement suffered by the point that represents the centre of mass of the cutting head and if the force required from the linear motor is lower than the maximum presented by the selected model. Therefore, the output is configured to contain just that. Also, to shorten the time consumed by the simulation, a one-step increment was implemented, having the total load to be applied at once. This does not affect the observed final output, but does result in an output file that has only the final displacement and not the curve of displacement in function of the force.

4.4.2.9 Optimization loop

Before the optimization loop is initialized, there is a setup stage that requires several steps. Regarding the finite element model, the python script that creates the model previously described was produced. Resorting to Abaqus, that scrip runs and the model is created. With that model created, an input file (*.inp file) is generated. This file contains all of the information that Abaqus requires to run the simulation, including an initial configuration in terms of ply thickness and acceleration. It differs from the script as it does not contain, for example, information on how to create the geometry or the discretization. Instead it has the coordinates of the nodes and how they are connected to each other to form the elements. It also associates to the elements their mechanical properties, and constraints.

Initially the loop was intended to run the script every time an evaluation needed to be performed, meaning, for each population element for all of the cycles. It was latter established that this way would be more time consuming. Not only would it add more steps (since the generation of the *.inp file is mandatory), the model generation from the script is a costly process. Therefore, the optimization loop operates directly on the *.inp file. As the *.inp file is generated, the setup required from the finite element side of the optimization process is concluded.

The setup of the PSwarm algorithm implies defining several parameters that will dictate the algorithm's behaviour. Regarding the variables, it requires upper and lower boundaries and linear constraints. The boundaries dictate the range of values that are considered admissible for a solution. From previous experience, it is safe to say that it is very unlikely that a section has, for any of the considered orientations, a thickness above 12 mm. The lower boundary is the inexistence of a given orientation, thus 0 mm. The acceleration will be varied between the current value (2 G) and the theoretical maximum verified if the gantry presents a mass of 0 kg (2.94 G).

In this case, the linear constrain establishes that all sections must have a positive thickness. Not only that, the minimum thickness was established as 0.01mm, which represents the minimum thickness of carbon fabrics available in the market. Therefore the linear constrains can be represented by eq. 4.8.

$$\begin{bmatrix} 0 & 1 & 1 & 1 & 0 & 0 & 0 & 0 & 0 & 0 & 0 & 0 & 0 & 0 & 0 & 0 & 0 \\ 0 & 0 & 0 & 0 & 1 & 1 & 1 & 0 & 0 & 0 & 0 & 0 & 0 & 0 & 0 & 0 & 0 \\ 0 & 0 & 0 & 0 & 0 & 0 & 0 & 1 & 1 & 1 & 0 & 0 & 0 & 0 & 0 & 0 & 0 \\ 0 & 0 & 0 & 0 & 0 & 0 & 0 & 0 & 0 & 0 & 1 & 1 & 1 & 0 & 0 & 0 & 0 \\ 0 & 0 & 0 & 0 & 0 & 0 & 0 & 0 & 0 & 0 & 0 & 0 & 1 & 1 & 1 & 0 & 0 \\ 0 & 0 & 0 & 0 & 0 & 0 & 0 & 0 & 0 & 0 & 0 & 0 & 0 & 0 & 0 & 1 & 1 & 1 \end{bmatrix} [x] \geq \begin{bmatrix} 0.01 \\ 0.01 \\ 0.01 \\ 0.01 \\ 0.01 \\ 0.01 \end{bmatrix} \quad \text{eq. 4.8}$$

The first variable is the acceleration, and is not subjected to linear constraints. The rest of the variables are grouped by line. Each line represents a section and each section has three layers. Being x matrix that contains the value of the variables, the linear constraints impose that each section presents a minimum thickness of 0.01 mm.

Based on the knowledge from previous optimization processes, the population size was set to 40 elements. The population will, therefore, be composed of forty elements that will travel through the solution space while, hopefully, converging to a region, where the best solution is present. This will be processed by evaluating the behaviour of the solutions coded by the values given to each variable. Each evaluation corresponds to changing the *.inp, performing the simulation and extracting the relevant outputs. This process takes approximately one minute using the 8 cores of an i7 processor @ 2.4 GHz with 16 GB of RAM. Also based on previous knowledge, it is estimated that a maximum of 2000 evaluations will ensure convergence to the near optimal value (since the process is not deterministic, the end result cannot be considered optimal). The other parameters of the algorithm, including the relative weight of social vs cognitive behaviour, was left at default levels that were set based on previous tests. Testing different parametrisation of the algorithm was deemed as out of the scope of the project and values that traditionally present adequate results for similar processes were adopted.

Despite the relevance of the previously mentioned parameters, the aspect that will mostly affect the end results is the objective function. This will define what the algorithm will be evaluating and how. Two things must be taken into account about PSwarm when defining the objective function:

- it is a single objective optimisation algorithm
- it is a minimisation algorithm.

The first is easy to fulfil, since the goal is to maximise the acceleration. But since the algorithm is a minimisation one, the acceleration output has to be multiplied by -1 so that the algorithm minimises the function but maximises the acceleration.

There is another aspect that must be accounted by the objective function, given that PSwarm does not account for nonlinear constraints, meaning, constraints related to the output variables. The aspect of the gantry's rigidity must be imposed when evaluating the results. If the displacement of the centre of mass of the cutting head for the gantry being analysed is larger than the one of the metallic part (analysed in 4.3.1), the solution is deemed invalid, regardless of how high the acceleration is. Also, the force required by the linear motor to apply the acceleration to the solution tested cannot be higher than the maximum specified by

the manufacturer, since the employed linear motors are not to be changed. The algorithm is not able of discarding results as non-valid, however the influence that elements have on the future behaviour of the population elements is very low if they behave poorly when evaluated. A bad behaviour, in the case of a minimisation algorithm, translates to a high value of the solution's objective function. Therefore a penalty is imposed to the solutions that violate the rigidity or force constraints and the objective function is defined by eq. 4.9.

$$f = \begin{cases} -a & \text{if } dof_i \leq dof_{i_{max}}, i \in [1, 6] \text{ and } m \leq m_{max}(a) \\ 1E + 20 & \text{if } dof_i \leq dof_{i_{max}}, i \in [1, 6] \text{ or } m \leq m_{max}(a) \end{cases} \quad \text{eq. 4.9}$$

where f is the objective function, a is the acceleration, dof_i is translation or rotation in any of the six degrees of freedom of the centre of mass of the cutting head for the composite part, $dof_{i_{max}}$ is translation or rotation in any of the six degrees of freedom of the center of mass of the cutting head for the metallic part, m is the mass of the composite gantry and m_{max} is the maximum mass the linear motor can apply the defined acceleration to.

As mentioned, a solution that violates the rigidity or mass constraints is given a very high value, which makes it a very undesirable solution. As explicit in eq. 4.9, mass is not considered in the objective function. The expectation was that the algorithm would be able to generate thinner and lighter solutions that will not violate the constraints and ensure higher admissible accelerations. Tests were performed with variations that accounted for other aspects to be accounted for in the objective function, namely gantry mass and the displacement suffered by the centre of mass of the cutting head. The relative relevance of these performance indicators was also studied.

As the configuration of the algorithm is terminated, the conditions to initialize the optimization loop are presented. The loop starts with the generation of the population (40 elements as previously defined). As each element is to be tested, the algorithm accesses the *.inp file and changes the thickness of each layer of the sections and the acceleration. When running the first loop, the *.inp file presents the random configuration that is used to generate the file when running the Abaqus script. This configuration is irrelevant as it changed for each evaluation. At this stage there could be a verification of the linear motor's required force by estimating the gantry's mass. This estimation would have to be extremely accurate since the problem's formulation leads to having the most desirable solutions on this area (taking most advantage of the linear motor's

capabilities). However, this was not implemented and is considered to be a required upgrade in future versions of the implemented loop. After the *.inp file is changed to address the solution under analysis, the simulation is run by Abaqus and the output file (*.odb file) is generated. The algorithm accesses this file and extracts the point of interest's displacement and writes it to a file together with the value of the other 19 variables. Based on these 25 values, the objective function is calculated, according to eq. 4.9. After each evaluation the algorithm checks if the stop criteria have been met. If so, the optimization process is terminated. At the end of an evaluation of the group of 40 elements, the algorithm performs a further verification, regarding the convergence of the population to a near-optimal solution. Being PSwarm a hybrid algorithm, it has the ability of initiating a poll step resorting to pattern search, to determine the direction that the population should follow based on the best element from the previous search (particle swarm) step. Either the poll step is required or not, the algorithm proceeds to generate a new set of values for the elements and test them resorting to Abaqus calculations after changing the *.inp file to represent the configuration that is to be tested.

Figure 4.28 summarizes the optimization process that was described.

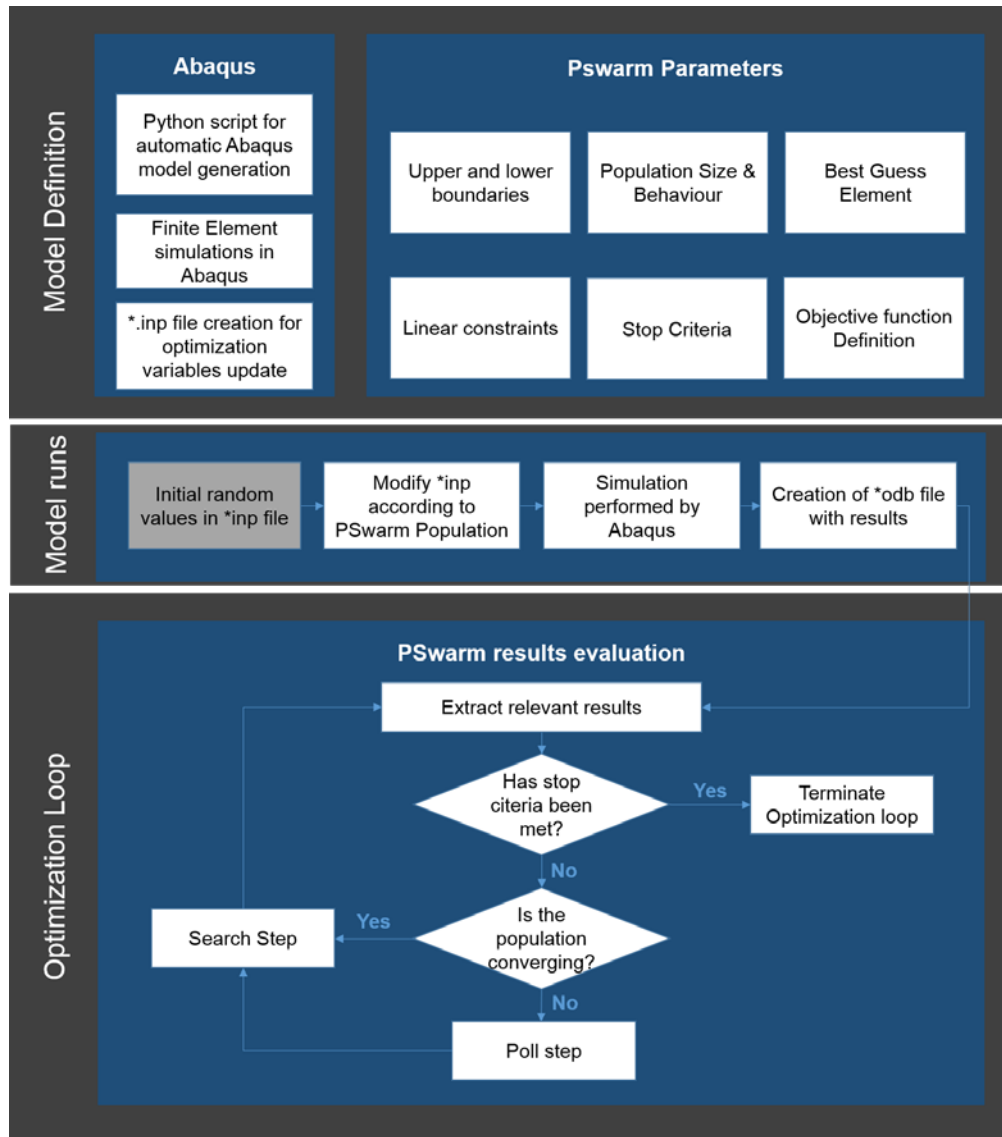


Figure 4.28 – Overview of the optimization loop created

Chapter 5: Production and Numerical Simulation of the Gantry Prototypes

Summary

This chapter is focused on the description of the work performed in order to obtain an improved version of a gantry, as an enabler of the development of an ILCM with higher productivity without accuracy loss.

This implies the characterization of the machine being studied, analysis of the loading scenarios and their effect on the current part, dimensioning of the proposed solution and the experimental validation of the methods and outcome of this process.

The analysis and dimensioning was performed using both analytic and numeric models. The difficulty in achieving a balanced solution between weigh/stiffness/acceleration, led to the implementation of an optimization routine linked to the numerical evaluation of the performance of the solutions created. The validation of the solution achieved and the methodology requires a validation of the FEM through the comparison with experimental data. In order to mitigate the risks linked to the implementation of a composite gantry on an ILCM (despite the identified potential advantages), the research methodology adopted an intermediate step and performed the initial tests with a scale prototype, previously to a full size and functional prototype.

5.1 NUMERIC MODEL VALIDATION

In order to obtain a validation of the FEA performed to both gantries (metallic and CFRP), a scaled down model was created. This represents an approach that is more prone to mitigate risks and reduce the budget required for this validation. The plan to validate the FEA had, therefore, to be rethought and a new idea on

how to validate the numerical simulations that supported the dimensioning and optimization tasks was proposed.

The steps where:

- Production of material samples for mechanical characterization
- Production of a scale prototypes of the gantry (both with and without internal reinforcements)
- Prototype loading with scenarios similar to the ones present in the simulations.

Both the material samples and the prototypes were instrumented in order to obtain data that can be input in the model (from samples) or compared to the model output (prototypes).

5.1.1 Material Mechanical Characterization

5.1.1.1 Raw materials

The materials used to manufacture the composite parts and samples studied and tested in this work were selected based on representability (they must be similar and illustrate the materials considered in previous chapters) and availability.

The composite samples were manufactured using the carbon fibre fabric PYROFIL™ TR3110M, a plain weave fabric with a density of 200 g/m² (see in Appendix A) and that on both warp and fill uses the yarn TR30S 3K from Mitsubishi Rayon Co Lda, with 3000 filaments and a density of 1.79 g/cm³ (see Appendix B).

The epoxy resin system from Hexion™ constituted by the EPIKOTE™ Resin 04908 mixed with the EPIKURE™ Curing Agent 04908 with a mass ratio of 100:30 (as per Appendix C), was used as matrix. This infusion resin presents low viscosity and ensures good wetting and adhesion on carbon fibres. EPIKURE™ Curing Agent 3253 (datasheet available in Appendix D) was added to the matrix as an accelerator in a ratio of 3:100 pbw. Finally, the epoxy based structural EPX™ DP490 from 3M™ Scotch-Weld™, was used as a gap filling two component epoxy adhesive, used for the construction of composite assemblies.

Tests were also performed on samples to determine the behaviour of both the carbon laminates and the adhesives. As the standards followed required the presence of tabs, an additional adhesive, namely

Loctite/Henkel epoxy adhesive Hysol® EA 9394, was used for gluing the tabs on the samples to perform both tests.

5.1.1.2 Standards followed

In the present work the following applicable standards were used to characterise the raw materials and composite laminates: ASTM aD3039/D3039M-08 - “Test Method for Tensile Properties of Polymer Matrix Composite Materials” (determination of the Young Modulus, Ultimate Stress and Poisson Coefficient) and ASTM D 3165-00 – “Standard Test Method for Strength Properties of Adhesives in Shear by Tension Loading of Single-Lap-Joint Laminated Assemblies” (Determination of the Ultimate adhesive Shear Stress).

5.1.1.3 Preparation of samples

Samples for tensile testing were produced using the raw-materials listed above by vacuum infusion processing. A plate of uniform thickness (approximately 2.5 mm) was produced with fibres oriented at 0°/90° and, then, cut into rectangles of 25 mm x 250 mm. The tabs applied on samples were also produced by vacuum infusion and cut in rectangles of 50 mm x 25 mm (Figure 5.1 a). Before bonding the tabs, and following Hysol® Surface Preparation Guide (Appendix G) the gluing areas on the samples were sanded using 400 grit emery paper (Figure 5.1 b) and cleaned using alcohol (Figure 5.1 c). Tabs and samples were then joined by using the Loctite/Henkel epoxy adhesive Hysol® EA 9394 because of the good results already obtained in previous works with this adhesive (Figure 5.1 d) [213, 214]. Finally, the samples were kept in a template shown in Figure 5.1 e for 5 days at room temperature during the curing stage, as it is recommended in the datasheet (see Appendix F). Figure 5.1 f and Figure 5.1 g show the typical final appearance of tested samples.

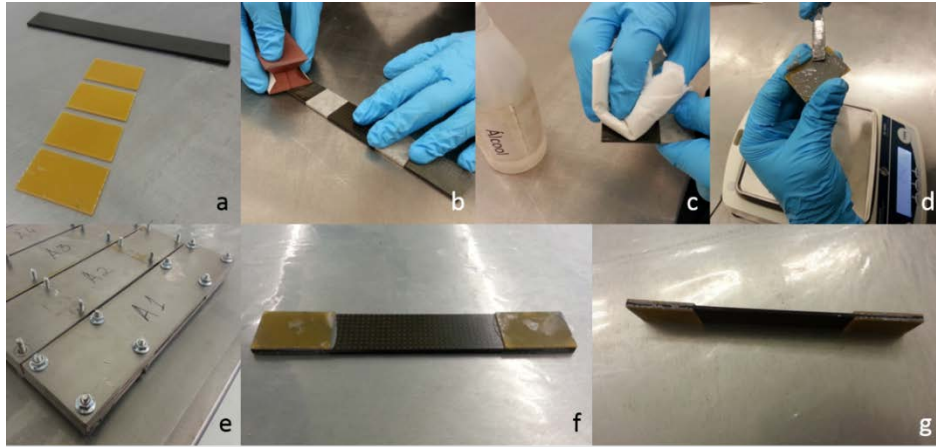


Figure 5.1 - Preparation of samples for testing

Regarding the adhesives, shear tests were performed on $0^\circ/90^\circ$ plain weave samples manufactured according to the ASTM D 3165-00 standard. In agreement with this standard, the length of the specimen overlap was established in order to ensure that failure will happen in the adhesive interface instead of the adherent material. Such specimen overlap length is defined by eq. 5.1:

$$L = \frac{F_{ty} T}{\tau} \quad \text{eq. 5.1}$$

where

L overlap length (mm)

T substrate thickness (mm)

F_{ty} substrate yield stress or stress at proportional limit (MPa)

τ 150% of the estimate average of the shear strength in the adhesive bond (MPa)

The standard also states that length of specimen overlap must have a maximum limit of 12.7 mm. Therefore, if eq. 5.1 returns a value of L larger than this limit, it should be ignored and the overlap length will be of 12.7 mm.

Considering the dimensions presented in the Figure 5.2, adapted from the standard used, the samples were produced to present a thickness as close as possible to 1.6 mm (in this case the average thickness was 1.7 mm).

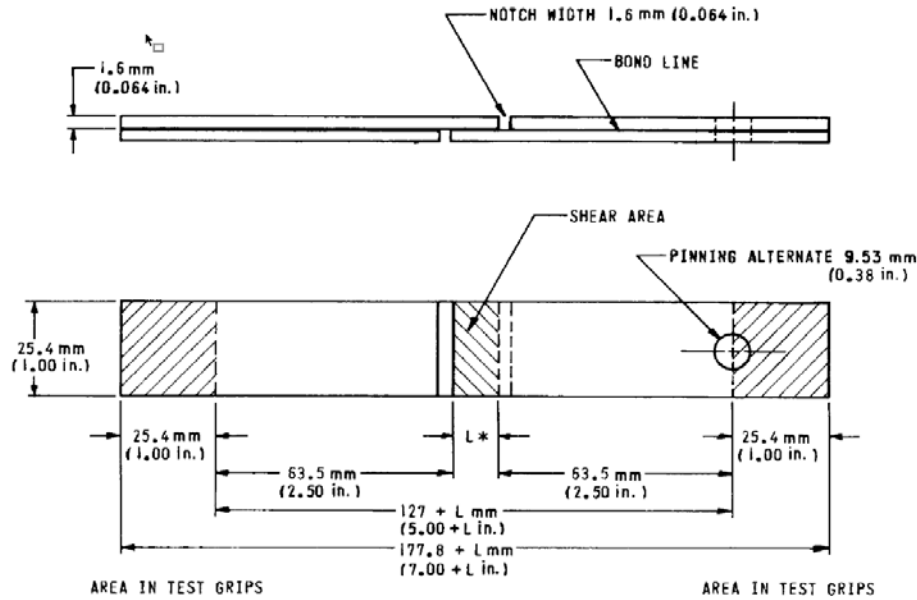


Figure 5.2 - Dimensions of shear testing samples according to the ASTM D 3165-00 standard

By considering the thickness of 1.7 mm, the ultimate stress of 781.05 MPa and an ultimate shear strength of 36.1 MPa, the overlap length calculated from eq. 5.1 was 24.5 mm. Therefore, as this value was higher than the maximum permissible one, it was assumed the limit value of 12.7 mm.

Thus, by considering $L = 12.7$ mm the total length of the samples to be produced was determined as 190.5 mm, being the overall dimension of each one of the two individual carbon fibre composite glued rectangles of 101.6 mm \times 25.4 mm. The tabs, also made from the same layup, were manufactured with a length of 87.3 mm.

The adhesive thickness was kept comprehended between 0.5 mm and 1.0 mm, as commonly recommended by manufacturers. Prior to adhesive application, bonding surfaces were sanded with a 400 grit emery paper and after cleaned with alcohol. The sanding process roughens the surface and eliminates contaminants, while alcohol is used for particle removal and degreasing.

The samples were then kept under pressure during 24 hours to ensure proper adhesion and the adhesive layer thickness and then, left for curing during 6 days (as per indication of the datasheet). Finally, these samples were allowed to cure at room temperature for 7 days.

Figure 5.3 presents a detail of the glued overlap (highlighted in white) produced for testing.

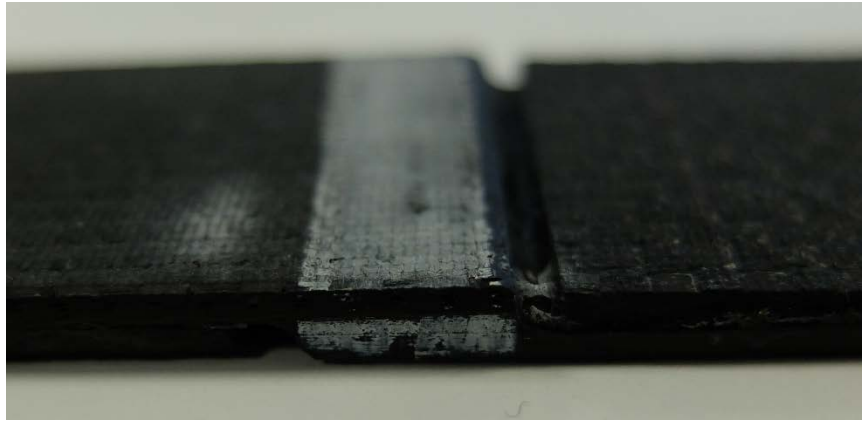


Figure 5.3 - Glued overlap (highlighted in white) used in the shear tests

5.1.1.4 Testing equipment

Tests were performed in a universal electromechanical testing equipment MTS Criterion Model 45 equipped with a LPS 305 load cell of 300 kN by using an alignment system model 609.25A-02 that reduces the effective maximum traction load to 250 kN. A hydraulic wedges flat clamps assembly, model 647.25A, was used for testing.

The equipment used, comprising the load frame, hydraulic control and data acquisition computer, is depicted in Figure 5.4.



Figure 5.4 - Universal testing equipment used for mechanical testing

5.1.1.5 Tensile tests

A total of 8 samples were used to tensile testing the materials according to ASTM D3039/D3039M 08 in order to determine its Young Modulus, Ultimate Stress and Poisson 's ratio. The tests were performed at room temperature and humidity.

As the determination of the Young Modulus and Poisson's ratio required the use of extensometers, two extensometers OMEGA SGT-4/350-XY41 were used per sample, one along the loading axis and another one perpendicular.

The ASTM D3039/D3039M-08 standard also suggests taking note of the failure mode of each sample when possible. The failure code is composed by three letters and attributed according to the conditions defined in Table 5.1.

Table 5.1 - Failure modes according to ASTM D3039/D3039M-08

First Character		Second Character		Third Character	
Failure Type	Code	Failure Area	Code	Failure Type	Code
Angled	A	Inside grip/tab	I	Bottom	B
Edge/Delamination	D	At grip/tab	A	Top	T
Grip/tab	G	<1W from grip/tab	W	Left	L
Lateral	L	Gage	G	Right	R
Multi-mode	M	Multiple areas	M	Middle	M
Long, Splitting	S	Various	V	Various	V
Explosive	X	Unknown	U	Unknown	U
Other	O				

5.1.1.6 Shear testing adhesives

By using the same mechanical testing equipment mentioned in the previous section 4.5.1.4, a total of 5 samples were used to test the materials according to and ASTM D 3165-00 in order to determine the ultimate shear stress of the adhesive Hysol® EA 9394. These tests were performed at room temperature and humidity.

5.1.2 Production of the prototype gantry

The scale prototype gantry schematically shown in Figure 5.5, constituted by three main different composite parts, was designed and produced to be submitted to experimental testing and allow validating the numerical simulations made. Two of those composite parts, Parts A and B (light and dark blue components shown in Figure 5.5), consist in two U-shaped half shells with a length of 700 mm that once assembled together form a 100 mm square cross-section. The upper U-shaped shell (light blue Part A in Figure 5.5) was designed with a tab etched along the bottom of its vertical flanges (presented in red colour in Figure 5.5) to allow guiding, mounting and bonding the lower U-shaped shell (dark blue Part B in Figure 5.5). The flange presents a width of 20 mm.

The third component is a 100 mm × 100 mm composite square plate (yellow part in Figure 5.5) that corresponds to the 6 internal ribs used as reinforcements and stiffeners to improve the gantry integrity. The flange for the adhesive application on the stiffeners is 10 mm wide.

Two different composite prototype gantries were produced to be submitted to testing in this work: one not having the internal ribs and another one with internal reinforcing ribs.

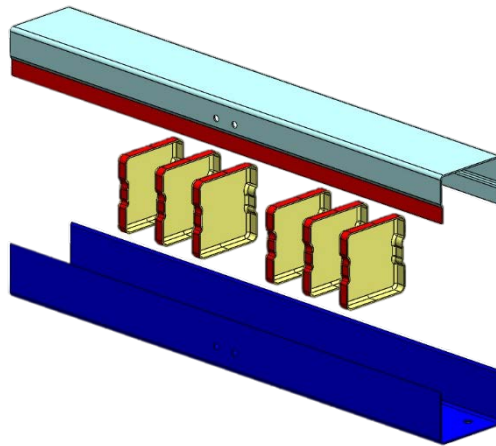


Figure 5.5 - Scale prototype gantry produced

The epoxy adhesive EPX™ DP490 was used to assemble and bind together all components. For such purpose the components were designed with tabs to allow the application of adhesives. These tabs are presented in red in Figure 5.5.

The design of all those parts had in mind the following specifications:

- each component must be representative of the part used in the optimisation process;

- each part must allow generating experimental testing data comparable to those obtained from the numerical simulations;
- all components must be able to be produced by vacuum infusion;
- the part production should be relatively simple;
- all parts should be produced within time and budget limitations;
- testing should be performed in the pre-existing equipment.

In terms of representativeness, this extends through several domains, meaning they must be produced with materials (in the case, carbon reinforced epoxy resin) and fibre orientations very similar to those used in the simulations and be also able to support a similar loading scenario. The loading conditions were also not supposed to cause plastic deformation or failure in the part, which should be able to withstand such loading with small displacements well below the ultimate stress, as it happens in the usage scenario of the optimised part.

Budget, testing equipment and time limitations dictated the construction of the scale prototype of the gantry produced. Therefore, the tested part does not present the real dimensions of the optimized parts.

5.1.2.1 Moulds manufacture

Moulds were manufactured according to the composite parts designed for being produced by vacuum infusion moulding. Open moulds produced from a homogeneous polyurethane based modelling block from Sika, SIKABLOCK™ M700, were used. This easily machinable material is able to keep good geometrical details and has the suitable mechanical properties required by this purpose, as may be seen in Appendix H.

Figure 5.6 presents the Computer-Aided Design (CAD) draws of two moulds designed and manufactured in this work. One of them will be used to produce the two outer U shaped shell parts (see Figure 5.6 a)). It was manufactured from a 1000 mm × 300 mm × 100 mm SIKABLOCK™ M700 block in order to obtaining a 100 mm wide and 80 mm deep groove that extends from one end to the other of the block. The extra length and depth will enable the production of larger parts than the final ones that were later trimmed to remove the areas in which where the composite layup was not completed.

A smaller mould, having dimensions of 680 mm × 205 mm × 75 mm, was used to manufacture the ribs (Figure 5.6 b)) and presents squared etched indentations with a larger depth (25 mm) than the corresponding

ones existent in the ribs, being the excess of material again trimmed after the curing process of the components.

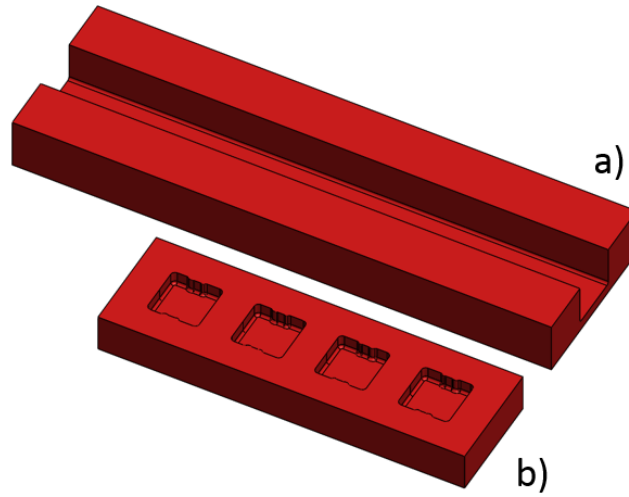


Figure 5.6 - The two polyurethane based moulds used in this work: a) for the outer U-shaped parts and b) for the internal reinforcing

The blocks were machined using an ELTE spindle mounted on a MOTOMAN MH50 6 axis robot. This Set, shown in Figure 5.7, presents a general accuracy of 0.5 mm.

The machining tools were programed through the Powermill Software based in the geometries desired for the parts defined in CAD draws.



Figure 5.7 - Robotic set used for machining the polyurethane based moulds.

Figure 5.8 displays the main phases of the production of the mould for both two U-shaped external shells.

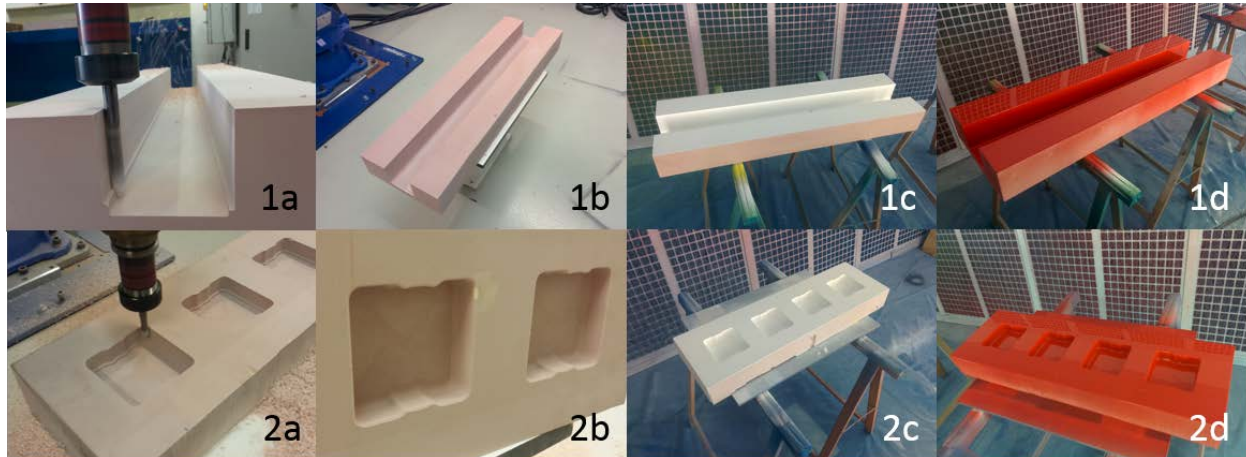


Figure 5.8 - Different phases of the production of moulds.

In a first stage the polyurethane SIKABLOCK™ M700 block was machined (photos 1a and 2a in Figure 5.8). In order to ensure an easy removal of parts and avoiding the small imperfections created by the machining process, the second phase was dedicated to the necessary work of sanding and painting the moulds for achieving a suitable polished surface (photos 1b and 2b in Figure 5.8). Sanding was performed with sandpaper with increasing grits up to 800. This resulted in moulds with smooth surfaces and ready to receive the primer (photos 1c and 2c in Figure 5.8).

After the primer application, sanding was again performed. This was followed by the application of the polyurethane based paint (photos 1d and 2d in Figure 5.8). Some more careful sanding work had also to be performed, mainly in the mould for rib's production. This mould has smaller and more intricate geometric features that make harder obtaining a homogeneous thickness in the paint layer to be applied. In this case, especially in the surfaces to be bonded to the other composite parts produced, a polish paste was used for surface treatment.

Finally, and before part production, a demoulding agent was applied on the mould surface. A water based Polytetrafluoroethylene (PTFE) liquid demoulding agent RELEASE ALL® SAFELEASE 30 from the Airtech Int. Inc. was applied because it had a good track record of enabling an easy removal of composite parts based on epoxy matrices. While wax could have also been used, the application of liquid release is much faster and can be directly made with the help of a cloth (one layer is enough, although two are advisable, and the cure takes only about 30 minutes). Thus, in spite of the worst visual aspect usually associated to the use of liquid

release agents, the use of wax was discarded due to time constraints, since it requires the application of several layers (common practices indicate using at least 5 layers to produce the first part and after 2 new ones between subsequent production cycles) and by knowing that will be needed about 50 minutes to apply each layer (including the application itself, drying of about 10 minutes, polishing and curing for, at least 30 minutes).

5.1.2.2 *Production of the composite parts*

The production of the parts begins with the cut of carbon sheets. For the external shell the sheets of carbon were cut with the length of 800 mm and width of 360 mm and for the ribs squares with lateral sides of 170 mm. Cutting was performed from a 1 m wide roll taken in account the orientation of the fibres required. Figure 6 shows some carbon fabric laminae cut with fibres oriented at $\pm 45^\circ$ (Figure 5.9).

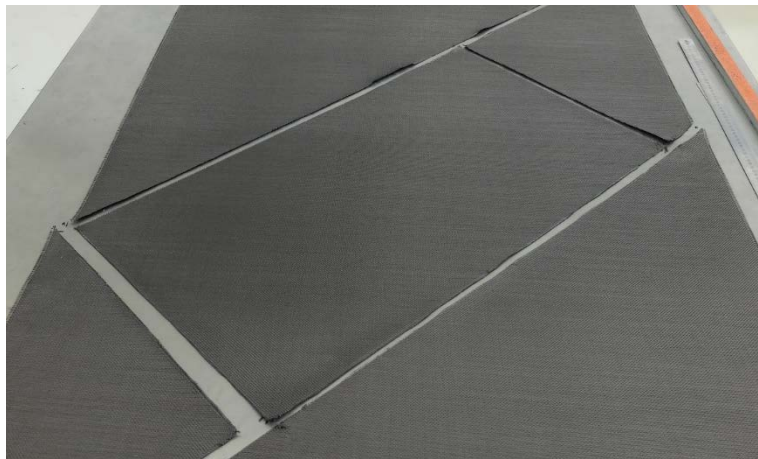


Figure 5.9 - Carbon fabrics cut with fibres oriented at $\pm 45^\circ$.

First the peel ply layers were applied in the areas where gluing will be employed. Then, the carbon layers were adjusted to the mould and successively overlapped until the required final configuration and thickness were achieved.

Table 5.2 shows the carbon fibres layup used in the production of the composite prototype gantry components.

The thickness of each layer was considered to be 0.2 mm (resulting in the approximate 1.8 mm total thickness obtained from the NDT ultrasound testing as can be seen later in Section 5.1.2.4).

Table 5.2 - Composite lay-up of the prototype gantry components

Layer sequence	Orientation
1	
2	$\pm 45^\circ$
3	
4	
5	$0/90^\circ$
6	
7	
8	$\pm 45^\circ$
9	

As it can be seen in Figure 5.10, two acrylic rulers were applied and glued on both sides of the mould for the U-shaped external shell. This enables the formation of an indentation tab designed to apply the glue for bonding the two external composite shells. These rulers were also coated with the release agent and dressed with peel ply.

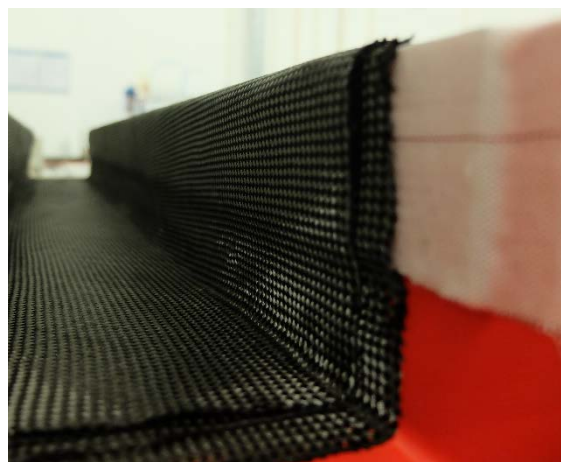


Figure 5.10 - Acrylic rulers used to allow forming the gluing tab.

This stage of the composite part production required some technical expertise because it is, simultaneously, necessary to ensure a good fit of the carbon fabric to the mould (adequate draping) and that the fibres'

orientations respect the parts' specifications. An inadequate draping easily leads to distortions of carbon plies (especially, in $\pm 45^\circ$ layers), which may result in unacceptable fibre orientations and unexpected mechanical behaviour of the final composite part. On the other hand, it was also essential to ensure that the carbon fibres follow the mould geometry otherwise the final part will present areas too much rich in resin (and, therefore, present subpar properties). In areas where proper draping was hard to ensure, a and/or was possible that fibres would suffer displacement during the layup process, spray glue was applied in thin layers because this was considered to have little or no influence in the infusion process and final material properties. Figure 5.11 shows some details of the fibre layup in two of most geometrically intricate locals and, therefore, critical cases: 1) a corner in the ribs. and, 2) a 90° fold.

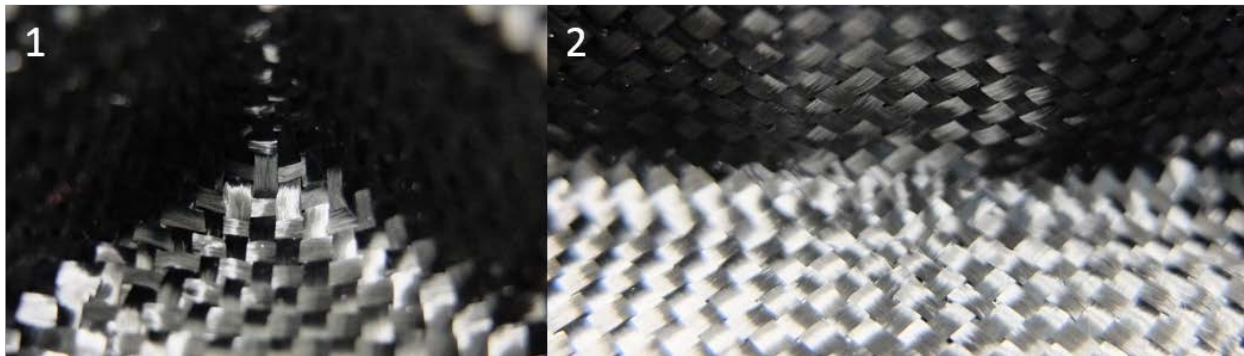


Figure 5.11 - Locals where fibre draping is particularly difficult. 1- rib corner; 2- 90° fold

It was also important to apply the tacky tape close to the mould extremities before beginning the deposition of fibre layers. This allows creating an adequate sealing between the mould and plastic layer and ensures the vacuum creation. Applying the tacky tape after the fibres deposition might cause the mould surface contamination by fibres and, therefore, compromise the tight seal of air.

Figure 5.12 shows the carbon fibre layers deposited on the mould and the tacky tape covered with a brown protective paper already placed near to the mould edges.

A tape was used to hold temporarily the carbon fibre layers in place and going beyond the dimensions of the final parts. After curing, the material in excess were trimmed.

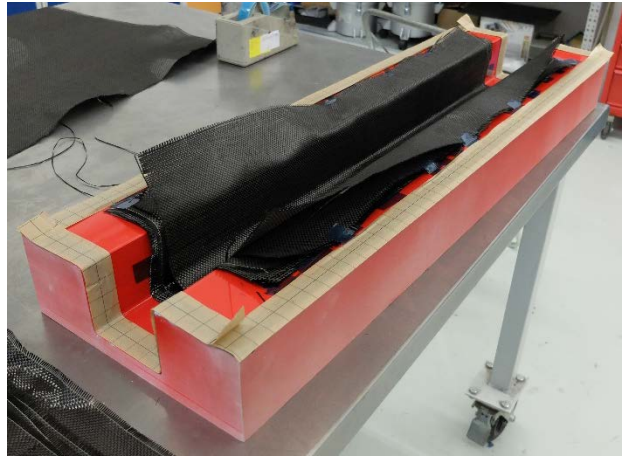


Figure 5.12 - Carbon layers and tacky tape protected by a brown paper placed on the mould

After deposition of all carbon fibre layers, two other particular layers were placed on the mould: the peel ply and the flow mesh. These layers are not intended to make part of the final composite structure. Instead they play an important role in the infusion process. The peel ply acts as filter avoiding the presence of foreign particles in the infused part and the flow mesh aids the resin flow. Figure 5.13 shows these two additional layers. The peel ply, which is firstly placed, is the white layer and the flow mesh, shown in yellow, is the last applied layer.

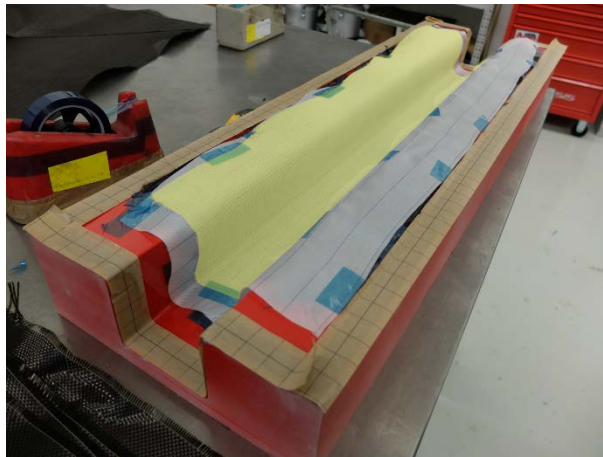


Figure 5.13 - Photo showing the peel ply (in white) and flow mesh (yellow) placed in the mould

The next step was placing the resin feeding plastic tube, the spiral for resin distribution inside the bag and, finally, the thermoplastic film bag and closure. Figure 5.14 shows these components mounted in the mould. The plastic tubes were held in place with tape and surrounded by tacky tape to ensure an air tight seal around

them. Small pieces of tacky tape were used to create some release folds and allow a better conformation between the bag and the underlying mould geometry during the vacuum application.



Figure 5.14 - Final setup of the vacuum infusion mould

To complete the setup for infusion the outlet plastic tube was linked to the vacuum pump (linked to the resin trap and consequently to the vacuum pump) and then vacuum was applied. Initially, it was verified if the tacky tape seals are airtight and the plastic cover and underlying layers properly adjusted to the mould. While the proper adjustment was verified by visual inspection, the effective vacuum was controlled and confirmed with help of the level of pressure in the sensor. The seal is considered well-functioning if the pressure is kept low and stable (around 50 mbar) for 15 minutes after sealing the air extraction tube with a clamp and switch off the vacuum.

Figure 5.15 shows the overall setup during vacuum application. In this Figure, arrows 1 and 2 indicate the resin intake and the air extraction plastic tubes, respectively, being the last one connected to the resin trap (3). To allow vacuum creation the resin intake tube is initially closed with the clamp (4) and only after connected to the resin vase.



Figure 5.15 - Infusion vacuum setup to switch on the vacuum

The amount of resin estimated to fulfil all the composite laminate was prepared in accordance to the resin/hardener/accelerator ratio referred in the manufacturer datasheet (see Appendixes C and D). To calculate the quantity of resin needed it was indispensable to take into account not only the resin required to completely fulfil all the composite part but also the one that will be lost in all the setup and mainly the one left along all the tubes.

As some air always becomes entrapped during the resin mixing process, the resin pot was introduced in a vacuum chamber to remove it. Only after air removal, the intake tube was introduced in the resin pot and the intake clamp finally removed.

The resin flow progress after opening the clamp from the air extraction tube is shown in Figure 5.16. It is important to control the speed at which the resin flow advances. Initially, the clamp should be totally opened to ensure a high resin flow which results in a homogeneous flow front formation. Photo 1 of Figure 5.16 shows that resin has already started to impregnate the layers within the area signalled in red, but it still has a long path to travel until reaching the end of the tube. Photo 2 shows the resin flow front already more parallel to the spiral that distributes the resin, although there is a point where the resin clearly didn't yet wet the layers which might be caused by a piece of tape interfering with the resin flow. Photo 3 in the same figure shows that this problem was overcome and the flow front is kept stable and, finally, the end of the resin flow process may be seen in photo 4 shown in Figure 5.16

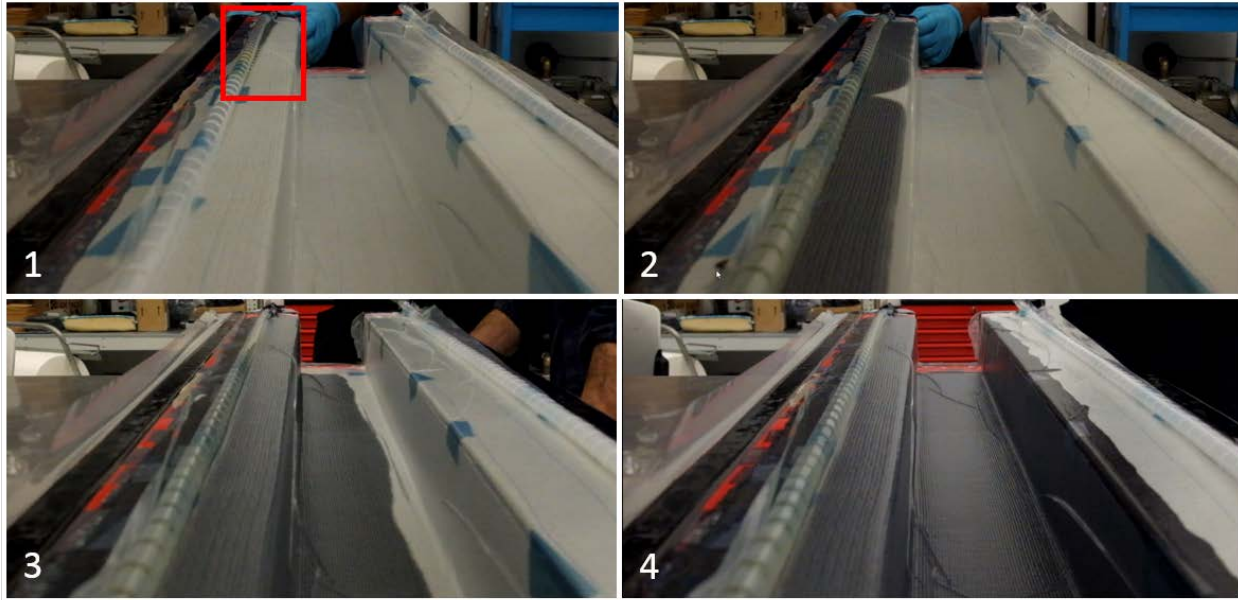


Figure 5.16 - Resin flow progress during vacuum infusion: 1) Beginning of process; 2) Interference in resin flow; 3) Normal resin flow at the middle of the process; 4) End of the resin flow

The next production step was curing, which took place at room temperature for 5 days. After curing is complete, the parts were extracted and trimmed to bring the composite parts to its final dimensions and discard parts with lower thickness and/or missing layers. The only exception was the length of the shell parts that was only submitted to final trimming upon the assembling process. The production implied a total of 6 infusion processes: two using the ribs mould and four using the one of external U-shaped shells. A total of 12 composite components were infused (8 ribs and 4 external shells).

5.1.2.3 *Composite parts finishing*

Two distinct prototypes were produced: one with internal ribs and one without them. The finishing process is quite similar for both of them, with the exception of the process of the ribs placement and joining. The process here described refers to the prototype with ribs.

Apart from the produced composite parts, steel load bearing components needed to be attached to them to allow submitting the scale model gantry to the desired loading conditions.

To attach these components to the composite parts T-nuts fasteners were integrated in the produced composite parts. These nuts initially present spikes that are used to carve them into wood (see Figure 5.17

on left). For this application these features were first flattened (Figure 5.17 on right). These nuts were selected because they present a large tab that can be used to glue them to the components. This approach implies that care must be taken when tightening the screws, as too much torsion moment might cause the adhesive failure.



Figure 5.17 - T-Nut fasteners used to attach the necessary steel components to the composite parts

The production of the two composite shell parts is, therefore, distinct. The part to which the ribs were firstly attached required:

1. drilling the holes for the load bearing component;
2. preparing the surfaces for joining, adhesive application for nuts and curing;
3. producing the template for rib placement;
4. preparing the surfaces for joining and adhesive application for the ribs and curing;
5. preparing the surfaces for joining and adhesive application for assembling of the shell components and curing;
6. preparing the surfaces for joining and adhesive application for the load bearing component and curing;
7. drilling holes for linking the part to the test equipment.

The other half U-shaped part without ribs did not require steps 3 and 4. Therefore, the above process will be described only for the part with ribs.

To drill the holes, the parts were placed in the U-shaped shell mould in a way that one the overlapping part would be facing up. Considering that the final composite assembly has a square section of 100 mm x 100 mm, both parts are kept pressed against the mould to ensure the accuracy of that dimension. One big

advantage of using a square section is the possibility given by employing the infusion mould as a template in some steps of the process. Once the positioning was assured, the hole placement was determined by two redundant mechanisms: first the hole locations were determined by measuring and checked by placing the load bearing component on top of the surface. After, the holes were drilled in order to allow fitting the M4 T-nuts with small adjustments.

Then, the composite part was removed from the mould, both nuts and composite components surfaces were sanded and cleaned with alcohol, the adhesive applied and, finally, the nuts were introduced and pressed against the adhesive. Small spacers cut from Medium Density Fibreboard (MDF) were used to have screws attached to the nuts and ensure pressure was being applied. All of the surfaces that did not receive adhesive were covered with release agent (such as, the screws for example), tape or both. After curing, screws and spacers were removed and the nuts held in place. A verification was performed to ensure it was possible to mount the load bearing element.

The template for rib placement used the U shaped shell mould as a basis structure, in which few laser cut MDF elements were mounted to precisely place the ribs at the desired locations. Figure 5.18 shows these MDF elements mounted in mould. Two lateral MDF elements were screwed to the mould using its end as a reference and the grooves they present allowed to place perpendicularly other elements that indicate the axial position of the ribs. The top of these perpendicular elements was below the top of the ribs to ensure a load could be applied during the first stage of curing (the first 24 hours that the adhesive takes to set).

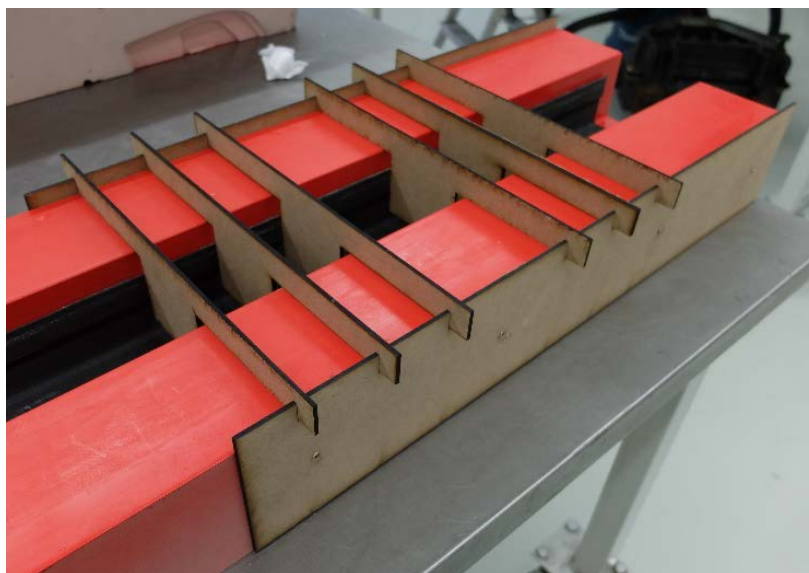


Figure 5.18 - MDF elements used to locate the position of ribs in the U-shaped shell mould

To ensure the desired thickness of the adhesive layer, small squares of a laminate, with approximately 5 mm × 5 mm and the desired thickness of 0.8 mm, were bonded to the components' tabs by using a cyanoacrylate glue (see Figure 5.19). The small dimensions ensure that the presence of these elements does not compromise the behaviour of the joint and allow obtaining a uniform thickness in the adhesive layer. Finally, the surfaces received the usual sanding treatment followed by cleaning with alcohol prior to the submission to adhesive application.



Figure 5.19 - Small laminate squares used to control the adhesive layer thickness

The following step was joining the two exterior shells and close the beam. This step is critical as a weak gluing accuracy will always result in deviations from the external dimensions and, consequently, in different inertial moments of the parts. The mould was once again used as a joining template and the adhesive applied to the tabs that were previously submitted to the sanding and alcohol cleaning surface treatment. In order to not contaminate the faces with glue, they were covered with masking tape. Dimensional control was performed with a calliper at several points. A distributed load was applied on the top side and spacers were inserted in locations where ribs were not present. These spacers ensure both the dimensions to be kept and the load to be transmitted to the lower joint. This load was kept for the initial stage of the cure (the first 24 hours).

After all composite components form the one final composite part through the process of adhesion, the steel load bearing component was attached. This component is attached to the rest both by bonding and with screws. As usual, the first stage was to make the surface preparation, i. e. sanding and cleaning with alcohol.

Figure 5.20 shows a detail of the sanded and cleaned area and allows also seeing the nuts with its tabs already glued to the inside.



Figure 5.20 - Treated area of final composite shell area used to attach the steel bearing component

The area was then contoured with tape and the adhesive applied. The screws were then mounted to provide the necessary pressure during the curing stage.

The last stage of part production was drilling the holes to link it to the testing equipment. As M10 steel screws were used in this attachment, a drill with adequate dimensions was used to perform the necessary holes in places previously and accurately located on the part.

5.1.2.4 Thickness verification

In order to verify the thickness of the manufactured parts, one of the external shells and 2 of the ribs were subjected to NDT ultrasound inspection (the parts were randomly selected and represent 25% of the production of each component). Each face of the external shell part was evaluated in 7 points (total of 21 points) with 3 measurements at each point. The ribs were inspected at 5 points each. Ultrasound technology was selected since it is commonly used for composite structure inspection and is capable of measuring the thickness on locals that are unable to be evaluated with a calliper. Figure 5.21 shows the points marked on composite parts targeted for thickness measuring by ultrasounds.

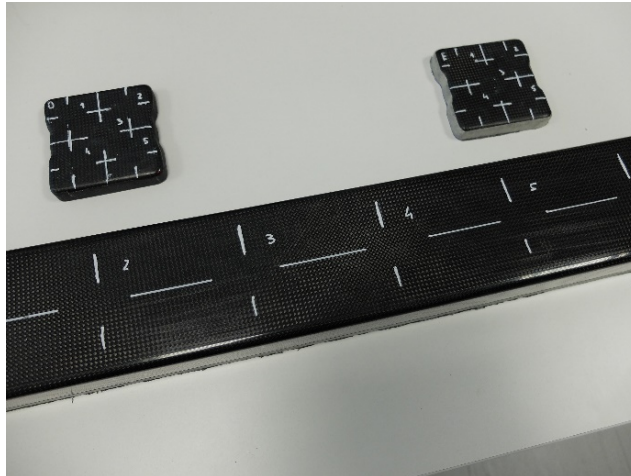


Figure 5.21 - Places to measure thicknesses marked on parts submitted to ultrasound inspection

The probe used was a circular Single Element Transducer, meaning it measures the thickness at one point and not in an area. In order to have proper coupling between the probe and the part a coupling gel was deposited on the part.

Calibration of the ultrasound system was performed adjusting the speed at which the sound propagates in the material, L_w . This essentially transforms the time the probe takes to have return of the eco into distance. The calibration was done by using several layup thicknesses obtained from the parts trimming stage of production and after validated was by comparing, at the same location, the measurements made with a calliper and the ultrasound probe. Figure 5.22 1) and 2) shows the calliper measuring the external shell part and the same location evaluated with the ultrasound probe, respectively. On the ultrasound equipment, the value to consider is displayed at Gate 1 (G1) and, as can be seen, it only differs 0.01 mm from the value measured with a calliper.



Figure 5.22 - Measuring the thickness of external shell composite part: 1) with a calliper; 2) with the ultrasound probe

The average thickness measured on the external shell component was $1.807 \text{ mm} \pm 0.044 \text{ mm}$ and for the ribs the average thickness was $1.914 \text{ mm} \pm 0.042 \text{ mm}$. These thicknesses were in accordance to the expected values and so to the desired fibre/resin ratio. The value also ensures enough room for the adhesive layer to have the desired thickness.

5.1.2.5 *Adhesive inspection*

As mentioned in the section dedicated to the production of the CFRP model (Section 4.5.2), a relevant aspect was to ensure that the adhesive layer had uniform thickness. A localized thickness decrease can lead to the joint failure. Thus, before fully testing the prototype, ultrasonic NDT took place to verify the quality of the joining process, as shown in Figure 5.23.

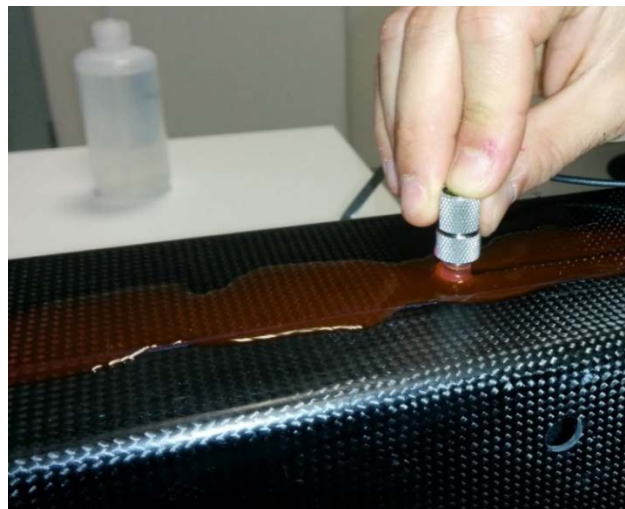


Figure 5.23 - Ultrasonic NDT tests made to verify the quality of parts joining

This process allowed to evaluate the adhesive layer, as the interface between the adherent and the adhesive produces an echo that is detected by the probe. A limitation of the used process was the fact that the probe calibration was performed on the laminate and not on the adhesive. In the probable event of the laminate and the adhesive having different L_w , the measurement performed will not be as accurate as possible regarding layers beyond the adhesive layer. Even though, this process is able to detect variations in the adhesive layer thickness and also voids.

Figure 5.24 shows how the information collected from the ultrasound probe is displayed. On the horizontal axis time is presented. The definition of L_w makes this correspond to distance. Considering distance, the edge of the probe is presented on the left and the corresponding distance is, therefore, 0. On the right extremity the distance is the maximum considered (in this case 6 mm). The vertical axis presents the echo collected by the probe. When an interface between distinct materials is reached part of the sound is reflected and this is signalled as a peak. Three gates were defined. The lengths of these gates are defined to encompass the range of locations where the interfaces can be located. The y coordinate of the gates is related to the intensity of the expected echo. If a peak appears with its maximum value above the gate and within the distances admitted a value is attributed at the header.

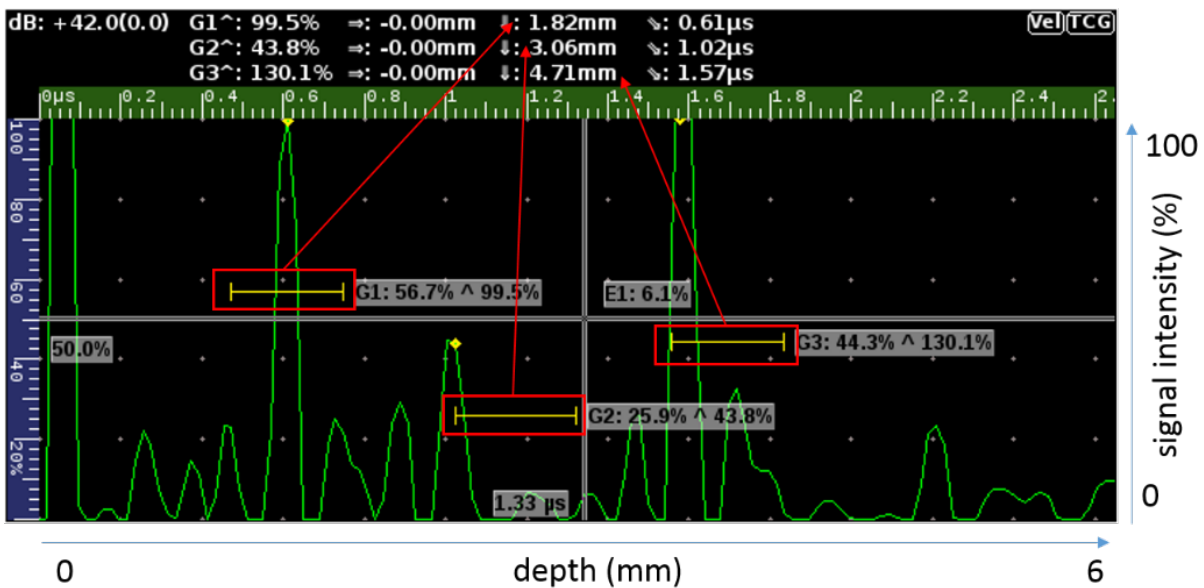


Figure 5.24 - Display of ultrasonic probe data

In the case shown in Figure 4.52 it is possible to identify three interfaces. The first interface is between the first laminate and the adhesive and occurs at 1.82 mm, which is coherent with the thickness measurements previously executed. The second interface is between the adhesive and the second laminate. Thus, to obtain the value of the adhesive the value of the first interface has to be subtracted to 3.06 mm and that indicates an adhesive thickness of 1.24 mm, which is a value well above the expected one. In the same way, the thickness of the laminate would be 1.65 mm.

Although the above measures are not coincident with the ones expected, these values are acceptable since no adjustment for the adhesive's L_w was performed. Therefore, it should be concluded that the absolute values determined this way are not completely reliable.

However, other relevant outputs can be obtained from the same data. This may be explained by results obtained as a function of time shown in Figure 5.25.

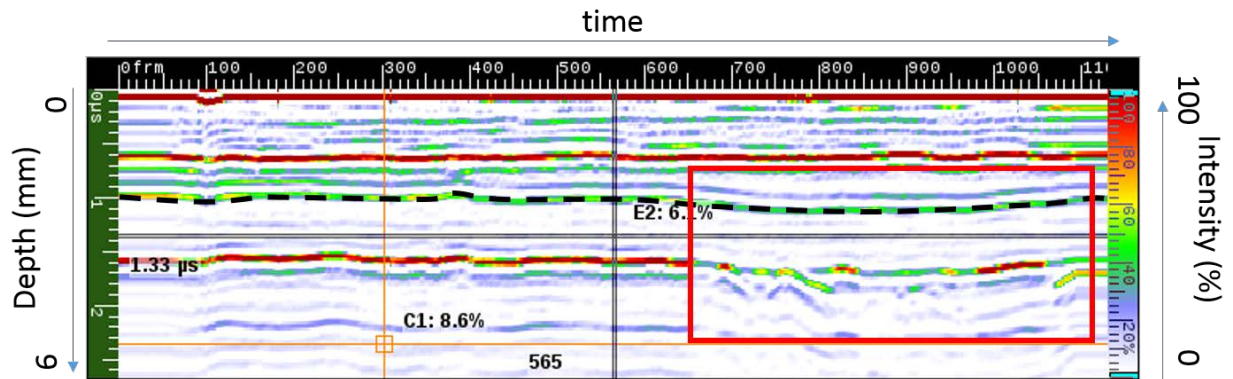


Figure 5.25 - Ultrasonic probe data obtained as function of time

The data plot shown in Figure 5.25 represents the echo intensities as a function of time in a colour scale, in which red corresponds to the maximum intensity. By following a straight line at a constant speed along the part it is possible to visualize the part cross section. Because the process is quite manual and the surface had small imperfections some small deviations can be seen, but nevertheless it is possible to observe the different layers in the part. The first red line, at the top and very near the time scale, is the outer surface of the part. There are punctual variations but overall the distance is constant. The second most noticeable line is the other surface of the laminate that is almost straight too. The third line, which requires highlighting to be noticeable, is under the dashed black line. It is coherent with the value obtained in Gate 2 in Figure 5.24, meaning the interface between the adhesive and the inner profile. The fourth line is quite visible but presents some discontinuities. This doesn't mean the adhesive layer is absent, as this would result in an inexistent line. Instead this might be the result of a slight tilting of the probe. As mentioned this is a manual process that is quite sensible to inevitable variations. Still it can be concluded that the observed joint is viable and functional. This was the overall result obtained for most of the joints.

The exception was the joint on the back of the ribbed part (the face opposite to the load bearing element).

Figure 5.26 shows the result of the ultrasound NDT performed to this joint.

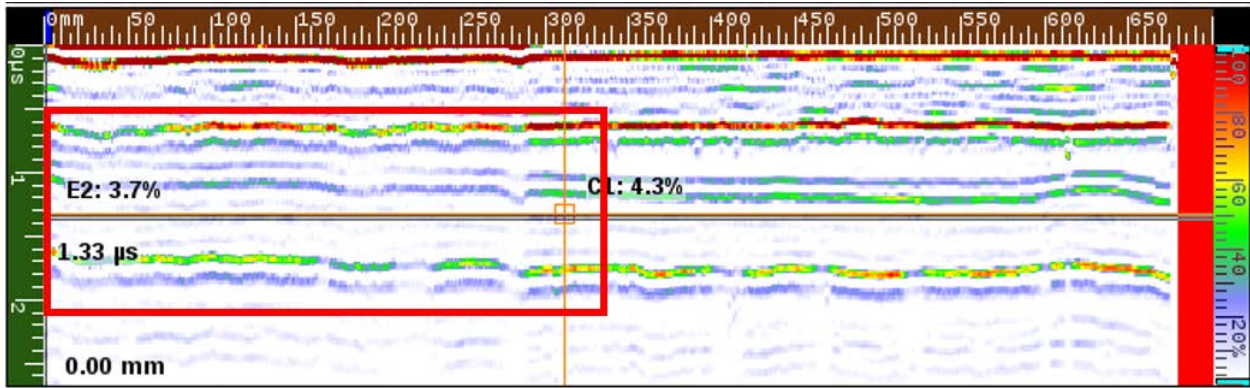


Figure 5.26 - Results obtained from ultrasound tests made on the joint at the back of ribbed part

Highlighted in red is an area where the adhesive was missing. This was obviously an error detected in the production process that could lead to a joint failure and subsequent impossibility of extracting relevant results from the experimental tests. The solution was to inject the same resin as the one used for the infusion process in the gap which was visible from outside. This somewhat cumbersome process allowed filling the detected gap with a resin in order to minimize the consequences of a production error. After the cure of the resin was completed the scan was repeated and results obtained are presented in Figure 5.27.

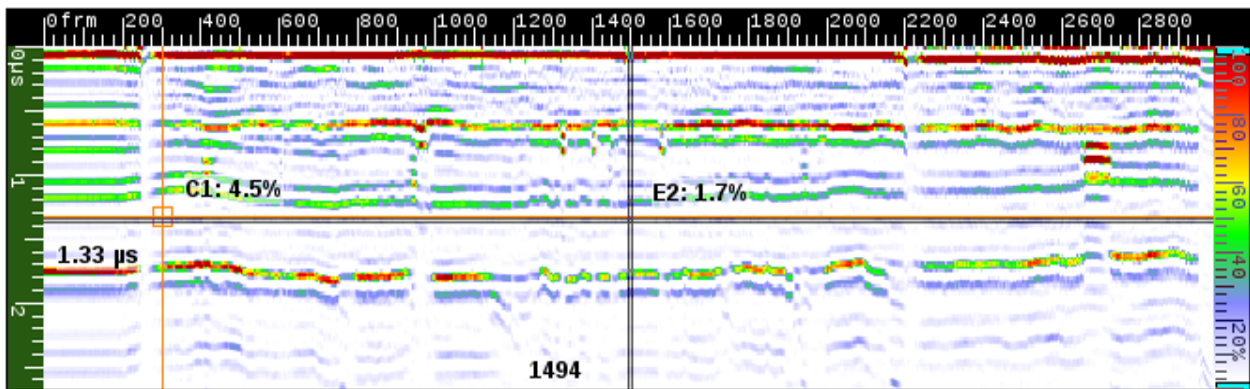


Figure 5.27 - Results obtained from ultrasound tests made after joint repairing

An improvement of the joint is clearly visible, although some imperfections are still present. The repairing resin surely has an inferior behaviour when submitted to shear forces (compared to the adhesive) but due to the small gap created, injecting a thick fluid such as the selected adhesive would render very limited results.

5.1.3 Mechanical testing of the gantry prototypes

The previously built composite gantry prototypes were mounted in structural testing apparatus existing in Pole for Innovation in Polymer Engineering (PIEP) to be tested by applying a static load. Two types of prototypes were produced and submitted to the defined tests: the first one without ribs and a second one reinforced with the internal ribs.

The loading (see Figure 4.56) consisted of an off-centred distributed load perpendicular to its longitudinal axis at the midpoint lengthwise. The load of 5 kN was applied on the 50 mm x 50 mm area shown in red in Figure 5.28, one metallic L-shaped loadbearing component that, as previously described (see Section 4.5.2.3), was glued to the face of the part and screwed with 4 M4 screws.

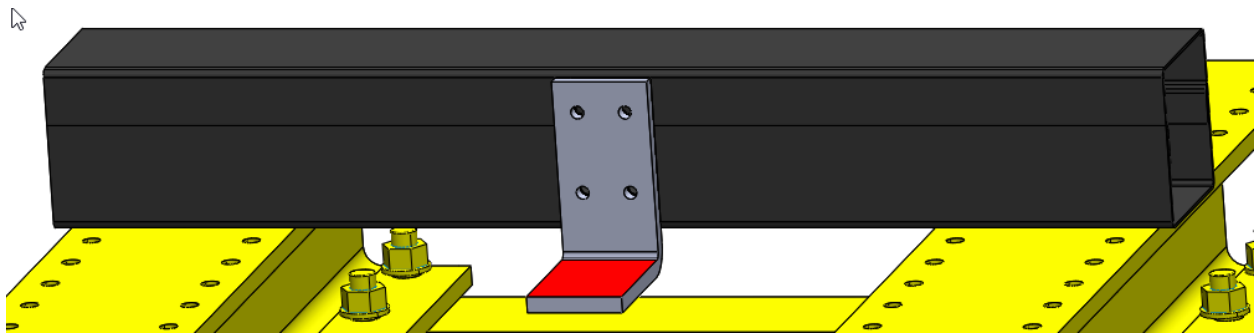


Figure 5.28 - Composite prototype gantry mounted in the testing structure and the L-shaped steel component where the load was applied (red area)

The testing was performed having the prototype gantry supported by two I section steel beams where the part was attached by 4 M10 screws on each fixation surface. The loading scenario used in the testing will result in submitting the composite part to bending and torsion loads, equivalent to the real gantry service conditions.

The load was applied using a hydraulic actuator having maximum capacity of 20 kN.

The experimental apparatus is schematically shown in Figure 5.29, in which the supporting structure and the actuator are highlight in yellow and blue, respectively.

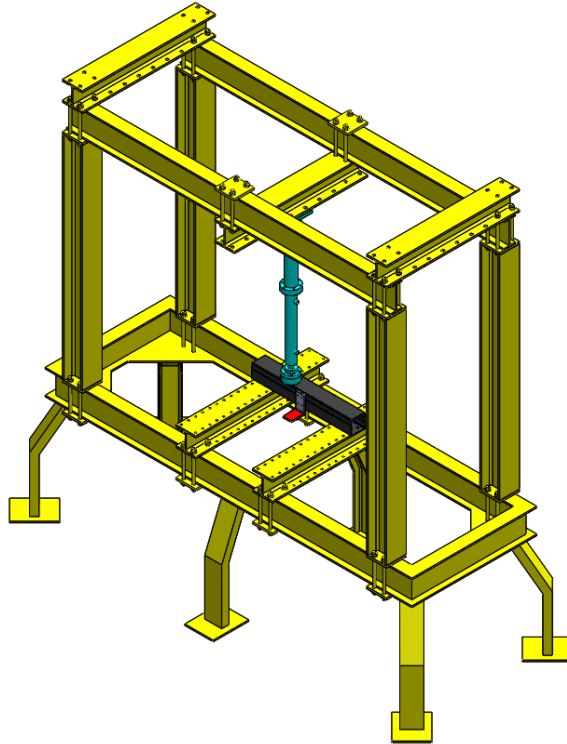


Figure 5.29 - Composite prototype gantry mounted in the experimental testing apparatus

Figure 5.30 presents photos that allow seeing the experimental set-up in more detail. To ensure the good load distribution a pultruded composite plate was used to compress the part's inferior wall against the I-shaped steel beams (detail 1 in Figure 5.30). The load transmission element selected (detail 2 in Figure 5.30) applied the load to the abovementioned area and ensures that, during loading, this surface remains constant (at least for the small displacement verified) as well as the load direction. Detail 3 of Figure 5.30, shows the location of the planar rectangular rosette strain gage used to measure the local strain. Three Linear Variable Differential Transformers (LVDTs) were used to measure displacement at three different points considered critical and possible to reach despite the constraints imposed by the experimental set-up. LVDT, designated by "a" in Figure 5.30, was located in the part's surface opposed to the loading location. Another LVDT, designate by "b", was at a distance of 150 mm from LVDT "a". Finally, a LVDT "c" was located touching the lower surface on the same plane perpendicular to the axis of the gantry as LVDT "a". These sensors monitor the linear displacements of the part at the points they are in contact with.

The 5 kN load was applied at the constant vertical speed of 1.5 mm/min. Values of the actuator's displacement and force were recorded and all the three LVDTs displacements and the strains captured by the rosette.

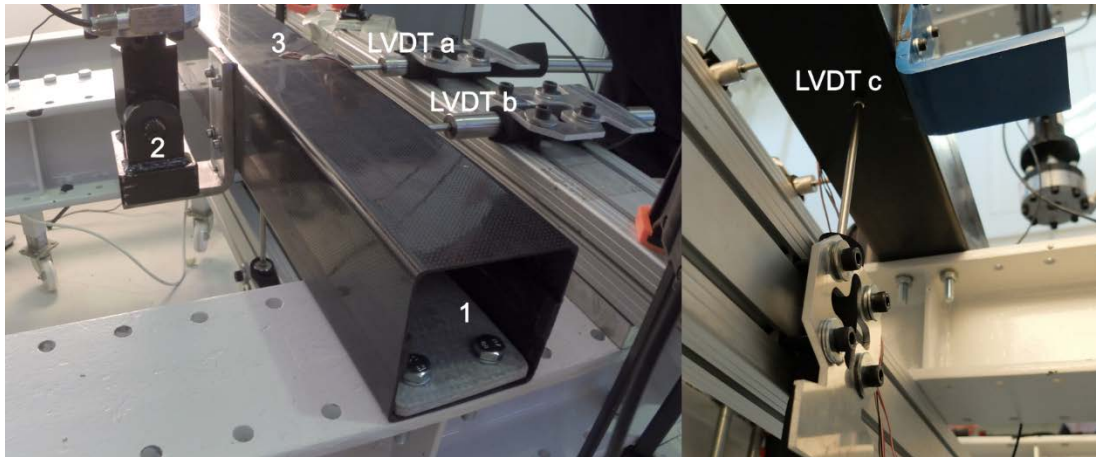


Figure 5.30 - Detailed views experimental testing set-up

The tests were initiated with the load transmission element barely touching the load bearing element. There was a visual control of the whole apparatus and safety measures were included to minimize the possibility of damages occurring to the test equipment or people observing the tests. These comprised adequate individual protection equipment and establishment of thresholds for both force and displacement of the actuator.

Both produced composite prototype gantries were tested. The one without ribs was first used to verify the testing equipment and validate the approach. Because it would suffer higher deformations and higher rotation of the load bearing element than that one reinforced with ribs, it also allowed to prove that a good coupling between the load transmission element and the load bearing element was achieved.

5.1.4 Numerical Simulation of the mechanical behaviour of the composite prototype gantry

Numerical simulations were performed using Abaqus/CAE 6.11-1 in order to predict the mechanical behaviour of the produced composite prototype gantries during testing. The geometry depicts the one of the two composite prototypes produced and the same number of composite components was also considered. The composite components were modelled as shell elements. The I section beams and the actuator were modelled as rigid elements, meaning they will do not suffer deformations. Figure 5.31 shows the overall assembly considered in the numerical calculations.

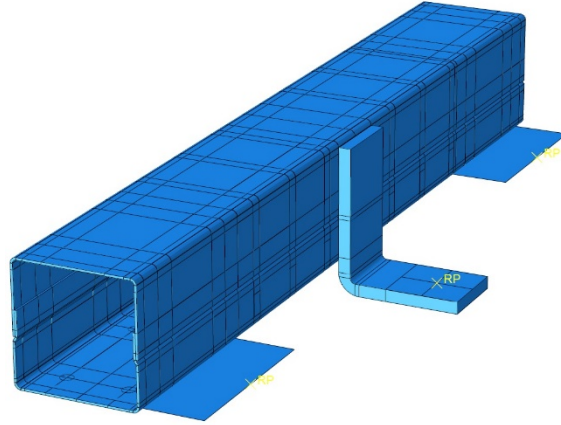


Figure 5.31 - Some of prototype gantry main components considered in the numerical model

5.1.4.1 Mechanical Properties

The mechanical properties attributed to the composite components were the ones determined experimentally and the remaining shell elements were considered rigid. The load bearing element was also modelled as a 3D element (meaning its thickness was also considered in its geometry).

Because the steel was not tested the mechanical properties used were the typical ones of a carbon steel. i.e. a Young Modulus of 212 GPa and a Poisson ' s ratio of 0.3.

An important consideration on the basis of the model development was the low level of stresses and strains that were expected to be developed in the components during testing. This implies that the materials would not reach their ultimate stress or strain and, in the case of the steel, it would not suffer any plastic deformation. Following this principle, only the elastic characteristics of materials were considered.

The tension state of the part was analysed according to a failure criterion for anisotropic materials, more specifically the Tsai-Hill Failure Criteria, which states that material failure occurs when the condition summarised in eq. 5.1 is verified

$$\frac{\sigma_1^2}{X^2} - \frac{\sigma_1\sigma_2}{X^2} + \frac{\sigma_2^2}{Y^2} + \frac{\tau_{12}^2}{S^2} \geq 1 \quad \text{eq. 5.2}$$

where σ_1 is the tensile stress in the fibre direction, σ_2 is the tensile stress in the direction transverse to fibres, τ_{12} is the in-plane shear stress, X is the ultimate strength of the ply in the fibre direction, Y is the ultimate

strength of the ply in the direction transverse to fibres, and S is the in-plane shear ultimate strength of the ply between the longitudinal and the transversal directions [215].

Tsai-Hill criterion predicts failure when the value calculated from eq. 5.2 in a laminate reaches 1

To model this criterion, additional properties were required to be input in Abaqus. These additional properties are, namely, the parameters for stress-based failure measures:

- Ultimate tensile stress in fibre direction
- Ultimate compressive stress in fibre direction
- Ultimate tensile stress in direction transverse to fibres
- Ultimate compressive stress in direction transverse to fibres
- Shear strength in the X–Y plane, S . [202]

The first value was experimentally determined according to the procedure described in section 5.1.1.5. The following value (compressive stress), was considered to be the same. Because the part is produced from and plain weave fabric, the properties in the transverse direction are considered to be the same. The shear strength was estimated according to the von Mises theory, according to which:

$$\tau_{xy} = \frac{S_y}{\sqrt{3}} \quad \text{eq. 5.3}$$

where τ_{xy} is the shear strength and S_y is the yield strength.

5.1.4.2 *Layup*

The orientation and thickness of each layer may be seen with higher detail in Figure 5.32. The thickness of each layer was considered to be 0.2 mm (which will result in an approximate thickness of 1.8 mm). The model was created according to the one described in Table 5.2.

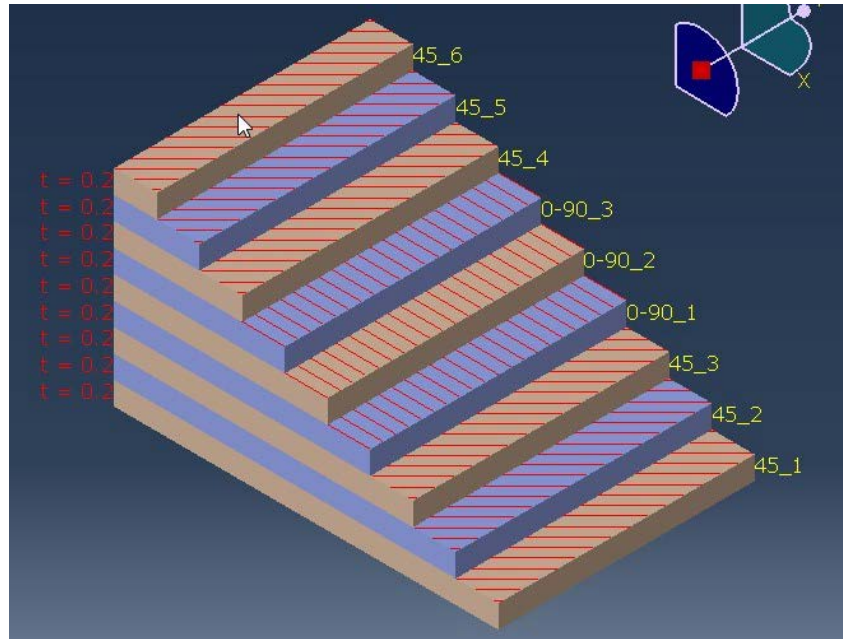


Figure 5.32 - Orientation and thickness of the layers in the composite lay-up.

5.1.4.3 Load

In this context, loading was a force applied to the centre of a rigid surface that represents the actuator. This results on a distributed load that is transmitted to the load bearing element. Such load, as happen in the experimental set-up, is applied along the same axis throughout the 5 kN loading. Figure 5.33 shows the load bearing element considered in the numerical model with the surface fixed to the rigid coupled surface.

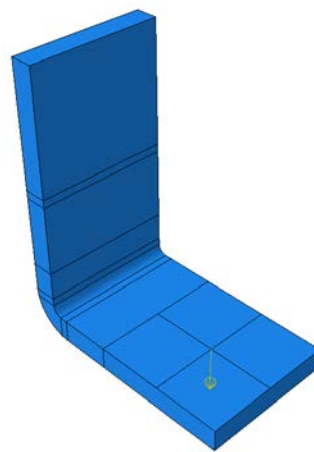


Figure 5.33 - Load bearing element used in the numerical model

The simulation was defined to retrieve results for, at least 100 increments, meaning that the load values present are spaced by 50 N. When problems of convergence occurred smaller increments were used, which implied lower variations in the load.

5.1.4.4 *Interaction Between the Parts*

The interactions between different parts were modelled using a tie constraint. This means that no separation is allowed between them. Underlying to the use of this formulation is the assumption that the adhesive will be able to withstand the loads it is subjected to. The shear stress was then evaluated in the outer layers of the areas bound by the adhesive. If the values of shear became near the ones determined experimentally for maximum adhesive shear, then a more detailed model of the adhesives behaviour would be required and implemented. A tie connection was also established between the parts and the sectional beams. Because these parts were considered totally fixed (neither translation nor rotation are allowed) this will also be reflected on the part that is overlaying the beams that will also be considered fully fixed. Nonetheless, surrounding areas were able to slide over the rigid supports (which represent the I-shaped beams from the experimental set-up), as they may become in contact while deformation. The actuator is also considered to be tied to the load bearing element. Figure 5.34 displays the tie links in the numeric model between the part and ribs (the ties are represented by yellow circles).

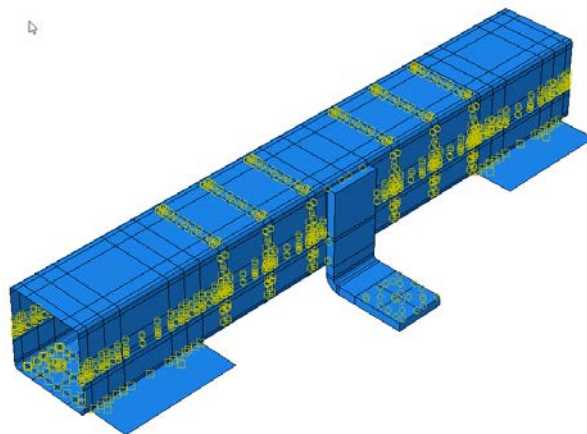


Figure 5.34 - Tie links between the part and ribs shown in yellow

5.1.5 Discretization

The lines presented in represented in Figure 5.34 are a result of partitions performed on the part to improve the discretization process (or mesh generation), which represents a critical step of the implementation of the Finite Elements method. The establishment of partitions creates lines along which nodes will be mandatorily created during the mesh generation. This procedure was used due to the following main reasons:

- definition of a mandatory node location (a node is always created on a vertex)
- properties attribution or interaction definition (properties or interactions can be defined regarding a smaller region)
- better performance of meshing algorithms (the division of a complex part into less intricate geometrical subsets leads to a better and more controllable performance from the meshing algorithms).

The two latest above mentioned facts were the main reasons (definition of interactions and obtaining a more regular configuration of the mesh elements) why partitions were introduced in the model described.

Abaqus encodes with different colours areas using dissimilar algorithms to generate the mesh. The partition was performed aiming to achieve the possibility of creating a structured mesh, which is colour coded in green. Meshes created this way are mainly composed by quad elements, having low deformation and size variations (unless explicitly required). The partition approach resulted in an all structured mesh presented in Figure 5.35.

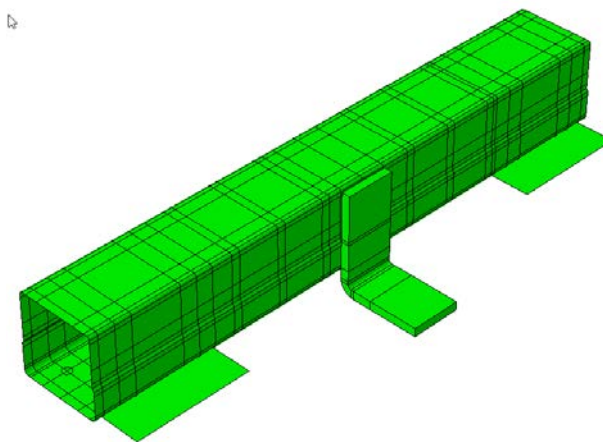


Figure 5.35 - Abaqus green code for the partition used in the model developed in the present work

Another important parameter for a good discretization outcome is the selection of an adequate element size. Different element sizes were tested and one relevant variable was selected to be plotted for each model as a function of the total number of elements. Figure 5.36 shows the result obtained by selecting the vertical displacement, y , as relevant variable.

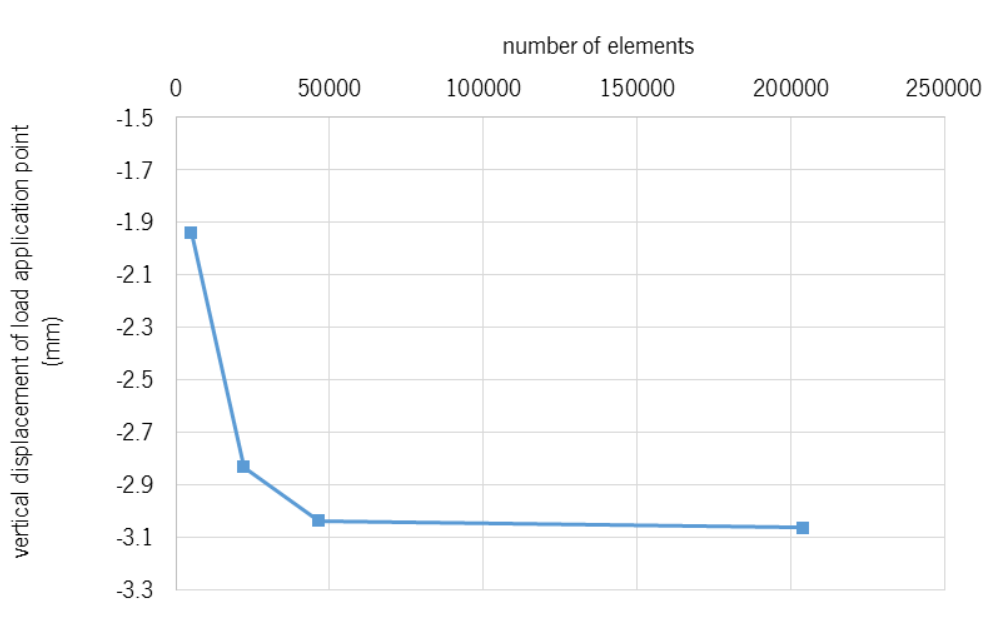


Figure 5.36 - Vertical displacement, y , plotted as function of number of elements for each model

The vertical displacement of the load application point, y , has been chosen as relevant output because it was a straight forward variable to be obtained and highly influenced by the rigidity of the whole system. As it can be seen in Figure 5.36, the component rigidity decreased when the number of elements increased (and their size decreased). A mesh with roughly five thousand elements results in an extremely rigid system. Increasing the number of elements to about twenty-one thousand elements has a great impact and the next step also makes the result slightly different (and the system less stiff). This third step presents a mesh of about forty-six thousand elements. Elevating the number of elements to just above two-hundred thousand elements begins to have no major impact since an increase of 341% of the number of elements results in a variation of only 0.86% in the observed variable. Thus, a mesh with forty-six thousand elements (corresponding to an average element size of 3 mm) was considered to be an acceptable trade-off between result accuracy and computational resources requirements. Figure 5.37 shows the overview of the mesh that was generated with such parameters.

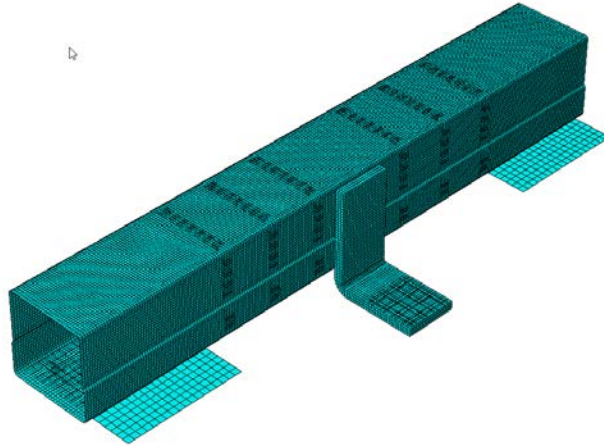


Figure 5.37 - Mesh generated in prototype gantry by using forty six thousand elements

Chapter 6: Results and Discussion

Summary

After the description of the main steps to optimize the ILCM composite gantry and validation of the numeric models in which its dimensioning was based upon, the obtained results are presented and discussed in the present Chapter. Because the dimensioning and validation comprised several steps, there was the need to go through all of them and discuss the results obtained that sustained all the process. The initial section discusses the behaviour of the system under two loading cases identified as the most critical ones, and highlights the most demanding one (that will be further considered). The next two sections aim an initial dimensioning of a CFRP gantry able to replace the present one made from steel. The results of the implemented optimization routine are presented in section 6.4, including the initial results and the improvements obtained from the adjustment of the objective function. Finally, section 6.5 is dedicated to the experimental work and comparing the FEA performed simulations against results obtained from the tests made on the produced prototypes.

6.1 IDENTIFICATION OF THE MOST CRITICAL LOADING SCENARIO

Two scenarios were considered as potentially critical, as it was mentioned in Section 4.2. It was necessary to identify the configuration most likely to lead to a loss of accuracy due to the gantry deformation. The study performed accounted for the part's deformation, as well as its impact in the optical path. The goal was to understand which, regardless of the gantry's section, was the most critical loading scenario. By combining the reflection equations with the ones describing the deformations suffered by the gantry, it was possible to assess the behaviour of the optical system through an analytic method. This way, the gantry's deformations

were transformed in translations and rotations of the optical elements (mirrors) and the incidence point of the laser for comparison to the one that would occur if no accelerations (or deformations) were imposed to the gantry.

A high number of simulations were ran for each loading scenario (about 120 000 possible configurations were considered), and that generated a difficulty in the analysis of the data. For example, two configurations with very similar EI_z flexural stiffness can originate errors that are very distinct and might lead to difficult interpretation plots (Figure 6.1).

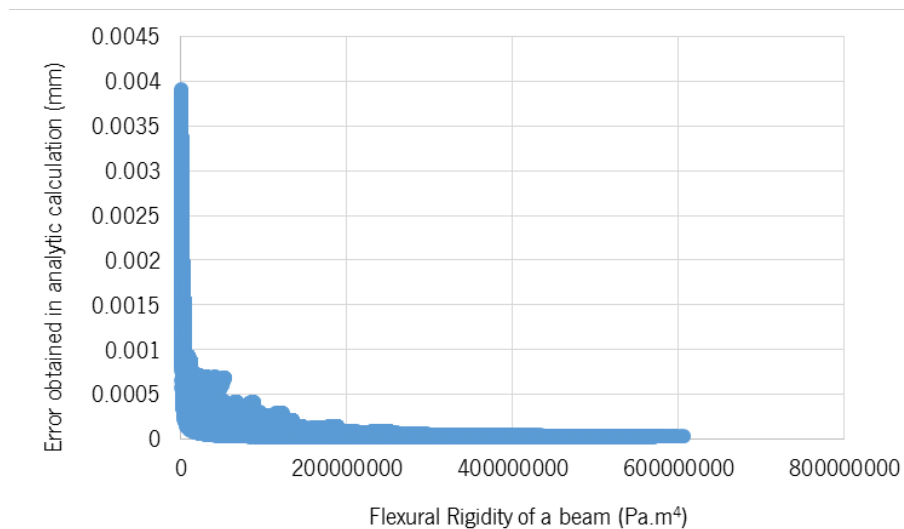


Figure 6.1 – Plot of the error as a function of the EI_z for loading scenario 2

To enable some conclusions, a limited number of data points capable of describing the variation of lowest error obtained for a given flexural rigidity where selected (Figure 6.2). With these points it is possible to represent the best results for the range of EI or GJ analysed.

The density of values is higher closer to the axis interception, since the remaining areas are easier to characterise.

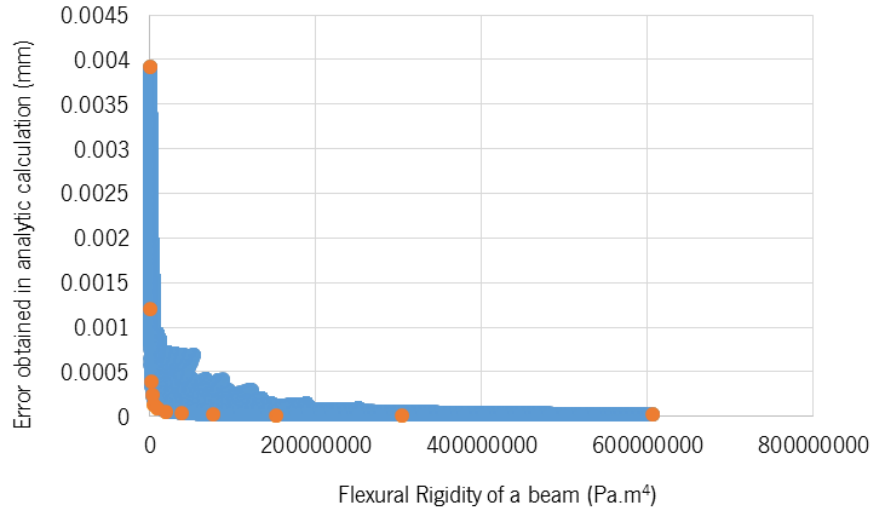


Figure 6.2 – Relevant points considered for system behaviour assessment

This comparison can then be established between the behaviours of gantries with the same configuration regarding the position of the laser head. Figure 6.3 shows that regarding the flexural stiffness EI_z .

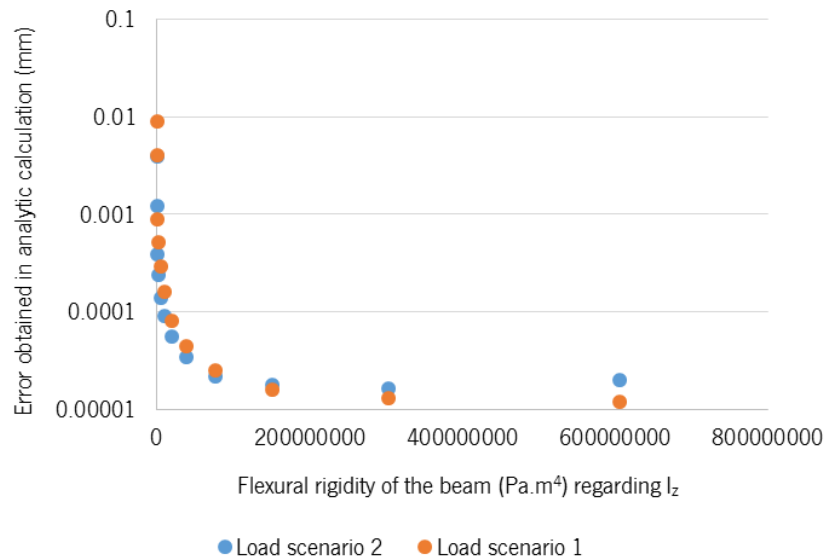


Figure 6.3 – Comparison between the errors produced by gantries with the same EI_z depending on the loading case.

The same was performed regarding the EI_y flexural stiffness as Figure 6.4 shows.

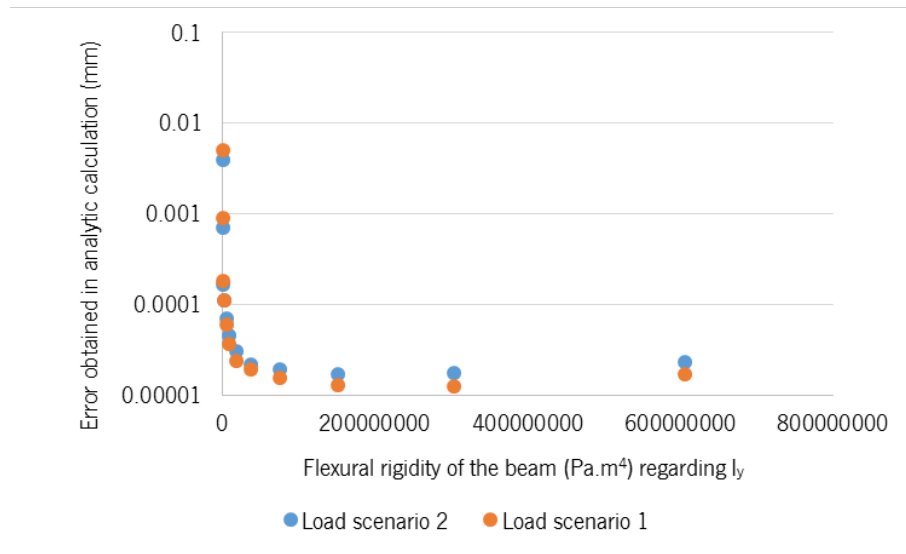


Figure 6.4 - Comparison between the errors produced by gantries with the same EI_y depending on the loading case.

Regarding torsion, Figure 6.5 also shows the influence of the laser head location in the error when different torsional rigidities were analysed.

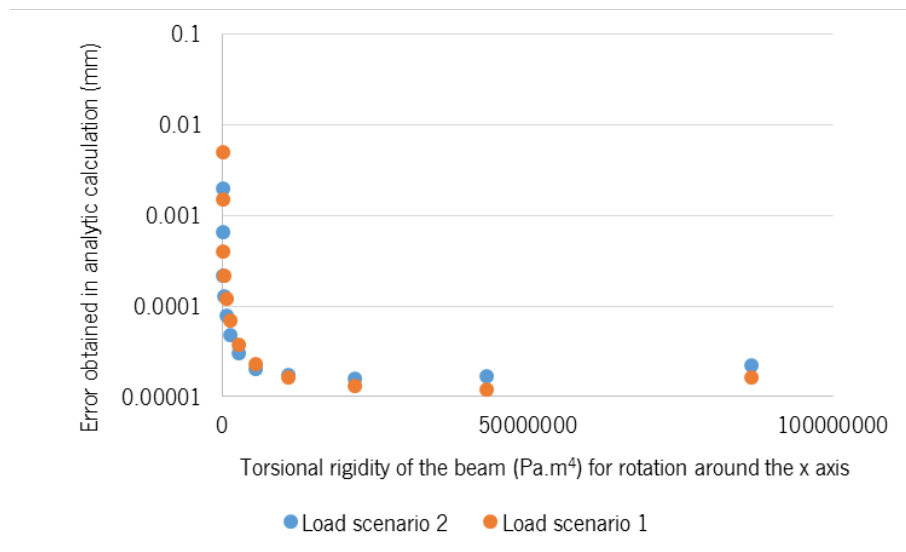


Figure 6.5 - Comparison between the errors produced by gantries with the same GJ_z depending on the loading case.

The data may also be expressed in terms of the ratio between the errors for the loading case 1 over case 2, regarding the same beam configuration, as there are shown in Figure 6.6, Figure 6.7, and Figure 6.8.

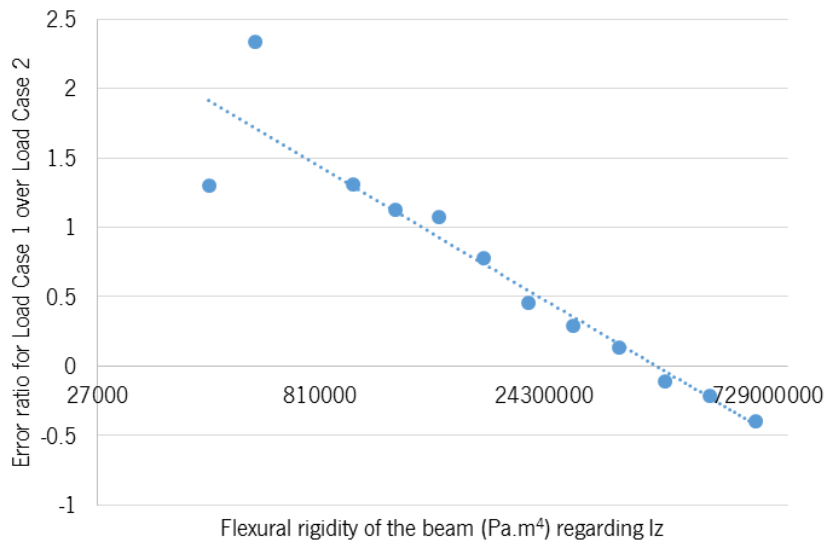


Figure 6.6 – Ratio of the error produced by gantries with the same EI_z for load case 1 relatively to load case 2.

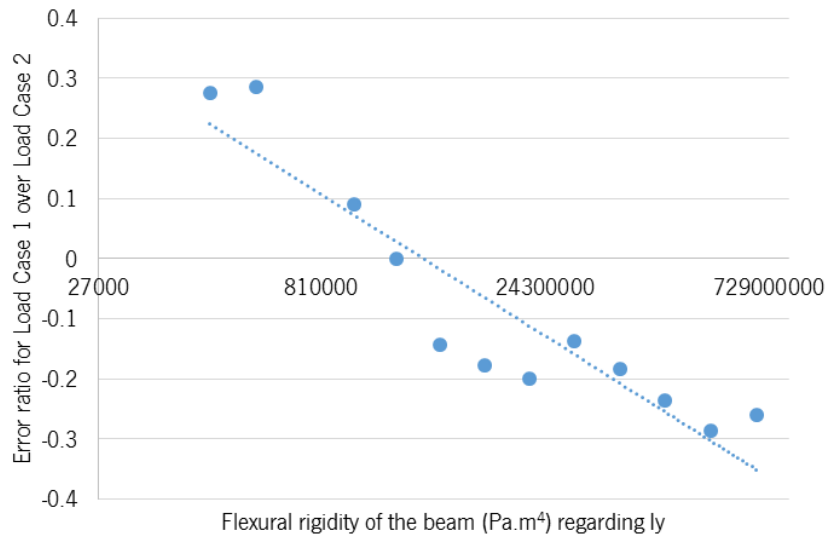


Figure 6.7 - Ratio of the error produced by gantries with the same EI_y for load case 1 relatively to load case 2.

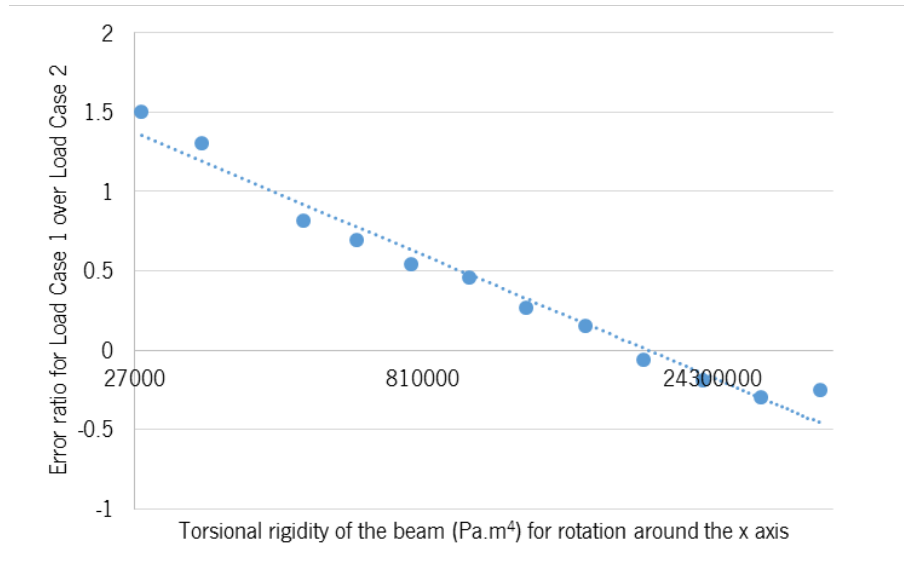


Figure 6.8 - Ratio of the error produced by gantries with the same GJ for load case 1 relatively to load case 2.

From the analysis of the error ratio, one can clearly conclude that for gantries under the same acceleration and with equivalent flexural or torsional rigidity, the error frequently was quite higher for loading case 1 when the system has the laser head centred. This was true in the versions with lighter configurations, below extremely stiff configurations, which is, expectedly, the type of solution that will result from this work. Regarding the flexural stiffness, EI , the tipping point for switching which of the scenarios is most demanding happens earlier, but difference is much lower in percentage, meaning that the two scenarios are very identical, especially in the cases offering lower resistance to deformation. Considering these results, the decision was to proceed with the dimensioning process based on Load Case 1, since a configuration able to provide enough accuracy in this scenario will also perform in a satisfactory manner under Load Case 2.

6.2 NUMERICAL ANALYSIS OF THE METALLIC GANTRY

The purpose of the analysis was to estimate the torsional and flexural rigidity of the currently used metallic gantry. This will enable the initial dimensioning of the composite gantry capable of presenting similar mechanical behaviour, even without taking into account the specific loads the gantry is subjected to under working conditions.

A study of mesh independence of the results was performed for the loading scenario on which the gantry suffered bending by considering the value of the vertical displacement of the edge to which the load is applied. The results obtained are displayed in Figure 6.9. As stated in section 4.3.1, instead of a realistic loading scenario, the metallic gantry was initially analysed as a cantilevered beam, having one edge totally fixed and a load or moment applied on the other extremity. Loads were applied individually, along the y and z direction and Torsional Moments around the y axis.

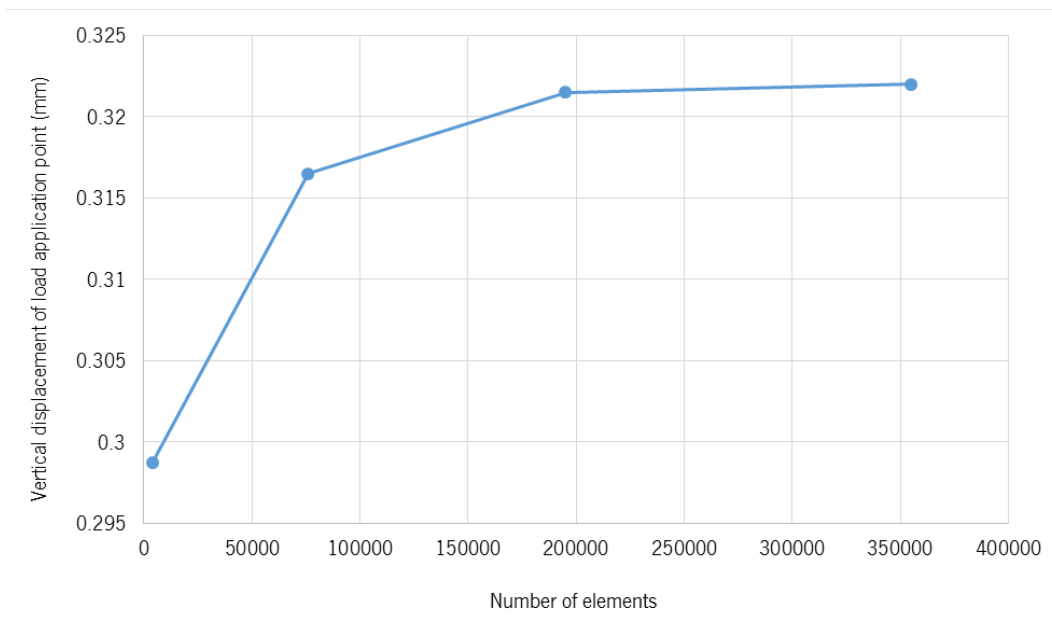


Figure 6.9 - Mesh independence of the results for the bending loading scenario.

It is possible to conclude that the mesh that presents roughly 196 thousand elements was able to return results from the simulation not greatly different from those obtained with a much finer mesh, even using significantly less computation time.

With this result it was possible to determine the deflections in z and y and the rotation in x suffered by the gantry. Figure 6.10 displays the deflection determined in the y axis.

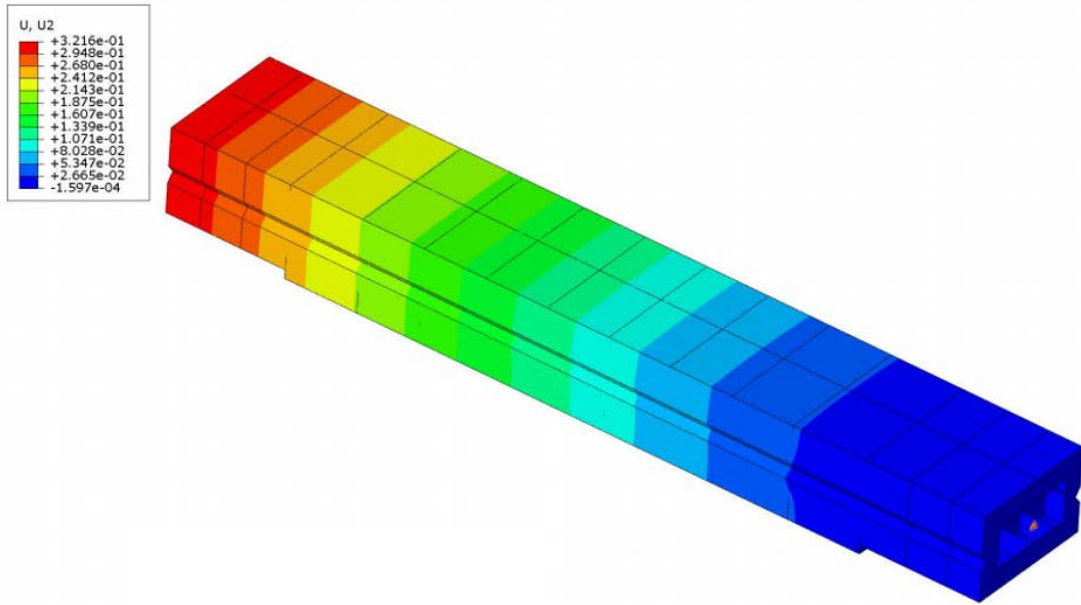


Figure 6.10 - Deflection suffered on the y axis

The maximum deflections, presented at the free edge, suffered when the gantry was considered to be a cantilevered beam are presented in Table 6.1.

Table 6.1 – Maximum deflections and rotations suffered by the metallic gantry as a cantilevered beam

Deformation	Value resulting from simulation
Deflection in y	0,32 mm
Deflection in z	0,62 mm
Rotation in x	0,02 rad

As it is possible to get from results obtained, the gantry is much stiffer in the y direction because it was subjected to higher accelerations along this axis (one fact also presented on its external configuration, where a larger section was used in the y direction).

6.3 SECTION ESTIMATION OF AN EQUIVALENT COMPOSITE GANTRY

After having a better understanding the mechanical behaviour of the current part, the next step was establishing a configuration that presents a similar behaviour for the new composite part. This was performed resorting to analytical calculations performed on a spreadsheet, as described in section 4.3.2

For both stages of the thickness determination, two materials were considered and compared: Glass Fibre with Epoxy Resin (60% Fibre Volume) and Carbon Fibre with Epoxy Resin (also 60% Fibre Volume). The final results of these calculations are presented in Table 6.2.

Table 6.2 - Minimum layer thicknesses that ensure enough rigidity for both Carbon Fibre and Glass Fibre. Weight for the design gantry is also displayed

Layer Denomination	Carbon Fibre	Glass Fibre
$L_{uni,xy}$	7.4 mm	24.2 mm
$L_{\pm 45,xy}$	11.8 mm	18.2 mm
$L_{uni,xz}$	3.3 mm	12.5 mm
$L_{\pm 45,xz}$	12.2 mm	18.4 mm
Weight	76.8 kg	210.2 kg

Due to the huge difference in terms of weight between the two solutions, the glass fibre solution was dropped. This decision was also based in production difficulties that arise from the required thicknesses, as well as the fact that the gantry would be much heavier than the current metallic solution (which presents a weight of roughly 100 kg). Carbon fibre proved to be an advantageous and viable alternative for producing a stiffer gantry with a lower mass. The values of thickness also provided an initial estimation for the composite gantry configuration.

6.3.1 Numerical analysis of composite gantry

Figure 6.11 shows the outcome of the numerical analysis of the metallic gantry for a movement along the y axis.

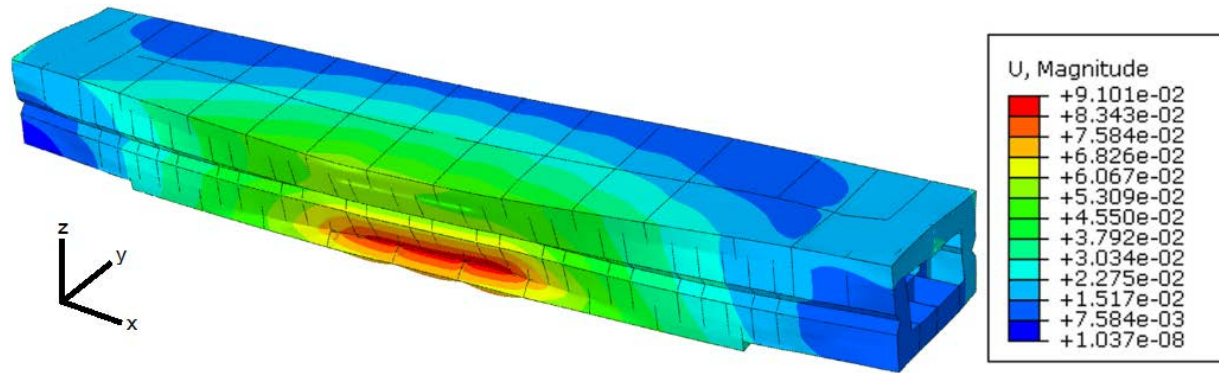


Figure 6.11 - Outcome of FEM simulation for the metallic gantry subjected to realistic loading conditions. The colour display the translational displacement magnitude. The deformation is magnified by 1400 times.

Loads were applied considered the values presented in Table 4.8, and emulate a movement along the y axis. Even considering the loads involved, the deformations suffered are quite small, which is as expected, since the gantry was designed and produced in order to ensure the stiffness and stability required by a part playing a critical role in the accuracy of the machine. The deformation depicted in Figure 6.11 was multiplied as to transmit a more visual resulting configuration, as the real deformations would be unnoticeable. The extremely rigid behaviour is, obviously, not created only by the external walls, but mainly by the complex and carefully designed rib structure that populates the interior of the part.

At this stage, the dimensioning of the composite gantry only had the external walls, which were unable to deal with punctual loads in such an effective manner.

When subjected to loads portraying the working conditions, the composite gantry showed concentrated deformations near the interface with some components, as displayed in Figure 6.12.

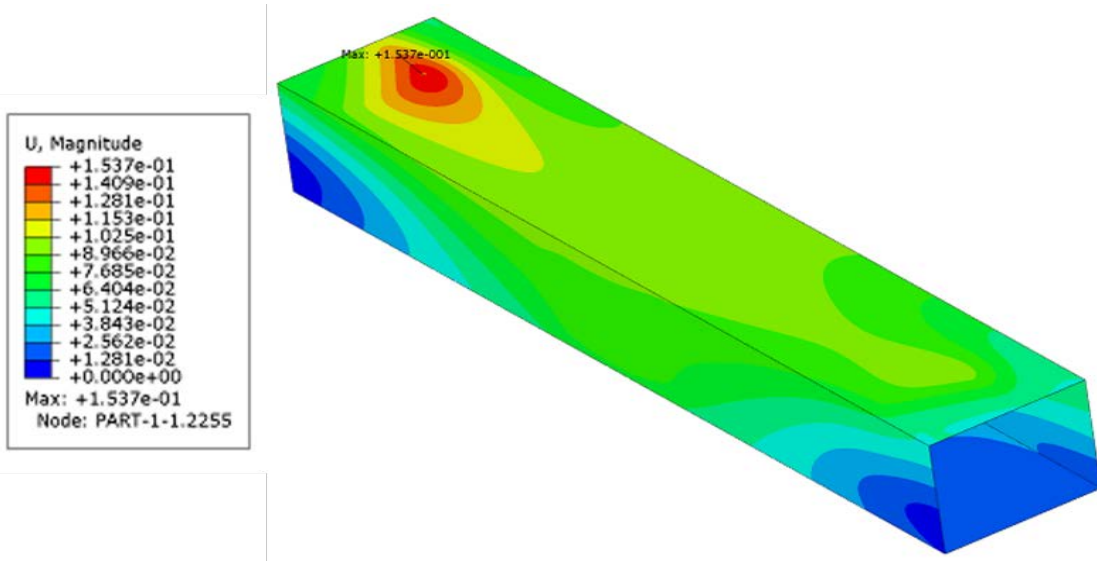


Figure 6.12 - Outcome of FEM simulation for the unreinforced composite gantry subjected to realistic loading conditions. The colour display the translational displacement magnitude. The deformation is magnified by 1400 times.

The approach selected to tackle this was the introduction of ribs along the axis of the gantry.

Initially ribs were only introduced where the higher deformations were found. The results showed the effectiveness of ribs to reduce local deformations. The material selected to fabricate the ribs was carbon fibre at $\pm 45^\circ$. Nonetheless the gantry still displays (see Figure 6.13) local deformations that are higher than the desired ones.

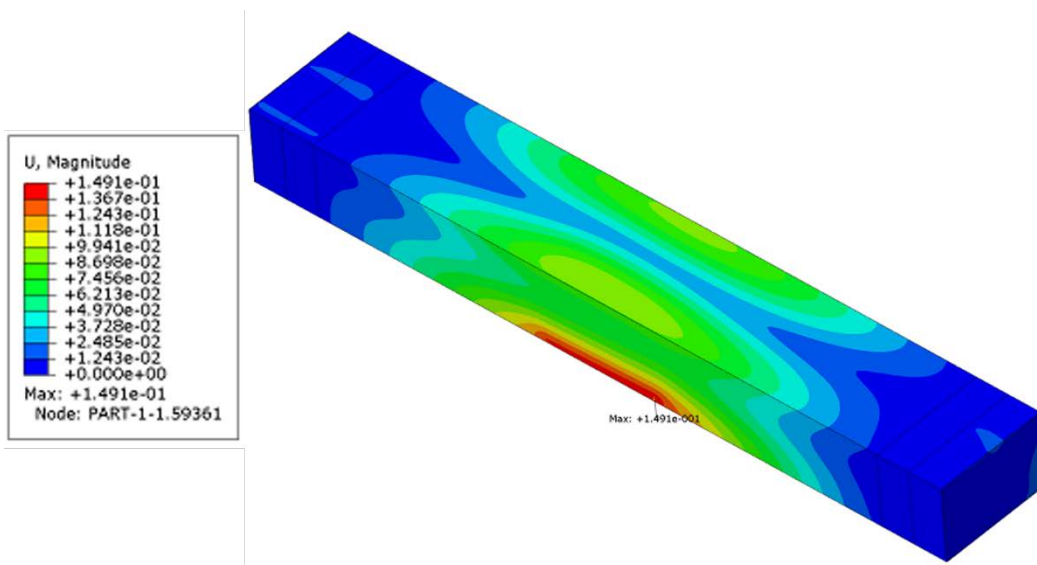


Figure 6.13 - Outcome of FEM simulation for the composite gantry reinforced closer to the edges and subjected to realistic loading conditions. The colour display the translational displacement magnitude. The deformation is magnified by 1400 times.

Then, ribs similar to the ones introduced in the edges were also implemented along the gantry to increase its stiffness and make it less prone to local deformations. The edges were also filleted, to reduce the stress concentration. Figure 6.14 shows the resulting structure's deformations when subjected to the loading conditions when a 3g acceleration is achieved.

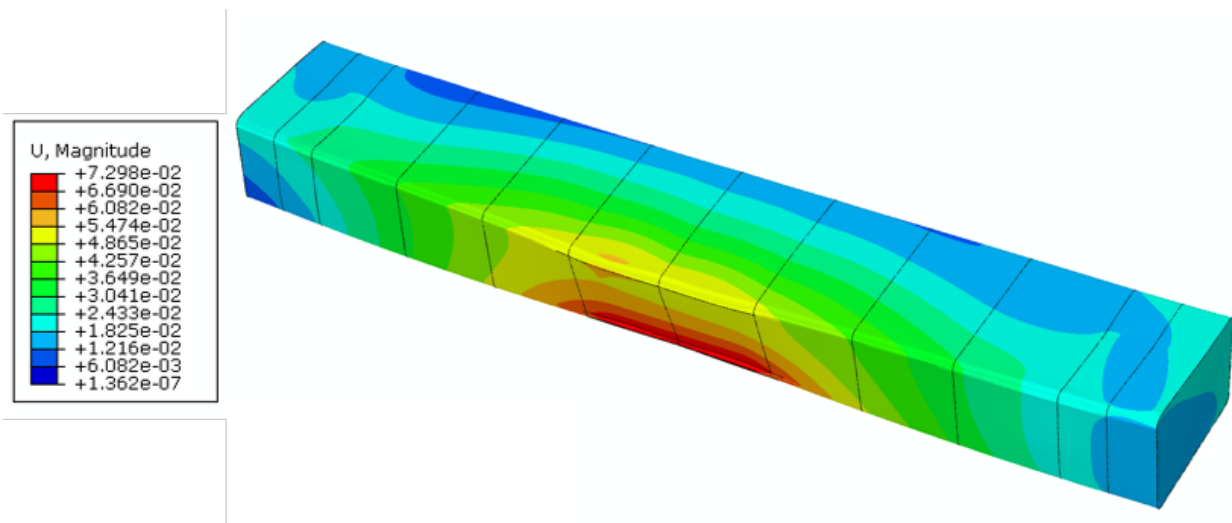


Figure 6.14 - Outcome of FEM simulation for the composite gantry subjected to realistic loading conditions. The colour display the translational displacement magnitude. The deformation is magnified by 1400 times.

The spacing between ribs was defined to ensure that the laser head's load, regardless of its location throughout the beam, is always transmitted by two ribs at minimum. This will ensure that the load transmitted to the directly contacted wall is effectively distributed to the entire section of the beam.

The composite part is also required to present additional components, such as rails and supports for the optical path. Such structures are visible in Figure 6.15, which presents the numeric model on the basis of the composite structure simulations.

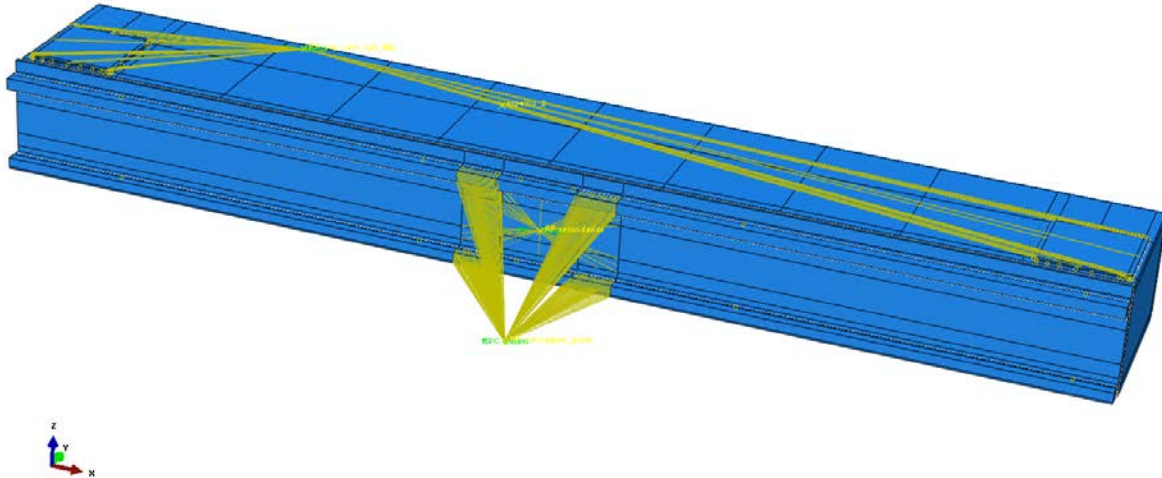


Figure 6.15 – Numeric model of the composite part subjected to the realistic loads.

The result of the dimensioning process that created the composite gantry capable of replacing the current metallic one was the part able to sustain loading conditions that emulate higher accelerations. The displacements suffered by the centre of gravity of the cutting head, critical for the analysis of the required machine accuracy, were comparable and generally lower than those ones it suffers in the current metallic gantry.

Table 6.3 shows the displacements suffered by the cutting head's centre of mass on both gantries, current metallic one and the composite made one.

Table 6.3. Comparison between the displacement of the centre of gravity of the cutting head on the metallic and on the composite component.

Displacement of Cutting Head's Gravitational Centre	Metallic Gantry	Composite Gantry
Translation in x (mm)	0,013	0,014
Translation in y (mm)	0,095	0,080
Translation in z (mm)	-0,119	-0,119
Rotation in x (rad)	$3,616 \times 10^{-4}$	$3,088 \times 10^{-4}$
Rotation in y (rad)	$-6,711 \times 10^{-6}$	$-4,425 \times 10^{-6}$
Rotation in z (rad)	$1,589 \times 10^{-5}$	$1,314 \times 10^{-5}$

The result of the reinforced composite structure shows a deformation profile similar to that of the metal structure (see Figure 6.11 and Figure 6.14) and cutting head displacements generally under the levels presented by the metallic structure (see The result of the dimensioning process that created the composite gantry capable of replacing the current metallic one was the part able to sustain loading conditions that emulate higher accelerations. The displacements suffered by the centre of gravity of the cutting head, critical for the analysis of the required machine accuracy, were comparable and generally lower than those ones it suffers in the current metallic gantry.

Table 6.3 shows the displacements suffered by the cutting head's centre of mass on both gantries, current metallic one and the composite made one.

Table 6.3). The only exception is the translation on the x axis, which presented a very slight and insignificant deviation in comparison to the one suffered by the metallic gantry, especially considered that this latter presented all other displacement and rotation values equal and higher than those from the composite gantry. The performance of the beam subjected to these loads greatly benefits from the introduction of ribs perpendicular to the axis. However, the introduction of the ribs increased the weight of the composite gantry to 81.3 kg, meaning that the composite component, as it is, allows to increase the maximum acceleration in 15% by taking into account the restrictions of the linear motors (as shown in Figure 4.14), while keeping the same precision and decreasing roughly the weight by 18%.

This result, although advantageous, still falls short from the ideal result. This process generated a gantry that ensures the rigidity required for the same precision level at 3 G but, because it is dimensioned for this maximum acceleration, it presents too high mass and establishes limitations as consequence of being an overdimensioned part. In fact, by aiming at an ambitious maximum acceleration this process results in a machine that falls short of its maximum potential. The analysis needs to also account for variations in the maximum desired acceleration while ensuring the mass required for a stiff gantry is kept to a minimum. This configures an optimization problem. The adoption of such an approach will ensure that a broader range of configurations can be tested, thus taking full advantage of the selected materials for the gantry construction.

6.4 OPTIMIZATION OF THE COMPOSITE GANTRY

The output of the optimisation process is presented in the form of the plot shown in Figure 6.16.

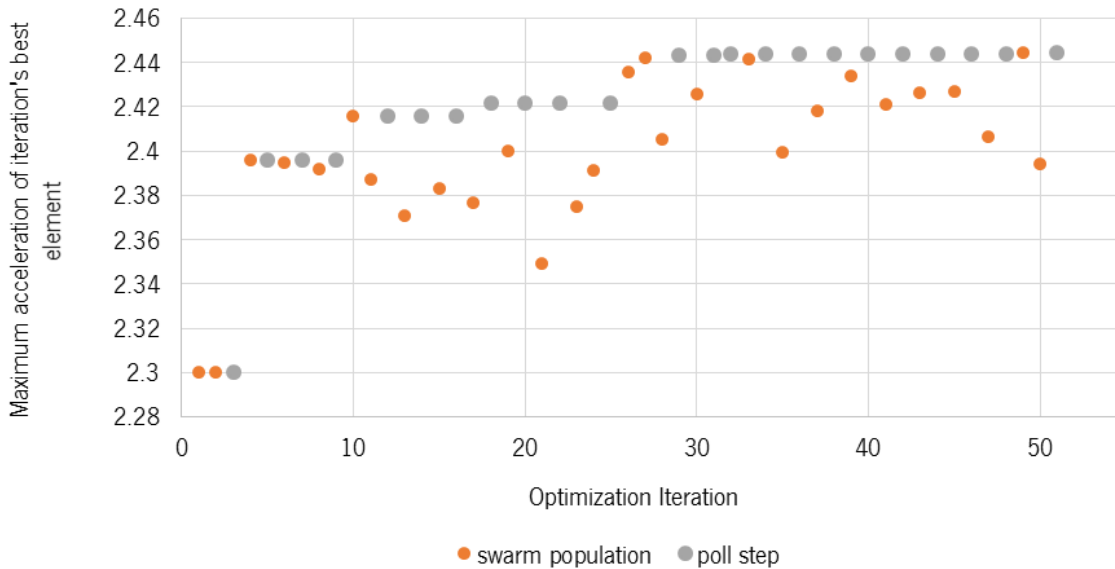


Figure 6.16 – Results of initial optimization process

As can be seen, the initial configuration presents an acceleration of 2.3 G, as the one provided as best guess. As the optimisation process evolved, the system tended to present best solutions with higher maximum accelerations, meaning the algorithm is able to extract values from the simulations run and generate new configurations based on the population elements that present better results. One can see that the search step, performed resorting to the swarm population, results in discontinuous improvements in the results. However, it then has difficulties in converging to higher accelerations, as happens, for example, after iteration ten. When this is verified, the algorithm creates a poll step that, starting from the best value obtained, tries to find the direction that will be more prone to lead to better results. With the first objective function, the maximum acceleration achieved is just below 2.45 G, which is already an improvement regarding the current machine's performance, and the one made possible through the conventional dimensioning of the gantry presented in section 6.3.1.

Nevertheless, it was deemed as interesting to test new objective functions as to understand if other performance indicators are also introduced in the objective function. Another reason as why this could be interesting was the fact that the best element for each optimisation process was not suffering a steady decrease, as initially expected. The mass of the best element of each iteration is plotted in Figure 6.17.

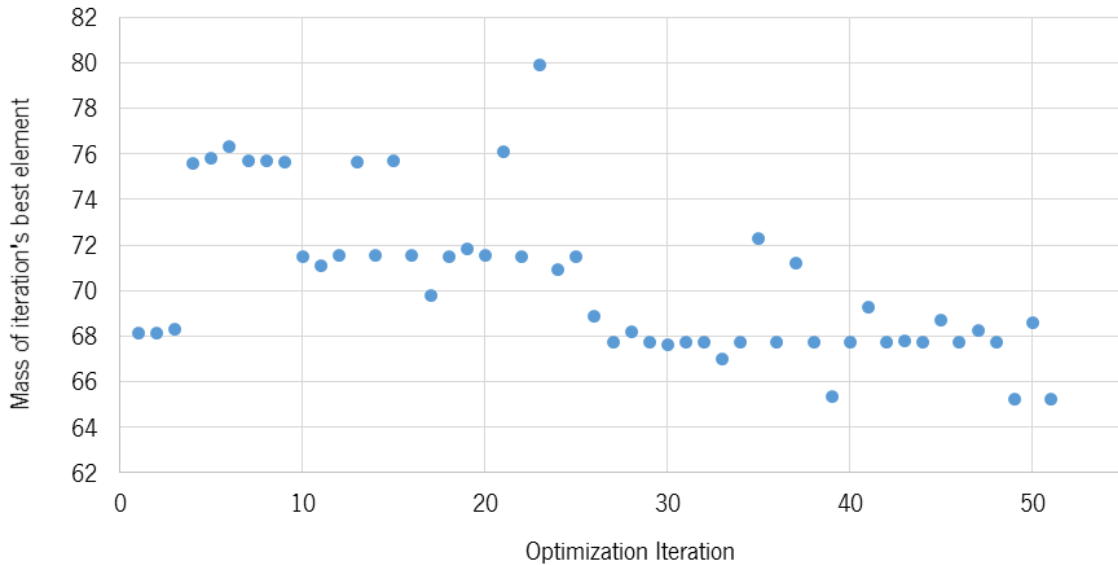


Figure 6.17 – Mass of the best elements of each iteration as optimization process evolves

The final result presented is just slightly below the one of the initial configuration that arose from the best guess provided to the algorithm before the optimisation process. In most cases, the process provides solutions that are heavier than the initial one. The results seem to present a trend for lighter solutions, but the convergence is slow and would require much more iterations until the algorithm provide substantially lighter solutions.

At this stage, the hypothesis that the inclusion of the system’s mass in the objective function would lead to better optimisation results was formulated.

This comes from the fact that including mass in the objective function will increase the tendency of lower mass solutions being selected. On the other hand, lower mass solutions can be subjected to higher acceleration without compromising the limitations imposed by the force required from the linear motors.

To test this, the objective function was formulated to force the algorithm to consider not only the acceleration, but also the mass of each configuration tested. Because PSwarm is a single objective optimisation algorithm, the two objectives must be combined in a single one. To do this, each of the objectives (acceleration and mass) were multiplied by a factor that will represent the relative importance of each factor.

The new objective function is expressed in eq. 6.1.

$$f' = \begin{cases} -a \times \alpha + m \times \beta & \text{if } dof_i \leq dof_{i_{max}}, i \in [1, 6] \text{ and } m \leq m_{max}(a) \\ 1E + 20 & \text{if } dof_i \leq dof_{i_{max}}, i \in [1, 6] \text{ or } m \leq m_{max}(a) \end{cases} \quad \text{eq. 6.1}$$

where α is the factor attributed to the acceleration and β is the factor attributed to m , the mass of the gantry. The ratio between α and β dictate the relative importance of each of the two system properties considered. In an optimisation based on an objective function where α/β is high, the solutions presented further down the optimisation process will result from a process more focused in increasing the acceleration. For a low ratio, the algorithm will be more aware of the system's mass. A detail that also had to be taken into account were different orders of magnitude that the mass in kg and the acceleration in G had in the system. For α/β equal to one, the system will be more focused in the mass, since a decrease of mass at a given percentage will vary the optimization function much more than an increase of the acceleration at the same percentage. Several combinations of α and β were tested. Figure 6.18 shows the result for $\alpha = 1$ and $\beta = 0.01$.

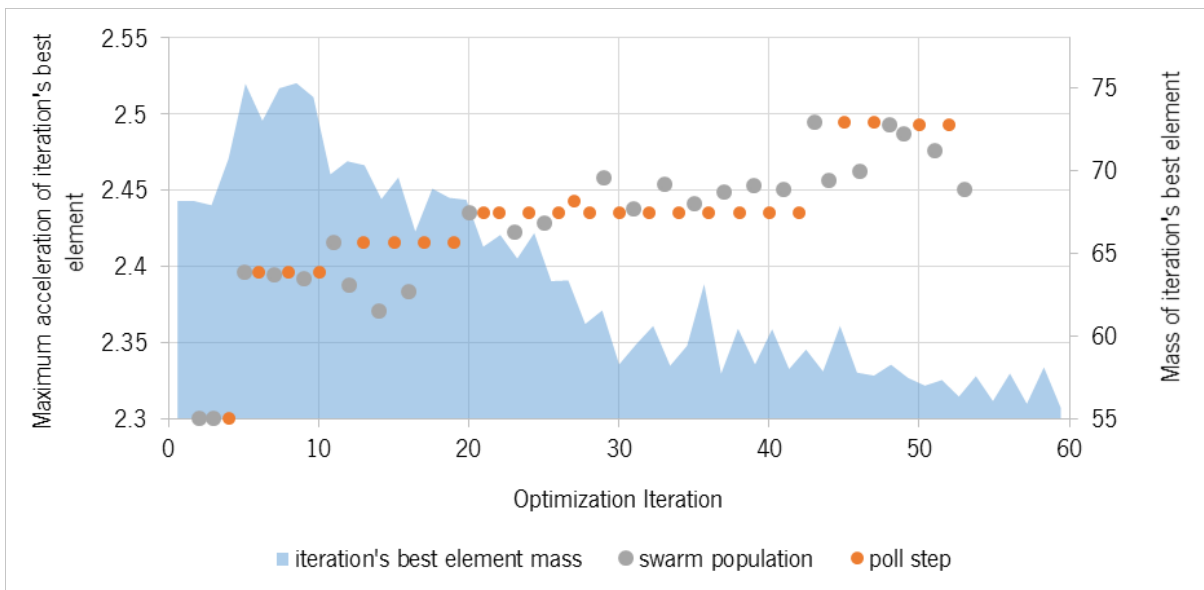


Figure 6.18 - Acceleration and mass evolution for an α of 1 and a β of 0.01

As it is shown, the inclusion of mass as one of the aspects to be accounted for in the objective function, leads to a clearer and faster tendency of mass decrease. The mass drops by roughly 10 kg from the initial solution. Also the maximum acceleration presents more interesting values, being in the vicinities of 2.5 G, an increase of 0.2 G from the initial best guess and allowing a system that has the maximum acceleration higher than

the current one by almost 25%. But it is interesting to watch what happens as the influence of the mass on the objective function increases. Keeping $\alpha = 1$ and increasing β to 0.1, the optimization behaves as shown in Figure 6.19

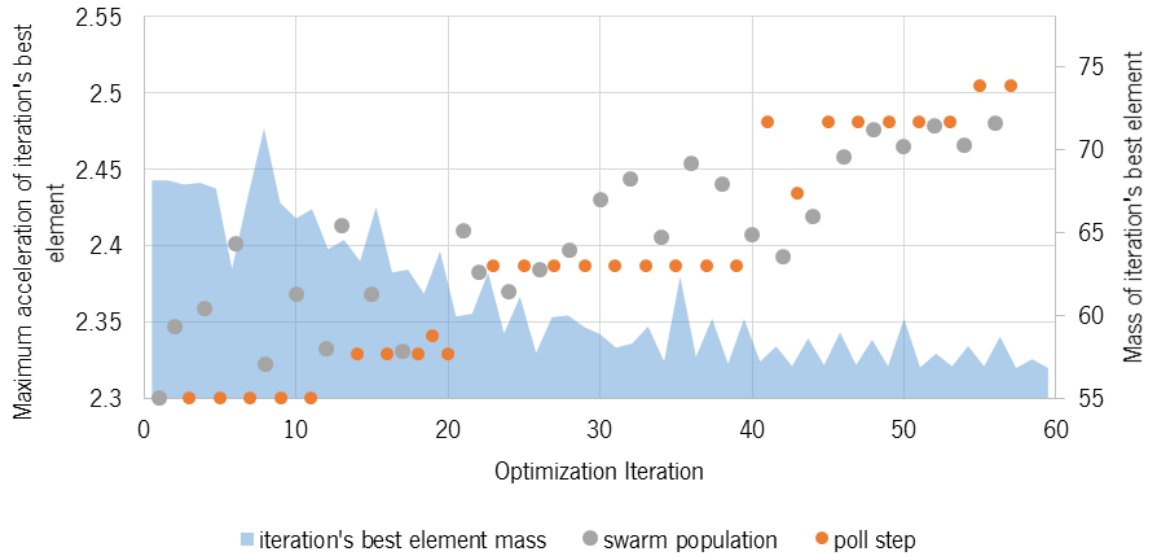


Figure 6.19 - Acceleration and mass evolution for an α of 1 and a β of 0.1

As it can be seen, not only the mass decreased faster, the maximum acceleration reached is also above 2.5 G. Overall, the optimisation seemed to converge in a smoother manner and reach better acceleration results.

It also must be taken into account that, as the optimisation algorithm used is non-deterministic, these improved results can be a consequence of other aspects in the process other than the objective function. Further studies should be performed to determine the relation between objective function and optimal results and the optimal values for α and β .

Still, it is interesting to analyse the optimisation result and understand the configuration resulting from the process used. As mentioned, from the 19 optimisation variables used in the process, 18 of them were related to the thickness of different ply orientations in 6 different sections (represented in Figure 4.17) and 1 referred to the maximum acceleration applied in the x direction. As shown in Figure 6.19, the maximum acceleration that is possible to apply resulting from the optimisation process is only slightly above 2.5 G, more specifically 2.505 G. This acceleration accounts for the limitations imposed by the linear motors used in the machine

under analysis and the mass estimated for the gantry that resulted from the optimisation process, which was 56.86 kg. Regarding the thickness, these are presented in Table 6.4.

Table 6.4 – Optimization results regarding thickness related variables

Variable (layer)	Value (mm)	Section	Total section Thickness (mm)
a_0	2.55		
a_{45}	7.62	Top horizontal face	10.32
a_{90}	0.15		
b_0	6.39		
b_{45}	8.45	Front vertical face	15.32
b_{90}	0.48		
c_0	3.89		
c_{45}	7.08	Bottom horizontal face	10.97
c_{90}	0.00		
d_0	4.98		
d_{45}	1.08	Back vertical face	6.06
d_{90}	0.00		
e_0	1.23		
e_{45}	1.24	Extremity ribs	2.56
e_{90}	0.09		
f_0	2.01		
f_{45}	2.63	Central Ribs	4.64
f_{90}	0.00		

The first point of interest in the analysis of a CFRP gantry dimensioned using optimisation results in a part that presents a mass reduction of 43% in regards to the current metallic part, resulting in an allowed maximum acceleration increase of 25% without accuracy loss.

Secondly, it is relevant to compare the optimised result to the maximum allowed acceleration curve (Figure 6.20). It is noticeable that the resulting solution is quite near the curve and that, therefore, presents a competent trade-off between accuracy and acceleration at a relatively low mass.

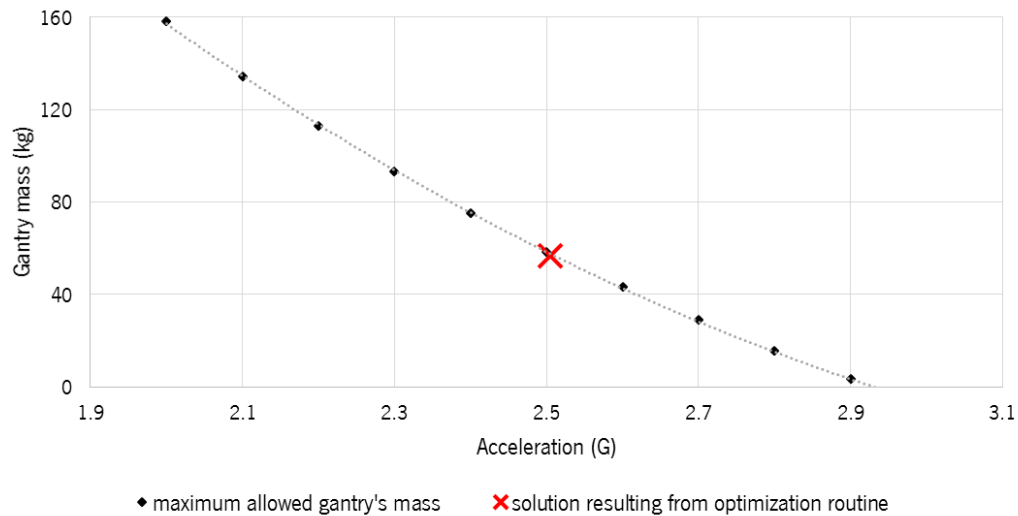


Figure 6.20 – Positioning of the optimised solution vs the curve of maximum possible accelerations as a function of the gantry's mass

It is also interesting to compare the mass of the gantry resulting from an optimisation process and the one dimensioned in Section 6.3, where an equivalent gantry in fibre reinforced polymer was estimated (results presented in Table 6.2 and Section 6.3.1). Not only was the mass higher in that approach (the mass after optimisation was reduced by roughly 24.4 kg, or 30%), but also the thicknesses previously estimated are significantly higher. The reduction in thickness ranges from 0.9% on the front vertical face (15.32 mm after optimisation and 15.46 previously) to 60.8% in the back vertical face (15.32 mm vs. 6.06 mm). On the horizontal faces, the reduction ranges between 42.7% (bottom face) and 46.1% (top face). It is important to state that the dimensioning that was performed initially accounted for a maximum acceleration of 3 G and not of 2.5 G as the optimisation results indicate. However, this is another advantage of a formal process of optimisation. It was possible to identify the ideal trade-off between two divergent objectives: maximize the acceleration of the machine (and, therefore, lowering its mass) while ensuring the same machine accuracy.

Without this analysis, the dimensioning of the gantry could be performed for an acceleration level that is too ambitious and, because of the mass limitation, effectively lower the machine's performance.

There is another indicator that makes clear that the optimisation loop was, in fact, capable of creating configurations that better adapt to the loads that the gantry is subjected to. The layups, which were initially configured to have the same total thickness and a uniform distribution between different orientations, proceed to change and present orientations that become more relevant, while others tend to become less prevalent, or even disappear. It is, for example, evident that the 90° orientation plies are residual or, in some cases, even non-existent. When they are present, they seem to be related to local loads, such as the frontal surface, where the cutting head creates higher loads and displacements, as presented in Figure 6.14. It is also interesting to notice how the different ribs (internal and external) present such distinctive layups, with the internal ones (responsible for load transmission) much thicker than the external ones.

6.5 NUMERIC MODEL VALIDATION

This section includes the tests performed on the scale model of the gantry, as well as the FEA performed to compare experimental and numerical results. The work performed regarding these aspects was reported in Chapter 5:

6.5.1 Tensile Tests

The stress-strain curves obtained from the 8 tested $0^\circ/90^\circ$ test specimens, prepared as described in section 4.5.1.3 and tested accordingly the procedure described in section 4.5.1.4 are presented in Figure 6.21.

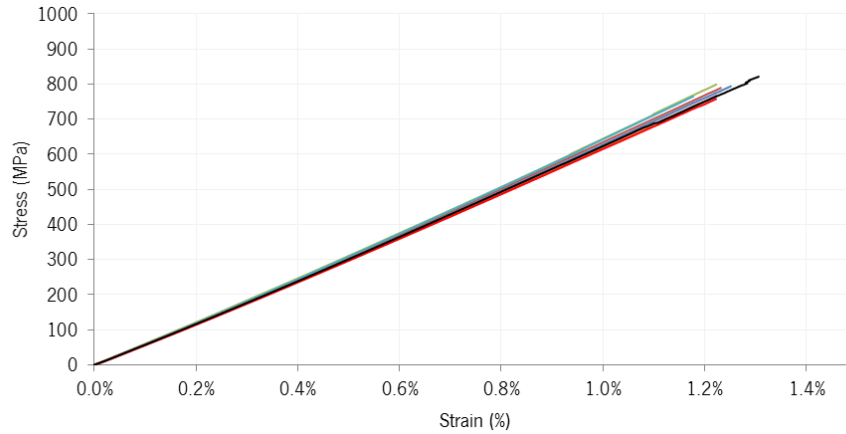


Figure 6.21 - Stress/strain curves obtained from the tensile tests of the $0^{\circ}/90^{\circ}$ plain weave samples

It is possible to see that samples presented, as expected, an almost linear or elastic tensile behaviour along the entire test and also a fragile failure.

Table 6.5 summarises the results obtained in the tensile testing of the $0^{\circ}/90^{\circ}$ plain weave samples.

Table 6.5 - Results obtained from the tensile tests made on the $0^{\circ}/90^{\circ}$ plain weave samples

Property	Average value	Standard Deviation
Ultimate stress (MPa)	781.05	23.41
Young Modulus (GPa)	59.81	0.98
Poisson's ratio	0.05	0.01

For $0^{\circ}/90^{\circ}$ plain weave samples the most common failure modes are LAT, LWT, LWB e LGT. In fact, out of 8 tested samples, 6 had a LAT failure, while two suffered a failure at the Gage (one LGM and other LGT). Figure 6.22 displays a sample that suffered the more typical failure observed, accordingly to the code LAT of ASTM aD3039/D3039M-08. For more info on the failure modes codification, check Table 5.1.



Figure 6.22 - Sample presenting the most common type of failure observed (code LAT of ASTM aD3039/D3039M-08)

The results obtained are in line with the expected outcome, although lower than those presented in the product datasheets that may be seen in Appendixes B and C. The tensile modulus for TR 30S 3L fibres is presented as 234 GPa and the tensile strength as 4 120 MPa. For the matrix, the defined values are 2.9 GPa for modulus and 74 MPa for tensile strength. According to [28], the tensile modulus in the fibre direction of an unidirectional composite can be determined by the law of mixtures as:

$$E_c = E_m V_m + E_f V_f \quad \text{eq. 6.2}$$

where E_c , E_f and E_m are the tensile moduli of the composite material, fibre and matrix, respectively, and V_f and V_m the fibre and matrix volume contents, respectively.

Considering that the fabric tested is a plain woven fabric with equal percentages of fibres that are positioned aligned and perpendicular to the applied load, the theoretical modulus can be calculated through:

$$E_c = E_m V_m + \left(\frac{E_f V_f}{2} \right) \quad \text{eq. 6.3}$$

For a composite having 60% carbon fibre volume fraction could be predicted as 71,36 GPa, which means the experimentally obtained from the tensile tests performed value is around 84% of the theoretically expected

one. Such difference can be explained by a lower fibre content and slight misalignments of the carbon in the composite samples or by mechanical properties of raw-materials given in manufacturer datasheets that are too optimistic.

Also through the law of mixtures, and for the plain weave material used:

$$\sigma_c = \sigma_m V_m + \left(\frac{\sigma_f V_f}{2} \right) \quad \text{eq. 6.4}$$

where σ_c , σ_f and σ_m are the ultimate stress of the composite material, fibre and matrix, respectively. Regarding this aspect, the value experimentally obtained (781.1 MPa) represents only 61.7% of the value theoretically expected. This might be related to the also limited value obtained for the strain observed when compared to the one in the fibre's datasheet (68.3%, meaning an average of 1.23% vs the expected 1.8% for the fibres) and the fact that the most samples most samples fail near the tabs, indicating a possible excessive grip on the samples (despite the presence of tabs). Other possibilities include misalignments of the carbon in the composite samples or unrealistically high mechanical properties in the datasheets.

6.5.2 Lap shear tests

Figure 6.23 presents the stress-strain curves obtained from the lap shear tests performed with 5 test samples, according to the ASTM D3165-00, to the adhesive EPX DP490 in this work.

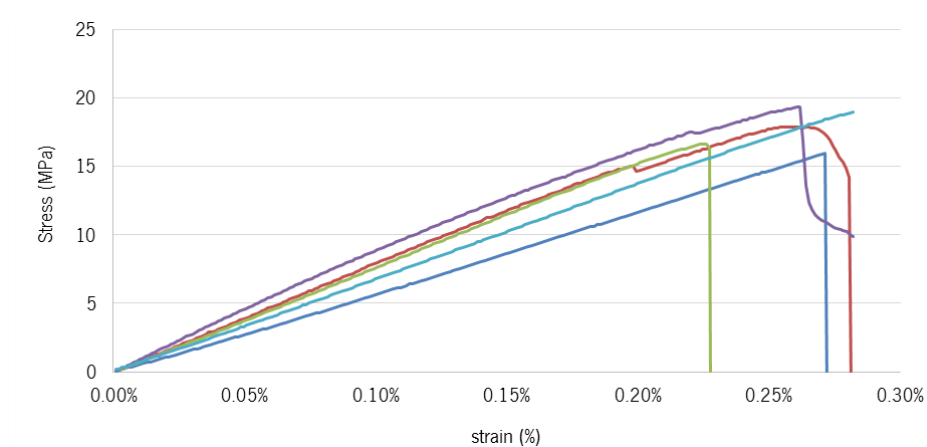


Figure 6.23 - Stress/strain curves obtained from the lap-shear tests made on the adhesives according to the ASTM D3165-00 standard

As can be seen in Figure 6.23, the data obtained presented some variation of the ultimate shear strength. The numerical values obtained are compiled in Table 6.6.

Table 6.6 - Results obtained from the lap-shear tests performed on the adhesives

Value	Adhesive layer thickness (mm)	Area (mm ²)	Ultimate Shear Strength (MPa)
Average	0.58	317.49	18.06
Standard Deviation	0.075	11.77	1.50

The failure of all the samples occurred at the interface between the adhesive and adherents [38]. This, combined with the fact that shear strength values slightly lower than those presented in the manufacturer datasheets (see Appendix E) were obtained, may indicate that the surface preparation or curing procedure could have been improved, although adequate standard practices had been followed. Another possible cause may result from some excessive bending that could occurred in the overlap zone instead of the presence of the tabs used to minimise it. In fact, the photos depicted in Figure 6.24 highlights that this phenomenon happened in some degree during the tests made.

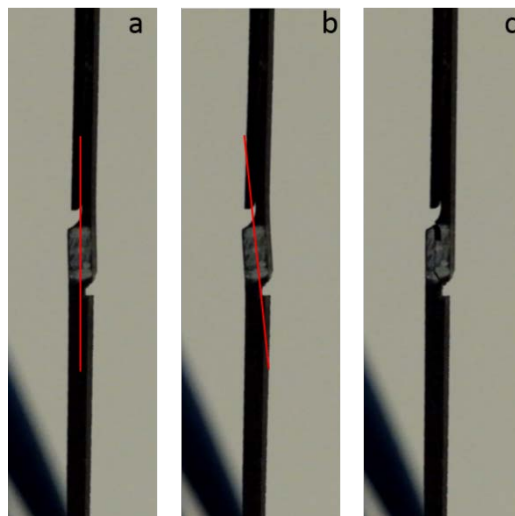


Figure 6.24 - Bending phenomenon occurring during the lap-shear tests

This slight rotation caused by eccentricity in the load path (even if tab ends had been used) and by the differential adhesive straining effect result in the generation of undesired bending moments in the adhesive and, consequently, in unexpected and non-uniform shear and peel stresses [216, 217]. Since adhesives are generally less efficient dealing with peel stress than shear stress, this loading state might lead to an adhesive failure at lower stresses.

6.5.3 Mechanical testing of the gantry prototypes

Figure 6.25 shows a composite part without ribs subjected to the test loading. Despite some camera movement, it is still possible to identify a horizontal line (in green) that is made parallel to the I-shaped steel beams used to support the composite prototype gantry under test (see section 5.1.3). The red line corresponds to the area where the load was transmitted to the L-shaped steel load bearing element that is connected to the composite prototype gantry. Despite an increasing angle between the green and red lines there was always contact between the actuator and the whole surface throughout the test (or, if any poor coupling happened, it was not detected). The dashed yellow line indicates the force direction produced by the actuator, perpendicular to the horizontal face of the load cell. Throughout the whole test, the force was kept vertical. As the actuator hinges, it ensures a full contact with the load bearing element. The force that is transmitted to the load bearing element varies through the test, because the output of the actuator varies, and also due to the fact that the angle between the dashed yellow and red lines changes.

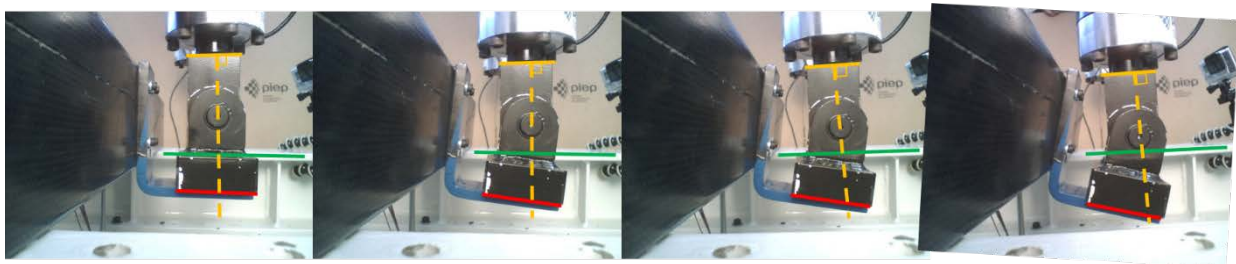


Figure 6.25 - Displacement of the set-up geometry during testing

The effect of the load bearing element's displacement and the changing angle between the load and the surface creates a decomposition of the force in two components. The component that is normal to the red

line is the effective load applied to the part. The component that is parallel to the red line and does not result in effective loading of the test parts. This decomposition of the force is illustrated in Figure 6.26.

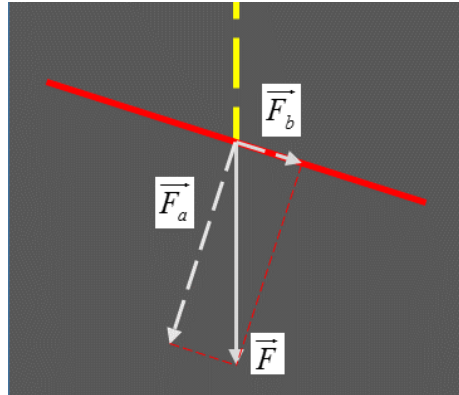


Figure 6.26 – Decomposition of the force applied by the actuator (\vec{F}) into the components relative to the load bearing element's horizontal surface: normal (\vec{F}_a), and parallel (\vec{F}_b)

Both prototypes were successfully tested and the corresponding data acquired. For the part with ribs, values were obtained for all of the LVDTs and the planar rectangular rosette. The LVDTs were used to measure linear displacement at three different points considered of interest and specified in section 5.1.3. These elements are essentially rods actuated by a spring that are placed in contact with the test specimen, have their movements limited to one direction and register changes in the position of its tip. The rosette measures the local strains along different directions in the underlying surface of the test part. The values measured with this equipment were used for comparison and validation of those obtained from the numeric simulation. While testing the prototype without ribs some problems occurred, namely it wasn't possible to obtain the data output from two of the LVDTs. All remaining data was captured successfully and can still be subjected to comparison. Although not desirable, this data acquisition problem was not critical since the main goal of the part without ribs is testing and validating the set up and not comparing the results obtained to the numerical ones.

Another problem that occurred during the test was the failure of the adhesive between the load bearing element and the CFRP components. Figure 6.27 displays the gap formed between these two components that was considered caused by the adhesive failure.

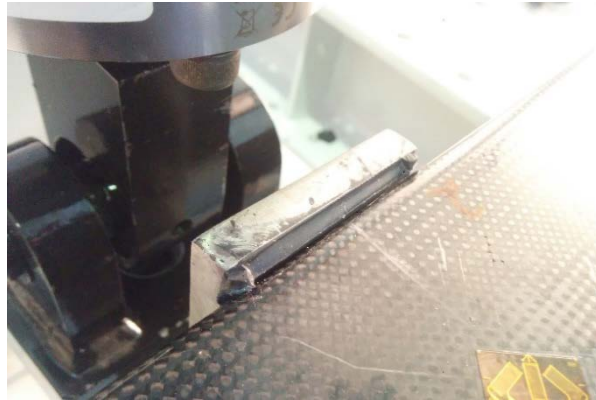


Figure 6.27 - Gap formed between the load bearing an shell caused by adhesive failure

It is important to understand that the adhesive that suffers this failure is not under a shear load, but rather subjected to a cleavage stress. The formed gap seemed to be present up to the top two screws that link the load bearing element and the composite shell. This gap only appeared during the load application. As Figure 6.27 also shows, the adhesive failure occurred quite near the rosette location. Thus, it was expected that such phenomenon will have a considerable influence in the values of strain collected by the rosette and might lead to an impossibility of obtaining a meaningful comparison with the numerical results.

One more issue detected during the experimental testing of the gantry prototypes was the formation of a gap between the pultruded plate and the part when the load was applied. As increasingly higher loads were applied, there was movement of the components that were gripping the gantry to the test rig structure and were held in place by the M10 screws, growing the distance between the pates and the iron beams, allowing for additional movement freedom from the part being tested. This is made explicit in Figure 6.28 by the insertion of a metal ruler between the gantry and the pultruded plate.



Figure 6.28 - Gap formed between the composite shell component and pultruded plate

As may be seen in Figure 6.28, there is a gap which is larger on the distal side from the load application. The ruler depicted in that Figure has a thickness of 1 mm. The fact that this gap appears only during the load application proves that there is some movement at the supports. Despite the screws being carefully tightened, it was known that small displacements would be possible.

6.5.4 Numerical Simulation of the mechanical behaviour of the composite prototype gantry

The results of the simulation have shown that the part presented, in general, low levels of stress when submitted to the 5 kN vertical load previously described in Section 5.1.3. The higher stress points are located on the interfaces either with the support structure or the load bearing element, as can be seen in Figure 6.29. This image portrays the mapping of the Tsai-Hill failure criterion throughout the laminates, with the highest value for the layers at each point of the surface. As mentioned in section 5.1.4.1, the Tsai-Hill criterion predicts failure when the failure index in a laminate reaches 1. If the local stresses caused by the interface are removed from the analysis, the maximum value of the whole parts lowers to just below 0.3, which means a safety factor between 2 and 3 for the whole prototype. In the case of the ribs, this value is even larger, reaching 9.

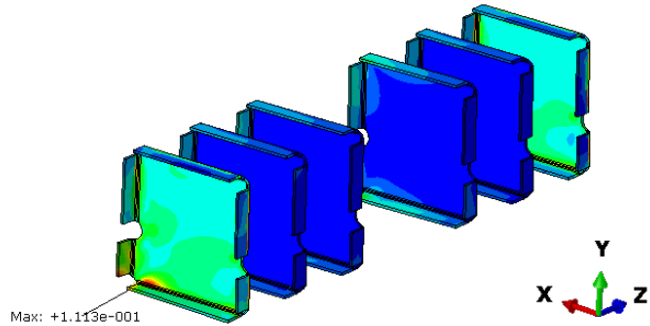
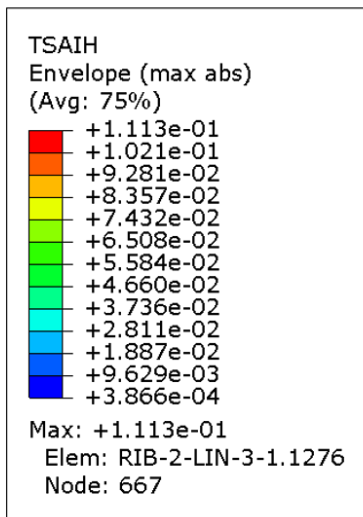
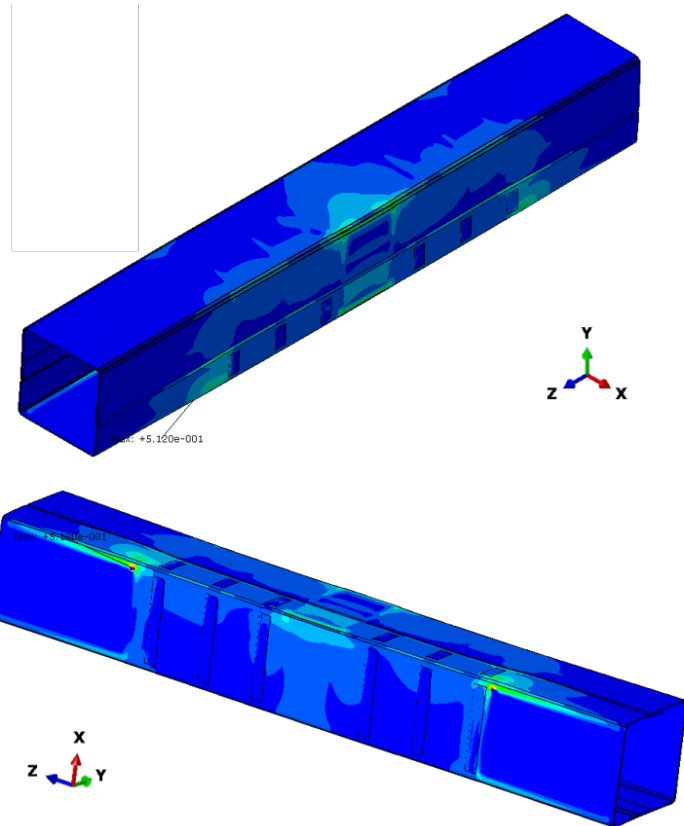
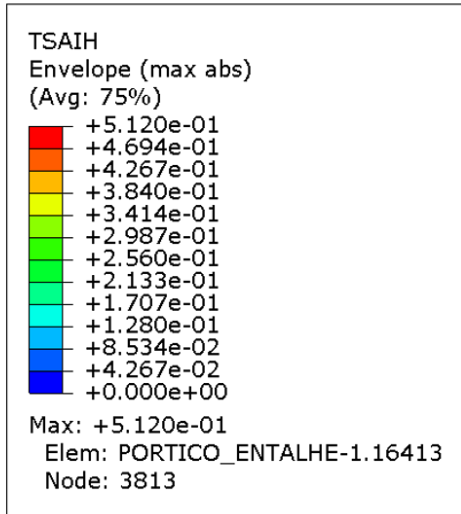


Figure 6.29 - Tsai-Hill criterion applied to the laminate of the part produced, with display of the isolated ribs of the produced prototype composite gantry submitted to 5kN vertical load. The images portrait highest value for Tsai-Hill criterion, regardless of the ply in which it is occurring

The Shear Stress in the adhesive interface is also quite below the one determined experimentally at failure. Therefore, it is expected that the employed adhesives will be able to sustain the loads they will be subjected to, more specifically the shear stress resulting from the loading scenarios considered.

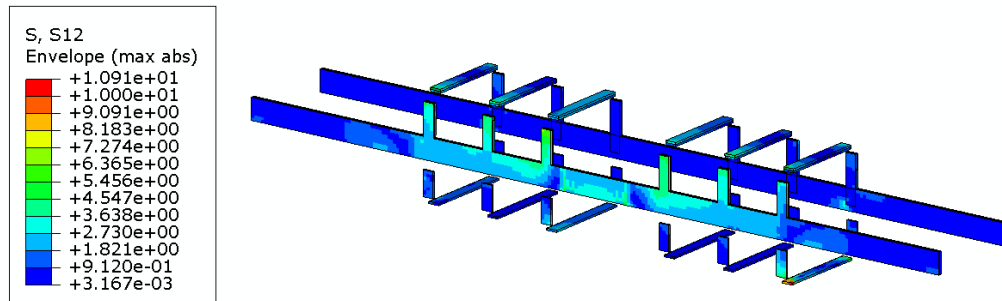


Figure 6.30 - Shear stresses developed in the mostly loaded composite gantry adhesives

6.5.5 Comparison between experimental and numerical results

As previously mentioned in section 5.1.3, the experimental tests were monitored by logging the force and displacement of the actuator, the values of the 3 LVDTs and of the planar rectangular rosette. Data for comparing with these control mechanisms was also extracted from the numerical simulation's results. The displacement data was obtained by determining the intersection of a straight line defined according to the position of the LVDTs with the surface of the part. The simplest solution would be to plot the displacement of a node in the direction of the LVDTs movement. But this would render incorrect results, as either the node would be constrained (thus introducing a restraint that does not correspond to the experimental conditions) or it would be able to move in other directions. Instead the data collection was performed by defining a point list path. The path is a line segment placed along the same line as the LVDT is the experimental test. Because the path is a line, it can be defined using just two points. These points have to be such that they will comprehend both the initial and final positions of the wall they are monitoring, as well as all in between. After the definition of this path, Abaqus was able to determine the interception between the path and the part but didn't present any tool capable to make this calculation available for a sequence of increments. Given that each simulation has, at least, 100 increments, the process becomes extremely cumbersome. Thus, a small python script was created to allow an automatic output of this information and making the comparison between the numerical and experimental results much easier.

The displacement was monitored resorting to three LVDTs (a, b, and c), with the positioning defined in Figure 5.30 in section 5.1.3 (and recaptured in Figure 6.31).

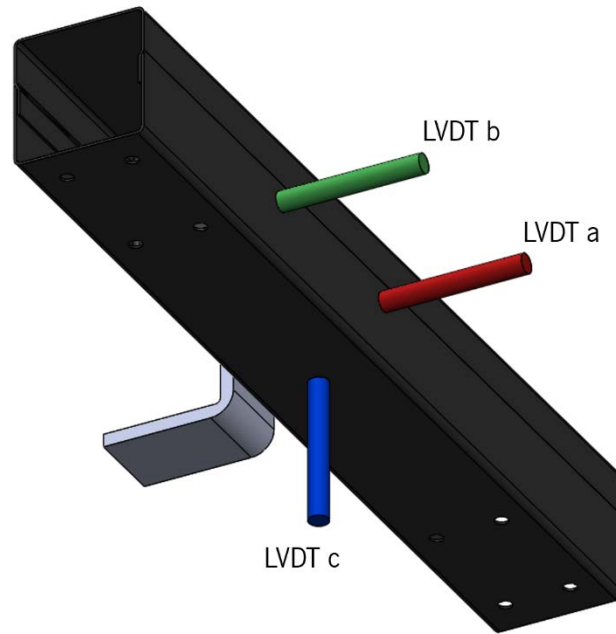


Figure 6.31 – Positing of LVDTs in the experimental set-up

Figure 6.32 presents the displacement obtained in, both the numerical simulation as well as the experimental testing. As can be seen, the displacement profiles determined numerically and experimentally are quite similar. It is also shown that the variations of the numerical displacements are directly proportional to the load, while the experimental tests had a slightly less linear behaviour. Thus, it may be concluded the approximation presented by the numerical model is valid and quite representative of the overall mechanical behaviour of the produced composite prototype gantry. Figure 6.32 also shows a slight deflection detected in the experimental data of LVDT b that might be caused by adhesive failure.

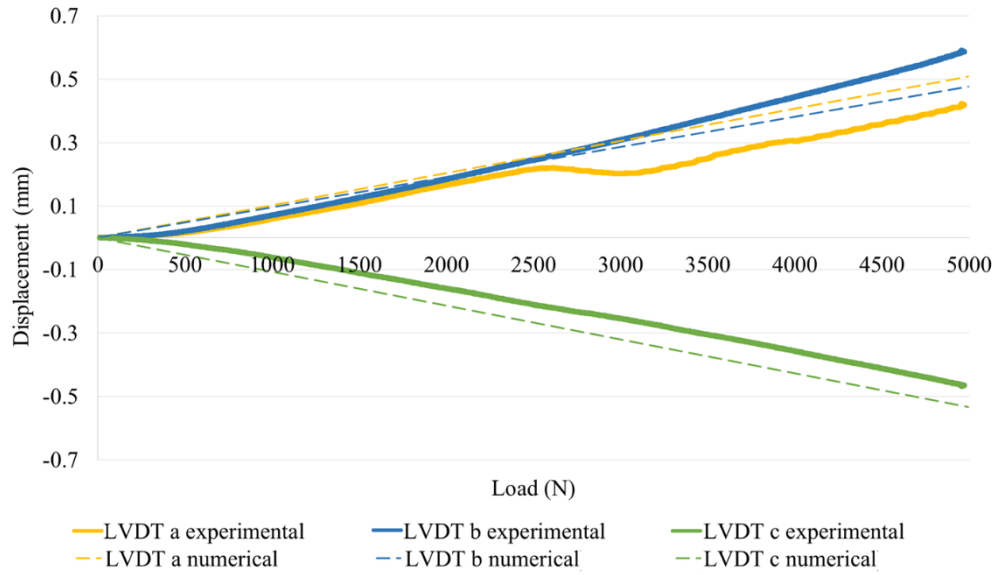


Figure 6.32 - Comparison between the deflections obtained from the numerical simulations and experimental testing

On the other hand, Figure 6.33 compares the actuator displacement as a function of force obtained from the numerical simulations and experimental tests.

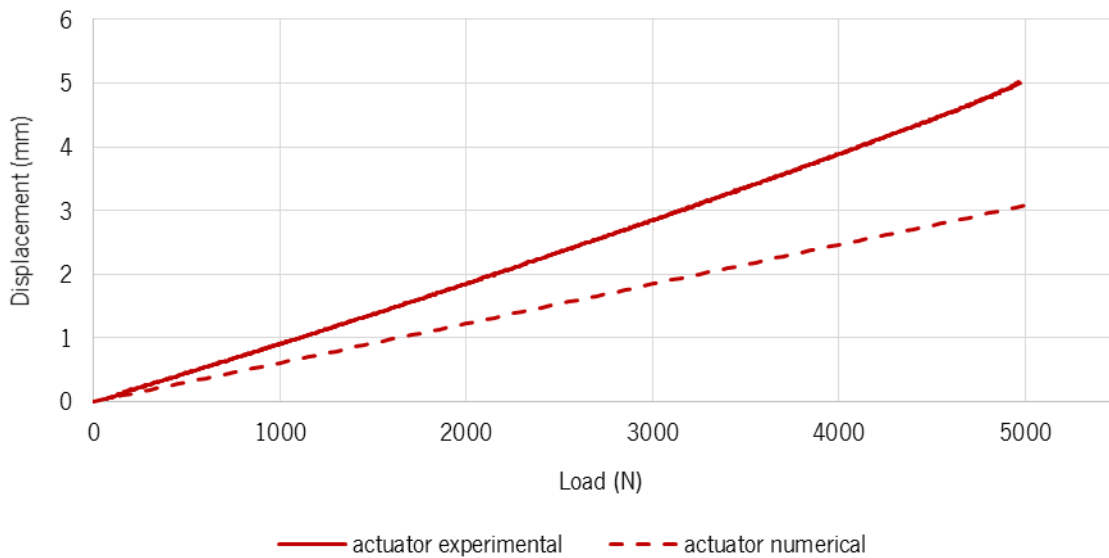


Figure 6.33 - Displacement/force curves obtained in the actuator from numerical simulations and experimental tests

As may be seen a larger difference was observed between the numerical and experimental results obtained for the displacement of the load bearing element of the actuator (since they are coupled, the values are considered to be same for both). The main justifications for the observed difference are:

- The properties of the steel used in the production of the load bearing element were not confirmed by experimental testing.
- The movement of the actuator relatively to the support beams (already shown before in Figure 6.25) has not been considered in the numerical simulations.
- There might be some deformation of the testing rig, which is considered rigid in the numerical model

Regarding the outputs from the planar rosette, it was very important to ensure that both experimental and numerical values consider the same orientation, meaning that both outputs have the axis of the rosette in the same direction.

The strain gage in the green direction that may be seen in Figure 6.34 was considered gage A and its output considered ε_A , the one in yellow determines ε_B and the red one corresponds to ε_C .

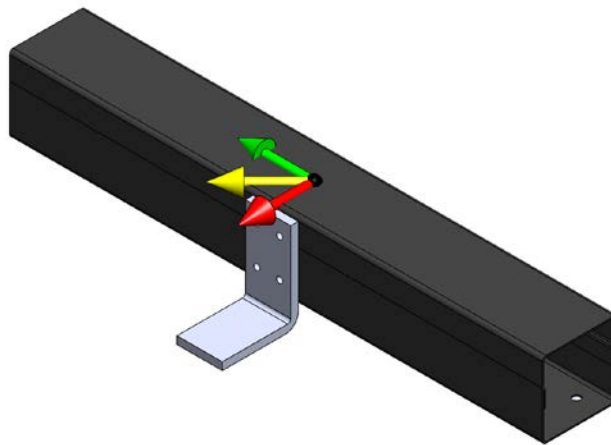


Figure 6.34 - Strain gages placed in the prototype composite gantry produced

After having the strains for each of the three directions of the rosettes (A, B and C), the maximum (eq. 6.5) and minimum strains (eq. 6.6), as well as the angle between principal strains with the A gage (eq. 6.7) were calculated by using the following well-known strain-transformation relationship [46].

$$\varepsilon_{max} = \frac{\varepsilon_A + \varepsilon_C}{2} + \frac{1}{\sqrt{2}} \sqrt{(\varepsilon_A - \varepsilon_B)^2 + (\varepsilon_B - \varepsilon_C)^2} \quad \text{eq. 6.5}$$

$$\varepsilon_{min} = \frac{\varepsilon_A + \varepsilon_C}{2} - \frac{1}{\sqrt{2}} \sqrt{(\varepsilon_A - \varepsilon_B)^2 + (\varepsilon_B - \varepsilon_C)^2} \quad \text{eq. 6.6}$$

$$\varphi = \frac{1}{2} \tan^{-1} \left(\frac{\varepsilon_A - 2\varepsilon_B + \varepsilon_C}{\varepsilon_A - \varepsilon_C} \right) \quad \text{eq. 6.7}$$

where

ε_{max} maximum principal strain (dimensionless)

ε_{min} minimum principal strain (dimensionless)

φ angle between principal strains (rad)

ε_A strain read in direction A (dimensionless)

ε_B strain read in direction B (dimensionless)

ε_C strain read in direction c (dimensionless)

Figure 6.35 compares the minimum and maximum strains (principal strains) determined from both experimental and numeric results, as well as their orientation with respect to the rosette A axis.

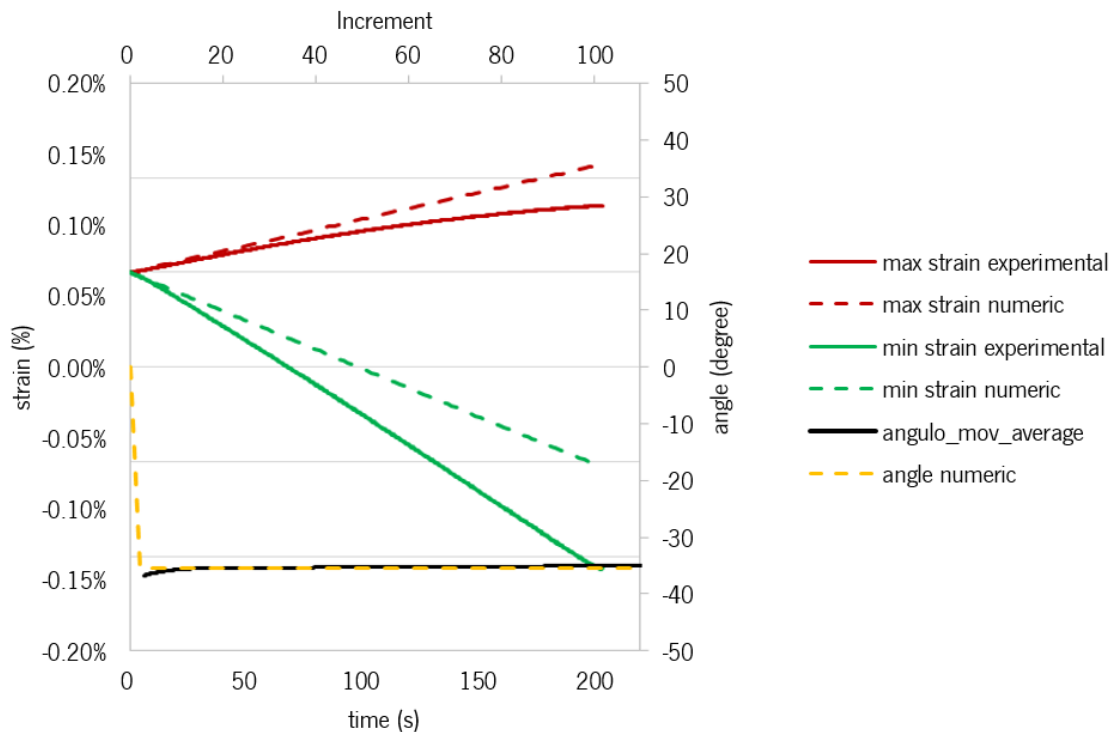


Figure 6.35 - Comparison between principal strain and their orientation obtained from the numerical and experimental results

As it may be seen almost coincident results were obtained for the direction of the principle strains from both methods. In respect to strains and despite the slight differences obtained it can be considered that the numerical simulations allowed to reproduce quite well the experimental determined results. From the analysis of the strain state at the location considered, it was possible to conclude that slight higher strains were obtained from the experimental tests. Despite these small differences, which seem to indicate that the finite element model is more rigid than the experimental system, it can be concluded that a quite good agreement was obtained between the theoretical and experimental results.

Chapter 7: Conclusions

Summary

In the last chapter, the main conclusions are condensed and framed with the Research objectives presented in the introduction chapter. Also identified is the Future work, which points out aspects potentially relevant for further research in the field of part project and optimization for composite materials.

7.1 MAIN CONCLUSIONS

The first goal of the research, and that is aligned with the RO1 (see Section 1.3), was to determine the most critical loading scenario between two considered as the most demanding ones. The implementation of an analytic model, proved capable of accounting for the deformations caused by the imprinted acceleration and its implication in the laser's optical path, allowed to determine that the greatest impact in accuracy occurred when the laser cutting head was located on the centre of the gantry and this latter one, simultaneously, was moving along the y axis.

A composite gantry, equivalent to the metallic one was dimensioned and proved to be capable of sustaining even higher accelerations with the same level of accuracy. The gantry that was projected this way allows to increase the maximum allowed acceleration in 50 % by reducing the gantry weight in 14 %. Such analysis made also possible to establish that a composite gantry to be developed to replace the metallic part should be produced in carbon fibre reinforced polymer, given the exceptional mechanical properties per weight unit required to ensure a rigid while simultaneously lighter than the current one. However, this part would be too heavy to reach such accelerations with the current machine's structure.

In order to ensure that the end result of the composite gantry project development is maximized, a formal optimization process was implemented. The optimization loop implemented consisted in (I) a population based derivative-free metaheuristic optimization algorithm, and (II) an objective function evaluation that is based in FEA. The objective function addressed the deformation of the system and the variation in the 6 dof of the laser cutting head, which were critical to assess the accuracy of the machine. The variables considered were related to the thickness of different fibre orientations in different areas of the part and the maximum acceleration. Also considered was the mass that the current machine can sustain at a given acceleration. If

the maximum force the machine was capable of outputting was exceeded, a penalty was applied and the solution is rendered unfit. With the first trials of the new method implemented it was possible to get to a viable near-optimal solution that presents capability for being subjected to higher accelerations while reducing the mass. There was a clear tendency in the algorithm output to increase the acceleration within allowed values. However, the mass variation did not present such a clear trend. The strategy to overcome this was introducing the mass as part of the objective function. Because the optimization algorithm is single objective, the relative relevance between accuracy and mass had to be defined. Among the several ratios tested, the one with better results lead to the selection of a configuration capable of sustaining an allowed maximum acceleration higher in 25% relative to the current one without loss of accuracy. Regarding mass, the gantry dimensioned using this optimization presented a mass reduction of 43% in regards to the current metallic one, and 30% relative to the composite part previously dimensioned.

Regarding the experimental tests performed in order to validate the FEA models, the comparisons between the experimental and numeric results showed a high level of agreement. A direct comparison between the results obtained from experimental tests and numerical simulations was performed in this study. The experimental results, determined on a CFRP part produced by vacuum infusion, were monitored using three LVDT sensors and a rectangular rosette, all of which located in points considered of strategic significance. The numerical results proved the part was able to withstand all required loadings without reaching the laminate ultimate stress nor the ultimate shear stress of the adhesives. The comparison between experimental and numerical results also demonstrated that the finite element model used rendered accurate results. However, results also showed that some deformations of non-composite components or testing equipment could be better assessed and included in the FEA for better accuracy.

7.2 FUTURE WORK

While the work presented had a satisfactory and positive outcome, thus fulfilling the research objectives defined in Chapter 1, there are aspects of that can be further explored in future research:

- Shape optimization of the part: The implementation of a routine that can lead to the development of a shape that is more efficient to bear the loads presented by the context is of great interest. Composite materials have a great flexibility in terms of the geometry they can assume and the creation of an

optimization routine that encompasses a step for geometry creation that changes more parameters would be of great interest and, potentially, further improve the results obtained;

- Test the efficiency of other optimization algorithms: PSwarm is a quite promising optimization algorithm for the application in hand. However, it would surely be interesting to conduct a benchmark test to determine if it would be possible to obtain better results and/or a shorter optimization time with other optimization algorithms.
- Consider dynamic simulations for the optimization loop: due to the need of keeping computation times relatively short, the simulations ran to perform the objective function evaluation had a limited complexity and not excessively computationally demanding. However, it would be interesting and more representative of the real loading conditions if it would be possible to implement either dynamic simulations that are lighter from the computational point of get access to higher computational power and the implementation of parallel computing, so several evaluations of the objective function can be run simultaneously.
- Creation of a full scale prototype and run an ILCM with the optimized composite gantry: due to budget limitations, this validation scenario was made impossible. However, to fully assess the potential of both the main purpose of this project as well as the applicability of the chosen methodology, this would be the most interesting prototyping scenario and the one that would bring more definitive answers.

Bibliography

1. Caristan, C., *Laser Cutting Guide for Manufacturing*. 2004: Society of Manufacturing Engineers, 2004.
2. Nallusamy, D., *Enhancement of Productivity and Efficiency of CNC Machines in a Small Scale Industry Using Total Productive Maintenance*. International Journal of Engineering Research in Africa, 2016. **25**: p. 119-126.
3. Radovanovic, M. and M. Madic. *EXPERIMENTAL INVESTIGATIONS OF CO2 LASER CUT QUALITY: A REVIEW*. 2011.
4. Technavio. *Laser Cutting Machine Market by Product, End-user, and Geography - Forecast and Analysis 2020-2024*. 2020 [cited 2021 06/04/2021]; Available from: <https://www.technavio.com/report/laser-cutting-machine-market-industry-analysis>.
5. Research, G.V. *Laser Cutting Machines Market Size Worth \$6.72 Billion By 2024*. 2017 [cited 2021 06/04/2021]; Available from: <https://www.grandviewresearch.com/press-release/global-laser-cutting-machine-market>.
6. Updates, M. *Global laser cutting machine market by manufacturers, regions, tpe and application, forecast to 2023*. [cited 2021 06/04/2021]; Available from: <https://www.360marketupdates.com/global-laser-cutting-machine-market-12485268>.
7. *Global Laser Cutting Machines Market by Technology (Solid-State lasers, Gas Lasers, and Semiconductor Laser), Process (Fusion Cutting, Flame Cutting, and Sublimation Cutting), and End User (Automotive, Consumer Electronics, Defense and Aerospace, Industrial, and Others): Global Opportunity Analysis and Industry Forecast, 2014-2022*. 2017 15/03/2018]; Available from: <https://www.alliedmarketresearch.com/laser-cutting-machines-market>.

8. Anghel, C., K. Gupta, and T.-C. Jen, *Effect of laser beam cutting parameters on productivity and dimensional accuracy of miniature spur gears of stainless steel*. IOP Conference Series: Materials Science and Engineering, 2020. **971**: p. 022081.
9. *Machining Dynamics - Fundamentals, Applications and Practices*. Springer Series in Advanced Manufacturing. 2009: Springer-Verlag London.
10. Tingting, Z., et al., *Investigation on the load-inertia ratio of machine tools working in high speed and high acceleration processes*. Mechanism and Machine Theory, 2021. **155**: p. 104093.
11. Santolini, G., et al., *Cut Quality Estimation in Industrial Laser Cutting Machines: A Machine Learning Approach*. 2019. 389-397.
12. Powell, J., *CO2 Laser Cutting*. 2 ed. 1998: Springer-Verlag London. 248.
13. *Amada, GmbH - Laser Technology - LCE Specifications*. 2021 [23/07/2021]; Available from: <http://www.amada.de/en/laser/lce/specifications.html>.
14. Tinoco, J.M.A., *Desenvolvimento de um sistema de troca automática do nozzle de corte para máquinas de corte por laser*, in *FEUP - Engineering Faculty*. 2011, University of Porto: Porto.
15. Belforte, D. *2015 industrial laser market outperforms global manufacturing instability*. 2016 [10/03/2018]; Available from: <https://www.industrial-lasers.com/articles/print/volume-31/issue-1/features/2015-industrial-laser-market-outperforms-global-manufacturing-instability.html>.
16. Riveiro, A., et al., *Laser Cutting: A Review on the Influence of Assist Gas*. Materials, 2019. **12**(1): p. 157.
17. Burdel, T. *Breaking speed barriers in laser cutting*. 2007 [14/03/2018]; Available from: <https://www.thefabricator.com/article/lasercutting/breaking-speed-barriers-in-laser-cutting>.
18. *Pushing the solid-state laser speed limit*. 2015 [14/03/2018]; Available from: <https://www.thefabricator.com/article/lasercutting/pushing-the-solid-state-laser-speed-limit>.
19. Graf, T., *Laser Technologies for the Manufacturing of the Future*. Laser Technik Journal, 2012. **9**(3): p. 1-1.
20. Ulrich, J. *The art of laser cutting*. 2003 [14/03/2018]; Available from: <https://www.thefabricator.com/article/lasercutting/the-art-of-laser-cutting>.
21. *Fiber laser processes thin sheets with 6g acceleration*. 2014 [14/03/2018]; Available from: <https://www.thefabricator.com/product/lasercutting/fiber-laser-processes-thin-sheets-with-6g-acceleration>.

22. Morey, B. *Laser Technologies Offer a Growing Array of Choices*. 2015 [15/03/2018]; Available from: <http://advancedmanufacturing.org/laser-technologies-offer-growing-array-choices/>.
23. Bagherpour, S., *Fibre Reinforced Polyester Composites*. 2012. 135-166.
24. Fan, J. and J. Njuguna, *Lightweight Composite Structures in Transport - Design, Manufacturing, Analysis and Performance*. Lightweight Composite Structures in Transport. 2016: Woodhead Publishing.
25. Wang, R.-M., S.-R. Zheng, and Y.-P. Zheng, *Polymer Matrix Composites and Technology*. 2011: Woodhead Publishing.
26. Barile, C., C. Casavola, and F., *Mechanical comparison of new composite materials for aerospace applications*. Composites Part B: Engineering, 2019. **162**: p. 122-128.
27. Jr., W.D.C. and D.G. Rethwisch, *Materials Science and Engineering: An Introduction, 9th Edition*. 2013, Wiley.
28. Gay, D., *Composite materials: Design and Applications*. 3rd Edition ed. 2015: CRC Press.
29. Campbell, F.C., *Structural composite materials*. 2010, Ohio: Materials Park. 612.
30. González, C., et al., *Structural composites for multifunctional applications: Current challenges and future trends*. Progress in Materials Science, 2017. **89**: p. 194-251.
31. Ashton, J.E., *Implications of the behavior of advanced composite materials*. Journal of the Franklin Institute, 1970. **290**(6): p. 549-566.
32. Möhring, H.-C., et al., *Materials in machine tool structures*. CIRP Annals-Manufacturing Technology, 2015. **64**(2): p. 725-748.
33. Gan, Y.X., *Effect of Interface Structure on Mechanical Properties of Advanced Composite Materials*. International Journal of Molecular Sciences, 2009. **10**(12): p. 5115-5134.
34. Geb, D., G. DeMoulin, and I. Catton. *Population-based optimization for heat sink design in electronics cooling applications*. in *Semiconductor Thermal Measurement and Management Symposium (SEMI-THERM), 2013 29th Annual IEEE*. 2013.
35. Avila, A.F., et al., *A dual analysis for recycled particulate composites: linking micro- and macro-mechanics*. Materials Characterization, 2003. **50**(4): p. 281-291.
36. Rajak, D.K., et al., *Recent progress of reinforcement materials: a comprehensive overview of composite materials*. Journal of Materials Research and Technology, 2019. **8**(6): p. 6354-6374.
37. S, P., et al., *Fiber Reinforced Composites - A Review*. Vol. 06. 2017.

38. Moura, M.F.d.S.F., A.M.B. de. Morais, and A.G.a. de. Magalhaes, *Materiais compósitos : materiais, fabrico e comportamento mecânico*. 2005: Publindústria.
39. Balasubramanian, M., *Composite materials and processing*. 2013: CRC Press.
40. FAA, *Aviation Maintenance Technician Handbook - Vol 1*. 2012.
41. *Compósitos Estruturais - Ciência e Tecnologia*. 2 nd ed. 2016: Blucher.
42. Obande, W., C.M. Ó Brádaigh, and D. Ray, *Continuous fibre-reinforced thermoplastic acrylic-matrix composites prepared by liquid resin infusion – A review*. *Composites Part B: Engineering*, 2021. **215**: p. 108771.
43. Mallick, P.K., *Fiber-Reinforced Composites: Materials, Manufacturing, and Design, Second Edition*. 1993: Taylor & Francis.
44. Hoa, S.V., *Principles of the Manufacturing of Composite Materials*. 2009: DEStech Publications, Incorporated.
45. Elanchezian, C., B.V. Ramnath, and J. Hemalatha, *Mechanical Behaviour of Glass and Carbon Fibre Reinforced Composites at Varying Strain Rates and Temperatures*. *Procedia Materials Science*, 2014. **6**: p. 1405-1418.
46. *TN-515 - Strain Gage Rosettes: Selection, Application and Data Reduction*. 2014, Micro Measurements.
47. Meltem and G. Hasan, *A review on machinability of carbon fiber reinforced polymer (CFRP) and glass fiber reinforced polymer (GFRP) composite materials*. *Defence Technology*, 2018. **14**(4): p. 318-326.
48. Das, T.K., P. Ghosh, and N.C. Das, *Preparation, development, outcomes, and application versatility of carbon fiber-based polymer composites: a review*. *Advanced Composites and Hybrid Materials*, 2019. **2**(2): p. 214-233.
49. Pham, D.-c., et al., *A review on design , manufacture and mechanics of composite risers*. *Ocean Engineering*, 2016. **112**: p. 82-96.
50. Taub, A., et al., *Materials for Automotive Lightweighting*. *Annual Review of Materials Research*, 2019. **49**(1): p. 327-359.
51. Möhring, H.C., *Composites in Production Machines*. Vol. 66. 2017. 2-9.
52. GMBH, M.W. *PRO.X1000 Powered by Carbon*. 09/11/2017]; Available from: <http://www.map-wzm.de/en/products/prox.html>.

53. Lee, C.S., et al., *Novel applications of composite structures to robots, machine tools and automobiles*. Composite structures, 2004. **66**(1): p. 17-39.
54. Lucisano, G., M. Stefanovic, and C. Fragassa, *Advanced design solutions for high-precision woodworking machines*. International Journal of Quality Research, 2016. **10**(1): p. 143-158.
55. Tlustý, J., *High-Speed Machining*. CIRP Annals, 1993. **42**(2): p. 733-738.
56. Suh, J.D., et al., *Damping characteristics of composite hybrid spindle covers for high speed machine tools*. Journal of Materials Processing Technology, 2001. **113**(1): p. 178-183.
57. Rudd, C.D., et al., *Liquid Moulding Technologies - Resin Transfer Moulding, Structural Reaction Injection Moulding and Related Processing Techniques*. 1997: Woodhead Publishing.
58. Advani, S. and K.-T. Hsiao, *Manufacturing techniques for polymer matrix composites (PMCs)*. 2012. 1-497.
59. Inc, C.I. *CYCOM® 5320-1 OUT-OF-AUTOCLAVE PREPREG*. 2012 [14/11/2017]; Available from: http://www.cytec.com/sites/default/files/files/CYT_12000_COLLECT_BROCH-CYCOM_5320-1.pdf.
60. Bodaghi, M., et al., *Experimental characterization of voids in high fibre volume fraction composites processed by high injection pressure RTM*. Composites Part A: Applied Science and Manufacturing, 2016. **82**(Supplement C): p. 88-99.
61. Williams, C., J. Summerscales, and S. Grove, *Resin Infusion under Flexible Tooling (RIFT): a review*. Composites Part A: Applied Science and Manufacturing, 1996. **27**(7): p. 517-524.
62. Summerscales, J., *A Taxonomy for Resin Infusion Processes*, in *ICMAC*. 2009: Belfast, Ireland.
63. Summerscales, J. and T. J Searle, *Low-pressure (vacuum infusion) techniques for moulding large composite structures*. Vol. 219. 2005. 45-58.
64. Correia, N.C., et al., *Analysis of the vacuum infusion moulding process: I. Analytical formulation*. Composites Part A: Applied Science and Manufacturing, 2005. **36**(12): p. 1645-1656.
65. Hammami, A. and B.R. Gebart, *Analysis of the vacuum infusion molding process*. Polymer Composites, 2000. **21**(1): p. 28-40.
66. Hsiao, K.T. and D. Heider, *10 - Vacuum assisted resin transfer molding (VARTM) in polymer matrix composites*, in *Manufacturing Techniques for Polymer Matrix Composites (PMCs)*. 2012, Woodhead Publishing. p. 310-347.

67. Li, W., et al., *Process and Performance Evaluation of the Vacuum-Assisted Process*. Journal of Composite Materials, 2004. **38**(20): p. 1803-1814.
68. Correia, N.C., et al., *Use of Resin Transfer Molding Simulation to Predict Flow, Saturation, and Compaction in the VARTM Process*. Journal of Fluids Engineering, 2004. **126**(2): p. 210-215.
69. Pirvu, A., D.J. Gardner, and R. Lopez-Anido, *Carbon fiber-vinyl ester composite reinforcement of wood using the VARTM/SCRIMP fabrication process*. Composites Part A: Applied Science and Manufacturing, 2004. **35**(11): p. 1257-1265.
70. Takeda, F., et al., *Research in the application of the VaRTM technique to the fabrication of primary aircraft composite structures*. Mitsubishi Heavy Industries. Technical Review, 2005. **42**(5).
71. Nguyen, L., T. Juska, and S. Mayes. *Evaluation of low cost manufacturing technologies for large scale composite ship structures*. in *Proceedings of the 38th Structures, Structural Dynamics and Materials Conference, Kissimmee, FL*. 1997.
72. Lazarus, P., *Resin infusion of marine composites*. Materials and Process Challenges: Aging Systems, Affordability, Alternative Applications., 1996. **41**: p. 1447-1458.
73. Griffin, D.A. and T.D. Ashwill. *Alternative composite materials for megawatt-scale wind turbine blades: design considerations and recommended testing*. in *ASME 2003 Wind Energy Symposium*. 2003. American Society of Mechanical Engineers.
74. Chajes, M.J., et al. *Delaware's First All Composite Bridge*. in *Advanced Technology in Structural Engineering*. 2000. ASCE.
75. Pike, T., M. McArthur, and D. Schade, *Vacuum assisted resin transfer modeling of a layered structural laminate for application on ground combat vehicles*. Technology transfer in a global community, 1996: p. 374-380.
76. Lewit, S.M. and J.C. Jakubowski, *Low cost VARTM process for commercial and military applications*. Society for the Advancement of Material and Process Engineering(USA), 1997: p. 1173-1187.
77. Wienhold, P.D. and J.J. Wozniak, *The application of SCRIMP VARTM fabrication technology to the compressed natural gas integrated storage system*. SAMPE journal, 1998. **34**(1): p. 5-10.
78. Garschke, C., et al., *Out-of-autoclave cure cycle study of a resin film infusion process using in situ process monitoring*. Composites Part A: Applied Science and Manufacturing, 2012. **43**(6): p. 935-944.

79. Reddy, J.N. and J.D.H. Robbins, *Theories and Computational Models for Composite Laminates*. Applied Mechanics Reviews, 1994. **47**(6): p. 147-169.
80. Cinefra, M. and S. Valvano, *A variable kinematic doubly-curved MITC9 shell element for the analysis of laminated composites*. Mechanics of Advanced Materials and Structures, 2016. **23**(11): p. 1312-1325.
81. Carrera, E., *Theories and finite elements for multilayered, anisotropic, composite plates and shells*. Archives of Computational Methods in Engineering, 2002. **9**(2): p. 87-140.
82. Clough, R.W. *The Finite Element Method in Plane Stress Analysis*. in *2nd Conference on Electronic Computation*. 1960. Pittsburgh, PA.
83. Hrennikoff, A., *Solution of Problems in Elasticity by the Frame Work Method*. Journal of Applied Mechanics, 1941. **8**(4): p. 169-175.
84. McHenry, D., *A Lattice Analogy for the Solution of Plane Stress Problems*. Journal of Institution of Civil Engineers, 1943. **21**: p. 58-82.
85. Courant, R., *Variational Methods for the Solution of Problems of Equilibrium and Vibrations*. Bulletin of the American Mathematical Society, 1943. **49**: p. 1-23.
86. Turner, M.J., et al., *Stiffness and Deflection Analysis of Complex Structures*. Journal of Aeronautical Sciences, 1956. **23**(9): p. 805-824.
87. Melosh, R.J., *A Stiffness Matrix for the Analysis of Thin Plates in Bending*. Journal of the Aerospace Sciences, 1961. **28**(1): p. 34-42.
88. Martin, H.C., *Plane Elasticity Problems and the Direct Stiffness Method*. The Trend in Engineering, 1961. **13**: p. 5-19.
89. Clough, R.W. and Y. Rashid, *Finite Element Analysis of Axisymmetric Solids*. Journal of the Engineering Mechanics Division, 1965. **91**: p. 71-85.
90. Wilson, E.L., *Structural Analysis of Axisymmetric Solids*. Journal of the American Institute of Aeronautics and Astronautics, 1965. **3**(12): p. 2269-2274.
91. Turner, M.J., et al., *Large Deflections of Structures Subjected to Heating and External Loads*. Journal of Aeronautical Sciences, 1960. **27**(2): p. 97-107.
92. Gallagher, R.H., J. Padlog, and P.P. Bijlaard, *Stress Analysis of Heated Complex Shapes*. Journal of the American Rocket Society, 1962. **32**: p. 700-707.

93. Belytschko, T., *Efficient Large-Scale Nonlinear Transient Analysis by Finite Elements*. International Journal of Numerical Methods in Engineering, 1976. **10**(3): p. 579-596.
94. Barbero, E.J., *Finite element analysis of composite materials using Abaqus*. Composite materials (CRC Press), ed. T.F.G. CRC Press. 2013.
95. Rao, S.S., *The Finite Element Method in Engineering*. 5th ed. 2011: Elsevier.
96. Reddy, J.N. and D.H. Robbins, *On Computational Strategies for Composite Laminates*, in *Advanced Technology for Design and Fabrication of Composite Materials and Structures: Applications to the Automotive, Marine, Aerospace and Construction Industry*, G.C. Sih, A. Carpinteri, and G. Surace, Editors. 1995, Springer Netherlands: Dordrecht. p. 145-169.
97. Haselbach, P.U., *An advanced structural trailing edge modelling method for wind turbine blades*. Composite Structures, 2017. **180**: p. 521-530.
98. Noor, A.K. and W.S. Burton, *Assessment of Computational Models for Multilayered Composite Shells*. Applied Mechanics Reviews, 1990. **43**(4): p. 67-97.
99. SIMULIA, *Abaqus 6.11 Theory Manual*. 2011, Providence, RI, USA: Dassault Systèmes.
100. Carrera, E. and S. Valvano, *A variable kinematic shell formulation applied to thermal stress of laminated structures*. Journal of Thermal Stresses, 2017. **40**(7): p. 803-827.
101. Noor, A.K. and M.D. Mathers, *Finite element analysis of anisotropic plates*. International Journal for Numerical Methods in Engineering, 1977. **11**(2): p. 289-307.
102. Pandya, B.N. and T. Kant, *Finite element analysis of laminated composite plates using a higher-order displacement model*. Composites Science and Technology, 1988. **32**(2): p. 137-155.
103. Mantari, J.L., A.S. Oktem, and C. Guedes Soares, *A new trigonometric layerwise shear deformation theory for the finite element analysis of laminated composite and sandwich plates*. Computers & Structures, 2012. **94-95**: p. 45-53.
104. Carrera, E. and L. Demasi, *Classical and advanced multilayered plate elements based upon PVD and RMVT. Part 1: Derivation of finite element matrices*. International Journal for Numerical Methods in Engineering, 2002. **55**(2): p. 191-231.
105. Carrera, E. and L. Demasi, *Classical and advanced multilayered plate elements based upon PVD and RMVT. Part 2: Numerical implementations*. International Journal for Numerical Methods in Engineering, 2002. **55**(3): p. 253-291.

106. Cox, K. and A. Echtermeyer, *Structural Design and Analysis of a 10MW Wind Turbine Blade*. Energy Procedia, 2012. **24**: p. 194-201.
107. Shokrieh, M.M. and R. Rafiee, *Simulation of fatigue failure in a full composite wind turbine blade*. Composite Structures, 2006. **74**(3): p. 332-342.
108. Bletzinger, K.-U., M. Bischoff, and E. Ramm, *A unified approach for shear-locking-free triangular and rectangular shell finite elements*. Computers & Structures, 2000. **75**(3): p. 321-334.
109. Oliveira Junior, H.A., et al., *Stochastic Global Optimization and Its Applications with Fuzzy Adaptive Simulated Annealing*. 2012: Springer Heidelberg.
110. Wolpert, D.H. and W.G. Macready, *No free lunch theorems for optimization*. Evolutionary Computation, IEEE Transactions on, 1997. **1**(1): p. 67-82.
111. Guohua, W., M. Rammohan, and S. Ponnuthurai Nagaratnam, *Ensemble strategies for population-based optimization algorithms – A survey*. Swarm and Evolutionary Computation, 2019. **44**: p. 695-711.
112. Conn, A. and P. Toint, *An Algorithm using Quadratic Interpolation for Unconstrained Derivative Free Optimization*, in *Nonlinear Optimization and Applications*, G. Di Pillo and F. Giannessi, Editors. 1996, Springer US. p. 27-47.
113. Holmstrom, A., *Derivative-free Algorithms in Engineering Optimization*. 2000, Chalmers University of Technology: Goteborg. p. 43.
114. Queipo, N.V., et al., *Surrogate-based analysis and optimization*. Progress in Aerospace Sciences, 2005. **41**(1): p. 1-28.
115. Rao, S.S., *Engineering Optimization: Theory and Practice*. 2009: John Wiley & Sons, Inc.
116. Khuri, A. and S. Mukhopadhyay, *Response surface methodology*. Wiley Interdisciplinary Reviews: Computational Statistics, 2010. **2**(2): p. 128-149.
117. Jones, D., *A Taxonomy of Global Optimization Methods Based on Response Surfaces*. Journal of Global Optimization, 2001. **21**(4): p. 345-383.
118. Bezerra, M.A., et al., *Response surface methodology (RSM) as a tool for optimization in analytical chemistry*. Talanta, 2008. **76**(5): p. 965-977.
119. Baş, D. and İ.H. Boyacı, *Modeling and optimization I: Usability of response surface methodology*. Journal of Food Engineering, 2007. **78**(3): p. 836-845.

120. Charles, A., et al., *A surrogate-model-based method for constrained optimization*, in *8th Symposium on Multidisciplinary Analysis and Optimization*. 2000, American Institute of Aeronautics and Astronautics.
121. Hooke, R. and T.A. Jeeves, *Direct search solution of numerical and statistical problems*. J. Assoc. Comput. Mach., 1961. **8**: p. 8.
122. Torczon, V., *On the Convergence of Pattern Search Algorithms*. SIAM Journal on Optimization, 1997. **7**(1): p. 1-25.
123. Kolda, T.G., R.M. Lewis, and V. Torczon, *Optimization by Direct Search: New Perspectives on Some Classical and Modern Methods*. SIAM Review, 2003. **45**(3): p. 385-482.
124. Nelder, J.A. and R. Mead, *A simplex method for function minimization*. The Computer Journal, 1965. **7**(4): p. 308-313.
125. Halim, A.H., I. Ismail, and S. Das, *Performance assessment of the metaheuristic optimization algorithms: an exhaustive review*. Artificial Intelligence Review, 2021. **54**(3): p. 2323-2409.
126. Kaveh, A., *Advances in Metaheuristic Algorithms for Optimal Design of Structures*. 2014: Springer.
127. Bianchi, L., et al., *A survey on metaheuristics for stochastic combinatorial optimization*. Natural Computing, 2009. **8**(2): p. 239-287.
128. Blum, C. and A. Roli, *Metaheuristics in combinatorial optimization: Overview and conceptual comparison*. ACM Comput. Surv., 2003. **35**(3): p. 268-308.
129. Gonzalez, T., *Handbook of approximation algorithms and metaheuristics*. Computer and information science series, ed. B.R. Chapman & Hall/CRC, FL. 2007.
130. Yang, X.-S., *Nature-inspired metaheuristic algorithms*. 2nd edn. ed, ed. U. Luniver Press. 2010.
131. Osman, I. and G. Laporte, *Metaheuristics: A bibliography*. Annals of Operations Research, 1996. **63**(5): p. 511-623.
132. Haiping, M., et al., *Multi-population techniques in nature inspired optimization algorithms: A comprehensive survey*. Swarm and Evolutionary Computation, 2019. **44**: p. 365-387.
133. Yang, X.S., *Engineering Optimization - An Introduction with Metaheuristic Applications* 2010: John Wiley & Sons, Inc.
134. Gendreau, M. and J. Potvin, *Handbook of Metaheuristics*. 2nd ed. 2010: Springer.
135. Boussaïd, I., J. Lepagnot, and P. Siarry, *A survey on optimization metaheuristics*. Information Sciences, 2013. **237**(0): p. 82-117.

136. Rios, L. and N. Sahinidis, *Derivative-free optimization: a review of algorithms and comparison of software implementations*. Journal of Global Optimization, 2013. **56**(3): p. 1247-1293.
137. Angeline, P., *Evolutionary optimization versus particle swarm optimization: Philosophy and performance differences*, in *Evolutionary Programming VII*, V.W. Porto, et al., Editors. 1998, Springer Berlin Heidelberg. p. 601-610.
138. Pham, D.T. and M. Castellani, *Benchmarking and comparison of nature-inspired population-based continuous optimisation algorithms*. Soft Computing, 2014. **18**(5): p. 871-903.
139. Deb, K., *Multi-Objective Optimization using Evolutionary Algorithms*. 2001: JOHN WILEY & SONS, LTD.
140. Adam, P.P., J.N. Jaroslaw, and E.P. Agnieszka, *Population size in Particle Swarm Optimization*. Swarm and Evolutionary Computation, 2020. **58**: p. 100718.
141. Blum, C. and D. Merkle, *Swarm Intelligence - Introduction and Applications*. Natural Computing Series. 1998: Springer.
142. Eberhart, R. and J. Kennedy. *A new optimizer using particle swarm theory*. in *Micro Machine and Human Science, 1995. MHS '95., Proceedings of the Sixth International Symposium on*. 1995.
143. Kennedy, J. and R. Eberhart. *Particle swarm optimization*. in *Neural Networks, 1995. Proceedings., IEEE International Conference on*. 1995.
144. Vaz, A.I.F. and L.N. Vicente, *PSwarm: a hybrid solver for linearly constrained global derivative-free optimization*. Optimization Methods and Software, 2009. **24**(4-5): p. 669-685.
145. Kennedy, J. and R. Eberhart, *Swarm Intelligence*. The Morgan Kaufmann Series in Evolutionary Computation, ed. D. Fogel. 2001: Academic Press.
146. Kennedy, J. and W.M. Spears. *Matching algorithms to problems: an experimental test of the particle swarm and some genetic algorithms on the multimodal problem generator*. in *Evolutionary Computation Proceedings, 1998. IEEE World Congress on Computational Intelligence., The 1998 IEEE International Conference on*. 1998.
147. Duan, Y., R.G. Harley, and T.G. Habetler. *Comparison of Particle Swarm Optimization and Genetic Algorithm in the design of permanent magnet motors*. in *Power Electronics and Motion Control Conference, 2009. IPEMC '09. IEEE 6th International*. 2009.

148. Hassan, R., et al., *A Comparison of Particle Swarm Optimization and the Genetic Algorithm*, in *46th AIAA/ASME/ASCE/AHS/ASC Structures, Structural Dynamics & Materials Conference*. 2005, American Institute of Aeronautics and Astronautics, Inc.: Austin, Texas.
149. Xiao, C.-L. and H.-X. Huang, *Optimal design of heating system for rapid thermal cycling mold using particle swarm optimization and finite element method*. *Applied Thermal Engineering*, 2014. **64**(1–2): p. 462-470.
150. Loja, M.A.R., *On the use of particle swarm optimization to maximize bending stiffness of functionally graded structures*. *Journal of Symbolic Computation*, 2014. **61–62**(0): p. 12-30.
151. Zahara, E. and Y.-T. Kao, *Hybrid Nelder-Mead simplex search and particle swarm optimization for constrained engineering design problems*. Vol. 36. 2009. 3880-3886.
152. Lin, H. *Hybridizing Differential Evolution and Nelder-Mead Simplex Algorithm for Global Optimization*. in *2016 12th International Conference on Computational Intelligence and Security (CIS)*. 2016.
153. Fan, S.-K.S. and E. Zahara, *A hybrid simplex search and particle swarm optimization for unconstrained optimization*. *European Journal of Operational Research*, 2007. **181**(2): p. 527-548.
154. Vaz, A.I.F. and L.N. Vicente, *A particle swarm pattern search method for bound constrained global optimization*. *Journal of Global Optimization*, 2007. **39**(2): p. 197-219.
155. Khwaja, A.S., M. Naeem, and A. Anpalagan, *Pattern-Search-Based Nonconvex Cooperative Sensing in Multiband Cognitive Radio Systems*. *IEEE Systems Journal*, 2016. **10**(2): p. 580-591.
156. Adeyemo, J. and D. Stretch, *Review of hybrid evolutionary algorithms for optimizing a reservoir*. *South African Journal of Chemical Engineering*, 2018. **25**: p. 22-31.
157. Vaz, A.I.F. *PSwarm Home Page*. 2010 24/01/2018]; Available from: <http://www.norg.uminho.pt/aivaz/pswarm/>.
158. Muc, A., *Optimal design of composite multilayered plated and shell structures*. *Thin-Walled Structures*, 2007. **45**(10): p. 816-820.
159. An, H., J. Singh, and D. Pasini, *Structural efficiency metrics for integrated selection of layup, material, and cross-section shape in laminated composite structures*. *Composite Structures*, 2017. **170**: p. 53-68.
160. Mazen, A.A., et al., *Efficient design optimization of nonconventional laminated composites using lamination parameters: A state of the art*. *Composite Structures*, 2019. **209**: p. 362-374.

161. Nikbakt, S., S. Kamarian, and M. Shakeri, *A review on optimization of composite structures Part I: Laminated composites*. Composite Structures, 2018. **195**: p. 158-185.
162. Kirsch, U., *Design-Oriented Analysis of Structures—A Unified Approach*. Vol. 129. 2003.
163. Kirsch, U., *Optimal Topologies of Structures*. Applied Mechanics Reviews, 1989. **42**(8): p. 223-239.
164. Conn, A.R., K. Scheinberg, and L.N. Vicente, *Introduction to Derivative-Free Optimization*. MPS-SIAM Book Series on Optimization, ed. SIAM. 2009.
165. Yildiz, A.R., H. Abderazek, and S. Mirjalili, *A Comparative Study of Recent Non-traditional Methods for Mechanical Design Optimization*. Archives of Computational Methods in Engineering, 2020. **27**(4): p. 1031-1048.
166. Aceves, C.M., A.A. Skordos, and M.P.F. Sutcliffe, *Design selection methodology for composite structures*. Materials & Design, 2008. **29**(2): p. 418-426.
167. Lund, E. and J. Stegmann, *On structural optimization of composite shell structures using a discrete constitutive parametrization*. Wind Energy, 2005. **8**(1): p. 109-124.
168. Lund, E., *Buckling topology optimization of laminated multi-material composite shell structures*. Composite Structures, 2009. **91**(2): p. 158-167.
169. Lindgaard, E. and E. Lund, *Nonlinear buckling optimization of composite structures*. Computer Methods in Applied Mechanics and Engineering, 2010. **199**(37–40): p. 2319-2330.
170. Maalawi, K.Y. and H.M. Negm, *Optimal frequency design of wind turbine blades*. Journal of Wind Engineering and Industrial Aerodynamics, 2002. **90**(8): p. 961-986.
171. Omkar, S.N., et al., *Quantum behaved Particle Swarm Optimization (QPSO) for multi-objective design optimization of composite structures*. Expert Systems with Applications, 2009. **36**(8): p. 11312-11322.
172. Omkar, S.N., et al., *Vector evaluated particle swarm optimization (VEPSO) for multi-objective design optimization of composite structures*. Computers & Structures, 2008. **86**(1): p. 1-14.
173. Monroy Aceves, C., et al., *Design methodology for composite structures: A small low air-speed wind turbine blade case study*. Materials & Design, 2012. **36**(0): p. 296-305.
174. Liu, B., S. Koziel, and Q. Zhang, *A multi-fidelity surrogate-model-assisted evolutionary algorithm for computationally expensive optimization problems*. Journal of Computational Science, 2016. **12**: p. 28-37.

175. Liu, T.-W., et al., *Multi-objective optimisation designs for thin-walled deployable composite hinges using surrogate models and Genetic Algorithms*. *Composite Structures*, 2022. **280**: p. 114757.
176. Rohit, G.R., J.M. Prajapati, and V.B. Patel, *Structural Shape Optimization By Coupled FE-MM and Swarm Intelligence-Based Algorithm*. *International Journal of Computational Methods*, 2020. **0**(0): p. 2050048.
177. Paluch, B., M. Grédiac, and A. Faye, *Combining a finite element programme and a genetic algorithm to optimize composite structures with variable thickness*. *Composite Structures*, 2008. **83**(3): p. 284-294.
178. An, H., S. Chen, and H. Huang, *Simultaneous optimization of stacking sequences and sizing with two-level approximations and a genetic algorithm*. *Composite Structures*, 2015. **123**: p. 180-189.
179. Fagan, E.M., et al., *Physical experimental static testing and structural design optimisation for a composite wind turbine blade*. *Composite Structures*, 2017. **164**: p. 90-103.
180. Jureczko, M., M. Pawlak, and A. Meżyk, *Optimisation of wind turbine blades*. *Journal of Materials Processing Technology*, 2005. **167**(2–3): p. 463-471.
181. Chen, J., et al., *Structural optimization study of composite wind turbine blade*. *Materials & Design*, 2013. **46**(0): p. 247-255.
182. Nolet, S.C., *Composite Wind Blade Engineering and Manufacturing*. 2011.
183. Roth-Johnson, P. and R.E. Wirz, *Aero-structural investigation of biplane wind turbine blades*. *Wind Energy*, 2014. **17**(3): p. 397-411.
184. Vianna Neto, J.X., et al., *Wind turbine blade geometry design based on multi-objective optimization using metaheuristics*. *Energy*, 2018. **162**: p. 645-658.
185. Garambois, P., S. Besset, and L. Jézéquel, *Multi-objective structural robust optimization under stress criteria based on mixed plate super-elements and genetic algorithms*. *Structural and Multidisciplinary Optimization*, 2016. **53**(2): p. 205-213.
186. Sun, S.H., et al., *Structural shape optimization by IGABEM and particle swarm optimization algorithm*. *Engineering Analysis with Boundary Elements*, 2018. **88**: p. 26-40.
187. Ertas, A.H., *Optimization of Fiber-Reinforced Laminates for a Maximum Fatigue Life by Using the Particle Swarm Optimization. Part II*. *Mechanics of Composite Materials*, 2013. **49**(1): p. 107-116.
188. Kovács, G., et al., *Analysis and optimum design of fibre-reinforced composite structures*. *Structural and Multidisciplinary Optimization*, 2004. **28**(2): p. 170-179.

189. Kathiravan, R. and R. Ganguli, *Strength design of composite beam using gradient and particle swarm optimization*. Composite Structures, 2007. **81**(4): p. 471-479.
190. Chen, J., et al., *Optimal design of composite laminates for minimizing delamination stresses by Particle Swarm Optimization combined with FEM*. Vol. 22. 2009. 665-683.
191. Chen, J., R. Ge, and J. Wei, *Probabilistic optimal design of laminates using improved particle swarm optimization*. Engineering Optimization, 2008. **40**(8): p. 695-708.
192. Fourie, P.C. and A.A. Groenwold, *The particle swarm optimization algorithm in size and shape optimization*. Structural and Multidisciplinary Optimization, 2002. **23**(4): p. 259-267.
193. Li, S. and M. Yang, *Particle swarm optimization combined with finite element method for design of ultrasonic motors*. Sensors and Actuators A: Physical, 2008. **148**(1): p. 285-289.
194. Perez, R.E. and K. Behdinan, *Particle swarm approach for structural design optimization*. Computers & Structures, 2007. **85**(19-20): p. 1579-1588.
195. Gao, Y., W. Du, and G. Yan, *Selectively-informed particle swarm optimization*. Scientific Reports, 2015. **5**: p. 9295.
196. Logan, D.L., *A First Course in the Finite Element Method*. 5th ed. 2012: Global Engineering.
197. Eslami, M.R., *Finite Elements Methods in Mechanics*. Solid Mechanics and Its Applications. 2014: Springer International Publishing.
198. Segerlind, L.J., *Applied Finite Element Analysis*. 2011: Wiley.
199. Zhuang, Z., et al., *Extended Finite Element Method*. 1st ed. 2014: Elsevier.
200. Brenner, S.C. and L.R. Scott, *The Mathematical Theory of Finite Element Methods*. 3rd ed. Texts in Applied Mathematics. 2008: Springer Science.
201. Fagan, M.J., *Finite Element Analysis*. 1992: Pearson Education
202. SIMULIA, *Abaqus 6.11 Analysis User's Manual*. Vol. Volume IV: Elements. 2011, Providence, RI, USA: Dassault Systèmes.
203. Larson, M.G. and F. Bengzon, *The Finite Element Method: Theory, Implementation, and Applications*. 2013: Springer.
204. Schmit, L.A. and B. Farshi, *Optimum laminate design for strength and stiffness*. International Journal for Numerical Methods in Engineering, 1973. **7**(4): p. 519-536.
205. Griva, I., S.G. Neash, and A. Sofer, *Linear and Nonlinear Optimization*. 2nd Edition ed. 2009, United States of America: Society for Industrial and Applied Mathematics. 740.

206. Adira - Homepage [cited 2018 28/02/2018]; Available from: <http://www.adira.pt>.
207. Bezugo, F.R.M., *Aplicação de técnicas Lean na montagem laser na ADIRA, S.A.* 2010, FEUP - Faculdade de Engenharia da Universidade do Porto. p. 69.
208. Bragança, T.F.G., *Sensorização de uma Máquina de Corte por Laser.* 2013, FEUP - Faculdade de Engenharia da Universidade do Porto. p. 69.
209. Estrela, J.M.A., *Racionalização da máquina de corte a laser CCL 3015 na ADIRA S.A.*, in *FEUP - Faculty of Engineering.* 2009, University of Porto: Porto. p. 115.
210. Silva, M.E.R.D., *Instalação, teste e lançamento em exploração de equipamentos de corte por laser.* 2008, FEUP - Faculdade de Engenharia da Universidade do Porto. p. 77.
211. Heisel, U. and M. Gringel, *Machine tool design requirements for high-speed machining.* CIRP Annals-Manufacturing Technology, 1996. **45**(1): p. 389-392.
212. Abdelkader, B. and K. Stanisław, *Multidisciplinary design optimization of aircraft wing using commercial software integration.* Aerospace Science and Technology, 2019. **92**: p. 766-776.
213. Shanker, A., R.W. Sullivan, and D.A. Drake, *Elastic Properties of CYCOM 5320-1/T650 at Elevated Temperatures Using Response Surface Methodology*, in *Composite, Hybrid, and Multifunctional Materials, Volume 4: Proceedings of the 2014 Annual Conference on Experimental and Applied Mechanics*, G. Tandon, Editor. 2015, Springer International Publishing: Cham. p. 29-37.
214. Shedden, J., *Simplifying the Testing and Calculation of Fracture Toughness of Thermoplastic and Thermoset Matrix Composite Materials*, in *Materials Engineering Department.* 2013, California Polytechnic State University: San Luis Obispo.
215. Jones, R.M., *Mechanics of Composite Materials.* 2nd ed. ed. (1999). : CRC Press.
216. da Silva, L.F.M., *Failure Strength Tests*, in *Handbook of Adhesion Technology*, L.F.M. da Silva, A. Öchsner, and R.D. Adams, Editors. 2011, Springer.
217. Cooper, P.A. and J.W. Sawyer *A Critical Examination of Stress in an Elastic Single Lap Joint.* 1979.

Appendix A – Woven Carbon Fibre Fabric Datasheet

PRODUCT LIST

Woven Fabric

Regular Woven Fabric

Designation	Style	Yarn		Count (ends/inch)		Weight (g/m ²)	Thickness (mm)	Width (mm)	Length (m)
		Warp	Fill	Warp	Fill				
TR3110M	Plain	TR30S 3L	TR30S 3L	12.5	12.5	200	0.23	1000	100
TR3523M	2x2Twill	TR30S 3L	TR30S 3L	12.5	12.5	200	0.20	1000	100
TR6110HM	Plain	TR50S 6L	TR50S 6L	9.0	9.0	288	0.32	1000	100
TR6120HM	Plain	TR50S 6L	TR50S 6L	11.0	11.0	350	0.39	1000	100
TRK101M	Plain	TR50S 12L	TR50S 12L	6.3	6.3	400	0.46	1000	50
TRK510M	2x2Twill	TR50S 12L	TR50S 12L	10.0	10.0	646	0.57	1000	50

Hybrid Woven Fabric

TR3160TMS	Plain	TR30S 3L	TR30S 3L	6.0	6.0	180	0.24	1000	100
		Aramid Fiber	Aramid Fiber	6.0	6.0				
TR3163TMS	Plain	TR30S 3L	TR30S 3L	9.0	9.0	184	0.23	1000	100
		Aramid Fiber	Aramid Fiber	3.0	3.0				

Unidirectional Fabric

TRK979PQRW	Plain	TR50D 12L	Glass Fiber Polyamide Fiber	6.6	8.0	212	0.25	500	50
TRK976PQRW	Plain	TR50D 12L	Glass Fiber Polyamide Fiber	9.9	8.0	317	0.33	500	50

Important: The technical information contained herein is not to be construed as warranties and no patent liability can be assumed.
This information can be used for material selection purposes only. JANUARY, 2013

Appendix B – Carbon Fibre Mechanical Properties

Typical Properties of Carbon Fiber

PYROFIL™

	Type	Number of Filaments	Filament Diameter	Yield	Tensile Strength			Tensile Modulus			Elongation %	Density g/cm3
			μ m		mg/m	kg/mm2	Mpa	Ksi	ton/mm2	GPa		
HT Series	TR 30S 3L	3,000	7	200	420	4,120	600	24.0	234	34	1.8	1.79
	TR 50S 6L	6,000	7	400	500	4,900	710	24.5	240	35	2.0	1.82
	TR 50S12L	12,000	7	800								
	TR 50S15L	15,000	7	1,000	510	5,000	720	24.5	240	35	2.1	1.82
	TR 50D12L	12,000	7	800								
	TRH50 18M	18,000	6	1000								
	TRH50 60M	60,000	6	3,200	490	4,830	700	25.5	250	36	1.9	1.81
	TRW40 50L	50,000	8	3,750	420	4,120	600	24.5	240	35	1.7	1.80
IM Series	MR 60H 24P	24,000	5	960	580	5,680	820	29.5	290	42	1.9	1.81
HM Series	MS 40 12M	12,000	6	600	450	4,410	640	35.0	345	50	1.3	1.77
	HR 40 12M	12,000	6	600	450	4,410	640	40.0	395	57	1.1	1.82
	HS 40 12P	12,000	5	430	470	4,610	670	46.0	455	65	1.0	1.85

GRAFIL™

	Type	Number of Filaments	Filament Diameter	Yield	Tensile Strength			Tensile Modulus			Elongation %	Density g/cm3
			μ m		mg/m	kg/mm2	Mpa	Ksi	ton/mm2	GPa		
HT Series	34-700	12,000	7	800	490	4,830	700	24.0	234	34	2.0	1.80
		24,000	7	1,600								
	37-800	30,000	6	1,675	560	5,520	800	26.0	255	37	2.1	1.81

Important: The technical information contained herein is not to be construed as warranties and no patent liability can be assumed. This information can be used for material selection purposes only.

NOVEMBER 2013

Appendix C – EPIKOTE™ Resin 04908 and EPIKURE™ Curing Agent 04908 Datasheet

BAKELITE® EPR 04908
BAKELITE® EPH 04908
new name: EPIKOTE™ Resin 04908
new name: EPIKURE™ Curing Agent 04908

Features

- Certified by German Lloyd
- Low viscosity
- Extended potlife
- Low exothermic heat

Application

Low viscous resin system designed for infusion applications with excellent wetting and adhesion characteristics on fibreglass, carbon- or aramid-fibres, particularly in boats and yacht-building and production of rotor blades. This system make it possible to manufacture construction elements of a superior quality, with outstanding surface characteristics and good resistance to thermal deformation and weathering.

Product physical properties: (at time of manufacturing)			
Property	Unit	EPR 04908	EPH 04908
Viscosity at 25°C	mPa·s	500 ± 250	10 ± 5
Epoxy equivalent weight	g/equiv.	165 ± 3	
Amine equivalent weight	g/equiv.		50
Density at 20°C	g/cm ³	1.15 ± 0.02	0.93 ± 0.02
Refractive index at 25°C		1.540 ± 0.003	1.468 ± 0.003
Mixing viscosity at 25°C	mPa·s		130 ± 10
Pot life at 25°C	minutes		300 ± 50
T _g (TMA)	°C		82

ATE-E1 Rev 02/07/06

In the process of international testing system harmonization, the national standards previously used are being increasingly replaced by ISO (DIN EN ISO) standards. All information, recommendations and suggestions offered by Hexion Specialty Chemicals GmbH, whether orally, in written form or in database, are provided to the best of our knowledge and belief. However, they may not be construed as legally binding statements and do not represent the basis of either a guarantee or specification. The same applies analogously to the data parameters stated for examples of cured binder systems; these represent analytical results and are only intended to simplify advance selection of the individual components of a binder. This information, these recommendations and suggestions describe our products and possible applications in general or exemplary terms, but do not refer to specific cases. Changes in the data parameters, tests and illustrations can result from the constant process of technical development and improvement of our products; possible changes are not specially mentioned in the text. Our support does not free the customer from the obligation to conduct their own review of our current information literature, in particular our product data sheets, safety data sheets and technical information leaflets. The customer must carry out tests of our products on its own responsibility to determine their suitability for the intended processes and uses, as well as to establish whether their processing characteristics are appropriate in a specific case, since the technical uses of our products are numerous and can vary widely in a specific instance. Therefore, such factors do not fall within our control, and are the exclusive responsibility of the customer. If a specific assurance of data parameters should be required, an appropriate agreement must be reached in this effect. Any applicable patents, existing laws and regulations must be observed by the customer in case of our products on its own responsibility. This publication does not represent a license, nor does it intend to indicate or

Page 1 of 4

Varziner Straße 49
47135 Duisburg-Melderich
Postfach 120552
47125 Duisburg
Germany
Phone: +49 (0) 203 42 96 01
Fax: +49 (0) 203 42 54 222
www.hexionchem.com

BAKELITE® EPR 04908
BAKELITE® EPH 04908
new name: EPIKOTE™ Resin 04908
new name: EPIKURE™ Curing Agent 04908

Processing Details

Mixing ratio

EPR 04908 100 parts by weight
EPH 04908 30 parts by weight

Mixing tolerance

The maximum allowable mixing tolerance is ± 2 pbw, but it is particularly important to observe the recommend mixing ratio as exactly as possible. Adding more or less hardener will not effect a faster or slower reaction - but an incomplete curing which cannot correct in any way. Resin and hardener must be mixed very thoroughly. Mix until no clouding is visible in the mixing container. Pay special attention to the walls and the bottom of the mixing container.

Processing temperature

A good processing temperature is in the range between 25°C and 35°C. Higher processing temperatures are possible but will shorten the pot life. A rise in temperature of 10°C reduces the pot life by approx. 50%. Different temperatures during processing have no significant effect on the strength of the hardened product. Do not mix large quantities at elevated processing temperatures. The mixture will heat up fast because of the dissipating reaction heat (exothermic reaction). This can result in temperatures of more than 200°C in the mixing container.

Exemplify curing cycle:

4- 6h at 80°C

ATE-E1 Rev 02/07/06

In the process of international testing system harmonization, the national standards previously used are being increasingly replaced by ISO (DIN EN ISO) standards. All information, recommendations and suggestions offered by Hexion Specialty Chemicals GmbH, whether orally, in written form or in database, are provided to the best of our knowledge and belief. However, they may not be construed as legally binding statements and do not represent the basis of either a guarantee or specification. The same applies analogously to the data parameters stated for examples of cured binder systems; these represent analytical results and are only intended to simplify advance selection of the individual components of a binder. This information, these recommendations and suggestions describe our products and possible applications in general or exemplary terms, but do not refer to specific cases. Changes in the data parameters, tests and illustrations can result from the constant process of technical development and improvement of our products; possible changes are not specially mentioned in the text. Our support does not free the customer from the obligation to conduct his own review of our current information literature, in particular our product data sheets, safety data sheets and technical information leaflets. The customer must carry out tests of our products on its own responsibility to determine their suitability for the intended processes and uses, as well as to establish whether their processing characteristics are appropriate in a specific case, since the technical uses of our products are numerous and can vary widely in a specific instance. Therefore, such factors do not fall within our control, and are the exclusive responsibility of the customer. If a specific assurance of data parameters should be required, an appropriate agreement must be reached in this effect. Any applicable patents, existing laws and regulations must be observed by the customer on use of our products on its own responsibility. This publication does not constitute a contract. See also the relevant conditions of sale.

Page 2 of 4

Varziner Straße 49
47135 Duisburg-Melderich
Postfach 120552
47125 Duisburg
Germany
Phone: +49 (0) 203 42 96 01
Fax: +49 (0) 203 42 54 222
www.hexionchem.com

BAKELITE® EPR 04908
BAKELITE® EPH 04908
new name: EPIKOTE™ Resin 04908
new name: EPIKURE™ Curing Agent 04908

Properties of the cured, non-reinforced resin system (curing: 4h at 70°C + 6h at 80°C)		
Property	Unit	Value
Density	g/cm ³	1.15
Tensile strength	MPa	74
Tensile strain	%	9.4
Modulus in tensile	MPa	2900
Flexural strength	MPa	112
Modulus in flexure	MPa	3100
Water absorption after 24h 23°C	pbw	0,180
Water absorption after 168h 23°C	pbw	0,432

Properties of the cured, reinforced resin system (curing: 4h at 70°C + 6h at 80°C)		
Property	Unit	Value
Tensile strength	MPa	447
Flexural strength	MPa	588
Modulus in flexure	MPa	23400
ILSS	MPa	40
T _g (DMTA)	°C	89

The values are measured on laminates made with glass fabric 181/Interglas 91745.

ATE-E1 Rev 02/07/06

In the process of international testing system harmonization, the national standards previously used are being increasingly replaced by ISO (DIN EN ISO) standards. All information, recommendations and suggestions offered by Hexion Specialty Chemicals GmbH, whether orally, in written form or in database, are provided to the best of our knowledge and belief. However, they may not be construed as legally binding statements and do not represent the basis of either a guarantee or specification. The same applies analogously to the data parameters stated for examples of cured binder systems; these represent analytical results and are only intended to simplify advance selection of the individual components of a binder. This information, these recommendations and suggestions describe our products and possible applications in general or exemplary terms, but do not refer to specific cases. Changes in the data parameters, tests and illustrations can result from the constant process of technical development and improvement of our products; possible changes are not specially mentioned in the text. Our support does not free the customer from the obligation to conduct his own review of our current information literature, in particular our product data sheets, safety data sheets and technical information leaflets. The customer must carry out tests of our products on its own responsibility to determine their suitability for the intended processes and uses, as well as to establish whether their processing characteristics are appropriate in a specific case, since the technical uses of our products are numerous and can vary widely in a specific instance. Therefore, such factors do not fall within our control, and are the exclusive responsibility of the customer. If a specific assurance of data parameters should be required, an appropriate agreement must be reached to this effect. Any applicable patents, existing laws and regulations must be observed by the customer on use of our products on its own responsibility. This publication does not constitute a contract. See also the technical information on

Page 3 of 4

Varziner Straße 49
47135 Duisburg-Melderich
Postfach 120552
47125 Duisburg
Germany
Phone: +49 (0) 203 42 96 01
Fax: +49 (0) 203 42 54 222
www.hexionchem.com

BAKELITE® EPR 04908
BAKELITE® EPH 04908
new name: EPIKOTE™ Resin 04908
new name: EPIKURE™ Curing Agent 04908

Shelf life

The resin and hardener can be stored at 20- 25°C for at least 12 months in their carefully sealed original containers.

It is rarely possible that the resin or the hardener crystallize at temperatures below 15°C. The crystallisation is visible as a clouding or solidification of the content of the container. Before processing, the crystallisation must be removed by warming up. Slow warming up to 50- 60°C in a water bath or oven and stirring or shaking will clarify the contents in the container without any loss of quality. Use only completely clarify products. Before warming up, open containers slightly to permit equalization of pressure. Caution during warm up! Do not warm up over open flame!

Precautions

When handling epoxy resins and hardeners, will you please observe the APME documentation "Epoxy resins and curing agents".

ATE-E1 Rev 02/07/06

In the process of international testing system harmonization, the national standards previously used are being increasingly replaced by ISO (DIN EN ISO) standards. All information, recommendations and suggestions offered by Hexion Specialty Chemicals GmbH, whether orally, in written form or in database, are provided to the best of our knowledge and belief. However, they may not be construed as legally binding statements and do not represent the basis of either a guarantee or specification. The same applies analogously to the data parameters stated for examples of cured binder systems; these represent analytical results and are only intended to simplify advance selection of the individual components of a binder. This information, these recommendations and suggestions describe our products and possible applications in general or exemplary terms, but do not refer to specific cases. Changes in the data parameters, tests and illustrations can result from the constant process of technical development and improvement of our products; possible changes are not specially mentioned in the text. Our support does not free the customer from the obligation to conduct his own review of our current information literature, in particular our product data sheets, safety data sheets and technical information leaflets. The customer must carry out tests of our products on its own responsibility to determine their suitability for the intended processes and uses, as well as to establish whether their processing characteristics are appropriate in a specific case, since the technical uses of our products are numerous and can vary widely in a specific instance. Therefore, such factors do not fall within our control, and are the exclusive responsibility of the customer. If a specific assurance of data parameters should be required, an appropriate agreement must be reached to this effect. Any applicable patents, existing laws and regulations must be observed by the customer on use of our products on its own responsibility. This publication does not represent a contract. See also the technical information on

Page 4 of 4

Varziner Straße 49
47135 Duisburg-Melderich
Postfach 120552
47125 Duisburg
Germany
Phone: +49 (0) 203 42 96 01
Fax: +49 (0) 203 42 54 222
www.hexionchem.com

Appendix D – EPIKURE™ Curing Agent 3253 Datasheet



Technical Data Sheet

Re-issued August 2007

EPIKURE™ Curing Agent 3253

Product Description

EPIKURE™ Curing Agent 3253, a tertiary amine, is tris (dimethyl amino-methyl) phenol. It is most often used as a co-activating accelerator for other epoxy resin curing agents including polyamides, fatty amidoamines, polysulfides and acid anhydrides. Secondary uses include catalysts for urethane elastomers, isocyanurate foams, epoxy homopolymerization and isocyanate trimerization.

Application Areas/Suggested Uses

- Accelerator for epoxy resin curing agents
- Catalyst for polyurethane elastomers
- Catalyst for isocyanurate foams
- Catalyst for isocyanate trimerization

Benefits

- High reactivity
- Low viscosity
- Low vapor pressure
- Good color

Sales Specification

Property	Units	Value	Test Method/Standard
Viscosity at 25°C	cP	180-380	ASTM D2196
Color	Gardner	6 max.	ASTM D1544
Water	% wt.	0.5	ASTM E203

Typical Properties

Property	Units	Value	Test Method/Standard
Amine value	mg/g	610 – 635	ASTM D2896
Pounds/gallon @ 25 °C	lbs/gal	8.1	ASTM D1475
Appearance		Clear and free of	

EPIKURE Curing Agent 3253

		foreign particles	

General Information

Table 1 / **Performance data**

	<u>Method</u>	<u>Units</u>	<u>Value</u>
Epoxy Resin, Bis-A type (EEW=190)		pbw	100
EPIKURE Curing Agent 3253		pbw	3.0
Handling Properties @ 25°C			
Pot Life, 25g		minutes	38
Cured State Properties			
HDT	ASTM D648	°C	91

Table 2 / **Starting point formulations**

<u>Polymeric system</u>	<u>phr</u>	<u>Application</u>
epoxy/aliphatic amines, polyamides and amidoamines	2-4	coatings, adhesives to wet concrete
epoxy/polysulfides	7-15	sealants, concrete adhesives
epoxy homopolymerization	9-11	bake cured adhesives and coatings
isocyanate trimerization	0.5-10	polyisocyanurate foams
polyol/isocyanate	1-2	urethane foams

Safety, Storage & Handling

Please refer to the MSDS for the most current Safety and Handling information.

EPIKURE Curing Agent 3253

Please refer to the Hexion web site for Shelf Life and recommended Storage information.

Product will absorb moisture and carbon dioxide which may affect viscosity or create foaming when reacted with epoxy resins.

Exposure to these materials should be minimized and avoided, if feasible, through the observance of proper precautions, use of appropriate engineering controls and proper personal protective clothing and equipment, and adherence to proper handling procedures. None of these materials should be used, stored, or transported until the handling precautions and recommendations as stated in the Material Safety Data Sheet (MSDS) for these and all other products being used are understood by all persons who will work with them. Questions and requests for information on Hexion Inc. ("Hexion") products should be directed to your Hexion sales representative, or the nearest Hexion sales office. Information and MSDSs on non-Hexion products should be obtained from the respective manufacturer.

Packaging

Available in bulk and drum quantities.

Contact Information

For product prices, availability, or order placement, please contact customer service:

www.hexion.com/Contacts/

For literature and technical assistance, visit our website at: www.hexion.com

© and ™ Licensed trademarks of Hexion Inc.

DISCLAIMER

The information provided herein was believed by Hexion Inc. ("Hexion") to be accurate at the time of preparation or prepared from sources believed to be reliable, but it is the responsibility of the user to investigate and understand other pertinent sources of information, to comply with all laws and procedures applicable to the safe handling and use of the product and to determine the suitability of the product for its intended use. All products supplied by Hexion are subject to Hexion's terms and conditions of sale. **HEXION MAKES NO WARRANTY, EXPRESS OR IMPLIED, CONCERNING THE PRODUCT OR THE MERCHANTABILITY OR FITNESS THEREOF FOR ANY PURPOSE OR CONCERNING THE ACCURACY OF ANY INFORMATION PROVIDED BY HEXION,** except that the product shall conform to Hexion's specifications. Nothing contained herein constitutes an offer for the sale of any product.

PDS-2677- (Rev.10/15/2016 7:19:55 AM)

Appendix E – EPX Adhesive DP490 Datasheet



Scotch-Weld™

EPX™ Adhesive DP490

Product Data Sheet

Updated : March 1996
Supersedes : November 1993

Product Description

DP490 is a black, thixotropic, gap filling two component epoxy adhesive with particularly good application characteristics.

It is designed for use where toughness and high strength are required and shows special benefits in the construction of composite assemblies.

The product has excellent heat and environmental resistance.

Physical Properties

Not for specification purposes

	BASE	ACCELERATOR
Specific Gravity	1.00	1.00
Consistency	Non-sag paste	Non-sag paste
Mix Ratio By Weight By Volume	100 100	50 50
Colour	Black	Off-White
Work Life	1.5 hours minimum at 23°C	
Time to Handling Strength	4 to 6 hours at 23°C	
Time to Full Strength	7 days (test to full performance at one week)	
Shelf Life	15 months from date of despatch by 3M when stored in the original carton at 21°C (70°F) & 50 % Relative Humidity	

Performance Characteristics

Not for specification purposes

Performance Characteristics of the Cured Adhesive.

Two cure cycles were evaluated as follows:

Cure Cycle 1	7 days at 23°C
Cure Cycle 2	24 hours at 23°C, 1 hour at 80°C

Date : March 1996
EPX Adhesive DP490

Performance Characteristics (Cont...)
Not for specification purposes

Temperature Performance in Shear and Peel.

(Etched Aluminium) Shear Strength to BS 5350 C5, Peel Strength was floating roller peel to BS5350 C9.

Tests were performed at 23°C unless otherwise stated.

Temperature (°C)	Shear Strength (1) (N/mm ²)	Shear Strength (2) (N/mm ²)	Peel Strength DaN/cm
-55	23.7	31.6	N/A
23	30.2	28.7	9.24
80	11.9	12.7	7.32
120	2.8	3.2	N/A
150	1.9	1.7	N/A

Adhesion to Etched Aluminium after Environmental Ageing

Ageing Condition	Shear Strength (N/mm ²)
RT Control	26.2
Water at 23°C, 750 hours	25.6
50°C, 96% RH, 750 hours	22.0
120°C, 750 hours	25.3
175°C, dry heat, 120 hours	29.6
Skydroll 500B at 23°C, 750 hours	27.6
JP4 at 23°C, 750 hours	28.7
Hydraulic Oil at 23°C, 750 hours	29.5

DP490 shows good adhesion to many plastic surfaces even by simply solvent wiping.

This can be improved still further by the use of 3M Scotchbrite abrasion and/or use of the primer Scotch-Weld 3901.

Plastics	Shear Strength (N/mm ²)
Carbon Fibre Reinforced Epoxy	36.1 (cohesive)
Polyester Sheet Moulding Compound	4.3 (substrate)
Glass Fibre Reinforced Phenolic	30.3 (cohesive)
ABS (filled)	3.2 (substrate)
PVC (filled)	2.9 (substrate)
Azloy (glass filled polycarbonate)	3.0 (adhesion)
Valox (glass filled PET)	1.4 (substrate)
PMMA	3.7 (adhesion)
Noryl (tm XTRA) (glass filled PPO)	4.9 (adhesion)

Date : March 1996
EPX Adhesive DP490

Storage Conditions	Store product at 15°C to 25°C for maximum storage life.		
Directions for Use /Clean Up	<p>Place the cartridge into the 3M EPX Applicator and clip into position.</p> <p>Remove the resealable cap.</p> <p>Expel a small quantity of adhesive and ensure both components flow freely.</p> <p>Attach correct mixer nozzle (this should have 20 or more elements).</p> <p>Dispense the adhesive as required.</p> <p>When finished either leave the nozzle in place and store, or remove the nozzle, wipe clean the tip, and replace cap.</p> <p>To re-start after storage remove the old nozzle with cured adhesive and re-fit a new nozzle, or remove the cap and fit a new nozzle.</p>	<p>Surface Preparation: The degree of surface preparation depends on the bond strength required and the environment likely to be encountered by the bonded structure. For most plastics solvent wiping with 3M VHB surface cleaner, followed by abrasion with 3M Scotchbrite 7447, followed by a further solvent wipe until clean, will give good performance (except for acetal, polyethylene and polypropylene and some other low surface energy materials). This also applies to powder coat paints and other stoved paint systems.</p> <p>The same surface preparation will also give good adhesion to metal surfaces. The objective is to remove loosely attached surface films such as oils, waxes, dusts, mill-scale, loose paints and all other</p>	<p>surface contaminants in addition to enhancing mechanical adhesion. Grit-blasting using a clean, fine grit also offers excellent adhesion on many metallic substrates.</p> <p>Where humid environments are likely to be encountered by metallic substrates we recommend additional priming with 3M Scotch-Weld 3901. Alternatively, chemical conversion coating techniques combined with priming can offer the best durability.</p> <p>Clean-Up: Excess uncured adhesive can be removed with the following solvents:</p> <p>3M VHB Surface Cleaner (mild alcohol based cleaner) 3M Scotch-Grip Solvent No2. (Ketone blend) 3M Industrial Cleaner (Aerosol).</p>
Additional Product Information	Please contact your 3M Salesperson for additional information on the preparation of difficult surfaces, or likely exposure to aggressive environments.		

Date : March 1996
EPX Adhesive DP490

Health & Safety Information

Precautions:

Causes severe eye irritation, may cause permanent eye damage. Irritating to skin. May cause sensitisation by skin contact. Avoid contact with the skin and eyes. Wear suitable gloves and eye/face protection.

Launder contaminated clothing before re-use. Avoid prolonged breathing of vapours. Avoid inhalation of dust when grinding or cutting cured material.

First Aid:

Eye Contact: Immediately flush eyes with copious amounts of water for at least 15 minutes, holding eyes open. Call a physician.

Skin Contact: Wash immediately with plenty of soap and water.

For further information please contact the Toxicology Department at the Bracknell Head Office on (0344) 858000.

3M, EPX, Duo-Pak, Scotch-Grip, Scotchbrite and Scotch-Weld are trademarks of the 3M Company.

Values presented have been determined by standard test methods and are average values not to be used for specification purposes. Our recommendations on the use of our products are based on tests believed to be reliable but we would ask that you conduct your own tests to determine their suitability for your applications. This is because 3M cannot accept any responsibility or liability direct or consequential for loss or damage caused as a result of our recommendations.



Specialty Tapes & Adhesives

© 3M United Kingdom PLC 1996

3M United Kingdom PLC
3M House,
28 Great Jackson Street,
Manchester,
M15 4PA

Customer Service :
Tel 0161 236 8500
Fax 0161 237 1105

3M Ireland
3M House, Adelphi Centre,
Upper Georges Street,
Dun Laoghaire, Co. Dublin,
Ireland

Customer Service :
Tel (01) 280 3555
Fax (01) 280 3509

Appendix F – Hysol® EA 9394 Datasheet



Hysol® EA 9394

Epoxy Paste Adhesive

Henkel Corporation
 Aerospace Group
 2850 Willow Pass Road
 P.O. Box 312
 Bay Point, CA 94565 USA
925.458.8000
 Fax: 925.458.8030
 www.aerospace.henkel.com

Description

Hysol EA 9394 is a two-part structural paste adhesive, which cures at room temperature and possesses excellent strength to 350°F/177°C and higher. Its thixotropic nature and excellent high temperature compressive strength also make it ideal for potting, filling and liquid shim applications. Hysol EA 9394 is qualified to MMM-A-132 Rev A, Type I, Class 3.

The mechanical properties in this data sheet are also valid for Hysol EA 9394S. Hysol EA 9394S is only available in Semkits and differs from Hysol EA 9394 as it has 1 part less thixotrope in the Part B to aid packaging. All other mechanical and handling properties similar.

Features

Room Temperature Cure
 Good Gap Filling Capabilities
 350°F/177°C Performance
 Potting Material
 Room Temperature Storage
 Outstanding Mechanical Properties
 Long Pot Life
 Low Toxicity

Uncured Adhesive Properties

	<u>Part A</u>	<u>Part B</u>	<u>Mixed</u>
Color	Gray	Black	Gray
Viscosity, 77°F	4000-8000 Poise	200-700 Poise	1600 Poise
Brookfield HBT	Spdl 7 @ 20 rpm	Spdl 4 @ 20 rpm	Spdl 5 @ 20 rpm
Viscosity, 25°C	400-800 Pa S	20-70 Pa S	160 Pa S
Brookfield HBT	Spdl 7 @ 2.09 rad/sec	Spdl 4 @ 2.09 rad/sec	Spdl 5 @ 2.09 rad/sec
Density (g/ml)	1.50	1.00	1.36
Shelf Life from date of shipment			
@ <77°F/25°C	1 year	1 year	

This material will normally be shipped at ambient conditions, which will not alter our standard warranty, provided that the material is placed into its intended storage upon receipt. Premium shipment is available upon request.

Handling

Mixing - This product requires mixing two components together just prior to application to the parts to be bonded. Complete mixing is necessary. The temperature of the separate components prior to mixing is not critical, but should be close to room temperature (77°F/25°C).

<u>Mix Ratio</u>	<u>Part A</u>	<u>Part B</u>
By Weight	100	17

Note: Volume measurement is not recommended for structural applications unless special precautions are taken to assure proper ratios.

Pot Life (450 gm mass) 90 minutes
 Method - ASTM D 2471 in water bath.

Application

Mixing - Combine Part A and Part B in the correct ratio and mix thoroughly. THIS IS IMPORTANT! Heat buildup during or after mixing is normal. Do not mix quantities greater than 450 grams as dangerous heat buildup can occur causing uncontrolled decomposition of the mixed adhesive. TOXIC FUMES CAN OCCUR, RESULTING IN PERSONAL INJURY. Mixing smaller quantities will minimize the heat buildup.

Applying - Bonding surfaces should be clean, dry and properly prepared. For optimum surface preparation consult the Hysol Surface Preparation Guide. The bonded parts should be held in contact until the adhesive is set. Handling strength for this adhesive will occur in 24 hours @ 77°F/25°C, after which the support tooling or pressure used during cure may be removed. Since full bond strength has not yet been attained, load application should be small at this time.

Note: Special precautions are recommended to minimize carbonate formation in large assemblies subject to extended open times in humid environments. A special memo is available upon request from Henkel providing users with suggestions for minimizing carbonate formation.

Curing - Hysol EA 9394 may be cured for 3 to 5 days @ 77°F/25°C to achieve normal performance. Accelerated cures up to 200°F/93°C (for small masses only) may be used as an alternative. For example, 1 hour @ 150°F/66°C will give complete cure.

Cleanup - It is important to remove excess adhesive from the work area and application equipment before it hardens. Denatured alcohol and many common industrial solvents are suitable for removing uncured adhesive. Consult your supplier's information pertaining to the safe and proper use of solvents.

Bond Strength Performance

Tensile Lap Shear Strength - tested per ASTM D1002 after curing for 5 days @ 77°F/25°C. Adherends are 2024-T3 bare aluminum treated with phosphoric acid anodized per ASTM D3933.

<u>Test Temperature, °F/°C</u>	<u>Typical Results</u>	
	<u>psi</u>	<u>MPa</u>
-67/-55	3,300	22.7
77/ 25	4,200	28.9
180/82	3,000	20.7
200/93	2,900	20.0
250/121	2,300	15.8
300/149	1,600	11.0
350/177	1,200	8.3
400/204	600	4.1

After Exposure to/Test Temperature	Typical Results	
	psi	MPa
Room Temperature Control (no exposure)	4,300	29.6
77°F/25°C Water - 7 days @77°F/25°C	4,100	28.2
Isopropyl Alcohol - 7 days @77°F/25°C	4,000	27.6
Hydraulic Oil - 7 days @77°F/25°C	4,100	28.2
JP-4 Fuel - 7 days @ 77°F/25°C	4,200	28.9

Peel Strength

T-Peel strength tested per ASTM D1876 after curing for 5 days @ 77°F/25°C.
 Adherends are 2024-T3 alclad aluminum treated with phosphoric acid anodized per ASTM D3933.

Test Temperature, °F/°C	Typical Results	
	Lb/in	N/25 mm
77/25	5	22.2

Bell Peel strength tested per ASTM D3167 after curing for 7 days @ 77°F/25°C.
 Adherends are 2024-T3 alclad aluminum treated with phosphoric acid anodized per ASTM D3933.

Test Temperature, °F/°C	Typical Results	
	Lb/in	N/25 mm
77/25	20	89.0

Service Temperature

Service temperature is defined as that temperature at which this adhesive still retains 1000 psi/6.9 MPa) using test method ASTM D1002 and is 350°F/177°C.

Henkel QC Acceptance Testing

This data sheet provides users with typical properties obtained from this adhesive. These values are not meant to be used to develop aerospace QC acceptance testing. Users interested in establishing values and tests for routine QC acceptance should request our internal specification (DAS), which provides detail test methods and values used to certify this adhesive.

Bulk Resin Properties

Tensile Properties - tested using 0.125 inch/ 3.18 mm castings per ASTM D638.

Tensile Strength, @ 77°F/25°C	6,675 psi	46.0 Mpa
Tensile Modulus, @ 77°F/25°C	615 ksi	4,237 Mpa
Shear Modulus, dry @ 77°F/25°C	212 ksi	1,461 Mpa
Shear Modulus, wet, @ 77°F/25°C	149 ksi	1,027 Mpa
Elongation at Break, % @77°F/25°C	1.66	
Shore D Hardness, @ 77°F/25°C	88	
T _g dry	172°F	78°C
T _g wet	154°F	68°C

Compressive Properties - tested with rectangular specimens 0.5 in/12.7 mm width by 1.0 in/25.4 mm length by 0.5 in/12.7 mm height.

Compressive Strength, °F/°C	Psi	MPa
77/25	10,000	68.9

Electrical Properties - tested per ASTM D149, D150.

	<u>0.1 KHz</u>	<u>1.0 KHz</u>	<u>10.0 KHz</u>
Dielectric Constant	7.72	7.51	7.20
Dissipation Factor	.017	.022	.033
Thermal Conductivity	7.92×10^{-4} cal/sec-cm-°C		[0.331 W/(m•K)]
Volume Resistivity	4.05×10^{13} ohm-cm		[4.05×10^{14} ohm]
Surface Resistivity	4.60×10^{13} ohm		
Coefficient of Thermal Expansion	55.6µm/m°C @ 40°C		
	80.6µm/m°C @ 100°C		

Handling Precautions

Do not handle or use until the Material Safety Data Sheet has been read and understood.
For industrial use only.

General:

As with most epoxy based systems, use this product with adequate ventilation. Do not get in eyes or on skin. Avoid breathing the vapors. Wash thoroughly with soap and water after handling. Empty containers retain product residue and vapors, so obey all precautions when handling empty containers.

PART A

WARNING! As with most epoxy based systems, the uncured adhesive may cause eye and skin irritation or allergic dermatitis. Contains epoxy resins.

PART B

DANGER! Causes severe skin and eye burns. Contains tetraethylenepentamine. Vapors may be irritating to the respiratory tract.

Hysol® is a registered trademark of Henkel Corporation.

Rev. 6/02

DISCLAIMER: The information supplied in this document is for guidance only and should not be construed as a warranty. All implied warranties are expressly disclaimed, including without limitation any warranty of merchantability and fitness for use. All users of the materials are responsible for assuring that it is suitable for their needs, environmental and use. All data is subject to change as Henkel deems appropriate.

Users should review the Material Safety Data Sheet (MSDS) and product label for the material to determine possible health hazards, appropriate engineering controls and precautions to be observed in using the material. Copies of the MSDS and label are available upon request.



Henkel Corporation
Aerospace Group
2850 Willow Pass Road
P.O. Box 312
Bay Point, CA 94665 USA
925.468.8000
www.aerospace.henkel.com

Appendix G – Hysol® Surface Preparation Guide



Hysol® Surface Preparation Guide

Henkel Corporation
Aerospace Group
2850 Willow Pass Road
P.O. Box 312
Bay Point, CA 94565 USA
925.458.8000
Fax: 925.458.8030
www.aerospace.henkel.com

General Considerations

To correctly prepare the surface to be joined, all grease, oil and foreign particles should be removed. With most high performance adhesives this step is critical, since for good wetting, the adherend should have a higher surface tension than the adhesive. Even a thumbprint on an otherwise clean surface can prevent the adhesive from spontaneously wetting and spreading.

Organic contaminants are removed by degreasing, while loose deposits are dislodged by scraping or washing with acids, alkali solutions or other such chemicals. Metals are best cleaned by vapor degreasing with trichloroethane, followed by sandblasting or, preferably, by chemical etching. Chemical treatments may be confined to the bonding areas, but degreasing should be done to the entire assembly. A cleaned assembly should be bonded as soon after the cleaning operation as possible or an adhesive primer should be applied. However, if storage is necessary, special precautions should be taken so that the assembly does not become contaminated. All parts should be tightly wrapped or placed in airtight and oil-free containers. Etched surfaces must never be touched with bare hands – even wiping the surface with a clean cloth can affect the bond. Handlers should wear clean cotton gloves and use clean tools.

Nonmetallic, nonporous materials should be degreased with a detergent solution, rinsed thoroughly with clean water, and then dried. Clean solvent may be substituted for detergent. The surfaces are then hand-sanded or sandblasted to give them a rough texture. With organic polymers, plasma or corona treatments are frequently being used to increase the surface activity and thus increase surface wetting and the strength of adhesive bonds.

Water is often used to test a metal surface for cleanness. A small portion is placed on the surface. If the water distributes evenly then the metal should wet well with an adhesive. But if it beads or crawls then the surface should be cleaned again and the test repeated.

Bonding should be performed in a room separate from other manufacturing operations. When bonding is done in the same area as plastic or rubber molding, a physical barrier should be erected between the two operations to prevent airborne mold lubricants from depositing on the metal. Similar hazards are presented by spray painting, electroplating, etching, and machining with coolants. Storage and assembly areas should be enclosed, and air to these areas filtered and under slight pressure.

Numerous studies are underway to find surface treatment methods that minimize or eliminate use of toxic materials or polluting substances. Some progress is being made, but replacement of such degreasing solvents as trichloroethane and such toxic materials as the dichromates will take time. For polymeric surfaces, plasma or corona discharge treatments are receiving much attention.

Degreasing Metals

To degrease metal surfaces with a degreasing unit, suspend the metals in a stabilized trichloroethane vapor bath for about 30 seconds. Check the bath frequently for accumulated contaminants. If a degreasing unit is not available, clean the surface with a white cotton rag or pieces of absorbent cotton dampened with trichloroethane. Rags should be changed frequently. Let the surface stand several minutes while the chemical evaporates. Although non-flammable, this solvent is toxic in both liquid and vapor forms, so the working areas should be well ventilated. Gloves should be worn when handling this solvent, and smoking should not be allowed.

Degreasing Non-Metals

Solvents or detergent solutions can be used to remove mold-release agents or waxes from plastics. Such commercial detergents as represented by “Sprex” (DuBois Chemical Co., 1120 West Front, Cincinnati, Ohio) are suitable. Acetone or methyl alcohol are effective solvents, depending on the type of plastic to be cleaned. The adverse effect of solvents on some polymeric materials should be checked before their use.

Surface Abrasion

Smooth surfaces can be improved for bonding by roughening with abrasives such as medium-grit emery paper. Abrasion should always be followed by degreasing to remove contaminants and loose particles.

Blasting with a fine grit is the best method for removing surface deposits – oxide films, tarnish, rust, mill scale and other contaminants – from metals. This method should be used only on structures thick enough to resist distortion. With thinner materials, contaminants should be removed by vapor honing. This method is similar to grit blasting but uses high-velocity water or steam instead of air. If neither method is appropriate, abrasive discs, belts, cloth, medium-grit emery paper, or wire brushes can be used. Plastics should be roughened with abrasive discs, belts, cloth or emery paper to remove mold release agents. Medium-grit emery paper will give the best results.

Surface abrasion can also remove other surface contaminants as well as weak, low molecular weight components which can be concentrated at the surface due to their exclusion during solidification or crystallization of some polymers.² Also during solidification of both thermoplastic and thermoset materials, there is often an orientation of the more polar groups towards the interior, leaving a concentration of lower polarity, lower energy groups on the surface.³ Abrasion can open up access to the more energetic polymer interior.

Chemical Treatment

Chemical or electrolytic pretreatments of a bonding surface can greatly increase the strength of the bond. Pretreating can etch the surface of a metal, and form a highly adherent oxide. Environmental resistance can often be greatly increased by such treatment. Etching solutions should be prepared in glass, porcelain, polyethylene, polypropylene or tetrafluoroethylene fluorocarbon laboratory ware and stirred with rods of the same material. Metals other than those to be etched should not touch the solutions. For solutions containing hydrofluoric acid or fluorides, TFE fluorocarbon should be used. Solutions in plastic trays can be heated by immersion in hot water baths; hot plates or infrared heaters can be used for glass and porcelain trays. See Caution section below for safe procedures.

Caution

The Occupational Safety and Health Administration of the Department of Labor has defined some of the following chemicals and substrates to be hazardous to health in varying degrees. Some are even extremely hazardous. You should familiarize yourself with the substrates and needed chemicals and know the safe handling procedures to be used before preparing the surfaces for adhesive bonding. Also, many of the solvents, degreasing solvents and etch bath chemicals are toxic or can be dangerous if not mixed and handled properly. Materials such as hydrofluoric acid and the chromates need very careful handling. Care should be taken in preparing such chemical solutions, not only because the wrong proportions can seriously weaken a bond but also because the chemicals can be harmful to the skin. Many are strong acids and bases. Remember that solutions containing concentrated sulfuric acid must be prepared by adding acid to water with stirring, and not vice versa. A violent reaction can occur if this is not observed. Use rubber gloves, aprons, face shields, etc.

While the information contained in this article is believed to be reliable, surface treating methods have been selected from many sources, substrates can vary considerably from source to source, and bonding conditions can vary with location and the experience of the operator. Therefore, all recommendations are made without guarantee and those following such listed procedures should become familiar with the general requirements of adhesive bonding and run controls with specific materials and processes before proceeding with the preparation of critical bonded structures.

Surface Treatment Tables

A number of abbreviations have been used on the surface treatment tables to reduce their length. These include the following: Parts by weight – pbw; distilled or deionized water – DI water; minutes – min.; hours – hr.; chemical names – chemical symbols, i.e., hydrofluoric acid – HF, hydrochloric acid – HCl, sulfuric acid – H₂SO₄, sodium dichromate – Na₂Cr₂O₇, sodium hydroxide – NaOH, etc.

References

1. Prepared by C. Lynn Mahoney. Based on Surface Preparation Bulletin G-600 and updated references.
2. H. Schonhorn, in: *Polymer Surfaces*, D.T. Clark and W. J. Feast, Editors, 1978, John Wiley and Sons, New York.
3. A. Herczeg, G.S. Ronay, and W.C. Simpson. Vol. 2, P221-231, 1970, National SAMPE Technical Conference Proceedings, Azusa, California, 1970.
4. A.H. Landrock, *Adhesives Technology Handbook*, 1985, Noyes Publications, Park Ridge, New Jersey.
5. R. Rosty, D. Martinelli, A. Devine, M.J. Bodnar, and J. Beetle, P34, *SAMPE Journal*, July/August, 1987.
6. J.S. Tira, P18, *SAMPE Journal*, July/August, 1987.
7. L.J. Matienzo, J.D. Venebles, J.D. Fudge and J.J. Velten, P302, 30th National SAMPE Symposium, March 19-21, 1985.
8. L.W. Crane, C.H. Hamermesh and L. Maus, *SAMPE Journal*, March/April 1976.
9. Szu-ly. Wu, A.M. Schuler and D.V. Keene, P277, SAMPE 19th International Technical Conference, Oct. 13-15, 1987.
10. Kaplan, S.L. and Rose, P.W., *Plastics Engineering*, May, 1988.
11. Kinloch, A.J. and Kodokian, G.K., Report No. AD-190994, Jan. 15, 1988. Available MTIS.

Metals

Adherend Material	Cleaning	Abrasion or Chemical Treatment	Method
Aluminum and Alloys	Degrease in vapor bath with appropriate solvent or alkaline cleaner. (See ASTM D2651 for general information. See Ref 4 for chromate-free P2 etch.)	(A) Chromic Acid Etch DI water 1 liter H ₂ SO ₄ (conc.) 300g Na ₂ Cr ₂ O ₇ ·2H ₂ O 60g 2024 Bare Aluminum 1.5g Dissolve the 20 mil aluminum sheet to "seed" the bath. (B) Phosphoric Acid Anodizing (Boeing Co. Patent Appl.) (for improved environmental resistance) (ASTM D3933-80) Prepare anodizing bath. H ₃ PO ₄ (75% conc.) 454g DI water 3.71 Add acid to water with stirring. Use titanium racks and a stainless steel cathode.	(A) <ul style="list-style-type: none"> Etch metal in bath for 12-15 minutes at 150-160°F (66-71°C). Do not delay rinse! Spray in tap water for 5 min. Follow with DI water soak rinse. Dry thoroughly at 120-140°F max. (49-60°C). Prime or bond within 16 hours. (B) <ul style="list-style-type: none"> Prepare etched metal as above in A. Anodize at 65-85°F (18-30°C). Slowly raise voltage to 10-11 volts for 20-25 minutes. Disconnect current, immediately remove parts and rinse in running water (DI or <150ppm solids tap-water) for 10-15 min. Dry at 160°F (71°C) max. Don't touch surface. Prime or bond within 16 hours.
Aluminum Honeycomb Core	Degrease.	Not used.	<ul style="list-style-type: none"> After degreasing, let stand for 2 hrs. at room temp. or 15 min. at 200°F (93°C).
Beryllium (highly toxic)	Degrease.	Dissolve NaOH in equal weight of DI water, then add water to reduce concentration to 20%W.	<ul style="list-style-type: none"> Immerse in conc. (20%W) NaOH soln. 3 min. at 180°F (82°C). Rinse thoroughly in cold running DI water. Finally, dry in oven for 10-15 min. at 300-350°F (149-177°C).
Cadmium	Degrease.	Abrade with emery paper. Preferable electroplate with silver or nickel for bonding.	<ul style="list-style-type: none"> Repeat degreasing step.
Copper and Alloys Brass, Bronze	Degrease. (Also see Ref 4 and ASTM D2651-79)	(A) For medium strength bonds, abrade with emery paper. (B) For high bond strengths etch metal surface in: 42% Aqueous FeCl ₂ soln. 15 pbw Conc. HNO ₃ (s.g. 1.41) 30 pbw DI water 197 pbw	(A) <ul style="list-style-type: none"> Repeat degreasing step. (B) <ul style="list-style-type: none"> Immerse for 1-2 min. at 77°F (25°C). Rinse in cold running DI water. Dry immediately with pressurized air at R.T.
Gold	Degrease with vapor bath or clean rag and solvent.	None.	<ul style="list-style-type: none"> Degreasing only treatment.
Iron Cast Iron (Alloys under Steel)	Degrease.	Grit blast or abrade with emery paper.	<ul style="list-style-type: none"> Repeat degreasing step.
Lead and Alloys, Pewter	Degrease.	Abrade with medium-grit emery paper.	<ul style="list-style-type: none"> Repeat degreasing step.

Metals – cont.

Adherend Material	Cleaning	Abrasion or Chemical Treatment	Method
Magnesium and Alloys	See ASTM D2651-79.	(A) For medium strength bond, abrade with medium-grit emery paper. (B) For high strength bonds, use etch procedure (ASTM D2651, Method A) Bath 1: Sodium Metasilicate 2.5 pbw Tetrasodium Pyrophosphate 1.1 pbw Sodium Hydroxide 1.1 pbw Nacconol® NR (Allied Chem Corp) 0.3 pbw DI water 95 pbw Bath 2: Chromium Trioxide 1 pbw DI water 4 pbw	(A) <ul style="list-style-type: none"> Repeat degreasing step. Dry in forced draft oven at 150-200°F (66-93°C). (B) <ul style="list-style-type: none"> Immerse metal for 10 min. in Bath 1 at 140-160°F (60-71°C). Rinse thoroughly in water. Immerse metal for 10 min. in Bath 2 kept at 140-190°F (60-88°C). Wash in cold running DI water. Dry in forced draft oven at <140°F (60°C). When cool, immediately apply adhesive.
Nickel	Degrease.	(A) For medium strength bond, abrade with medium-grit emery paper. (B) For higher bond strengths, conc. HNO ₃ (s.g. 1.41) (Ref 4).	(A) <ul style="list-style-type: none"> Repeat the degreasing step. (B) <ul style="list-style-type: none"> For stronger bond, immerse in metal for 5 seconds in conc. HNO₃ solution at room temp 77°F (25°C). Rinse etched metal thoroughly in cold running DI water. Air dry at 104°F (40°C).
Platinum	Degrease.	No other treatment needed.	
Silver	Degrease.	Using fine-grit emery paper, remove any tarnish from bonding area.	<ul style="list-style-type: none"> Repeat degreasing step.
Steel and Iron Alloys (except Stainless Steel)	Degrease.	(A) Sandblast or abrade with medium-grit emery paper. (B) If cannot sandblast or abrade Acid Bath 1: Conc. Orthophosphoric Acid (Sig 1.73) 1 pbw Ethyl Alcohol (denatured) 1 pbw or Acid Bath 2: Conc. HCl 1 pbw DI water 1 pbw	(A) <ul style="list-style-type: none"> Repeat degreasing step. (B) <ul style="list-style-type: none"> Immerse for 10 min. in acid Bath 1 at 140°F (60°C) or 5-10 min. in Bath 2 at 68°F (20°C). Remove black residue with stiff brush under running DI water. Dry at 250°F for 1 hour. If cannot be stored at less than 30% R.H., bond prepared surfaces in short time.
Steel, Ferrous Alloys	Degrease.	(A) Gritblast if possible (B) If cannot abrade Conc. HCl 1 pt/wt DI water 1 pt/wt	(A) <ul style="list-style-type: none"> Repeat degreasing step. (B) <ul style="list-style-type: none"> If cannot abrade, immerse for 3-10 min. at 77°F (25°C) in HCl bath. Rinse thoroughly in cold running DI water. Oven dry at 150°F (66°C) for 10 min.
Stainless Steel	Degrease. (See Ref 6 for alternate procedures. Also see ASTM D2651.)	Remove surface deposits with non-metallic agent – alumina grit paper. (A) General Purpose Treatment Bath 1: See under Magnesium and Alloys.	<ul style="list-style-type: none"> Repeat degreasing. Vapor degrease for 30 seconds. (A) <ul style="list-style-type: none"> Immerse in Bath 1 for 10 min. at 160-180°F (71-82°C). Rinse thoroughly in running tapwater, then cold DI water. Oven dry at 200°F (93°C) for 10 min. Bond as soon as possible.

Metals – cont.

Adherend Material	Cleaning	Abrasion or Chemical Treatment	Method
Stainless Steel (cont.)		<p>(B) For high temperature use, further treat the metal. Bath 2: Oxalic Acid 1 pbw Conc. H₂SO₄ (s.g. 1.86) 1 pbw DI water 8 pbw Dissolve oxalic acid before stirring in the H₂SO₄.</p> <p>(C) For resistance to high peel stresses, further treat metal from (A). (Do not combine B & C treatments.) Bath 3: Na₂Cr₂O₇·2H₂O 3.5 pbw DI water 3.5 pbw Conc. H₂SO₄ (s.g. 1.86) 200 pbw</p>	<p>(B)</p> <ul style="list-style-type: none"> Immerse metal for 10 min. in Bath 2 at 185-195°F (85-90°C). Under cold running water, scrub away any black residue with clean, stiff bristle brush. Rinse in DI water. Dry in oven at 200°F (93°C) for 10-15 min <p>(C)</p> <ul style="list-style-type: none"> Immerse in Bath 3 at 140-160°F (60-71°C) for 15 min. Scrub under cold running water with stiff bristle brush. Rinse in DI water. Dry in oven at 200°F (93°C) for 10-15 min
Tungsten and Alloys	Degrease.	<p>(A) Abrade using medium-grit emery paper. (B) For maximum strength, also use a chemical etch. Conc. HCl 30 pbw DI water 15 pbw HF 5 pbw Conc. H₂SO₄ 50 pbw Hydrogen peroxide few drops Add HCl and HF to the water, stir in the H₂SO₄ then add the hydrogen peroxide.</p>	<p>(A)</p> <ul style="list-style-type: none"> Repeat degreasing step. <p>(B)</p> <ul style="list-style-type: none"> Immerse for 1-5 min. at 77°F (25°C). Rinse thoroughly in cold running DI water. Dry for 10-15 min. in a 160-180°F (71-82°C) oven.
Zinc, Alloys, Galvanized Metals	Degrease.	<p>(A) Abrade using medium-grit emery paper. (B) For maximum strength Conc. HCl 20 pbw DI water 80 pbw</p>	<p>(A)</p> <ul style="list-style-type: none"> Repeat degreasing step. <p>(B)</p> <ul style="list-style-type: none"> Immerse for 2-4 min. with the solution at 77°F (25°C). Rinse thoroughly in cold running DI water. Dry for 20-30 min. in a 150-160°F (66-71°C) oven. Apply adhesive as soon as possible.
Tin	Degrease.	Abrade with medium-grit emery paper.	<ul style="list-style-type: none"> Repeat degreasing.
Titanium and Alloys (Many procedures in literature, also see ASTM D2651.)	Vapor degrease with trichloroethane. Remove surface deposits with non-metallic abrasive.	<p>(A) Bath 1: Sodium Metasilicate Soln. (See Magnesium) (B) For stronger bonds Bath 2: (Polyethylene vessel) Sodium Fluoride 10 pbw Chromium trioxide 5 pbw DI water 250 pbw Conc. H₂SO₄ (add with last stirring) 50 pbw (C) Alternate Treatment (ASTM D2651) Bath 3: Alkaline-clean Oakite HD 126 1.5 oz to 1 gal DI water to 1 gal Bath 4: Acid Pickle HF (70%) 2-3 oz (fl) Na₂SO₄ (anhyd.) 3 oz HNO₃ (70%) 40-50 oz DI water to 1 gal</p>	<p>(A)</p> <ul style="list-style-type: none"> Immerse at 160-180°F (71-82°C) for 10 min Rinse in cold, running DI water. Dry in oven at 150-200°F (66-93°C) for 10-15 min. <p>(B)</p> <ul style="list-style-type: none"> Immerse in Bath 2 at R.T. for 5-10 min. Rinse in cold, running DI water. Dry in oven at 160-180°F (71-82°C) for 10-15 min. <p>(C)</p> <ul style="list-style-type: none"> Immerse in Bath 3 for 3-5 min at 150°F (66°C). Rinse in running tapwater at 105°F (40°C) for 2 min. Immerse in Bath 4 for 2 min. at R.T. Rinse in cold water. <p>(continued next page)</p>

Metals – cont.

Adherent Material	Cleaning	Abrasion or Chemical Treatment	Method
Titanium and Alloys (cont.)		Bath 5: Etch Bath Trisodium Phosphate 6.5-7 oz Potassium Fluoride 2.5 oz HF (70%) 2.2-2.5 oz DI water to 1 gal	<ul style="list-style-type: none"> Immerse in Bath 5 for 2 min at R.T. Rinse in DI water at 150°F (66°C) for 15 min. Repeat rinse. Dry at 140°F (60°C) for 30 min. in air circulating oven. Wrap in clean Kraft paper.

Thermoplastics

ABS (Ref 4)	Degrease in acetone. (Alcohol is probably better to use.)	(A) Abrade with medium-grit sandpaper. (B) Etch Solution Conc. H ₂ SO ₄ 26 pbw K ₂ Cr ₂ O ₇ 3 pbw DI water 11 pbw (Add acid to stirred water) (C) Plasma or Corona Treatment (Ref 10)	(A) <ul style="list-style-type: none"> Wipe free of dust. Prime with Dow Corning A-4094 or G.E. SS-4101. (B) <ul style="list-style-type: none"> Etch at room temp. for 20 min. Rinse in tapwater. Rinse in DI water. Dry in warm air.
Cellulose Plastics	Degrease with methyl alcohol or isopropyl alcohol.	Abrade using fine-grit emery paper.	<ul style="list-style-type: none"> Repeat degreasing step. Heat to 200°F (93°C) for 1 hr. and apply adhesive while hot.
Diallylphthalate	Degrease with acetone or MEK.	Abrade using medium-grit emery paper.	<ul style="list-style-type: none"> Repeat degreasing step.
Fluorocarbons Polymonochloro- trifluoroethylene Polytetrafluoro- ethylene Tetrafluoroethyl- ene Polyvinyl fluoride	Degrease with acetone or MEK. (Also see Ref 4, Flame Treatment, Corona Discharge and plasma treatments are also being increasingly used. See Ref 10.)	Use chemical etch. Sodium metal 23 g Naphthalene 128 g Tetrahydrofuran 1L Prepare under anhydrous conditions. (Dry solvents, closed flask, stirrer, drying tube.) Add naphthalene to the THF, carefully add 1/4" to 1/2" cubes of sodium, one at a time while stirring. Let soln. stand 16 hrs. at R.T., then stir 2 hrs. Store in bottles with glass stoppers—keep free from air and moisture. Use near exhaust ventilator.	<ul style="list-style-type: none"> Immerse in the solution for 15 min. at 77°F (25°C). Wash in acetone or MEK then in cold DI water. Dry thoroughly. Proprietary solutions may be used. "Bondaid" W.S. Shambrand Co. "Fluorobond" Joclin Mfg. Co.
Nylon	Degrease with acetone or MEK.	Abrade using medium-grit emery paper.	<ul style="list-style-type: none"> Repeat degreasing step.
Polycarbonate or Polymethyl-methacrylate or Polystyrene	Degrease with methyl alcohol.	Abrade using medium-grit emery paper. (Also plasma or Corona treatment. Ref 10)	<ul style="list-style-type: none"> Repeat degreasing step.
Polyether (chlorinated) or Polyethylene or Polypropylene or Polyformalde- hyde	Degrease with acetone or MEK. (See Ref 5 for alternate procedures. Flame or plasma treatment may also be used. See Refs 4 and 10.)	Chemical pretreatment is necessary. K ₂ Cr ₂ O ₇ 75 pbw DI water 120 pbw Conc. H ₂ SO ₄ 1500 pbw Dissolve the K ₂ Cr ₂ O ₇ in water and stir in the H ₂ SO ₄ .	(A) <ul style="list-style-type: none"> Immerse in the chromic acid solution as follows: <ul style="list-style-type: none"> - Chlorinated Polyether – 5 min at 160°F (71°C). - Polyethylene and Polypropylene – 60 min. at 77°F (25°C). - Polyformaldehyde – 10 sec. at 77°F (25°C). Rinse in cold running DI water. Dry at R.T. Flame or plasma treatments may be used also.

Thermoplastics – cont.

Adherent Material	Cleaning	Abrasion or Chemical Treatment	Method
Polyethylene-terephthalate or Linear Polyesters	Degrease with methyl alcohol. (See Ref 4, plasma treatments also used.) (Ref 10)	(A) Abrade using medium-grit emery paper. (B) For a stronger bond use chemical etch. Sodium hydroxide soln. (20%W)	(A) • Repeat degreasing step. (B) • Immerse for 2-10 min. at 160-200°F (71-93°C). • Wash thoroughly in cold running DI water. • Dry with hot air.
Polyvinyl-chloride rigid	Degrease with methanol or trichloroethane.	Abrade using medium-grit emery paper.	• Repeat degreasing step.

Engineering Thermoplastics (Examples of Representative Commercial Materials)

Polyarylate (Ardel®, U.C.) (Ref 4) or Polyaryl Sulfone (Astrel® 360, 3M) (Ref 4)	(A) Ultrasonic clean in alkaline-etching solution.	(A) Using alkaline-etching solution. Sandblast with 150 mesh silica sand. (B) Acid Etch Solution Na ₂ Cr ₂ O ₇ ·12H ₂ O 3.4% Conc. H ₂ SO ₄ 96.96% (C) Plasma or Corona Treatment (Ref 10, 11).	(A) • Water wash. • Alcohol wash. • Dry with dry nitrogen. (B) • Immerse 15 min. at 150-160°F (66-71°C). • Cold water wash. • Dry at 150°F (66°C) in an air circulating oven.
Polyether-etherketone (PEEK, ICI) (Ref 4)	Degrease with isopropyl alcohol.	(A) Abrade. (B) Flame Treatment Blue oxidizing flame. (C) Chromic Acid Etch Bath composition not given in Ref. 4. (D) Plasma or Corona Treatment (Ref 10, 11).	(A) • Repeat degrease. (B) • Abrade. • Degrease. • Flame treat (blue oxidizing flame). (C) • Abrade. • Degrease. • Chromic acid etch. • Water wash.
Polyphenylene-sulfide (Ryton®, Phillips) (Ref 4)	(A) Degrease with acetone. (B) Wipe surface with ethyl alcohol soaked paper.	(A) Sandblast. (B) Sand with 1220-grit sandpaper. (C) Plasma or Corona Treatment (Ref 10, 11).	(A) • Repeat degreasing. (B) • Clean off dust with stiff bristle brush.
Polysulfone (Udel®, U.C.) (Ref 4)	Degrease in alcohol.	(A) Grit-blast with 27-50 micron aluminum oxide. (B) Etch in sodium dichromate-sulfuric acid soln. (C) Plasma or Corona Treatment (Ref 10).	(A) • Clean in ultrasonic cleaner in Neutra-Clean (Shipley Co., Inc.) • Rinse in tap and then DI water. • Rinse in IPA for 30 sec. • Flush with dry N ₂ • Dry in air at 150°F (66°C). (B) See Polyaryl Sulfone treatment.

Thermosets

Adherend Material	Cleaning	Abrasion or Chemical Treatment	Method
Epoxy, Epoxide Resins	Degrease with acetone or MEK.	Abrade using medium-grit emery paper.	<ul style="list-style-type: none"> Repeat degreasing step.
Furane Resins	Degrease with acetone or MEK.	Abrade using medium-grit emery paper.	<ul style="list-style-type: none"> Repeat degreasing step.
Melamine Formaldehyde Plastics (Formica)	Degrease with acetone or MEK.	Abrade using medium-grit emery paper.	<ul style="list-style-type: none"> Repeat degreasing step.
Phenolics Polyester Polyurethane Resins	Degrease with acetone or MEK.	Abrade using medium-grit emery paper.	<ul style="list-style-type: none"> Repeat degreasing step.
Polyimide (Vespel®, DuPont) (Ref 4)	(A) Degrease. (B) Degrease in acetone.	(A) Abrade with dry or wet abrasive blast. (B) Etch Solution Sodium Hydroxide 5 pbw Water 95 pbw (C) Plasma or Corona Treatment (Ref 10).	(A) <ul style="list-style-type: none"> Repeat degreasing. Dry. (B) <ul style="list-style-type: none"> Etch for 1 min. at 140-194°F (60-90°C). Rinse in cold water. Dry in hot air.

Carbon and Carbon Fiber and Glass Fiber Composites

Carbon	Degrease with acetone or MEK.	Abrade using fine-grit emery paper.	<ul style="list-style-type: none"> Repeat degreasing step. Allow solvent to evaporate.
Glass Reinforced Laminates	Degrease with acetone or MEK.	Abrade using fine-grit emery paper.	<ul style="list-style-type: none"> Repeat degreasing step.
Graphite	Degrease with acetone or MEK.	Abrade using fine-grit emery paper.	<ul style="list-style-type: none"> Repeat degreasing step. Allow solvent to evaporate.
Carbon Fiber Epoxy Composites (Ref. 4)	(A) Solvent wipe (MEK, toluene, etc.) (B) Use peel ply during initial curing. (C) See Ref 6 for the effect of abrasion procedures. See also Refs 7 and 9.	(A) Lightly abrade with medium-grit emery paper. Avoid exposing the reinforcing fibers.	(A) <ul style="list-style-type: none"> Wipe with solvent. Check surface by water break test. Repeat if necessary.
Carbon Fiber Polyetheretherketone (PEEK)	Solvent wipe with MEK.	Abrade lightly with Scotch-brite – Bon Ami. Good strengths require A or B treatment. (A) Chromic Acid Etch Exact composition of etch solution not defined in Ref 9. (B) Plasma Treatment Gave good bond strengths also. (Ref 11) See Ref 10 for general plasma treatments.	<ul style="list-style-type: none"> Rinse in tap water and DI water. Air dry. (A) <ul style="list-style-type: none"> Immerse for 15 min. at R.T. Rinse in tap and then DI water. Dry at 200°F (93°C) for 30 min.

Rubbers

Rubber, Natural and Rubber, Synthetic Chloroprene Neoprene	Degrease with methyl alcohol.	For maximum strength use – Chemical etch: Bath 1, concentrated sulfuric acid. Neutralizing solution: Bath 2, 0.2% soln. of caustic.	<ul style="list-style-type: none"> Immerse for 5-10 min. in conc. sulfuric acid at 77°F (25°C). (Bath 1) Wash thoroughly in cold DI water. Neutralize by immersing for 5-10 min. at R.T. in Bath 2. Rinse with cold running DI water. Dry.
--	-------------------------------	---	---

Ceramics, Glass, etc.

Adherend Material	Cleaning	Abrasion or Chemical Treatment	Method
Ceramics, Porcelain, Glazed China	Degrease with MEK.	Abrade using emery paper or sandblasting.	<ul style="list-style-type: none"> Repeat degreasing step. Evaporate the solvent.
Glass, Quartz, nonoptical	Degrease with MEK.	(A) Abrade using carborundum powder and water or fine-grit paper. (B) For maximum strength, continue abrading and use chemical etch. Chromium trioxide 1 pbw DI water 4 pbw	(A) <ul style="list-style-type: none"> Repeat degreasing step. Dry for 30 min. at 210°F (100°C). (B) <ul style="list-style-type: none"> Immerse for 10-15 min. at 77°F (25°C). Dry for 30 min. at 210°F (100°C). Apply adhesive while still hot.
Glass, optical	Degrease in an ultrasonically agitated detergent bath.		<ul style="list-style-type: none"> Rinse thoroughly. Dry <100°F (38°C).
Jewels	Degrease with MEK.		<ul style="list-style-type: none"> Dry at R.T.

Construction Materials

Bricks, fired Nonglazed Building Mat'ls	Degrease in acetone or MEK.	Abrade using a wire brush.	<ul style="list-style-type: none"> Remove all contaminants.
Concrete	Decontaminate with a detergent solution.	Clean by one of these procedures: (A) Sandblast about 1/15" from bonding surface. (B) Remove 1/8" by mechanical scarification. (C) Chemical etch. Hydrochloric acid soln. (15% by wt.).	<ul style="list-style-type: none"> Wash thoroughly with water. Remove all dust. Spread solution with a stiff bristle broom. Remove sludge with water from high pressure hose. Check with litmus paper for residual acid. If present, rinse with 1% ammonia. Flush with water. Allow to dry.
Stonework	Dry thoroughly.	Abrade using a wire brush.	<ul style="list-style-type: none"> Remove all contaminants.
Wood	Dry thoroughly.	Decontaminate with a sander, plane, smooth with sandpaper.	<ul style="list-style-type: none"> Remove all contaminants.

Hysol® is a registered trademark of Henkel Corporation.

Rev. 1/01

DISCLAIMER: The information supplied in this document is for guidance only and should not be construed as a warranty. All implied warranties are expressly disclaimed, including without limitation any warranty of merchantability and fitness for use. All users of the materials are responsible for assuring that it is suitable for their needs, environmental and use. All data is subject to change as Henkel deems appropriate.

Users should review the Materials Safety Data Sheet (MSDS) and product label for the material to determine possible health hazards, appropriate engineering controls and precautions to be observed in using the material. Copies of the MSDS and label are available upon request.



Henkel Corporation
 Aerospace Group
 2850 Willow Pass Road
 P.O. Box 312
 Bay Point, CA 94565 USA
 925.458.8000
 www.aerospace.henkel.com

LT-4536

Appendix H – SikaBlock® M700 Datasheet

SikaBlock® M700

Model board

Areas of Application

- Manufacture of data control models and cubings
- Manufacture of master models
- Manufacture of moulds for low pressure reaction injection moulding
- Vacuum forming moulds for lower number of pieces

Product Benefits

- Very high dimensional stability
- High compressive strength and edge stability
- Good solvent resistance
- High heat distortion temperature
- Easy machinability
- Low dust formation when milled
- Very dense, fine surface
- Easy to seal and good to varnish

Description

- Basis Polyurethane, light brown
- Adhesive **Biresin® Kleber braun Neu**, two component PUR system, brown
- Filler **Biresin® Spachtel braun Neu**, two component polyester system, brown

Physical Data (approx. -values)

SikaBlock® M700			
Density	ISO 845	g/cm ³	0.7
Shore hardness	ISO 868	-	D 66
Flexural strength	ISO 178	MPa	26
E-Modulus	ISO 178	MPa	1,000
Compressive strength	ISO 604	MPa	25*
Impact resistance	ISO 179 Ue	kJ/m ²	7
Heat distortion temperature	ISO 75 B	°C	90
Linear thermal expansion coefficient α_T	DIN 53 752	K ⁻¹	55×10^{-6}

* at 10% compressive strain

Processing Data

		Biresin® Kleber braun Neu	Biresin® Spachtel braun Neu
Adhesive / Filler			
Mixing ratio A : B	in parts by weight	100 : 65	100 : 2
Potlife	min	20	5
Setting time	h	8 - 10	> 20 min

Packaging

Board materials	SikaBlock® M700	1500 mm x 500 mm x 30 mm, 30 pieces / pallet 1500 mm x 500 mm x 50 mm, 36 pieces / pallet 1500 mm x 500 mm x 75 mm, 24 pieces / pallet 1500 mm x 500 mm x 100 mm, 18 pieces / pallet 1500 mm x 500 mm x 150 mm, 12 pieces / pallet
Adhesive	Biresin® Kleber braun Neu , resin (A) Biresin® G53 , hardener (B)	1.5 kg net 4 kg; 0.975 kg net
Filler	Biresin® Spachtel braun Neu , resin (A) BPO-Paste , hardener (B)	2 x 8.34 kg net cartridges (A) 6 x 1.76 kg net tins (A) in a box 2 x 0.16 kg net sticks (B) (for cartridges - A) 6 x 0.04 kg net tubes (B) in a box (for tins - A)

Processing

- The material must be acclimatised to 18 - 25°C prior to machining.
- Machining of the block is easily accomplished by sawing, milling and so on with high performance tools or by hand.
- Bonding areas must be clean, dry and free of dust and grease or oil. For bondings use e. g. Biresin® Kleber braun Neu (for more information see Technical Data Sheet).
- For more information about milling please seek advice from cutting tool manufacturer or our separate leaflet.
- For correction or finishing of surface use Biresin® Spachtel braun Neu (for more information see Product Data Sheet).

Storage

- Product has un-limited shelf life when stored flat in dry conditions.
- During storage and transport of finished tools and models temperature variations should be kept as moderate as could be.

Health and Safety Information

For information and advice on the safe handling, storage and disposal of chemical products, users shall refer to the most recent Safety Data Sheet (SDS) containing physical, ecological, toxicological and other safety related data.

Disposal considerations

Product Recommendations: Must be disposed of in a special waste disposal unit in accordance with the corresponding regulations.

Packaging Recommendations: Completely emptied packagings can be given for recycling. Packaging that cannot be cleaned should be disposed of as product waste.

Value Bases

All technical data stated in this Product Data Sheet are based on laboratory tests. Actual measured data may vary due to circumstances beyond our control.

Legal Notice

The information, and, in particular, the recommendations relating to the application and end-use of Sika products, are given in good faith based on Sika's current knowledge and experience of the products when properly stored, handled and applied under normal conditions in accordance with Sika's recommendations. In practice, the differences in materials, substrates and actual site conditions are such that no warranty in respect of merchantability or of fitness for a particular purpose, nor any liability arising out of any legal relationship whatsoever, can be inferred either from this information, or from any written recommendations, or from any other advice offered. The user of the product must test the product's suitability for the intended application and purpose. Sika reserves the right to change the properties of its products. The proprietary rights of third parties must be observed. All orders are accepted subject to our current terms of sale and delivery. Users must always refer to the most recent issue of the local Product Data Sheet for the product concerned, copies of which will be supplied on request.

Further information available at:

Sika Deutschland GmbH
Subsidiary Bad Urach Tel: +49 (0) 7125 940 492
Stuttgarter Str. 139 Fax: +49 (0) 7125 940 401
D - 72574 Bad Urach Email: tooling@de.sika.com
Germany Internet: www.sika.com



BUILDING TRUST

